Laser-Accelerated Proton Beams as a New Particle Source

Laserbeschleunigte Protonenstrahlen als neue Teilchenquelle
Zur Erlangung des Grades eines Doktors der Naturwissenschaften (Dr. rer. nat.)
genehmigte Dissertation von Dipl.-Phys. Frank Nürnberg aus Offenbach am Main
November 2010 — Darmstadt — D 17

Laser-Accelerated Proton Beams as a New Particle Source
Laserbeschleunigte Protonenstrahlen als neue Teilchenquelle

genehmigte Dissertation von Dipl.-Phys. Frank Nürnberg aus Offenbach am Main

1. Gutachten: Prof. Dr. Markus Roth
2. Gutachten: Professor Dr. Dr. h.c./RUS Dieter H.H. Hoffmann

Tag der Einreichung: 30.09.2010
Tag der Prüfung: 15.11.2010

Darmstadt — D 17

XSELR8R

Zusammenfassung

Die vorliegende wissenschaftliche Arbeit befasst sich mit der Erzeugung von Protonenstrahlen durch Hochintensitätslaser. Aktuelle Hochleistungslaser können sehr kurze Laserpulse mit Intensitäten bis zu 10^{21} W/cm^2 erzeugen. Wenn diese auf dünne Metallfolien fokussiert werden, bilden sich auf der Folienrückseite Feldgradienten in der Größenordnung von TV/m aus, die eine Beschleunigung von Protonen bis zu mehreren MeV ermöglichen. Die Strahlen weisen ein exponentielles Spektrum mit bis zu 10^{13} Teilchen auf. Dieser Prozess der sogenannten *Target Normal Sheath Acceleration* (TNSA) beschleunigt Protonenstrahlen, die in manchen Strahleigenschaften konventionelle Protonenquellen übertreffen.

Im Rahmen dieser Arbeit wurde eine Messtechnik entwickelt, die es ermöglicht, mit Hilfe von Strahlabbildungen in radiochromischen Filmen (*radiochromic film imaging spectroscopy* – RIS) den gesamten laserbeschleunigten Protonenstrahl zu rekonstruieren. RIS charakterisiert den Protonenstrahl in Bezug auf reale und virtuelle Quellgröße, Öffnungswinkel und Mikro-Divergenz, normalisierte transversale Emittanz, Phasenraum und Energieverteilung. Hierfür wurden besondere Goldfolien mit einer rückseitigen, Mikrometer großen Linienstruktur hergestellt. Als hochauflösenden Protonendetektor wurden kalibrierte *GafChromic* radiochromische Dosimetriefilme in Stapelanordnung verwendet, die eine räumliche und spektrale Auflösung ermöglichen. Da die Expansion des Protonenstrahls einer Plasmaexpansion mit begleitenden Elektronen entspricht, wurde eine Elektronenspektrometer entwickelt, gebaut und getestet, um den niederenergetischen Teil des Elektronenspektrums zu vermessen, der mit dem Energiebereich des Protonenstrahls assoziiert wird. In positiv geladenen Teilchenstrahlen mit hoher Teilchendichte tragen Elektronen wesentlich zur Ladungsneutralisation bei und minimieren Raumladungseffekte. Erste experimentelle Ergebnisse zeigen ein Elektronenspektrum, das nicht die erwartete exponentielle Form aufweist, sondern eine spitze Verteilung um eine mittlere Energie. Es ist nicht an die Protonenverteilung gekoppelt, was demnach eher einer adiabatischen Expansion der Elektronen um den Protonenstrahl entspricht und nicht einer erwarteten Expansion von mitfliegenden Elektronen ($v_e = v_p$) mit exponentieller Energieverteilung.

Am VULCAN Petawatt Lasersystem wurden zwei Experimente durchgeführt, deren Ziel die dynamisch Kontrolle und Verbesserung der Protonenbeschleunigung durch Benutzung von mehreren Laserpulsen und defokussiertem Laserlicht war. Mit einem langen Laserpuls niedriger Intensität (10^{12} W/cm^2) wurde auf der Folienvorderseite vor dem Erreichen des Hauptpulses ($\sim$ns) ein Vorplasma erzeugt. Bei einer optimalen Vorplasma-Skalenlänge von 60 µm konnte eine Erhöhung der maximalen Protonenenergie (bis zu 25%) und des Protonenflusses (Faktor 3), sowie eine Verbesserung des Strahlprofils beobachtet werden. Die Ergebnisse der zweiten Kampagne führten auch zu einer signifikanten Erhöhung des Protonenflusses. Hier wurde der intensive Laserpuls auf die Folienvorderseite defokussiert. Laserpulse mit niedriger Intensität und einem größeren Fokus in Kombination mit dünneren Targetfolien ermöglicht eine effizientere Erzeugung von Protonenstrahlen wie bei Verwendung von Standardparametern. Ein Optimum wurde erreicht für Foliendicken von 2 µm, einer Intensität von 10^{19} W/cm^2 und einem Fokusdurchmesser von 60 µm. Im Experiment konnten Laser- zu Protonenenergie Konversionseffizienzen von bis zu 7.8% gemessen werden (vorher 2.2%), die den bis jetzt am höchsten gemessenen Werten entsprechen. Desweiteren führte RIS zu einem tieferen Verständnis des Optimierungsprozesses und der gemessenen Protonenparametern. Im Rahmen dieser Arbeit wurden am TRIDENT Lasersystem zwei weitere Experimente durchgeführt, in denen gezeigt werden konnte, dass diese Protonenstrahlen mit ihren hohen Teilchenzahlen und kurzen Pulsdauern für die Erzeugung von isochor-geheizten, extremen Materiezuständen sehr gut geeignet sind.

Neben der direkten Manipulation von Protonenstrahlparametern während der eigentlichen Erzeugung lag das Hauptaugenmerk dieser Arbeit auf dem Einfangen, der Kontrolle und dem Transport von laserbeschleunigten Protonenstrahlen mit Hilfe eines Solenoiden. Die Arbeitsgruppe Laser- und Plasmaphysik der Technischen Universität Darmstadt hat die Entwicklung eines Teststands zum Transport, zur Fokussierung und zur Phasenrotation dieser Strahlen mit konventionellen Ionenoptiken und RF Technologien angestoßen. In Zusammenarbeit mit der Beschleunigerabteilung des GSI Helmholtzzentrums für Schwerionenforschung wird die mögliche Injektion in einen Nachbeschleuniger untersucht. Diesem Projekt untergeordnet wurde am PHELIX System ein Experiment zum Einfang laserbeschleunigter Protonenstrahlen durchgeführt. Im Vergleich zu früheren Experimenten mit permanenten Quadupolen konnte eine deutliche Verbesserung der Protonentransmission durch den Solenoiden ohne Verlust der Strahlqualität erzielt werden. Mit einer Feldstärke von 7.5 T konnte erstmals ein Protonenstrahl bei einer Energie $>$10 MeV kollimiert werden. Zusätzlich wurde im Fokussiermodus bei einem Abstand von 40 cm von der Quelle eine Protonenflusserhöhung von bis zu einem Faktor von 174 erreicht im Vergleich zu einem Strahl ohne Benutzung des Magnetfeldes.

Für eine quantitative Analyse des Experiments wurden numerische Simulationen mit dem WarpRZ Code durchgeführt. Im Rahmen dieser Arbeit konnte der Code, der eigentlich für Studien von Ionenstrahlen hoher Teilchendichten und zur Forschung auf dem Gebiet der Schwerionen getriebenen Trägheitsfusion verwendet wird, modifiziert werden, so dass nun laserbeschleunigte Protonen als Teilchenquelle eingebunden werden können. Zusätzlich werden alle energieabhängigen Strahlparameter miteinbezogen, die mit RIS experimentell bestimmt wurden. Die Kriterien, die im Rahmen von Plasmaphysik Simulationen berücksichtigt werden müssen, wurden im Detail untersucht, und eine exakte Kopie des Experimentaufbaus beschreibt im Code die geometrischen Randbedingungen. Bei Vergleich mit den experimentellen Ergebnissen zeigt sich eine sehr genaue Übereinstimmung mit dem simulierten Filmstapel. Die Raumladungseffekte der eingebundenen Elektronen konnten klar herausgearbeitet werden und haben einen maßgeblichen Einfluss auf die Protonenstrahlpropagation. 2.99×10^9 kollimierte Protonen in einem Energiebereich von 13.5$\pm$1 MeV (ΔE/E = 7%) konnten mit diesem Aufbau über eine Strecke von 40 cm transportiert werden. Desweiteren wurden 8.42×10^9 Protonen in einem Energiebereich von 6.7$\pm$0.2 MeV (ΔE/E = 3%) auf einen Fleck mit einem Durchmesser von $<$2 mm fokussiert. Die erzielte Transmission durch den Solenoiden beträgt für beide Fälle 18%.

Die im Rahmen dieser Arbeit durchgeführten Experimente und Simulationen sind die Basis für die Realisierung des Teststand Projektes zur Einkopplung laserbeschleunigter Protonenstrahlen in konventionelle Beschleunigerstrukturen. Darüber hinaus ermöglicht der entwickelte Simulationscode zukünftige Parameterstudien bevor ein Experiment durchgeführt wird, um somit die Strahlparameter für weitere Anwendung direkt anpassen zu können.

Abstract

The framework of this thesis is the investigation of the generation of proton beams using high-intensity laser pulses. Today's high power, ultrashort pulse laser systems are capable of achieving laser intensities up to 10^{21} W/cm^2. When focused onto thin foil targets, extremely high field gradients of the order of TV/m are produced on the rear side of the target resulting in the acceleration of protons to multi-MeV energies with an exponential spectrum including up to 10^{13} particles. This acceleration process, called *Target Normal Sheath Acceleration* (TNSA), generates high-current proton beams with characteristics that are superior to properties from conventional proton sources.

In this work, an experimental method to fully reconstruct laser-accelerated proton beam parameters, called *radiochromic film imaging spectroscopy* (RIS), was developed. RIS allows for the characterization of proton beams concerning real and virtual source size, envelope- and microdivergence, normalized transverse emittance, phase space, and proton spectrum. Therefore, thin gold foils with a microgrooved rear side were manufactured and characterized. Calibrated *GafChromic* radiochromic films in stack configuration were used as spatial and energy resolved proton detector. The target rear side structure is transported by the beam, mapped into the detector and retains information about the beam. Since the proton beam expansion is a plasma expansion with accompanying electrons, a low-energy electron spectrometer was developed, built and tested to study the electron distribution matching to the proton beam energy distribution. Electrons in high-current proton beams have significant influence on beam neutralisation and space-charge effects. First experimental results show, that the observed electron spectrum is apparently not of the expected exponential shape, but more a peaked distribution around an avergage energy. Hence, it is not coupled to the proton spectrum, which argues for an adiabatic expansion of the electrons around the proton beam instead of co-moving electrons ($v_e = v_p$) with an exponential energy distribution.

Two experiments were carried out at the VULCAN Petawatt laser with the aim of showing dynamic control and enhancement of proton acceleration using multiple or defocused laser pulses. Irradiating the target with a long pulse, low-intensity laser (10^{12} W/cm^2) prior to the main pulse ($\sim$ns), an optimum pre-plasma density scale length of 60 µm is generated leading to an enhancement of the maximum proton energy ($\sim$25%), the proton flux (factor of 3) and the beam uniformity. The experimental results of the second campaign on defocusing of high-intensity laser pulses onto the target show significant improvements in proton flux. Proton beams were generated more efficiently than previously by driving thinner target foils at a lower intensity over a large area. The optimum condition was a 2 µm foil irradiated with an intensity of 10^{19} W/cm^2 onto a 60 µm spot. Laser to proton beam efficiencies of 7.8% have been achieved (2.2% before) – one of the highest conversion efficiencies ever achieved. RIS has contributed significantly to the understanding of the beam optimisation process and the proton parameters. In the frame of this work, two separate experiments at the TRIDENT laser system have shown that these laser-accelerated proton beams, with their high number of particles in a short pulse duration, are well-suited for creating isochorically heated matter in extreme conditions.

Besides the manipulation of the proton beam parameters directly during the generation, the primary aim of this thesis was the capture, control and transport of laser-accelerated proton beams by a solenoidal magnetic field lense for further purpose. In a joint project proposal, the laser and plasma physics group of the Technische Universität Darmstadt initiated the development of a test stand to transport, focus and bunch rotate these beams by conventional ion optics and RF technology. In collaboration with the accelerator department of the GSI Helmholtzzentrum für Schwerionenforschung,

a possible injection into a post-acceleration unit will be studied. Subordinated to this project, an experimental campaign to capture laser-accelerated proton beams was carried out at the PHELIX system. Compared to previous experiments, a significant increase in proton transmission through the solenoid could be achieved by maintaining the beam quality. The field strength of 7.5 T enabled collimation of protons with an energy of $>$10 MeV for the first time. In addition, the focusing capability of the solenoid provided a flux increase in the focal spot of about a factor of 174 at a distance of 40 cm from the source, compared to a beam without using the magnetic field.

For a quantitative analysis of the experiment numerical simulations with the WarpRZ code were performed. The code, which was originally developed to study high current ion beams and aid in the pursuit of heavy-ion driven inertial confinement fusion, was modified to enable the use of laser-accelerated proton beams as particle source. The calculated energy-resolved beam parameters of RIS could be included, and the plasma simulation criteria were studied in detail. The geometrical boundaries of the experimental setup were used in the simulations. The results from the virtual simulated film stack show a remarkable agreement with the observed proton signals in the film stack of the experiment. The importance of the space-charge effects of the electrons (included as second particle species) could be pointed out showing a significant influence on the results. 2.99×10^9 collimated protons in the energy range of 13.5$\pm$1 MeV (ΔE/E = 7%) could be transported over a distance of 40 cm. In addition, 8.42×10^9 protons in the energy range of 6.7$\pm$0.2 MeV (ΔE/E = 3%) were focused into a spot of $<$2 mm in diameter. The transmission through the solenoid for both cases was about 18%.

The experiments and simulations carried out in the scope of this work are the basis for the realization of the test stand for coupling laser-accelerated proton beams into conventional accelerators structures. Furthermore, the code development enables future parameter studies prior to experimentation to optimize the output for additional applications.

Contents

1 Introduction

Particle beams from accelerators as a tool in research have told us almost everything we know about nature's fundamental forces and the essential building blocks all matter is composed of. Today it is possible to create laboratory conditions that have occurred only shortly after the Big Bang. Such accelerators reveal nature's deepest mysteries. But this is only a small part of the reasons to care. An incredible number of accelerators, from gigantic machines to only room-sized or smaller, serve as tools for basic research and material science, for diagnosing and treating illnesses, and for a growing host of tasks in manufacturing and energy technology.

The earliest particle accelerators, such as Van de Graaff or Cockcroft-Walton accelerators, used static electric fields to accelerate charged particles to energies conventional voltage sources could not provide. In the 1920's, Wideröe pointed directly toward the modern linear accelerator. The principle of a DC voltage acceleration was replaced by an AC linear accelerator of several acceleration elements to overcome arcing, because higher voltages are required to reach higher particle energies. Almost 10 years later, Lawrence was the first who applied the work of Wideröe to a circular accelerator when he invented the cyclotron. The cyclotron opened up a totally new field of research in nuclear physics, including the production of unstable nuclei and non-naturally occurring elements. It also enabled particle-beam treatment of cancer. Since then, technology advances have driven a million-fold increase in accelerator energies. The now upcoming Large Hadron Collider (at CERN, Genf, Suisse) is one of the grandest scientific instruments ever built.

But longer-term accelerator research is exploratory and aims for developing new concepts and acceleration technologies, because the accelerator size becomes huge and the construction costs explode. High-intense laser systems are capable of accelerating ions with self generated electric fields in excess of 10^{12} V/m. These fields are higher by several orders of magnitude compared to conventional particle accelerators that usually operate at 10^{8} V/m. Simulations have shown that those higher fields lead to an acceleration length of the order of 1 mm at most for particles in the energy range of several 100 MeV. Therefore, high-power lasers are a promising alternative to conventional radio-frequency-based accelerators.

Based on this idea the Technische Universität Darmstadt initiated the project of developing a *test stand* to transport, focus and phase rotate laser generated proton bunches by conventional ion optics and RF technology. In the frame of the project, this thesis deals with experimental and numerical support to implement this project at the GSI Helmholtzzentrum für Schwerionenforschung, where the capabilities of PHELIX as a world-class high power laser is combined with the accelerator know-how of GSI.

1.1 Laser-Accelerated Ion Beams

Since the invention of the laser in 1960 [1], the interaction of laser light with matter is an extensive research area. With the advent of Chirped-Pulse-Amplification (CPA) in 1982 [2], high energy laser systems with very short, ultra-intense pulses could be developed. Beyond intensities of 10^{18} W/cm^2 a large variety of new phenomena opens up. The motion of electrons in the electromagnetic field of the laser becomes relativistic, as the electron velocity approaches the speed of light within only one oscillation period. Today's laser laboratories develope or already reach peak powers in the order of a petawatt (10^{15} W) pushing the limit of achievable intensities beyond 10^{21} W/cm^2 [3–6].

By irradiating solid matter with intense laser pulses, the light wave couples to the electrons of the target, which start to oscillate in the electromagnetic field. The intensity of the prepulse or the rising edge of the pulse is already high enough (10^{12} W/cm^2) to couple a sufficient amount of laser energy into the target to ionize the surface layer. The matter heats up, a plasma evolves and expands, and the main part of the laser pulse now interacts with this plasma. Emerging electric fields are capable of accelerating particles. During the last decade of laser development, a dramatic increase of particle energies accelerated in laser-plasma experiments could be achieved. Collimated electron beams are most efficiently accelerated with energies in the range of several keV to more than a GeV [7–9]. Laser-plasmas also represent X-ray sources in the MeV-range [10, 11], and with laser-induced fusion reactions neutrons can be generated [12, 13].

In the past 30 years, ion acceleration by intense laser beams has been extensively studied and promoted. The production of ions up to energies of several 100 keV was well known [14, 15]. But the observation of directed multi-MeV ions, mostly protons, during the interaction of high-intensity laser pulses with thin foils has attracted a great deal of attention due to the unique properties of such beams [16–21]. Laser-accelerated proton beams originating from water vapor and hydrocarbon contaminations on the target rear surfaces [22] exhibit a remarkably low emittance and an almost laminar flow [23, 24]. Containing up to 10^{13} particles in a pulse duration comparable to the laser pulse duration ($<$1 ps), such beams are well suited for a number of applications, e.g. as diagnostic tool in proton radiography experiments [25], as a compact particle accelerator [26, 27] for the creation of high-energy density (HED) matter [28], or for proton fast ignition [29]. In addition, there are already studies in relation to a possible application in medicine for radiation therapy [30, 31].

For all the applications, the generation of proton beams with controllable and reproducible parameters such as energy spectrum, brightness, and spatial profile is crucial. However, the relativistic laser matter interaction and ion acceleration is very complex and up to now not really understood in detail. Nevertheless, the basic mechanisms driving the ion acceleration have been found. The laser field accelerates electrons by various mechanisms to relativistic energies. The bulk of this electrons propagate into the target foil. As soon as they leave the target and enter the vacuum at the rear side, a strong electric field is created due to the displacement of a large number of electrons. Compared to the fast oscillating laser field, these space-charge fields are stable on a time scale of up to picoseconds but have a field strength of the same order of magnitude as the laser field. This field is able to ionize the protons at the surface, which are then accelerated in target normal direction.

Following the first measurements, the process of laser-driven ion acceleration has been investigated by several experimental teams under very different physical conditions and using laser systems with different characteristics (review in reference [32]), because each system covers only a small parameter range. More than three orders of magnitude in focused laser intensity have been used, from few times 10^{17} W/cm^2 [26, 33] up to a few 10^{20} W/cm^2 [18, 34]. A wide range of target thicknesses have been explored, ranging from tens of nm [35, 36] over a few µm [16, 37], up to hundreds [18, 19, 21, 38], or even thousands of µm [26, 39] of different materials, e.g. Al, Au, Cu, Pb, Si, Ti, Mo, C or Mylar. Even cleaned targets [21], coated foils [40] and shaped target configurations [28, 41] were used to optimize the ion beam output. Up to now there is no analytical model or computer simulation covering the entire process. A lot of experiments have been done and there are still various questions open. Ongoing studies bring more pieces of the puzzle together and eventually lead to a better understanding of the optimization and the control of of the full laser-ion acceleration mechanism.

In the past four years, several groups worldwide follow a different approach to optimize laser-accelerated proton beams concerning future applications. Great efforts were done to externally compensate the main drawbacks. On the one hand, the proton spectrum matches an exponential distribution with a laser and target parameter dependent high-energy cutoff. Compared to particle bunches injected into conventional accelerators, the large production energy spread of up to 100% is far away

from the required value of $<1\%$, e.g. for precise focusing on a tumor [42] or post-acceleration [43]. On the other hand, the ion emission from the rear side of the foil is indeed directed, but it still has a full envelope-divergence of up to 60° [44] leading to a decreasing cross section density or a considerable loss of particles during injection into a post-accelerator. Different approches were tested to collimate or focus laser-accelerated proton beams: the laser triggered microlense to focus a particular energy interval [45], a more stable setup of permanent magnet quadrupoles to transport protons over longer distances [46, 47] or a first test of a pulsed high-field solenoid to increase the capture efficiency and preserve the beam homogeneity [48]. In addition, a debuncher device was tested to phase-rotate the beam distribution to achieve intervals with a small energy spread and an increased number of particles [49].

The work presented in this thesis combines both approaches. One main topic is the active, optical control of the acceleration process either by variation of parameters of the main driver laser pulse, or by using other separately controlled laser pulses to change the plasma conditions. And on the other hand, on basis of the past findings, an optimized pulsed solenoid was developed and successfully tested. Laser-accelerated protons could be collimated and transported over a distance of 40 cm. Particle-in-cell simulations focus on gaining a deeper understanding of the physics behind the transport of this special high-current beams including a picture of the occuring space-charge effects. In conclusion, the combination of optimization process during the proton beam generation and the subsequent ion optic which catches and controls the beam, enables beam parameter which are promising for future applications.

1.2 Thesis Structure

The thesis is divided into four major parts.

In chapter 2, an introduction to the physics of laser-plasma interaction will be given. The theoretical concept of energy absorption, electron acceleration and proton beam formation is presented. In terms of beam transport, the relevant parts of accelerator physics are addressed related to laser-accelerated proton beams.

In the second part, the main tool to characterize laser-accelerated proton beams is described. In chapter 3, a method called *Radiochromic Film Imaging Spectroscopy* is invented which enables energy resolved measurements of almost all beam parameters. Therefore, a film detector was absolutely calibrated and tested at different laser systems. In addition, a spectrometer to measure the low-energy spectrum of the accompanying electrons is explained, and the general setup of an experiment to accelerate protons by intense laser pulses will be illustrated in detail.

The third part covers the experiments carried out at the VULCAN Petawatt system and at the TRIDENT facility, described in chapter 4. Here the focus is on optical manipulation and control of the proton acceleration mechanism. Using multiple laser pulses or defocusing the main laser pulse lead to an enhancement in proton flux and beam quality. In an continuative experiment, a possible application of laser-accelerated protons is presented. The spectral behaviour and the short pulse duration make them suitable to heat samples up to the region called *warm dense matter*.

The fourth and main part of the thesis is dedicated to experimental observations and simulation studies on capture and control of laser-accelerated proton beams with a solenoidal magnetic field. An optimized solenoid lens is used at the PHELIX system to collimate and focus protons (chapter 5). Parallel particle-in-cell simulations with the Warp code illustrate the physics behind the experiment, allow a quantitative analysis and highlight the importance of space-charge forces in high-current beams of charged particles (chapter 6).

Finally, chapter 7 and 8 summarise this work and give a perspective for the future, suggesting further experiments and numerical investigations concerning the capture, transport and control of laser-accelerated proton beams. In addition, the future project of a *test stand* close to the PHELIX laser and the transport beamline to the heavy ion synchotron at the GSI Helmholtzzentrum für Schwerionenforschung is presented. The proof of principle experiments and the simulations shown in this thesis are parts of the project which allows a realization in the near future.

2 Proton Generation by Laser-Matter Interaction

During the interaction of ultra-short laser pulses exceeding intensities of 10^{18} W/cm^2 with solid targets, the laser pulse interacts with a highly ionised and strongly preheated plasma on the target frontside. This pre-plasma has been formed by the unavoidable low-intensity prepulse pedestal of the laser due to amplified spontaneous emission (ASE), by pre-pulses or by the leading edge of the main pulse itself. The laser field accelerates plasma electrons to velocities close to the speed of light, where relativistic effects dominate the electron motion. At these laser intensities, a large fraction of the laser-pulse energy is converted into kinetic energy of relativistic electrons. Furthermore, the electrons in the MeV-range propagate through the target and escape. Due to the charge separation caused by the leaving electrons and the resulting positive charged target, the generated electric field at the rear surface is capable of accelerating ions to kinetic energies in the MeV-range. In this chapter, the underlying mechanisms of the laser- or rather electron-induced ion acceleration are described on the basis of the interaction of the laser pulse with plasma electrons. In the past 10 years, a large number of publications appeared describing the physics of the laser-matter interaction. In this thesis only a part is mentioned as references.

2.1 Laser-Plasma Interaction and Electron Acceleration

All laser experiments described in the following chapters have been carried out with linear polarized laser pulses. The electromagnetic wave propagating in z-direction is given as the solution of Maxwell's equations of electromagnetism

$$\mathbf{E} = E_0\,\mathbf{e}_x\,\exp\left[i\left(\mathbf{k}\,\mathbf{z}-\omega_L t\right)\right] \tag{2.1}$$

$$\mathbf{B} = \frac{1}{c}\,E_0\,\mathbf{e}_y\,\exp\left[i\left(\mathbf{k}\,\mathbf{z}-\omega_L t\right)\right]] \tag{2.2}$$

where E_0 is the laser electric field amplitude, ω_L the laser angular frequency, c the speed of light, k the laser wave vector, t the time and $e_{x,y}$ the unit vectors defining the orthogonality of E, B and the propagation direction z.

The intensity of the laser pulse is equal to the energy flux density (the Poynting vector) time averaged over the fast oscillations of the laser field

$$I = \left\langle \left| \mathbf{E} \times \frac{\mathbf{B}}{\mu_0} \right| \right\rangle = \frac{\epsilon_0\, c}{2} E_0^2 \tag{2.3}$$

where μ_0 is the permeability and ϵ_0 the permittivity of the vacuum. Hence, a laser pulse with an intensity above 10^{18} W/cm^2 has a corresponding electric field amplitude of $E_0 \approx 3$ TV/m. With the relationship between the electric and magnetic field amplitude $B_0 = E_0/c$, one obtains the corresponding magnetic field amplitude $B_0 \approx 10^4$ T.

2.1.1 Electrons in the Laser Field

These fields interact with free electrons of the plasma. A single electron of charge e and mass m_e is described by its equation of motion (*Lorentz* equation)

$$\frac{\mathrm{d}\mathbf{p}}{\mathrm{d}t} = \frac{\mathrm{d}}{\mathrm{d}t}\left(\gamma m_e \mathbf{v}\right) = -e\left(\mathbf{E} + \mathbf{v} \times \mathbf{B}\right) \tag{2.4}$$

where $\mathbf{v}$ and $\mathbf{p}$ are velocity and momentum of the electron, respectively. $\gamma = 1/\sqrt{1-\beta^2} = \sqrt{1 + \left(|\mathbf{p}|\,/m_e c\right)^2}$ is the relativistic Lorentz factor, $\beta = v/c$. To differentiate between three present regimes, the dimensionless electric field amplitude a_0 is introduced

$$a_0 = \frac{e\,E_0}{m_e \omega_L c}. \tag{2.5}$$

In the classical, non-relativistic regime $a_0 \ll 1$ where $\gamma \approx 1$, the electron motion is dominated by the electric field. The solution of equation (2.4) leads to a harmonic oscillation in x-direction. Nevertheless, at the end of the laser pulse the electron velocity is zero again, because it does not gain energy from the laser, which is know as the *Lawson-Woodward* theorem [50]. For $a_0 \approx 1$ the electron approaches the speed of light already during a laser-half cycle and the interaction has to be treated fully relativistic. For $a_0 \gg 1$, the regime is called ultra-relativistic. In the experiments described in this thesis, the average intensity on target was 3×10^{19} W/cm^2 with a laser wave length of $\lambda_L = 1.054$ µm resulting in a dimensionless electric field amplitude of $a_0 \approx 5$.

In reality, laser pulses are far from being an ideal plain wave, which is the assumption for solving the classical case above. The laser is tightly focused resulting in a varying transverse intensity profile. The electron starting on the laser axis, where the fields are at maximum, is displaced sideways during the first laser-half cycle into regions of reduced intensity. Thus the restoring force acting on the electron is smaller and it will experience a weaker return effect during the second half-cycle of the laser oscillation. The electron does not return to its initial position and finally leaves the focus with a finite velocity. The force driving it away from regions of higher intensity is called the **ponderomotive force** [51, 52]. The ponderomotive force for a single electron is given by

$$\mathbf{F}_p = -\frac{1}{4}\frac{e^2}{m_e\,\omega_L^2}\nabla\left(\mathbf{E}\cdot\mathbf{E}^*\right) \tag{2.6}$$

Up to this point, only the interaction of a single electron with the laser field is described. The rising electrostatic potential due to laser-induced charge separation has been neglected. This effects has significant influence on the collective behaviour of the plasma electrons, as will be shown below.

Compared to electrons, ions have a much higher rest mass leading to an increased electric field amplitude a_0. Protons for example, as the lightest ion ($m_p = 1836 m_e$), have their relativistic threshold not at $a_0 = 1$ but at $a_0 = 1836$ resulting in a required intensity of $>10^{24}$ W/cm^2 for $\lambda_L = 1.054$ µm. This is far beyond the present laser development. Laser fields of current laser systems can not trigger relativistic proton oscillations as for electrons. So the plasma ions are assumed to form an immobile, positively charged background.

The correct equation of motion in a plasma for the relativistic case has been derived by Bauer *et al.* [53]. The solution is very complicated and has to be done numerically, because the force is a nonlinear function of the electron's momentum and position. The time averaged kinetic energy electrons gain during

one laser cycle can be obtained by integrating the **ponderomotive potential** U_p via $F_p = m_e \nabla U_p$. The energy W_p gained by the relativistic ponderomotive potential can be expressed in terms of measurable laser parameters or with the dimensionless electric field amplitude a_0

$$W_p = m_e c^2 \left(\sqrt{1 + \frac{e^2 I \lambda^2}{4\pi^2 \epsilon_0 m_e^2 c^5}} - 1 \right) = m_e c^2 \left(\sqrt{1 + \frac{a_0^2}{2}} - 1 \right). \tag{2.7}$$

For laser intensities of around 3×10^{19} W/cm^2 and wave lengths of $\lambda_L = 1.054$ µm, one obtains for a proton $W_p^p = 1.7$ keV and for an electron $W_p^e = 1.3$ MeV.

Another important collective effect in a plasma is the characteristic of shielding electric fields. On a macroscopic scale, the electric field is compensated by an opposite orientated field generated by the arrangement of the charged particles in the plasma. The plasma appears to be quasi-neutral. But on a microscopic scale, the ions are encircled by electrons that shield the electric potential of the ions. In a homogeneous plasma, charge neutrality is provided on a scale larger than the characteristic shielding length λ_D

$$\lambda_D = \sqrt{\frac{\epsilon_0 \, k_B \, T_e}{n_e \, e^2}}. \tag{2.8}$$

λ_D is called the ***Debye* length**, k_B is the *Boltzmann* constant, T_e the electron temperature and n_e the electron density.

Light Propagation in a Plasma

As the laser propagates into a plasma, its electromagnetic field acts on the electrons. On the other hand, the collective behaviour of the electrons effects the laser propagation itself - an interplay. If the plasma electrons are displaced by the ponderomotive force, a restoring force builds up due to the electric fields arising from the charge separation and the electrons start to oscillate around the position of the charge equilibrium. The characteristic oscillation frequency of the collective motion of the electrons within the plasma is determined by solving the wave equation for a laser in a plasma leading to the dispersion relation [54]:

$$\omega^2 - \frac{e^2 \, n_e}{m_e \, \epsilon_0} = k^2 c^2. \tag{2.9}$$

For the relativistic case, the cycle-averaged gamma factor $\bar{\gamma} = \sqrt{1 + a_0^2/2}$ has to be included (can already be found in equation (2.7)) and the **electron plasma frequency** ω_p yields to

$$\omega_p = \sqrt{\frac{e^2 \, n_e}{\bar{\gamma} \, m_e \, \epsilon_0}}. \tag{2.10}$$

This frequency only depends on the density n_e of the plasma electrons. As long as the laser frequency $\omega = \omega_L$ exceeds the plasma frequency ω_p (see equation (2.9)), the wave can propagate in the plasma. As already mentioned, the pedestal of the laser pulse or even pre-pulses with intensities above 10^9 W/cm^2 [55] are able to create a inhomogeneous pre-plasma, which expands isothermal [56] with an exponentially decaying profile. The further the main laser pulse propagates into the plasma, the higher is the electron density. If ω_p approaches ω_L, the wave vector k approaches zero. Hence, at this point the

laser is unable to propagate any further and is reflected. The **critical density** n_c at which the reflection occurs can be defined by $\omega_p = \omega_L$:

$$n_c = \frac{\omega_L^2 \, \epsilon_0 \, \bar{\gamma} \, m_e}{e^2}. \tag{2.11}$$

The critical density is used to describe two different plasma regimes: the *underdense* plasma where $n_e < n_c$ and the *overdense* plasma where the density exceeds $n_c = 1.1 \times 10^{21}\ \mathrm{cm}^{-3}$, which is the calculated critical density for $\bar{\gamma} = 1$ and 1.054 µm laser wave length (for comparison: solid density $\sim 10^{23}\ \mathrm{cm}^{-3}$). In the relativistic case when $\bar{\gamma} > 1$ the critical density increases. Thus the laser light can propagate even further in the plasma. This characteristic behaviour is called **relativistic transparency** [57]. Furthermore, the laser light propagation is even more influenced, if the pulse is focused into the plasma. This leads to a reduction of the refractive index η_r of the plasma on the laser axis compared to the wings of the focus.

$$\eta_r = \sqrt{1 - \frac{\omega_p^2}{\omega_L^2}} = \sqrt{1 - \frac{n_e}{n_c}} \tag{2.12}$$

The ponderomotive force, as discussed earlier, displaces plasma electrons out of the region of higher laser intensity. The radial-dependent electron distribution results in a refractive index profile with a maximum on the laser axis. This profile acts like a convex lens and focusses the laser pulse even more and thereby increasing its intensity further. This effect is known as **relativistic self-focusing** [58, 59].

2.1.2 Laser Absorption and Electron Acceleration

A large number of absorption mechanisms contributes to the electron heating indicating that the laser absorption and the hot electron generation is still not well understood. The transfer of laser energy into electrons depends on several effects, e.g. the density profile of the pre-plasma [60] or its size [61], laser pre-pulse effects [62] as well as the irradiation under non-normal incidence [33]. In this section, the main heating mechanisms will be pointed out.

For laser pulses with durations of the order of 1 ps, the radiation pressure $P_{rad} = 2I/c$ has significant influence on the laser absorption. At intensities of $5 \times 10^{19}\ \mathrm{W/cm^2}$, the radiation pressure $P_{rad} = 3.3 \times 10^{10}$ bar is extremely high. Due to the material ablation from the front surface, a laser induced pressure wave travels into the solid material of the target to maintain momentum conservation. But in addition, the pressure pushes the critical density inwards. This effect is stronger in the center of the focus compared to its wings and leads to a hole in the overdense plasma. Hence, the effect is called **laser-hole boring** [63]. The convex deformation of the critical surface enables a better coupling of the electric field to the electrons increasing the energy absorption [64].

As already mentioned earlier, the ponderomotive force expels electrons from the focal region. Due to this charge separation, a plasma wave is generated following the laser pulse in its wake. The longitudinal electric field in the plasma wave can trap electrons, which can gain a large amount of kinetic energy. This efficient mechanism is called **laser wakefield acceleration** [65]. For very short and intense laser pulses, the scheme changes to the **bubble acceleration** [66]. Here, quasi-monoenergetic electron jets up to GeV energies are generated [9, 67]. If the region of underdense plasma on the front side of the target is very long (large plasma scale length), a plasma channel is formed along the laser axis. The ponderomotive force pushes radially electrons and additionally drive a strong electron current along the channel. This leads to the formation of strong radial electric fields and strong azimuthal magnetic fields due to the high current. Electrons are bent back on axis by these fields and start to oscillate in the channel. If the phases between electron and laser field match, the electron can gain a large amount of energy directly from the laser fields. This mechanism is called **direct laser acceleration** [68].

Energy can also be transfered to electrons by **inverse Bremsstrahlung**. Bremsstrahlung radiation is produced when an electron is de-accelerated by charged particles. Inverse Bremsstrahlung is the opposite phenomenon, where an electron is accelerated by the laser electric field resulting in a transfer of energy from the laser photons to the electrons. For intensities $>10^{18}$ W/cm^2, the effect is not important. The **resonance absorption** [56] for intensities in the same range is also not a dominant mechanism but contributes a fraction. If a laser pulse has an incident angle to the target normal axis and is p-polarized then the electric field component parallel to the plasma density gradient can resonantly excite an electron plasma wave, which results in an energy transfer from the laser either via wave breaking or through damping [52].

As soon as the plasma scale length (distance where the exponential density profile of the front side plasma is decayed to 1/exp(1) of the initial value) is of the order of the laser wave length [69], the resonance absorption turns into the phenomenon of vaccum heating. This effect also known as **Brunel heating** is one of the main mechanisms for laser absorption and electron acceleration. In vacuum, the electric field of the laser accelerates electrons sideways and due to the restoring force they start to oscillate around the laser axis. But in a plasma in regions close to the critical surface of the solid, the electrons are accelerated towards low density regions in the first laser-half cycle, turn round and are accelerated behind the critical density. Because the laser cannot penetrate into overdense regions, the electrons feel no restoring forces any more, can gain energy and enter the solid along the direction of the gradient.

The dominant mechanism for laser absorption at high intensities ($>10^{18}$ W/cm^2) is the **relativistic $\mathbf{j} \times \mathbf{B}$ heating** [70]. It depends on the high frequency $\mathbf{v} \times \mathbf{B}$ term of the *Lorentz* equation (2.4). Hence, it is most efficient for an angle of incidence at or near the target normal. The *Lorentz* force acts along the laser propagation axis and electrons are able to gain sufficient energy during oscillation to escape the laser field into the overdense plasma. The mean energy or the **effective temperature** $k_B T_e$ of the electron population accelerated in that way can be estimated by the ponderomotive potential, equation (2.7), to 1.3 MeV.

For intensities in the range of 10^{18}-10^{20} W/cm^2 the **conversion of laser light** to energy that is absorbed into the preplasma as fast electrons can be given by the following scaling [71]

$$\eta = 1.2 \times 10^{-15}\, I^{0.74}, \tag{2.13}$$

resulting in $\eta = 0.31$ for laser pulses used in experiments which are described in this thesis. Analytical models including intensities $>10^{20}$ W/cm^2 predict conversion efficiencies of 60% for near-normal incidence and up to 90% for irradiation under 45° [72]. The total number N_e of the electron population can be estimated to be the total energy of the population divided by their mean energy (with $E_L = 72$ J for example at PHELIX):

$$N_e \approx \frac{\eta\, E_L}{k_B\, T_e} = 1.1 \times 10^{14}. \tag{2.14}$$

2.1.3 Fast Electron Transport and Recirculation

The current available laser intensities are not high enough to enable a direct ion acceleration by the laser. The ion acceleration on the back side of the target is induced by hot electrons leaving into vacuum. Hence, the electron transport physics in dense plasmas is important to understand the energy transfer into the electrons. In the last section, mechanisms to accelerate up to 10^{14} hot electrons were described. As the acceleration process takes place within the laser pulse duration of $\tau_L = 500$ fs, the electron current entering the target can be calculated by $j_e = eN_e/\tau_L = 35$ MA. Assuming a straight electron

transport [73], the current creates a magnetic flux density of $\sim 7 \times 10^5$ T. By calculating the field energy, this huge magnetic field stores more energy than the laser field, which violates the energy conservation criterion. These self-generated magnetic fields prevent the fast electrons from propagating. The maximum current that can propagate without the self-generated magnetic fields is given by the ***Alfén* limit** $I_{max} = 1.7 \times 10^4 \beta\gamma$ [74] with the relativistic parameters β and γ. The above estimated electron current exceeds by far the *Alfén* limit of $I_{max} = 58\,\mathrm{kA}$. Hence, a **return current** j_{ret} must exist to ensure that the net current does not exceed the limit. This cold return current is drawn back towards the target front surface by the electron beam self-generated fields [73] and balances the forward propagating hot electrons.

Straight electron transport in a cylindrical volume is an easy assumption to estimate the current, but measurements demonstrate an **angular distribution** of the electrons injected into the dense plasma according to $\tan\theta = [2/(\gamma - 1)]^{0.5}$ [75]. This injection angle certainly depends on the pre-plasma density gradient and also on the incident laser direction. As soon as the electrons reach the cold solid region multiple small-angle scattering with the background material rises and broadens the electron distribution. Besides broadening, beam filamention can also occur during the transport in the solid. Two counter-propagating electron beams are highly unstable with respect to the **Weibel instability** [76]. Small local perbutations in the current densities can lead to the formation of beam filaments, each carrying up to one *Alfén* current, that is cylindrically surrounded by a return current.

When the electrons reach the rear side, they leave the target building up a charge-separation sheath. In addition, the leaving current generates a toroidal magnetic field B_θ, that can spread the following electrons over large transverse distances ($\mathbf{E} \times \mathbf{B}_\theta$ force [77]). The increasing electric field re-injects lower-energy electrons back into the target. If the target is thin enough, they again can be accelerated by the laser at the target front side. This process occurs as long as the laser is present, i.e. over the order of the laser pulse length, and is called **recirculation** [37, 78]. Electrons reaching the target rear side for the first time encounter electrons that have already been recirculated back. Thus, the effective electron density at the rear surface increases. By decreasing the target thickness this effect is even stronger and has direct influence on the ion acceleration.

2.2 Laser-Ion Acceleration and Beam Expansion

As already mentioned in chapter 2.1.1, the presently achievable laser intensities are by far not high enough to accelerate ions directly. Hence, the conversion of laser energy to accelerated protons is arranged by the hot electrons. They can generate high enough electric fields to accelerate ions up to MeV energies. These fields can be of the same magnitude as the laser fields but not fast-oscillating. The time scale is comparable to the laser-pulse duration giving the ions a significantly longer time to be accelerated. In the following sections, the target front and rear side acceleration will be described. In the first scenario, the ions can be accelerated by their own space charge repulsion, when the ponderomotively expelled electrons leave the laser focus region at the target front side. At the target rear side, the accelerated electrons leave the target and form an electrostatic sheath, that provides strong and long-lasting electric fields. The most efficient mechanism for fast ion acceleration, the *Target Normal Sheath Acceleration*, is discussed in detail and the different ionisation mechanisms are pointed out. For times longer than the laser pulse duration, the accelerating fields drop, because no more hot electrons are provided, and the ion beam propagation is described by a quasi-neutral expansion with co-moving electrons.

The ion acceleration at the target front side is discussed only briefly, because it is not the mechanism which generates the ion beams discussed in the experiments and simulations of this thesis. Nevertheless, the conflicting interpretations of the generation of MeV ions first discoved in 2000 provided lively discussions. Four independent groups published their experimental results almost at the same time. Krushelnick *et al.* [26] and Clark *et al.* [17] assign these ions to the front side acceleration mechanism

(backwards towards the impinging laser), but on the other hand Maksimchuk *et al.* [16] and Snavely *et al.* [18] propose the target rear side acceleration (in laser direction). In the meantime, the common explanation for the ions at the front side is the acceleration of low energy ions by the ponderomotive potential. As already discussed in the last chapter, if a laser pulse with relativistic intensity arrives at the critical surface, electrons are ponderomotively expelled out of the focal region and an electrostatic potential is rising due to the charge separation. When a single proton experiences this potential, it can gain a maximum kinetic energy equal to the potential difference, equation (2.7) for a proton: $E_{max} = 1.3\,\mathrm{MeV}$. This holds true, as long as the acceleration field lasts long enough for the proton to be accelerated to this energy. The life-time of the field was calculated by Sentoku *et al.* [79] to less than a tenth of the laser pulse duration. However, the ion beams accelerated at the target front side are not of high quality. The laser focus in a real experiment has a finite diameter, and hence the charge separation sheath in which the acceleration takes place will no longer be plane but convex-shaped. This results in an ion acceleration with a large opening angle up to 180°. Finally, it was found in almost all experiments that the rear surface emission was the dominante source of ions with maximum energy being significantly higher than ions originating from the front surface. A comparision of measured maximum proton energies from the front and the rear surface yields to $\mathrm{E}_{front} = 8\,\mathrm{MeV}$ and $\mathrm{E}_{back} = 27\,\mathrm{MeV}$ [80].

2.2.1 Target Rear Side Acceleration: TNSA-Mechanism

The acceleration of ions from the non-irradiated rear side of the target has been identified as the most effective mechanism to generate high-quality ion beams, e.g. in terms of particle number, pulse duration and directed propagation. At present available laser intensities up to 10^{21} W/cm^2 the dominant mechanism for ion acceleration from thin foils is refered to the *Target Normal Sheath Acceleration* (TNSA) [20] discovered by independent groups almost at the same time [16–19]. Since then, several international groups have experimentally demonstrated the generation of protons with energies up to 70 MeV [81] and heavier ions with energies up to 7 MeV per nucleon [21, 82]. The proton beams have a number of unique properties including high brightness (10^{12} ions in picosecond-scale bunches) [18, 83] and low transverse emittance [24, 44].

Since more than 10 years there is no significant increase in ion maximum energy due to the slow-growing laser development. Contrast improvement and higher intensities are required to reach the GeV energy regime. Several theoretical models are already proposed and waiting for experimental verification. Very efficient acceleration of highly monoenergetic proton beams extending to GeV energies from ultra-thin (nm-sized) foils by circularly polarized, ultra-high contrast laser radiation has been studied, described as *Radiation Pressure Acceleration* (RPA) [84]. For linear polarization and ultra-high contrast as well, the *Laser-Breakout Afterburner* effect (BOA) [35] can lead to GeV energies by irradiating nm-thin foil. As soon as high-energy lasers exceed intensities of 10^{23} W/cm^2 with an ultra-high contrast the *Laser-Piston Acceleration* regime [85] could be reached, where the radiation pressure can directly accelerate ions to GeV energies.

This thesis focuses on the TNSA process shown in a schematic in figure 2.1. As already discussed in the section before, the pre-pulse of the laser is intense enough to create a plasma before the main pulse arrives. Relativistic electrons generated in the laser focus propagate through the target. Measurements of the optical self-emission (transition radiation) of the electrons leaving the target rear side have resulted in a divergent electron transport inside the target. The electron distribution is broadened by multiple small-angle scattering with the target material in the cold solid region. Depending on laser energy, intensity and target thickness, the full-cone angle was determined for rather thick targets ($>40\,\mu\mathrm{m}$) at intensities around 10^{19} W/cm^2 to $\sim 30°$ and for thinner targets ($<10\,\mu\mathrm{m}$) to $\sim 150°$ at most [86–88].

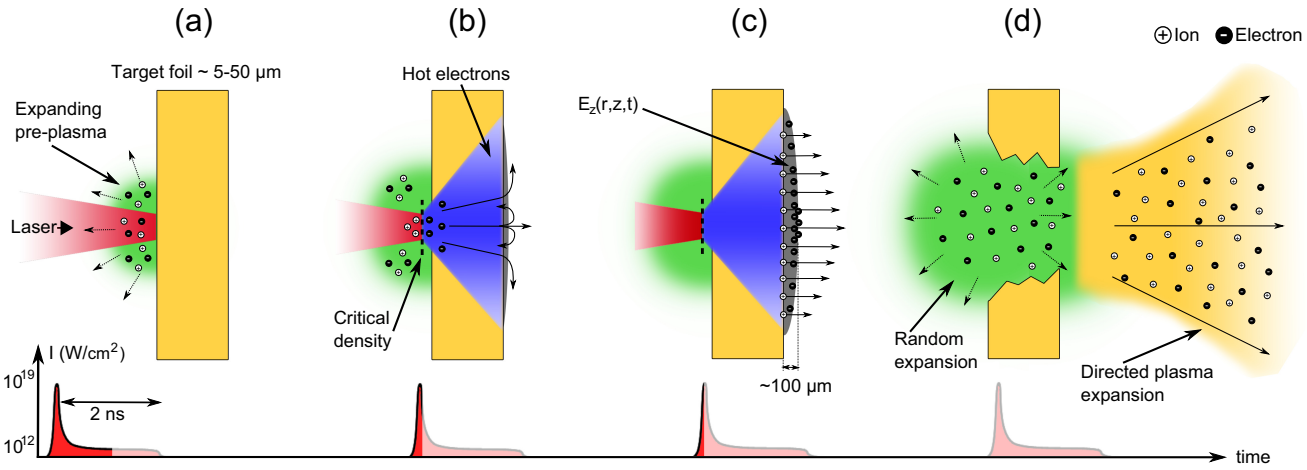

Figure 2.1: Sketch of the TNSA-mechanism. The laser pulse coming from the left is focused into the preplasma on the target front side generated by amplified spontaneous emission of the laser system (a). The main pulse interacts with the plasma at the critical surface and accelerates hot electrons into the target material (b). The electrons are transported under a divergence angle through the target, leave the rear side and form a dense electron sheath. The strong electric field of the order of TV/m generated by the charge separation is able to ionize atoms at the rear side (c). They are accelerated over a few µm along the target normal direction. After the acceleration process is over and the target disrupted (∼ns), the ions leave the target in a quasi-neutral cloud together with comoving electrons (d).

After the fastest electrons have escaped at the rear side leaving the target positively charged, a strong electrostatic potential is built up due to the charge separation, because the remaining electrons are trapped by Coulomb forces. They are held back and forced to return into the target. Due to this mechanism an electron sheath is formed at the rear surface of the target. The sheath can only extend over a thin layer before it is completely shielded. The characteristic distance is called the *Debye* length, see equation (6.24). Typically, λ_D is a few µm [21] for the laser and target parameter within the framework of this thesis. The initial electric field strength in vacuum can be obtained analytically [89, 90] by solving Poisson's equation for the one dimensional case:

$$\epsilon_0 \frac{\partial^2 \Phi}{\partial z^2} = e\, n_e. \tag{2.15}$$

The electron density in vacuum follows a Boltzmann distribution, where the kinetic energy of the electrons is replaced by the potential energy $E_{pot} = -e\,\Phi$:

$$n_e = n_{e,0} \exp\left(\frac{e\,\Phi}{k_B T_e}\right) \tag{2.16}$$

with an initial value of $n_{e,0} \approx 10^{20}$ cm^{-3}. The solution of equation (2.15) can be transformed to the expression for the maximum electric field at $z = 0$ by solving $E(z) = -\partial\Phi/\partial z$:

$$E_{max} = \sqrt{2}\,\frac{k_B T}{e\,\lambda_D}. \tag{2.17}$$

A sheath field of 2 TV/m (or MV/µm) is calculated for $k_B T_e = 1.3\,\text{MeV}$ and $\lambda_D = 0.9\,\mu\text{m}$. However, for later times the field strength is a function of the dynamics at the rear side, e.g. ionization and ion acceleration.

This initial fields are by far strong enough to ionize atoms at the target rear surface (see next chapter). Since protons are the lightest ions and the easiest to ionize, they are therefore favored by the TNSA process and are the first ions to leave the target surface. Now, one can question where the accelerated protons coming from. Allen *et al.* [91] characterized the contaminations present on a gold target foil by x-ray photoemission spectroscopy (XPS) [92], which showed a 12 Å = 1.2 nm thick layer consisting of 27% gold, 60.5% hydrocarbons (CH_2), and 12.2% water vapor (H_2O). The total number of protons available to be accelerated by the rear surface electrostatic sheath is calculate to be $\sim 10^{13}$. But this value depends on the target material, vacuum conditions and proton source size.

Thomson parabola spectrometers [93, 94] are capable of measuring not only the accelerated protons but also other ions leaving the target, such as ionized carbon or oxygen ions in different charge states up to 5 MeV/u (O^{+6}). Because of its low ionization potential and high charge-to-mass ratio hydrogen is among the first ion species produced and most effectively accelerated, thereby screening the space-charge fields for all other ion species. Hence, the particle number for heavier ions and their maximum energy is limited. Nevertheless, it is possible to increase both parameters by various cleaning techniques of the target rear side, e.g. coating [21], resistively heating [95], laser ablation [96], ion sputtering [91]. These techniques remove almost all contaminations of the target surface minimizing the proton signal. But it is also possible to enrich the target rear side with a proton-rich material to change the contamination composition and hence the number of protons and energy distribuion [40].

The obtained electric field is a solution of Poisson's equation (2.15) for the one dimensional case in z-direction (perpendicular to the target surface). Thus, the field lines point normal to the target surface, which means that the ions will be accelerated in the same direction and therefore the acceleration mechanism has derived its name *Target Normal Sheath Acceleration*. Henceforth, this thesis will concentrate only on accelerated proton beams, development of proton detectors, studies on beam parameter optimization and possible applications for these beams.

2.2.2 Ionisation Mechanisms

Several ionization mechanisms occur to enable the transition from the solid target into the plasma state and charged particle beams respectively. At the target front surface, the main mechanisms are direct laser ionization (as described in the previous sections) and collisional ionization within the expanding plasma. The front side electrons ionized by the incident laser field collide with target atoms and already present ions causing ionization to occur [97]. In addition, a large number of electrons are passing through the target and are reflected due to the electric sheath. The resulting return current through the foil will cause further ionization.

The ionization at the rear surface is dominated by collisional and electric field ionization. However, the cross section for collisional ionization is much smaller than the cross section for field ionization for the electron densities and electric fields present at the target rear surface [21]. Hence, field ionization of atoms is the main mechanism at the target rear side. A simple model to estimate the field strength above ionization occurs is the *Field Ionization by Barrier Suppression* (FIBS) [98]. The electric field deforms the potential wall of the atom such that it becomes flat enough for electrons (below binding energy of the electron) to escape the Coulomb potential or allow tunneling to occur, hence the atom is ionized. The minimum field strength for field ionization is given by

$$E_{FIBS} = \frac{\pi \, \epsilon_0 \, U_{bind}^2}{e^3 \, Z} \tag{2.18}$$

with the electron binding energy U_{bind} in units of eV. The necessary field strength to ionize a hydrogen atom with $Z = 1$ and $U_{bind} = 13.6$ eV can be estimated to $E_{FIBS} = 3 \times 10^{10}$ V/m, which is two orders

of magnitude below the field strength of the electron sheath calculated with equation (2.17). Most of the protons on the rear side are ionized and accelerated as long as the field exist. The lifetime of the electric field is comparable to the laser pulse duration. Only during this time periode new hot electrons are delivered to the target back side to keep the accelerating field up. In the ideal case, the maximum field of 2 TV/M would accelerate a proton in 500 fs over a distance of 24 µm to a maximum energy of 52 MeV. Therefore, the field has to be constant over the acceleration distance. But the field strength has its maximum value only at $z = 0$, and for $z > 0$ it decays like [89]

$$E(z) = \frac{2\,k_B T_e}{e} \frac{1}{z + \sqrt{2}\lambda_D}. \tag{2.19}$$

Assuming the same initial electric field, $k_B T_E = 1.3\,\text{MeV}$ and $\lambda_D = 0.9\,\mu\text{m}$, it is possible to calculate numerically the position and the energy of a proton after a 500 fs acceleration periode. A maximum energy of 6.5 MeV and a travel distance of 12 µm could be achieved, which is almost an order of magnitude lower than the ideal case of constant field. Both assumptions point out that it is very important to include all present mechanisms responsible for acceleration, absorption and reflection. The sheath form and size as well as the target condition also influence the electric field strength. Thus, the spectrum of proton energies can cover low energies and also energies in the range of tens of MeV.

2.2.3 Beam Expansion

It is still a great deal of theoretical and numerical simulation work to investigate the processes of ion acceleration, in particular the TNSA mechanism, which generates the proton beams discussed in this thesis. A variety of different models and approaches are used to explain the plasma expansion behaviour at the rear side of the target starting with simplified, analytical calculations over electron-proton fluid models up to fully relativistic, three dimensional particle-in-cell (PIC) simulations. Parameters like maximum ion energy as well as the ion energy distribution can be obtained analytically, whereas numerical simulations has to be done to describe the particle dynamics.

Since 2003, the strong electric fields due to the charge separation and their influence on the plasma expansion are subject of theoretical attention [90, 99] based on earlier work on freely expanding plasma model [100] assuming an isothermal expansion. Old models have been advanced and new developed to take into account the finite size of the target [101], adiabatic cooling of electrons [102] involved by the energy transfer between ions and electrons, and the effect of two electron populations with different temperatures [103]. As the accelerated ion beam expands into vacuum, energy is gradually transfered from the fast electrons to the ions (via the Coulomb force between them) resulting in an energy adaption of the electrons and a following electron co-propagation with the ions within a few hundred microns. Hence the expanding plasma consists of a very hot electron distribution leaving the target very fast and the accelerated ions together with comoving electrons forming a quasi-neutral plasma cloud ($n_e = n_p$).

The established model by Mora [90] predicts an exponential proton spectrum

$$\frac{\mathrm{d}N}{\mathrm{d}E_p} = \frac{n_{e,0}\,c_s\,t_{acc}}{\sqrt{2\,k_B T_e\,E_p}} \exp\left(-\sqrt{\frac{2\,E_p}{k_B T_e}}\right) \tag{2.20}$$

where $c_s^2 = k_B T_e / m_p$ is the sound velocity and t_{acc} the proton acceleration time, which can be approximated with the laser pulse duration τ_L ($t_{acc} = 1.3 \times \tau_L$ [71]). The maximum (cutoff) energy that can be gained by the accelerated protons based on the self-similar, isothermal, fluid model is given by

$$E_{p,max} = 2\, k_B T_e\, \ln^2 \left(\tau + \sqrt{\tau^2 + 1} \right). \tag{2.21}$$

with the normalized acceleration time $\tau = \omega_{pp}\, t_{acc} / \sqrt{2\, \exp(1)}$ and the ion plasma frequency ω_{pp} for protons, see equation (2.10): $m_e \rightarrow m_p$). Fuchs *et al.* [71] compared experimental results and PIC simulations with Mora's model and found very good agreement.

As the protons are accelerated by the electron sheath, the form of the sheath and the spatial distribution of the electron have direct influence on the proton beam propagation and the beam parameters respectively. The above described model predicts a proton beam with a broad energy distribution within a very short pulse duration comparable to the acceleration time or rather to the laser pulse duration ($\sim$1 ps). Since one dimensional models can only provide conclusions about one dimensional parameters, such as particle spectrum and maximum energy, the spatial informations require precise, three dimensional PIC simulations.

In order to understand the proton expansion, some main results presented in chapter 3 will be anticipated. Measurements have shown, that the relativistic electron sheath has a nearly Gaussian-radial distribution in its density profile [24]. The field-ionized protons feel an electric field strength, which is proportional to $n_e^{1/2}$ (the local density of the hot electrons forming the sheath [90, 104]) and is directed normal to the local density gradient. Thus, the existing transverse part of the electric field is proportional to the total field times the transverse gradient of the initial electron density. This field component leads to an emission angle for all protons, which are not accelerated in the symmetry point of the bell-shaped sheath. In addition, this sheath profile effects a radius-dependent electric field. Protons ionized in the center are accelerated by a higher electric field, than protons sitting at the edge of the Gaussian sheath. These characteristics are schematically summarized in figure 2.2, where the envelopes are illustrated. For increasing proton energy the emission zone (source size) and the emission angle (envelope divergence) decreases. As soon as the accelerating field drops to zero, it can be assumed that the protons propagate ballistically (force-free) into vacuum, confirmed by PIC simulations and electric field measurement [25].

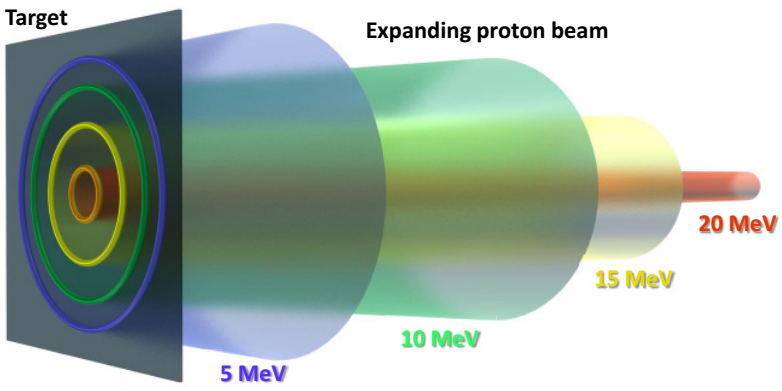

Figure 2.2: Sketch of the proton beam expansion. The profile of the accelerating sheath leads to an energy dependent source size and envelope divergence. For increasing proton energy the radius and hence the proton emission area increases (marked by circles with increasing radius on the target surface). Due to the transverse field component, protons of different energies expand in different cones (illustrated for four different energies): the high-energy protons in a small one, the low-energy protons in a cone with a big divergence angle. Note: only the envelopes are shown. There are also low-energy protons, that are emitted in the center.

2.3 Applications for Laser-Accelerated Proton Beams

Since the first experiments reporting multi-MeV proton acceleration from laser-irradiated foils, the research on developing a high-quality, controllable, laser-driven proton source gained incredible interest. The field of applications for this kind of beams could range from a tool for plasma physics to interdisciplinary areas. In the following section, the different applications of laser-accelerated proton beams are discussed in terms of already successfully implemented, demonstrated in proof of principle experiments and for potential future applications.

Proton Radiography and Imaging

Conventionally accelerated ion beams have been used for some time to detect aereal density variations in different samples with spatial resolution. Here, the energy deposition properties of particles in matter are used. For example, at the experimental area Z6 at the *GSI Helmholtzzentrum für Schwerionenforschung*, the energy loss of ion bunches in laser-produced plasmas is studied [105]. Based on the detected ion energies it is possible to draw conclusions on the plasma parameters. The use of ion beams from accelerators as a diagnostic tool to measure electric fields in plasmas via the detection of the proton deflection [106] is limited due to difficulties and high cost involved in providing externally produced particle beams of sufficiently high energy. In addition, the duration of the ion pulses produced from conventional accelerators is too long than it could be used as diagnostic tool for this kind of physics. Therefore, laser-accelerated proton beams with their unique properties in terms of spatial quality, high degree of laminarity and temporal duration have opened a totally new area for application in proton probing. The virtual, point-like source characteristic (described in section 3.3) enables imaging with a high spatial resolution. The temporal resolution is obtained by the nature of the source. All protons are generated on very small scale, but due to their energy dispersion, different proton energies probe different time periods and conditions of the sample. In combination with a detector providing spatial and energy resolution (radiochromic films, see section 3.3) the temporal resolution can be achieved [107]. Via a mesh pattern imprinted in the proton beam and its deflection, studies on the expansion, the electric field and the ion front can be done [25, 108, 109]. Because of the different interaction mechanism, protons can provide complementary information to more common techniques such as x-ray backlighting. Compound targets of different materials were analyzed by proton radiography [95]. With this technique, a negative image of the areal density of the target could be measured. Density diagnostic via proton radiography has potential application in inertial confinement fusion. Current accelerated protons with energies greater 50 MeV would be sufficiently energetic to probe cold, compressed cores used at the National Ignition Facility.

Proton Heating

Carbon, for example, is one of the most common elements on earth and up to now its phase diagramm is not experimentally examined in detail to understand the interior of giant planets such as Uranus and Neptune. Accurate equation of state (EOS) data are needed to develop realistic models for planetary formation and to describe the structure of giant planets [110, 111]. Today's conventional, accelerator-based ion beams do not match both the high particle number and the short pulse length required to create fluid carbon at ambient pressure without noticeable hydrodynamic expansion during the heating period. Laser-accelerated proton beam characteristics make them well-suited for creating isochorically heated matter in extreme conditions [28]. In the first experiments, the temperature of the rear surface emission of a heated aluminum foil was measured to 4 eV. The isochoric heating by the protons is volumetric, but not uniform, because of the nature of the exponential energy spectrum of the protons. Due to the significant temperature gradient along the direction of the beam, with the highest energy deposition and thus temperature at the front surface of the foil, a complex experiment setup and target design is essential to be sure to measure an uniformly heated sample that is in a single temperature

and density state. In the frame of this work, experiments were carried out to optimize the targetry and diagnostics for carbon foils heated by laser-accelerated proton beams [112].

Proton initiated Nuclear Reactions

The interaction of laser-accelerated proton beams and secondary targets can initiate nuclear reactions, which can be used to diagnose properties of the beam. By using copper plates in stack configuration, the ^{63}Cu (p,n) ^{63}Zn reaction enables the construction of the energy spectrum of the protons [113, 114]. The β^+ decay on ^{63}Zn can be measured with a coincidence counting system. Convolved with a detector calibration and the cross sections, one obtain a proton number per energy interval from each copper layer. Laser-accelerated ions enable nuclear physics experiments in laser laboratories rather than at big accelerators. McKenna *et al.* [82, 115] have shown that laser-accelerated high-Z ions create compound nuclei in excited states by interacting with a secondary sample. They de-excite through the evaporation of protons, neutrons, and α-particles. The well defined γ-energies of the nuclei de-excitation together with the calculated reaction cross sections enable quantitative measurements of accelerated heavy ions.

Proton Fast Ignition

The Fast ignition approach to inertial confinement fusion separates the initial compression and the following heating phases. The compression could be done with long pulse laser beams, and the heating of the compressed matter to temperatures close the fusion limit could be done by laser-accelerated proton beams [29, 116, 117]. Protons do have several advantages compared to other particles. Because of their highest ion charge to mass ratio, they are accelerated most efficiently up to the highest energies. The quadratic dependence of the stopping power on the charge state enables a deeper penetration into the target to reach the high density region where the ignition spot is to be formed. Finally they have their characteristic Bragg peak in their stopping ranges, where the main proportion of the energy of the proton is deposited at the end of their range, which is desirable in order to heat a localized volume efficiently. Patel *et al.* [28] proposed a curved target foil to focuse the proton beam to the point in the target where the energy is to be deposited having the right pulse length and high enough particle numbers. Numerical simulations [116] have surprisingly shown that a monochromatic proton beam is not the optimum for this application. An increasing plasma temperature leads to a decrease of the stopping power in the nuclear fuel. The high-energy part of the exponential spectrum generated by the TNSA mechanism penetrate deep into the fuel and preheat it. The lower initial energy of the following protons in combination with the reduced stopping power lead to a deeper penetration for these energies resulting in an energy deposition within the same volume. Furthermore, the low energy end of the spectrum has the most particles and hence, the highest contribution to the deposited energy.

Radiation Therapy

Using protons or carbon ions in radiotherapy have several advantages compared to tumor treatment with x-rays. The fixed propagation length for a given energy and the maximum energy deposition in the Bragg peak preserve the healthy tissues in the vicinity of the tumor. The *GSI Helmholtzzentrum für Schwerionenforschung* as a conventional accelerator facility developed a tumor treatment program [118] and worked out a proposal for building the *Heidelberger Ionenstrahl Therapiezentrum* (HIT), a running facility since november 2009 to treat patients and continue clinical studies on ion beam therapy [119]. Laser-based accelerators have been proposed as an alternative, which could lead to advantages in terms of device compactness and costs [30, 120]. The current proton energies are in agreement with numerical simulations and indicate that proton energies within the therapeutic window (50-200 MeV) should be obtained in the very near future using modern, high intensity and very compact laser systems bringing the "lab to the hospital – rather than the hospital to the lab". A laser accelerator could be used simply as a high efficiency ion injector for the proton accelerator, or finally could replace a conventional proton accelerator after all. However, a collimation and energy selection device is required, because of the beam

energy spread and the divergence [31, 46, 48, 121]. In the frame of this work, the capture and control of laser-accelerated proton beams is studied to optimize the beam parameters for further application, e.g. injector.

Technological Applications

Industrial applications where laser-driven ion beams are of interest include ion implantation in substrates and manufacturing techniques such as lithography and micro-machining [122, 123], especially when high-repetition table-top, moderate cost laser systems with the required parameters are available. However, due to the bragg peak effect, the broad energy spectrum and the divergence angle, the laser-accelerated proton beams need an energy selection and collimation devices to enable three dimensional micro-machining [124].

2.4 Control of Laser-Accelerated Proton Beams

As already pointed out in the last section, for most of the possible applications of laser-accelerated proton beams a capture and control device is required to assure a collimated beam with a well defined energy. This section describes some conventional ion optics, which can be included into the beam path to optimize the beam parameters. In addition, important beam parameter for charged particle beams are explained. A detailed description can be found in [125, 126].

The transverse motion of charged particles, in this case protons, can be affected by shaped electric and magnetic fields. These fields bend charged particle orbits in a manner analogous to the bending of light rays by shaped glass lenses. Hence, similar equations can be used to describe both processes.

Due to the limited transverse dimensions of accelerators and the natural divergence of laser-accelerated protons, forces must be applied to reduce the initial divergence to transport the particles through the system. Charged particle lenses perform three types of operations:

Mapping: As well known in optics, lenses are used to transport an image. For charged particle beams, electric or magnetic lenses do exactly the same. Particles that leave a point in one plane are mapped into another at a different longitudinal position.

Collimation: The main purpose this lenses should be used in connection with laser-accelerated protons is to confine the beams. For transporting beams over long distances, a constant beam radius has to be achieved.

Focusing: Another function of lenses is to focus beams or compress them to the smallest possible radius. This feature is very important concerning future applications, e.g. heating or machining.

The requirement for an electrostatic lense is a radial electric field, which can bend or focus protons. The inside of a positive charged cylinder is field-free (*Faraday shield*). Hence, only the fringe fields have a radial component, but the field strength is very small, even if the length is decreased resulting in a pinhole aperture. For example, aperture lenses are used as charged particle extractor in combination with a grid of opposite or zero potential. But there is always a longitudinal field component in propagation direction of the beam. Thus, charged particles are accelerated. The combination of collimated transport and acceleration is used in *Wideröe* accelerators [127]. In addition, cavities generating electric fields are very susceptible to charged particle impact and electromagnetic pulses always present in laser experiments. As particles propagate close to the speed of light, electric and magnetic fields have the same impact $\vec{\mathbf{E}} = c\vec{\mathbf{B}}$. A magnetic field strength of $B = 1\,\mathrm{T}$ is equivalent to an electric field strength of $E = 3\times10^8\ \mathrm{V/m}$. This value is by far above the technically feasible field strength. Thus, for beam guidance, today's accelerators use magnets almost without exception.

The motion of charged particles in magnetic fields is described by the balance between the Lorentz force and the centrifugal force. Due to small transverse beam dimensions compared to large bending radii, it is possible to describe the magnetic field in the vicinity of the ideal beam trace in terms of a multipole expansion leading to

$$\frac{q}{p}B_y(x) = \frac{q}{p}B_{y,0} + \frac{q}{p}\frac{\mathrm{d}B_y}{\mathrm{d}x}x + \ldots = \frac{1}{R} + kx + \ldots \tag{2.22}$$

where q is the particle charge and p the momentum. Each multipole has a different effect on the particle trajectories. The first term in equation (2.22) represents the dipole strength $1/R$ (beam deflection) and the second term the quadrupol strength k (beam focusing). Multipoles of higher order (sextupole, octupole, etc.) are unwanted field errors. Hence, the deflecting forces are either constant or linear and one speaks of the *linear particle optics*.

Dipoles are beam guidance elements, which are used for a change in the beam propagation direction, but in the instance of laser-accelerated proton beam not necessary, because the propagation is directed. But quadupole fields could be used for beam focusing. A quadrupole consists of four poles of hyperbolic shape with alternating north-south pole orientation. Hence, the characteristic is a different focusing behaviour along the x and y coordinate. If there is focusing in y than the beam is defocused in x and the other way around. Therefore, the quadrupole strength for focusing is defined as $k < 0$ and for defocusing $k > 0$. Related to focusing, three common terms are applied to lenses: the focal length, the lens power and the f-number. By extrapolating the orbits of focused particles back to the lense, the distance from the intersection of the extrapolation and the beam symmetry axis to the focus point can be defined as the focal length of the ion optic. The strength of a lens is determined by how much it bends orbits. Shorter focal lengths mean stronger lenses. The lens power is defined as the inverse of the focal length, $P = 1/f$. The f-number $f\#$ is the ratio of focal length to the lens diameter: $f\# = f/D$. The f-number is important for describing focusing of nonlaminar beams. It characterizes different optical systems in terms of the minimum focal spot size and maximum achievable particle flux.

Quadrupole lenses are used extensively for beam transport applications. But a single lens cannot be used to focus a beam to a point. An initially parallel beam is compressed to a line rather than a point in the image plane. A lens with this property is called *astigmatic*. A lens that focuses equally in both directions can focus to a point or produce a two-dimensional image. Such a lens is called *stigmatic*. Stigmatism can be achieved with quadrupoles in a configuration called the triplet. A possible setup would be, that the entrance and exit sections have the same length ($l/2$) and pole orientation, while the middle section of length l is rotated 90°. By solving the transfer matrix of the system, it can be shown, that the net effect of equal focusing and defocusing quadrupole lenses is focusing. The proof of principle experiment already demonstrated the transporting and focusing of laser-accelerated protons by permanent magnet mini quadrupole lenses providing field gradients as high as 500 T/m [46].

The decision, if this lense is the perfect device to catch a charged particle beam or not, is not made on the basis of difficulties in manufacturing. Quadrupoles can be built with different dimensions and field strengths, with permanent magnets or in pulsed operation, even superconducting. The ion optic should match the beam parameters to get the optimum output. A big advantage of combining quadrupoles to focus charged particles is the stronger net focusing effect than for a series of solenoid lenses at the same field strength. If the initial beam would be a collimated beam, quadrupoles would be the first choice. Here in this case, the laser-accelerated proton beam is a highly divergent beam. The first quadrupole in fact focuses in one plane, but defocuses in the other coordinate leading to an even more divergent beam. The limited aperture of the quadrupole causes an huge particle loss before the second quadrupole can focus in the other plan.

Laser-accelerated proton beams are in need of a different ion optic. Three different conditions have to be met. First, the distance to the point, where the protons are accelerated, has to be large enough to minimize the influence of the magnetic field on the acceleration mechanism. Due to this distance, the aperture has to be wide enough to catch as much protons of the divergent beam as possible. Finally, a high enough field strengh to collimate protons in the MeV range is requirement. The solenoidal magnetic lense is best suited for laser-accelerated proton beams.

The solenoidal magnetic field or lens [126] consists of a region of cylindrically symmetric radial and axial magnetic fields produced by axicentered coils carrying azimuthal current. Since the magnetic field is static, there is no change in particle energy when passing through the solenoid. Therefore, it is possible to perform relativistic derivations without complex mathematics. Particles in the fringe field of the solenoid are passing a region of radial magnetic fields. The *Lorentz* force ($q v_z \times B_r$) acts azimuthal. The resulting velocity v_θ leads to a radial force when the particles entering the B_z fields inside the lense. Independent of charge state or transit direction, the particles are deflected toward the symmetry axis of the solenoid.

The equations of motion (assuming constant relativistic γ factor - no acceleration) are

$$\gamma m_0 \frac{\mathrm{d}v_r}{\mathrm{d}t} = -q v_\theta B_z + \gamma m_0 \frac{v_\theta^2}{r}, \tag{2.23}$$

$$\gamma m_0 \frac{\mathrm{d}v_\theta}{\mathrm{d}t} = -q v_z B_r - \gamma m_0 \frac{v_r v_\theta}{r}. \tag{2.24}$$

The second terms beside the *Lorentz* force in the radial and azimuthal force equations (2.23) and (2.24) are the *centrifugal* and the *coriolis* force. The third equation for the axial motion is not relevant for the focusing behaviour of beam. By solving equation (2.24) − approximations and description in reference [126] − one obtains

$$v_\theta - \frac{q r B_z}{2\gamma m_0} = constant = 0. \tag{2.25}$$

Equation (2.25) implies that particles gain no net azimuthal velocity passing completely through the lens, because they must cross opposite directed radial magnetic field lines at the exit that cancel out the azimuthal velocity gained at the entrance. Summarized, the solenoidal field is a focusing and collimating field which conserves particle energy and optimizes particle divergence.

As soon as the charged particles move inside the solenoid ($B_z = const.$, $v_r = v_\theta = const.$), they are constrained on a gyration (here: counter-clockwise rotation for electrons and clockwise for protons) with the given *Lamor* radius or gyroradius r_g:

$$r_g = \frac{m v_\perp}{|q| B_z} \quad \xrightarrow{rel.} \quad r_g = \frac{p_\perp}{|q| B_z} \tag{2.26}$$

where m is the mass of the charged particle, $v_\perp$ the velocity component perpendicular to the direction of the magnetic field (superposition of v_r and v_θ), q the charge of the particle, and B_z the constant longitudinal magnetic field. For the relativistic motion, the numerator is replaced by the relativistic momentum.

The above introduced focal length of the solenoidal lens is derived by substituting v_θ of equation (2.23) with equation (2.25) and transforming the temporal integral to a local integral $\mathrm{d}v_r/\mathrm{d}t = \mathrm{d}v_r/\mathrm{d}z \cdot \mathrm{d}z/\mathrm{d}t = \mathrm{d}v_r/\mathrm{d}z \cdot v_z$ to give:

$$f = -\frac{r}{r'} = -\frac{r \cdot v_z}{v_r} = \frac{4}{\int \mathrm{d}z \left[(q\,B_z)/(\gamma\, m_0\, v_z)\right]^2} \tag{2.27}$$

Each ion optical element in an accelerator modifies beam parameters and the beam quality respectively. Before introducing a measurement for the beam quality, a property of the beam propagation called *transverse momentum blurring* is discussed. In a betatron for example, charged particles are enclosed in a toroidal vacuum chamber centered on a main circular orbit. But beams always have spreads in angle and position. These orbital instabilities result in oscillatory motion of particles around the main orbit. Source of the so called *betatron oscillations* is the quasielastic restoring force of the magnetic field on particles that are deflected from the main orbit, which may e.g. occur by scattering of beam particles on the molecules of residual gas in the beam line. By solving the equation of motion, the transverse displacement $x(z)$ is given by:

$$x(z) = \sqrt{\epsilon}\sqrt{\beta(z)}\cos\left[\psi(z) + \phi\right] \tag{2.28}$$

where ϵ is the emittance (definition below), $\beta(z)$ the beta function dependent on the longitudinal position z, $\psi(z)$ the betatron oscillations and ϕ the phase. The amplitude $E(z) = \sqrt{\epsilon\,\beta(z)}$ defines the beam envelope. At a given z position along the accelerator x and $x' = v_x / v_z$ characterize the transverse particle motion in the so called *phase space* (Laser accelerated proton beams are symmetric in the x-y-plane. Hence, the definition for x and x' can also be assigned to y and y'). The quality of the beam, also called emittance ϵ, is defined in this space as the ellipse of minimum area occupied by the beam divided by π:

$$\epsilon_{\text{ellipse}} = \frac{1}{\pi}\int\int \mathrm{d}x\,\mathrm{d}x', \tag{2.29}$$

in units of π-*mm-mrad*. This emittance is also called *total* or *100% emittance*. Conservation of the phase-space volume occupied by a particle distribution is a fundamental theorem of collective physics (*Liouville's theorem*). Furthermore, the theorem is the basis for the principle of emittance conservation. The forces in the form of the magnetic fields do not lead to a change of the beam emittance, as they have a purely deflecting effect on the particles and no acceleration.

The size of the emittance can be given as the ellipse enclosing the distribution (practical quantity) or as the *root-mean-square* (rms) emittance (statistical quantity) [128]

$$\epsilon_{\text{rms}} = \sqrt{\langle x^2\rangle\langle x'^2\rangle - \langle xx'\rangle^2}, \tag{2.30}$$

with the second moment in x (y can substitute for x as symmetry is assumed) defined by:

$$\left\langle x^2 \right\rangle = \frac{\int x^2 f(x,x')\,dx\,dx'}{\int f(x,x')\,dx\,dx'} \tag{2.31}$$

$$\Longrightarrow \frac{\sum_i a(x_i)\,b(x_i')x_i^2\,\Delta x_i\,\Delta x_i'}{\sum_i a(x_i)\,b(x_i')\,\Delta x_i \Delta\, x_i'}. \tag{2.32}$$

The other second moments $\left\langle x'^2 \right\rangle$ and $\langle xx'\rangle$ are defined in a similar fashion. a and b are the weighting factors of the beam intensity. For the measurements of laser-accelerated proton beams a and b are equal 1. For a uniform beam distribution the relation between the two quantities is $\epsilon_{\text{ellipse}} = 4 \cdot \epsilon_{\text{rms}}$.

Unfortunately, there is no global definition of emittance that is consistently used in accelerator and ion beam physics, a fact that often causes confusion when results and publications are compared. The definition can involve a phase space area, divided by π or not, or the *rms* emittance or only an area including a fraction of the whole beam. In this thesis two different approaches will be used. First, the emittance is calculated by the ellipse definition including nearly 100% of the proton beam and second the *rms* emittance is determined by using the measured data to average the whole particle distribution.

The emittance, as defined here, depends on the kinetic energy of the particles (see [129]). The change is inversely proportional to the relativistic parameters γ and β. To compare the beam quality, the normalized emittance for different energies is introduced:

$$\epsilon_{\text{norm}} = \beta\,\gamma\,\epsilon, \tag{2.33}$$

with $\gamma = 1 + E/E_0$ and $\beta = \sqrt{1 - 1/\gamma^2}$, where E is the particle energy and E_0 the proton rest energy. The normalized transverse emittance $\epsilon_{\text{trans,norm}}$ is a well known parameter in accelerator physics, because it is constant during acceleration and a comparison of emittance values in different acceleration phases (different proton energies) is possible.

For the operation of an accelerator, it is important that the transverse phase space of the beam fits into the accelerator components, e.g. entrance apertures and beam lines, without particle losses at the inner walls. As shown in equation (2.28), the radius of the beam is proportional to $\sqrt{\beta(z)}$. Therefore, the aperture of the beam line is not directly a measure of the beam size. The ratio $d/\sqrt{\beta(z)}$ is crucial, where d is the radius of the accelerator element. This ratio varies along the orbit. The z-position in the accelerator, at which the ratio reaches the minimum value, is the narrowest point and defines the restriction of the transverse phase space. The acceptance A is defined as the emittance with the maximal phase ellipse possible to fit in the accelerator:

$$A = \left(\frac{d^2}{\beta}\right)_{min} \tag{2.34}$$

where d and β are taken at the optical narrowest position.

Due to the large divergence angle, a solenoidal magnetic lense needs an adequate acceptance to catch most of the beam. But by increasing the inner diameter non-linear effects emerge. The transverse focusing force invariably increases more rapidly near the coils that generate the fields. This non-linear lens cannot focus a beam to a point, even if the beam is laminar. The force of the lens exceeds the linear value at large displacements, resulting in overfocusing of peripheral particles. There is no downstream location where the particle orbits meet in one focal point. A related problem occurs in imaging applications and is called *spherical aberration*. In the case of laser-accelerated proton beams, non-linear focusing forces, which are present in quadrupoles as well as in solenoids, inevitably lead to beam emittance growth. Focusing systems with linear lenses preserve both the area and general shape of beam distributions. In particular, an elliptical distribution remains an ellipse. Non-linear focusing systems do not have this property. A non-linear lens distorts the shape of the elliptical distribution, leading to emittance growth. The beam emittance is higher because the smallest elliptical curve that can surround the final distribution is larger than the boundary of the input distribution.

TRACE3D estimations concerning chromatic and spherical effects for a solenoid setup were already carried out [130]. For a given solenoid and spot radius, but varying opening angle α, the transverse emittance obeys a scaling

$$\epsilon \propto \alpha^2 \frac{\Delta E}{E}. \tag{2.35}$$

To suppress the estimated emittance growth up to a value of 50 π-mm-mrad, a significant reduction either of the production cone angle α or of the energy width $\Delta E/E$ is necessary to bring the emittance down to values competitive with beam quality in conventional accelerators. More details on the transverse emittance and the solenoid abberations can be found in chapter 3.3 and **??**.

As soon as the beam is collimated, it is possible to transport the protons over a longer distance. But for some applications, where an almost monochromatic beam is need, the exponential energy spectrum is

not suitable. By using two solenoidal magnetic lenses, where the first is working in focusing mode and the second in collimation mode, a particular energy interval can be selected. Depending on the energy, the number of particles might be too small. At this point it is possible to include a further ion optic called *debuncher*. The longitudinal velocity spread of an energy interval causes the beam to expand. The debuncher (a radio frequency cavity) is phased so that particles at the leading edge of a bunch (higher momentum particles) are decelerated while the trailing particles are accelerated, thereby reducing the energy spread of the beam and increasing the number of particles for the particular energy [131].

Both ion optics and their impact on the capture and transport of laser-accelerated proton beams is summarized in figure 2.3. The solenoidal magnetic lense as collimating device collects as much particles as possible and bend the particle orbits to the point where the initial divergence vanishes (see phase space illustrations). After a certain drift section, the stretched bunch enters the debunching unit. The number of particles for the energy, which is in phase with the frequency of the cavity, is increased by deceleration of the leading edge and acceleration of the trailing protons.

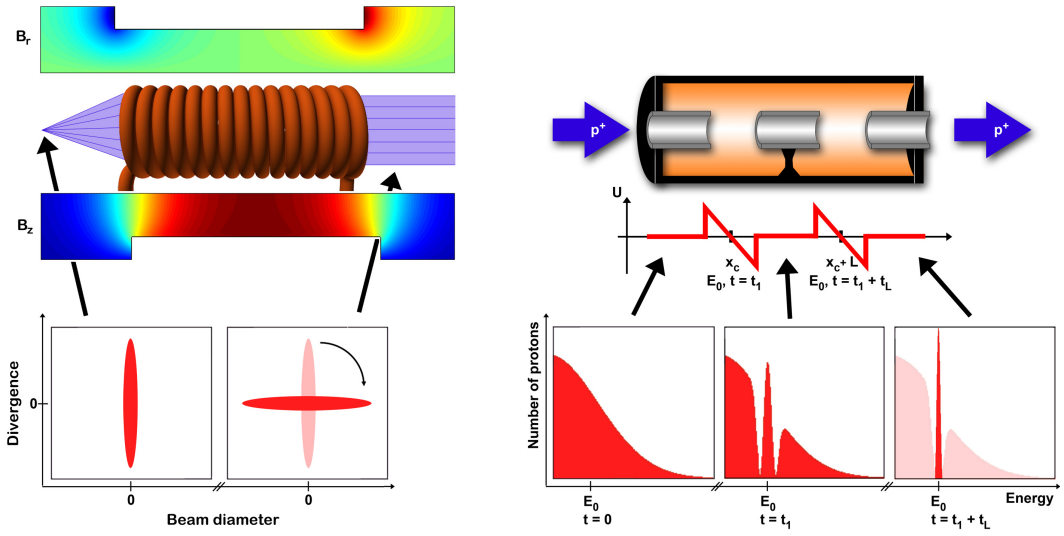

Figure 2.3: Sketch of the ion optics used for capture and transport of laser-accelerated proton beams. The radial and longitudinal magnetic field of the solenoid leads to a phase space rotation of the initial proton distribution for a matched energy interval. The protons leaving the solenoid have a vanishing divergence and a constant beam radius. After a certain drift, the particles enter the debunching section. Here, the part of the energy spectrum, which is in phase with the frequency of the cavity, is modified. Protons lagging behind the synchronous particles experience a higher gap voltage and gain a larger velocity increment while advanced particles are retarded. Hence, the number of particles for the synchronized proton energy is increased, and the energy spread for this energy interval is reduced.

3 Experimental Setup and Diagnostics

In the scope of this work, experiments on laser-ion acceleration were performed at three different laser systems:

VULCAN Petawatt laser: VULCAN [3] located at the Central Laser Facility (Rutherford Appleton Laboratory, Didcot, UK) is a high power Nd:glass laser system that is capable of delivering up to 2.6 kJ of laser energy in long pulses (nanosecond duration) and up to 1 PW (10^{15} W) peak power in short pulses (sub-picosecond duration) at a wavelength of 1054 nm. In its short pulse mode, VULCAN is capable of delivering ultra-high focused intensities greater than 10^{21} W/cm^2.

TRIDENT laser facility: The TRIDENT facility [132] located at the Los Alamos National Laboratory (Los Alamos, NM, USA) provides laser-matter interactions with powers exceeding 200 TW, energies greater than 120 J and very short pulse duration in the sub-ps regime. Two additional long pulse beam lines are capable of delivering up to 500 J at 1054 nm and can be frequency doubled with an output of 200 J depending on pulse duration (100 ps to 1 µs).

PHELIX: PHELIX [6] – **P**etawatt **H**igh **E**nergy **L**aser for heavy **I**on e**X**periments – located at the GSI Helmholtzzentrum für Schwerionenforschung (Darmstadt, Germany) is also a Nd:glass laser system currently operation at an energy of 1 kJ and a peak power of 0.5 PW. In the short pulse mode, PHELIX is currently capable of delivering 120 J in a pulse duration of 500 fs at a wavelength of 1053 nm achieving intensities up to 10^{20} W/cm^2.

The basic layout of all three laser systems is very similar as well as the experimental setup for proton acceleration. Hence, the following section exemplarily describes the PHELIX laser system and its target chamber setup for laser-particle acceleration. Before talking about application of such beams, it is crucial to characterize the bam parameters and understand their behaviour. Therefore, several particle detectors are used. As pointed out in section 2.1.3, the accelerated protons are accompanied by low energy electrons in the keV range. Their spectrum is important concerning beam transport simulations. A low-energy, magnetic electron spectrometer was developed and calibrated to characterize these electrons (section 3.4). Sections 3.2 and 3.3 address on an experimental method to fully reconstruct laser-accelerated proton beam parameters called radiochromic film imaging spectroscopy (RIS). RIS allows for the characterization of proton beams concerning real and virtual source size, envelope- and microdivergence, normalized transverse emittance, phase space, and proton spectrum. This technique requires particular targets and a high resolution proton detector. Therefore, thin gold foils with a microgrooved rear side were manufactured and characterized. Calibrated *GafChromic* radiochromic films (RCFs) in stack configuration were used as spatial and energy resolved film detectors. In the scope of this work, these technique was developed and optimized. Characterizations of proton beams generated at different laser systems are published in F. Nürnberg *et al.*, Rev. Sci. Instrum. **80**, 033301 (2009).

3.1 PHELIX System and Setup for Laser-Particle Acceleration

The PHELIX system is capable of operation in stand-alone mode and, in combination with the heavy ion accelerator UNILAC (**UNI**versal **L**inear **A**ccelerator). This unique combination at GSI enables a large variety of experiments [6]. Novel research opportunities are spanning from the study of ion-matter interaction, through experiments in atomic physics, nuclear physics, and astrophysics, into the field of relativistic plasma physics. An overview of the building is shown in figure 3.1.

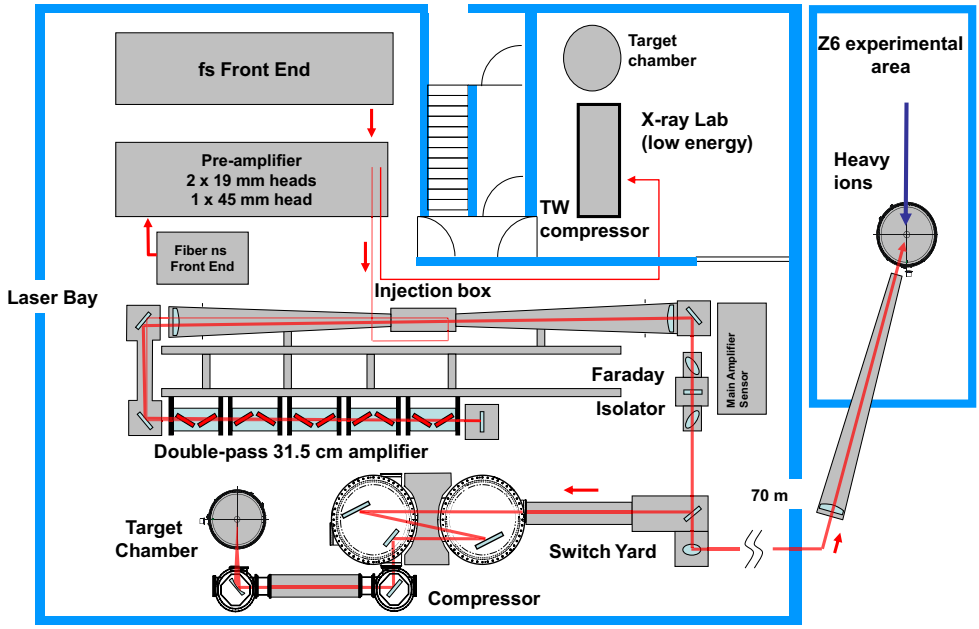

Figure 3.1: Schematics of the PHELIX laser system. The laser is presently used at three different target areas. Behind the preamplifiers, the low energy beam can be switched into the x-ray lab. In the switch yard behind the main amplifiers, the long pulse version can be transfered to the experimental area Z6 close to the UNILAC accelerator. The PHELIX experiments presented in this thesis were performed in the laser bay, where the short pulse version is provided in a target chamber after passing a compressor. Courtesy of V. Bagnoud.

The system is capable of delivering short and long pulses depending on the used front-end. For laser-ion acceleration, the short pulse mode is used to achieve the required high intensities. The femtosecond front-end is a commercial laser oscillator (Coherent Mira) and generates short pulses with durations of 100 fs and energies around 4 nJ at a repetition rate of 76 MHz. The pulses are temporally stretched to 2.3 ns full-width half maximum (FWHM) in a pulse stretcher and then amplified. Two titanium-doped sapphire regenerative amplifiers with a repetition rate of 10 Hz provide an energy of 30 mJ before the pulse is injected into the next amplifier chain by a ultra fast Pockels cell. The pre-amplifier consists of three flash-lamp-pumped Nd:glass amplifiers with a maximum exit beam diameter of 70 mm to keep the fluence below the damage threshold of the optics. The laser pulse with energies up to 3 J is expanded further more to a diameter of 28 cm before passing through the main amplifier set up in double-pass configuration. Here, the pulses can gain energy up to 160 J and are then re-compressed to a pulse duration of <1 ps in a vacuum tank. From the beginning of the main amplifier up to the interaction chamber the laser light propagates in vacuum (10^{-5}-10^{-6} mbar) to avoid non-linear interactions with the air, that would compromise the pulse propagation. The pulse compressor uses multi-layer dielectric gratings to confine the pulses in time. The incident beam profile is horizontally limited to 12 cm and in vertical direction to 24 cm due to the size of the gratings, so that the beam is elliptical. The energy limiting elements in the beam path are the final optics, in this case the threshold of the final grating. The main amplifier is capable of delivering more energy than only 160 J, but this would destroy the expensive grating structure. With an compressor efficiency of 80%, the achievable energy on target is about $\sim$130 J for a pulse duration of 500 fs corresponding to an output power of 240 TW. A diamond turned off-axis parabola made of copper focuses the beam down onto the target. The above described laser architecture is called the **C**hirped **P**ulse **A**mplification technique (CPA) and was invented in 1985 by D. Strickland and G. Mourou [2].

Due to the cooling time of the main amplifier, the repetition rate of this laser is one shot every 90 min. The laser parameters for the PHELIX experiment described in section 5.2 are less than the optimum

described above. The laser delivered 72 J on target in a pulse duration of 500 fs in a focal spot shown in figure 3.2(a). The full-width-half-maximum (FWHM) dimensions are in vertical direction 8.5 µm and in horizontal direction 17 µm containing 22% of the full laser energy leading to an intensity of 3×10^{19} W/cm^2. Because of previous experiments, a lot of target debris has been settled on the surface of the copper parabola, and hence the focusing ability was limited to this spot size and the not preventable, extensive energy distribution around.

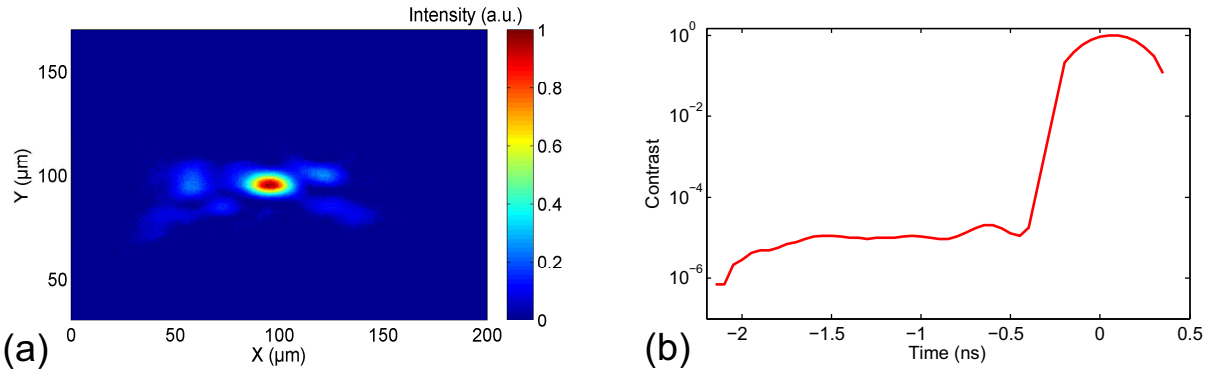

Figure 3.2: (a) Intensity distribution of the focal spot and (b) prepulse contrast measurement. The full-width-half-maximum (FWHM) dimensions of the focal spot are in vertical direction 8.5 µm and in horizontal direction 17 µm containing 22% of the full laser energy. The prepulse measurement shows an almost constant ASE prepulse in intensity, 1.7 ns long at a contrast ratio of 10^{-5} to the main pulse.

In general, the experimental setup for laser-proton acceleration always looks the same independent of the laser system. The incident laser pulse is focused by a parabola into the target chamber. The spatial location of the best focus is defined as the position of the target. The target consists of metallic foils (e.g. Cu, Al, Au) with a thickness in the range of several µm up to 100 µm. For PHELIX, the incidence angle onto the foil is 0° (in target normal direction), because the back-reflected light into the laser chain can be blocked by a *Faraday* isolator. Different systems are working under an angle up to 45° to prevent damage of the frontend by amplified light traveling backwards. The reproducible target alignment to exactly the same point in space is provided by different viewing systems. For measuring the dimensions of the focal spot, a microscope camera is placed at the focus position. This measurement is mostly done previous to the shot under air. At TRIDENT, a novel backscatter focus diagnostic [133] allows imaging of the on-shot full-power focal spot backwards into the laser chain onto a separate camera.

The particle and radiation diagnostic for the experiment is placed around the point of the laser-target interaction with a direct view. The following list summarizes the most common diagnostics for laser generated plasmas and accelerated particle beams:

Laser interferometry: Time- and space resolved probe interferometry can be used to obtain a complete density mapping of laser produced plasmas [134]. A part of a second laser passes the expanding plasma at the front or back side of the target and is interfered with the non-disturbed part by a *Wollaston* prisma. Hence, the interferometry pattern gives information about the plasma density.

Pinhole camera: A pinhole camera produces an image of the plasma space-resolved but time-integrated onto a detector [135, 136].

X-ray streak camera: This type of camera is a high speed diagnostic which is applicable in determining the temporal, spatial and spectral properties of X-rays emitted by the plasma [137]. A standard x-ray CCD camera can also be used but is time-integrating.

HOPG crystal: A **H**ighly **O**rdered **P**yrolytic **G**raphite crystal can be used as a powerful optic for x-ray diagnostics as well as for x-ray absorption and emission spectroscopy [138].

Magnetic spectrometer: For charged particle detection magnetic dipole spectrometers are used. Electrons [67, 139, 140] and protons [31, 71] are deflected in opposite directions, and the strength depends on the particle energy. Hence, an energy resolved spectrum can be measured.

Thomson parabola: This spectrometer is very similar to the last one, but it has parallel magnetic and electric fields [21, 93, 94, 141]. Beside the proton energy distribution, spectra of heavier ions in different charge states can be measured.

Metal foils: By irradiating for example copper plates in stack configuration with laser-accelerated protons, the ^{63}Cu(p,n)^{63}Zn reaction enables the construction of the energy spectrum of the protons [113, 114].

Image plates: IPs can be used as x-ray imaging detector [142, 143] or as detector for protons [144, 145] and electrons [67, 139]. These large detectors are in principle a rewritable memory film (image plate). The radiation intensity is read in by using visible light and is stored electronically. After reading the information, the IP can be deleted and re-used for a new measurement.

CR-39: CR-39 is a solid state nuclear track detector for protons [146] and heavy ions [141]. It is sensitive to single ion events but insensitive to electromagnetic radiation and electrons. An ion striking a CR-39 plate destroys the polymer matrix along its path, which is transformed into cone-shaped craters when the CR-39 is etched in NaOH solution. Information about the number of ions can be achieved by counting each crater under an optical microscope.

Radiochromic films: The widely used radiochromic film detector is capable of measuring the laser-accelerated proton distribution energy- and space-resolved [44]. Special electron features can also be seen [48]. In the scope of this work, this detector was used as the main diagnostic and is described and characterized in section 3.2 and 3.3.

Specifics, laser parameters and the diagnostic setup of each experiment is described in detail at the appropriate place in the text.

3.2 Radiochromic Films for Proton Diagnostic

In this section the main detector to characterize all important proton beam parameters will be described in detail. For the reconstruction of the laser-accelerated proton beams, it is necessary to have a high-resolution detector to get the spatial-resolved dose distribution of the protons. A common and ideal detector is *Gafchromic* radiochromic film (RCF) of the types HD-810, HS and MD-55 [147] with the given configurations and compositions shown in figure 3.3. These dosimetry films measure radiation dose, in this case provided by the protons, because their stopping power/range is higher compared to other particles or radiation being generated during the experiment (e.g. heavy ions, electrons or x-rays). After interaction with ionizing radiation the film changes its color from nearly transparent to blue, induced by polymerization [148]. The self-developing film has a spatial resolution of more than 10^4 dots per inch (dpi) or less than 2.54 µm according to the manufacturer.

Transmission densitometers, spectrophotometers or film scanners can be used to digitize the radiochromic films. Attention should be paid to the time of reading. Nearly complete dyeing of the film (90%) appears within milliseconds. However, during the first 24 hours after irradiation, an increasing dyeing cannot be neglected. It is recommended to read in the films at the earliest of 2 days after exposure, as it was done for the data of this thesis.

The RCFs have been calibrated for protons by Hey *et al.* [149] with a micro-densitometer. However, we have used the transmission film scanner *Microtek ArtixScan 1800f* instead of a densitometer to scan larger films faster with the same accuracy. More information about differences in RCF analysis with

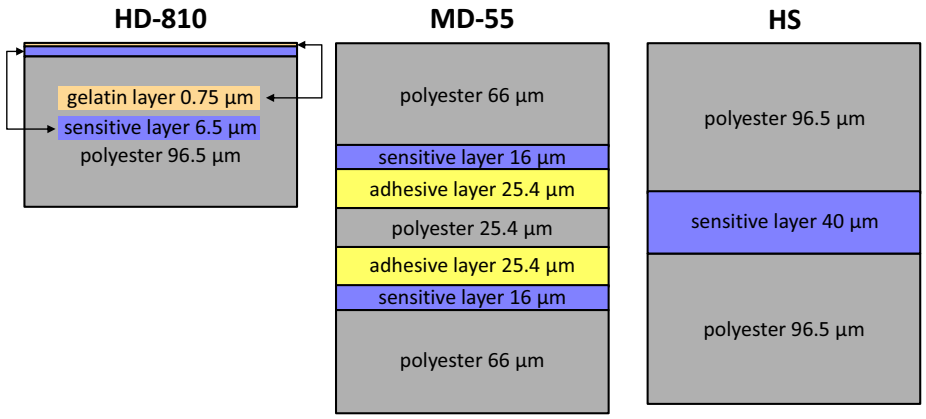

Density (g/cm³)	Composition			
	C (%)	H (%)	O (%)	N (%)
1.35	45.44	36.36	18.20	0.00
1.08	29.14	56.80	7.12	6.94
1.20	33.33	57.14	9.53	0.00
1.20	22.31	53.52	11.12	12.75

Figure 3.3: Layer configuration, density and chemical composition of the radiochromic film types HD-810, MD-55 and HS.

different scanner types can be found in [149–151]. The scanner calibration was done with a grey scale wedge [152] to convert the raw data into optical density (OD). The films were scanned with a resolution of 500 dpi and a dynamic range of 16 bit grey scales. The same scan parameters were used for both, the calibration and the experiments, in order to have the same conditions. This scanner can read ODs up to 2.5, the saturation value.

The next step is to convert optical density into deposited energy of the protons, which requires a calibration of the sensitive layer of the RCF. During the last few years the chemical composition and also the thickness of the sensitive layer have been changed by the manufacturer. This means that ideally a calibration for each type and production code is necessary. In addition to the effect of the composition difference the data differ from scanner to scanner so that no universal calibration curve for the RCF exists. But the following calibration data is applicable if the same scanner is used. The calibration for the RCFs was done at the proton accelerator at the *Max-Planck-Institut* for nuclear physics in Heidelberg, Germany. The accelerator delivered 8 MeV protons. The deposited energy E_{dep} of the protons (given in keV/mm^2) propagating through the film is determined by the SRIM code package [153] and integrated over the volume of the sensitive layer to obtain the total deposited energy.

Figure 3.4(a) shows the double logarithmic plot of the film calibration curves for the three different film types. As an appropriate approximation for this highly nonlinear slope, an exponential function:

$$E_{dep} = \exp\left(\sum_i a_i \, \mathrm{OD}^{b_i}\right) \frac{\mathrm{keV}}{\mathrm{mm}^2} \tag{3.1}$$

is suitable to have a calibration function for further implementation (see section 3.3.2). The tabulated fit parameters can be found in table 3.1. Otherwise an interval spline interpolation is also fine. This approximation is only valid in the OD region of the measured data. For lower ODs of the MD-55 and HS film, it was not possible to achieve measurable data. The shutter closing-time of the proton accelerator did not enable measurement of time periodes less than one second in length, that were necessary for low optical densities. The region with optical densities less than 0.1 was approximated by a power law $E_{dep} = a \cdot \mathrm{OD}^b + c$ similar to [150, 154].

$$E_{dep}(MD-55) = 3.74 \times^1 0^{10} \cdot \mathrm{OD}^{1.19} + 5 \times 10^7 \tag{3.2}$$

$$E_{dep}(HS) = 2.6 \times^1 0^{10} \cdot \mathrm{OD}^{1.19} + 5 \times 10^7 \tag{3.3}$$

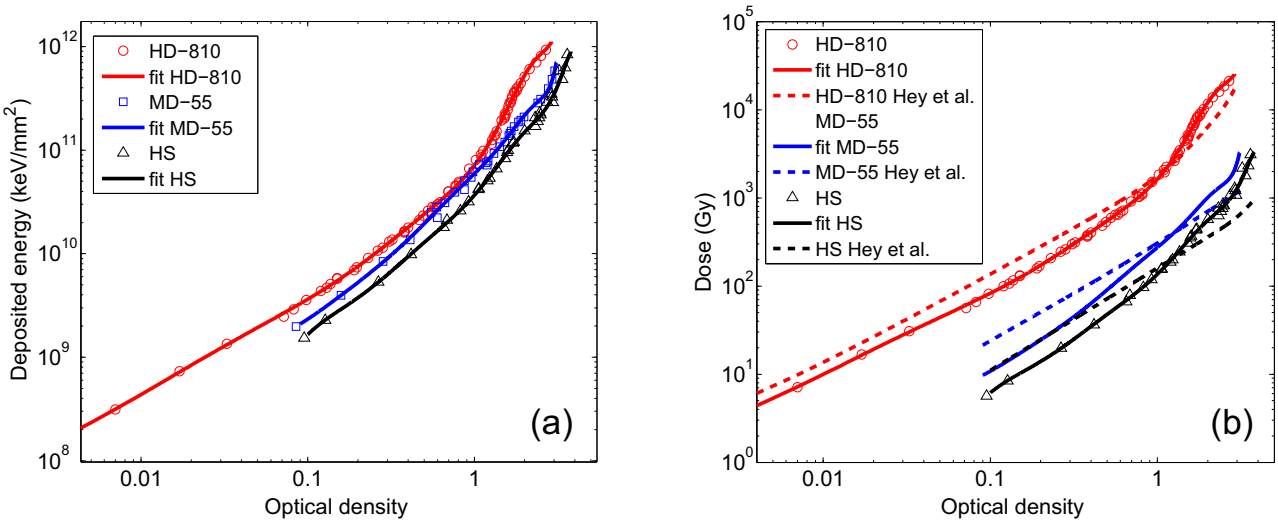

Figure 3.4: Calibration curves for the radiochromic film types HD-810, MD-55 and HS. Deposited energy (a) and dose (b) illustrations. For lower ODs of the MD-55 and HS film, it was not possible to achieve measurable data. The region with optical densities less than 0.1 was approximated by a power law similar to [150, 154]. The slopes of the dose curves find a good agreement with the calibration of Hey *et al.* [149], shown as the dashed lines.

	a_1	a_2	a_3	a_4	a_5	a_6	a_7	a_8	a_9
HD-810	17.7	-2.4	65.4	-244.6	494.5	-486.7	307.5	-140.2	13.9
MD-55	431.8	-817.9	1518.0	-3103.6	4001.8	-2784.9	1191.8	-447.2	35.5
HS	-855.2	1674.8	-2695.2	4872.3	-5535.9	3391.8	-1197.2	395.2	-25.8
	b_9	b_2	b_3	b_4	b_5	b_6	b_7	b_8	b_9
all types	0.0	0.1	0.5	0.9	1.3	1.7	2.3	2.7	3.3

Table 3.1: Fit parameters for equation (3.1).

In the range OD > 2.5, the scanner is working within its range of saturation and so the values are not usable. The calibration curves OD vs. dose D are shown in figure 3.4(b). Here the different film sensitivities are clearly visible. The dose curve of the insensitive film HD-810 is situated above the more sensitive films MD-55 and HS. For both MD-55 and HS films a lower deposited dose induces the same optical density as for type HD-810. So film types MD-55 and HS can be used for the detection of lower fluxes as the energy deposition of each particle is higher than in the film type HD-810, equivalent to a darker coloring. The slopes of the dose curves are in good agreement with the calibration of Hey *et al.* [149], shown as the dashed lines. For the recently new invented film type MD-55-V2 with slightly different layer thicknesses no calibration curve exist. But this film type could be cross-calibrated with the MD-55. If the MD-55-V2 film is converted with the calibration curve of the MD-55 film, the deposition values have to be multiplied with a constant scaling factor: E_{dep}(MD-55-V2) = 0.72$\times$ E_{dep}(MD-55).

The sources of error for the determination of the optical density as well as of the calculation of the deposited energy depend on the accuracy of the delivered beam parameters of the proton accelerator, the film composition and the measurement. The accuracy of the proton energy from the accelerator is about 0.1%. Beside this, the error of the spot size and the inaccuracy of the current measurement during the calibration can be neglected. The main effect is the inhomogeneity of the beam profile: a uniform irradiation of the film could be assured within an error of 5%. Another source of error is given

by the accuracy of the scanner of about 3%. The largest error is due to batch-to-batch variations in the film sensitivity of up to 10% [147]. Hence, an overall error of this calibration of 15-20% is an acceptable value as also published by Hey *et al.* [149]. Beside the errors for the OD, the inaccuracy of the code SRIM for calculating the deposited energy in the films is on the order of 4% [153].

3.3 RCF Imaging Spectroscopy - RIS

With the help of micro-structured target foils and RCF detectors in stack configuration it is possible to specify energy resolved proton beam parameters with a high spatial resolution. The micro-corrugations on the foil rear side, figure 3.5(a), generate beamlets in the laser-accelerated proton beam. These perturbations in momentum space of the protons are embedded in the expansion of the beam to a point where the divergence angles originating from different micro-grooves are well separated from each other. This is when a contrast pattern or magnified image forms in the RCF detector (distance target - RCF detector: 3-6 cm). This effect is called *micro-focussing*[1] [23, 24, 155], see schematic diagram in figure 3.5(b). Therefore, the proton beam maps the rear side structure of the foil onto the film detector. Due to deviations of the mapped image in the detector from the ideal image of the inserted grooves in the target, information about the transverse emittance and the source size of the protons can be extracted. The symmetry and the divergence can also be determined by the imprint in the film. By using the RCFs in stack configuration an energy-resolved measurement is possible. Protons with lower energies are stopped in the previous layers whereas protons with higher energies penetrate through and are stopped in the rear films of the stack. So each RCF can be attributed to an energy bin corresponding to an average proton energy. The energy resolved proton distribution obtained from the film stack completes the beam reconstruction.

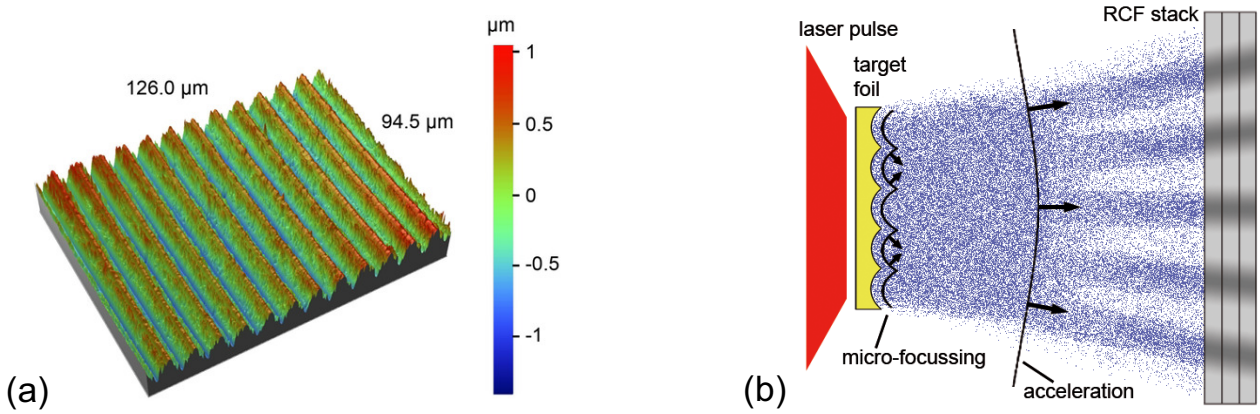

Figure 3.5: (a) Interferometry image of the rear side of a micro-structured gold foil with a sine structure: period 10 µm and amplitude less than 1 µm. (b) Scheme of the foil-induced microfocusing of the laser-accelerated protons. The grooved rear surface of the target foil and the acceleration in target normal direction cause microfocusing of the protons at the beginning of the acceleration. The separation of these beamlets due to the propagation of the beam is visible in the RCF detector as modulations of the proton density distribution.

In the last few years different fabrication methods for micro-structured foils were tested at the detector and target lab of the *Technische Universität Darmstadt, Institut für Kernphysik*. Structuring by laser ablation, evaporation of a lithographically structured silicon wafer or direct diamond planing of a thin foil turned out to be too imprecise and extensive. With a micro-structured copper wafer (manufactured by the LFM, laboratory for precision machining Bremen, Germany) delivering the required micro-structure

[1] T.E. Cowan, M. Roth and P. Audebert, *Method and apparatus for nanometer-scale focusing and patterning of ultra-low emittance, multi-MeV proton and ion beams from a laser ion diode*, US Patent # 6852985, 2005.

with the desired accuracy, and using electroplating techniques, micro-structured gold foils of different thicknesses could be fabricated. The precision in the distance of the inserted equidistant grooves on the submicrometer scale are a few 100 nm. Micro-structured gold foils of (5-50) µm thickness with equidistant grooves on the rear surface were produced. The grooves with a line spacing of (3-20) µm have a depth between 1 µm and 3 µm. Three different groove profiles can be manufactured: a cycloid, an inverse cycloid or a sine structure. More details about the fabrication methods can be found in reference [156].

3.3.1 Proton Beam Parameters of Phelix

In the following, the beam reconstruction method will be described in detail including the definitions of the beam parameters forming the basis of the method and the technique on how to extract the parameters from the measured data. As an example, a proton beam of the PHELIX campaign is analyzed in detail, see figure 3.6. The film detector in stack configuration consisted of nine HD-810 films with copper absorbing layers (50 µm, 100 µm, 150 µm) in between to increase the detectable energy range. Due to the high sensitivity of RCFs according to parasitic radiation, the first layer of the stack is a copper sheet for x-ray and debris shielding. This stack configuration enables an energy resolved measurement. High energy protons penetrate through the first films and will be fully stopped in the subsequent films of the stack. Therefore, each film layer can be attributed to a certain proton energy. The energy value written in the corner of each layer represents the Bragg peak energy. Protons of that energy have their absorption maximum in the sensitive layer of this film. Hence, almost all coloring is generated by these protons. In addition, the imprint in the detected proton beam due to the micro-structured target and the resulting micro-focusing can clearly be seen in all layers.

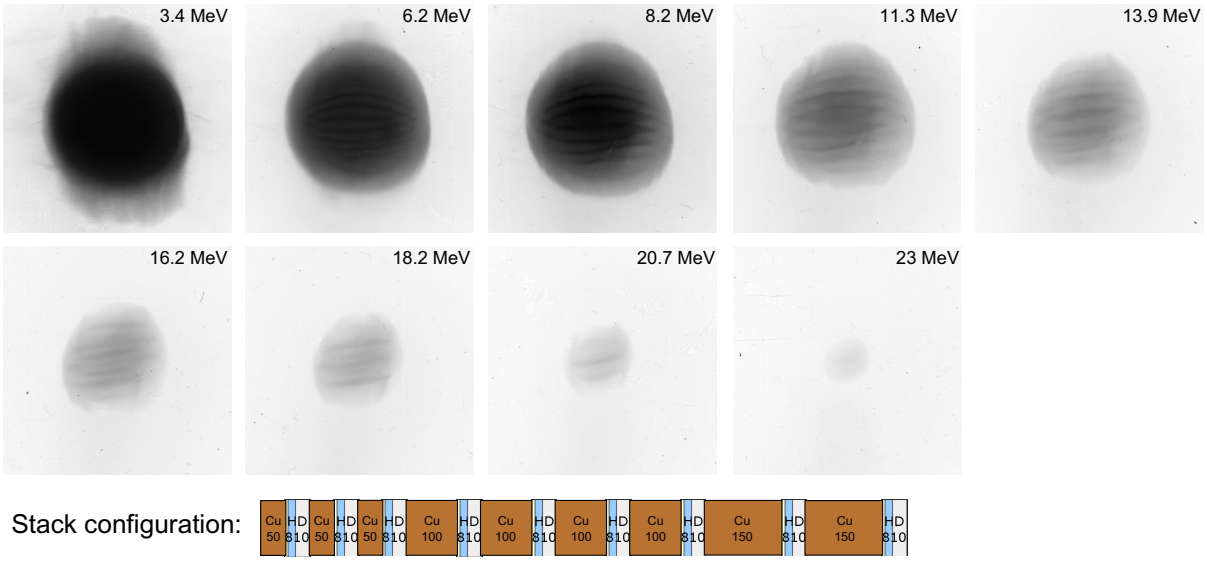

Figure 3.6: Radiochromic film stack exposed by a laser-accelerated proton beam of the PHELIX system. Target: 25 µm thick gold foil with sinusoidal grooves of 20 µm spacing and 1 µm depth. Laser parameters: 86 J in 500 fs at best focus 8.5 µm×17 µm. RCF stack position: 31 mm behind the target.

Envelope- and micro-divergence

As already mentioned, the stack detector is placed 31 mm behind the target perpendicular to the target normal direction. A radiochromic film is a two-dimensional detector in space. Therefore, a transverse cross-section of the proton beam profile is visible on the film. With its size and the distance between

target and detector, it is possible to determine an envelope-divergence angle of the proton beam. A second divergence dimension also well known in accelerator physics is the micro-divergence. It can be measured using either the *Pepper-pot* method [157] or the transverse slit scanners [158]. The micro-divergence characterizes the broadening of the particle trajectories and is important for the emittance calculation (see below). By using micro-grooved targets, the micro-divergence can be estimated by measuring the line width of a groove mapped in the RCF detector.

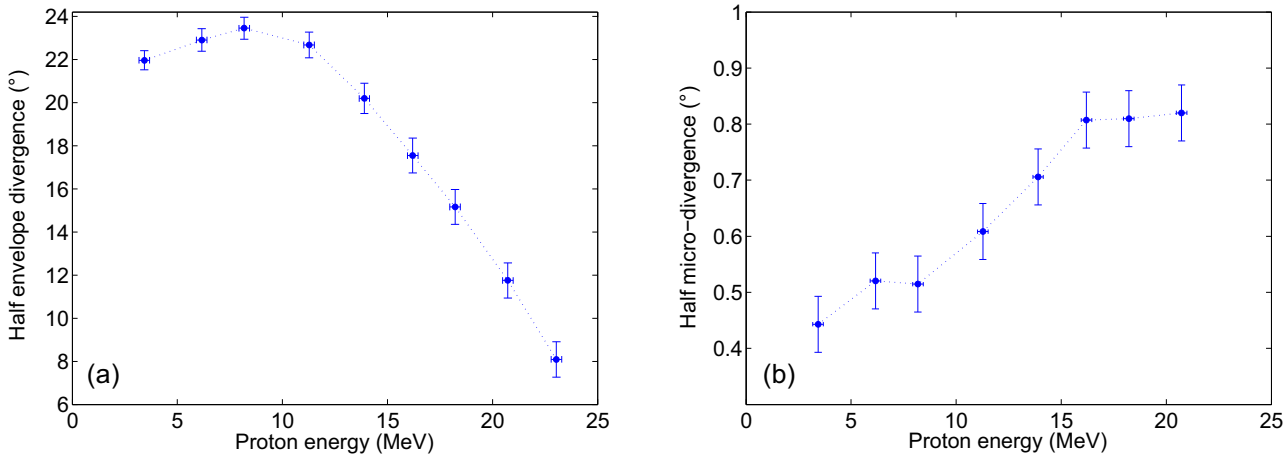

Figure 3.7: (a) Half envelope-divergence of the PHELIX proton beam. For small proton energies the angle of beam spread is nearly constant, but for increasing energy the angle decreases approximately linear/parabolic. (b) The micro-divergence, the real divergence of the expanding protons, is increasing for increasing proton energy.

Up to a proton energy of ∼11 MeV, the envelope-divergence stays constant (figure 3.7(a)). In most cases the opening angles decrease parabolically with increasing energy. However, at PHELIX the decrease of the envelope-divergence with increasing energy is close to linear. The slope of the decrease (parabolic or linear) is a result of the initial electron sheath distribution [159], as already shown in figure 2.2. A Gaussian sheath distribution results in a strongly curved envelope-divergence, whereas a parabolic hot electron sheath results in a linear dependency. On the other hand, the micro-divergence, the real divergence of the expanding protons, is increasing for increasing proton energy (figure 3.7(b)). The micro-divergence is defined by the spread of the proton trajectories given by the deviation of the proton trajectories from the ideal. Hence, it is comparable with the thermal spread of the beam. Regardless the increasing micro-divergence, the envelope-divergence is decreasing, because the energy dependent proton source size decreases (shown below) and hence the transverse component of the acceleration field.

Real and virtual source size

By counting the line pattern in each RCF and by multiplying with the original line space of the micro-structured foil, the energy resolved real source size, i.e. the proton emission zone on the target rear surface, can be determined. Figure 3.8(a) shows the real source size of the PHELIX proton beam. The highest energy protons are accelerated in the center. This fits nicely to a bell-shaped distribution of the electrons in the sheath responsible for the proton acceleration [24, 159]. To get quantitative information about the quality of laser-accelerated proton beams, the virtual source size is more suitable, the point source where the protons appear to originate, if a laminar expansion is assumed. The virtual source size can be determined by extrapolation of the proton trajectories to a region in front of the target [80]. With the well known micro-structure in the target and the measured line pattern in the RCFs, the necessary data set is available for the extrapolation. The width of the virtual source size is a suitable parameter for comparison of beam quality between different proton beams.

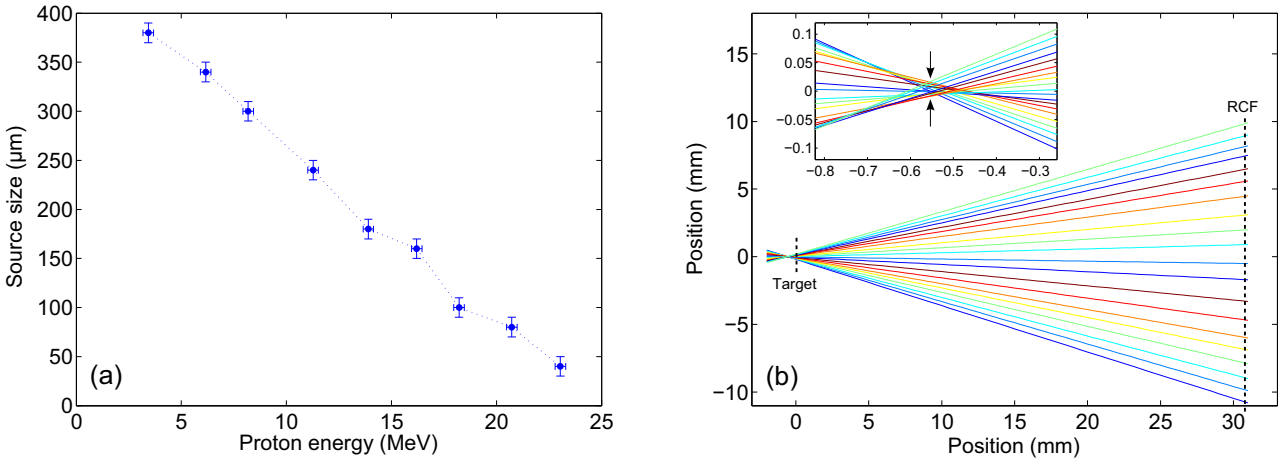

Figure 3.8: (a) Diameter of the proton source on the rear surface of the target. The emission zone decreases linear with increasing proton energy from 380 µm to 40 µm. (b) Linear extrapolation to the virtual source position for stack layer 2 (6.2 MeV). The focus point is determined to 525 µm in front of the target. The inset shows, that the virtual source is the waist diameter of the envelope of the extrapolated trajectories of 27 µm.

Figure 3.8(b) shows that such an extrapolation to a point source is not possible for laser-accelerated proton beams. Only a waist diameter of the envelope can be defined as virtual source size. The extrapolation for layer 2 of the RCF stack (6.2 MeV) yields to a virtual source size of 27 µm in diameter positioned 525 µm in front of the target. Values already published from different laser systems [44, 160] are up to one order of magnitude lower. For increasing proton energy the virtual source size decreases from 30 µm to 5 µm and moves closer to the target from 550 µm to 200 µm. Different publications [44, 160] report smaller values, but this is expected for different laser systems.

Transverse emittance

The evolution of the beam particles is described by the x-x' phase space. The behaviour is different if linear or non-linear forces act on the protons. When forces are linear, particles tend to move on ellipses of constant area. The whole particle distribution can be described by an ellipse of minimum area including the proton beam, see figure 3.9(a). At the source origin, the ellipse is in the vertical direction, during expansion the ellipse will become sheared. The envelope-divergence x' is constant, but the beam diameter x increases. However, the area of the ellipse is still conserved according to *Liouville*'s theorem. A useful fit for the normalized, transverse emittance is the parallelogram approximation of the ellipse in phase-space and equations (2.29) and (2.33) pass into

$$\epsilon_{\text{real}} \approx (\beta\gamma)\ S_{\text{real}} \cdot \Delta\alpha, \tag{3.4}$$

with the real source size S_{real} and the mico-divergence $\Delta\alpha$ of the proton trajectories. The error of this area approximation is $A_{ellipse}/A_{parallelogram} = (\pi\, a\, b)/(2a\, 2b) = \pi/4 \longrightarrow 27\%$ with the semi-axis a and b of the ellipse. The dashed parallelograms in figure 3.9(a) show the approximation of the ellipse area to calculate the transverse emittance. Non-linear force components distort orbits and cause undesirable effects as shown in figure 3.9(b). The gray area is not an ellipse anymore. So the effective phase space area grows (dashed ellipse). There are elements in accelerator physics to compensate this effect, but only on small scales. The acceptance of an accelerator limits the size of the area in phase space. If particles are located in larger areas they will disappear in the accelerator. Nevertheless, the gray area is still conserved. In this case, it is not possible to calculate the transverse emittance using equation (3.4). This area does not reflect the effective emittance area and results in a misleading value.

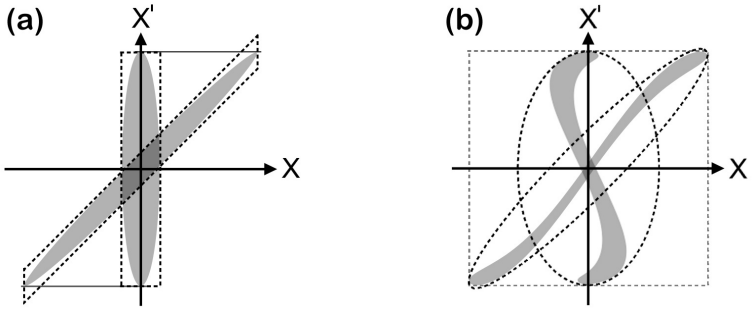

Figure 3.9: Schemes of particle beams affected by different forces. (a) The whole particle distribution can be described by an ellipse of minimum area including the proton beam. At the origin, it is in the vertical direction; during expansion the ellipse will be elongated/shrinked and rotate. The dashed parallelograms show the approximation of the ellipse area. (b) Nonlinear force components distort orbits and cause undesirable effects. The transverse emittance increases and parallelogram approximations yield in incorrect results.

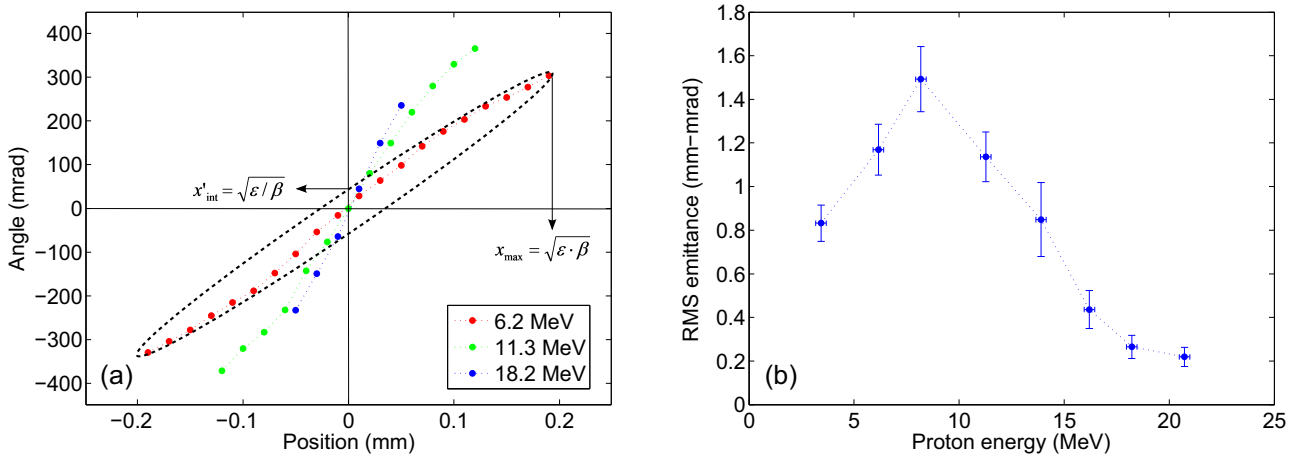

Figure 3.10: (a) Proton phase-space for three different energies. The non-linear effects of the laser-accelerated proton beams can be seen by a slight S-shaped behaviour highlighted by the dashed connecting lines of the data points. The dashed ellipse is fitted to the 6.2 MeV data. (b) Normalized transverse RMS emittance for the PHELIX proton beam.

Figure 3.10 shows the x-x' phase space of the PHELIX proton beam. The non-linear effects can be seen by a slight S-shaped behaviour highlighted by the dashed connecting lines of the data points. The counter-clockwise rotation of the phase space ellipse for increasing proton energy is a characteristic that can also be seen in simulations [161]. For higher proton energies the S-shaped distortion on the data decreases and the effective emittance decreases as well. To calculate the area A_{ellipse} of the ellipse the semi-major and semi-minor axis have to be determined. By projecting the ellipse onto the x axis, the values for the semi-axes can be read off the coordinate axes [129]:

$$\epsilon = x_{max}\, x'_{int} = \sqrt{\hat{\beta}\epsilon}\,\sqrt{\epsilon/\hat{\beta}}, \tag{3.5}$$

where $\hat{\beta}$ is a *Twiss* parameter of the *Courant-Snyder* formulation. Due to the visible shaping in the phase-space because of the non-linear effects, the ellipse fit is only an upper approximation of the occupied volume. Hence, the *root-means-square* (RMS) emittance defined by equation (2.30) is used, which can directly be estimated with measured data and the discretized second moments according to equation (2.32). For a more precise statistical value, virtual data points were extrapolated. More data on the dashed connecting line in figure 3.10(a) does not change the emittance only the transverse/angular be-

haviour. Here, two attitudes of the phase space of laser-accelerated proton beams have to be considered to scale the value of the extrapolated data points. The line-out over the whole proton spot in the RCF image is more or less a flat-top in the center and decreases linear in the boundary area to 50% of the flat-top intensity. Beside the change in beam intensity the line pattern profile is important for the transverse extrapolation. A lineout yields to a parabolic intensity profile of a line pattern with decreasing intensity to 10% of the peak value.

The normalized, transverse RMS emittances in units of mm-mrad are summarized in figure 3.10(b). Considering the non-linear effects in phase space it was not possible to reach values on the order of 3.14×10^{-3} mm-mrad already found by Cowan *et al.* [24]. In comparison to conventional sources as the *HIT* ECR source (ϵ = (450-900) mm-mrad [162]), the transverse emittance of laser accelerated proton beams is at least two orders of magnitude smaller. This better laminarity is one of the major advantages of these beams for further applications such as focusing, because the minimum focal spot of a given beam is determined by the emittance.

Deconvolved proton spectrum

The RCF detector in stack configuration enables measurement of the energy spectrum of a laser-accelerated proton beam. Protons penetrating through the RCFs lose kinetic energy in the film material, besides charge transfer and scattering of the protons. Figure 3.11 illustrates the energy deposition for different proton energies in one HD-810 film and the proton energy dependent deposition in all stack layers identified by their *Bragg* peak energy. For the film type MD-55 with two sensitive layers the resulting energy deposition curve is an overlap of two shifted curves (not shown in figure). Hence, this energy deposition curve has two maxima. Besides the deposition curves calculated with SRIM2006 [153] the necessary film data to calculate the spectrum were digitized by reading in the RCFs with the same scanner parameters as used for the calibration. After the subtraction of the radiation background (HD-810: OD = 0.05, MD-55: OD = 0.2, HS: OD = 0.24), outsized impurities like dust or scratches in the spot are marked and removed with an additional filter.

As already indicated, protons deposit a fraction of their energy in all layers penetrating through before being stopped. So the measured total deposited energy E_{total} in a specific RCF is the convolution of the spectrum with the response function of the RCF (energy deposition curves in figure 3.11):

$$E_{\text{total}} = \int \frac{\mathrm{d}N\left(E'\right)}{\mathrm{d}E} \times E_{\text{loss}}\left(E'\right)\ \mathrm{d}E', \tag{3.6}$$

where $\mathrm{d}N/\mathrm{d}E$ is the particle number spectrum and E_{loss} the calculated energy loss of a proton with energy E in the given layer. This fact requires each layer to be de-convolved by the nonlinear detector response function to determine the particle spectrum $\mathrm{d}N/\mathrm{d}E$. The way it is been done is a convolution with an assumed function for the proton spectrum. Recent publications as well as *Thomson Parabola* data have shown an exponential behaviour of the proton spectrum. There are still different types used, e.g. a simple exponential decay as a *Boltzmann* distribution for a thermal plasma expansion, equation (3.7), a modified exponential by Fuchs *et al.* [71] as a result of an isothermal, quasi-neutral plasma expansion, equation (3.8) [102] or a *Gaussian* including an adiabatic plasma expansion [80], equation (3.9),

$$\frac{\mathrm{d}N}{\mathrm{d}E} = \frac{N_0}{E} \times \exp\left(-\frac{E}{k_B T}\right), \tag{3.7}$$

$$\frac{\mathrm{d}N}{\mathrm{d}E} = \frac{N_0}{\sqrt{2Ek_B T}} \times \exp\left(-\sqrt{\frac{2E}{k_B T}}\right), \tag{3.8}$$

$$\frac{\mathrm{d}N}{\mathrm{d}E} = \frac{N_0}{E} \times \exp\left(-\left(\frac{E}{k_B T}\right)^2\right). \tag{3.9}$$

With the function for the proton spectrum and the E_{loss} values given by *SRIM* a theoretical total deposited energy is calculated for each RCF layer in the stack. The integral in equation (3.6) is solved by *Simpson*'s rule for numerical integration. The calculated energy values of the RCFs are compared to the experiment, see figure 3.12(a). By minimization of the root mean square deviation, the parameters N_0 and $k_B T$ are iteratively determined resulting in the spectrum shown in figure 3.12(b). For this PHELIX proton beam, the best fit function is given by equation (3.7) and the fit parameters are $N_0 = 6.69 \times 10^{12}$ and $k_B T = 3.97\,\mathrm{MeV}$.

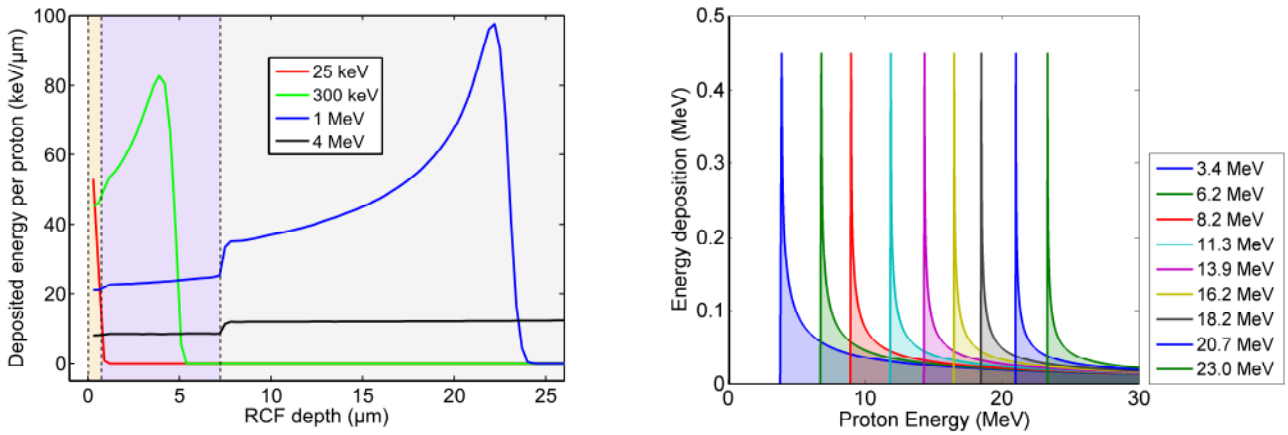

Figure 3.11: Bragg and energy deposition curves of protons in RCFs. Protons with different energies deposite parts of their energy in different composition layers (gelatin, sensitive or polyester layer) of a HD-810, shown here from left to right. For a particular proton energy, here 300 keV, the deposition in the sensitive layer is maximal (*Bragg* peak). Hence, every film of the given RCF stack can be attributed to a special proton energy. In addition, the fraction of deposited energy of protons with higher energy penetrating through the film can also be calculated leading to kind of "inverse" *Bragg* curve. Calculations done by SRIM2006 - The Stopping and Range of Ions in Matter [153].

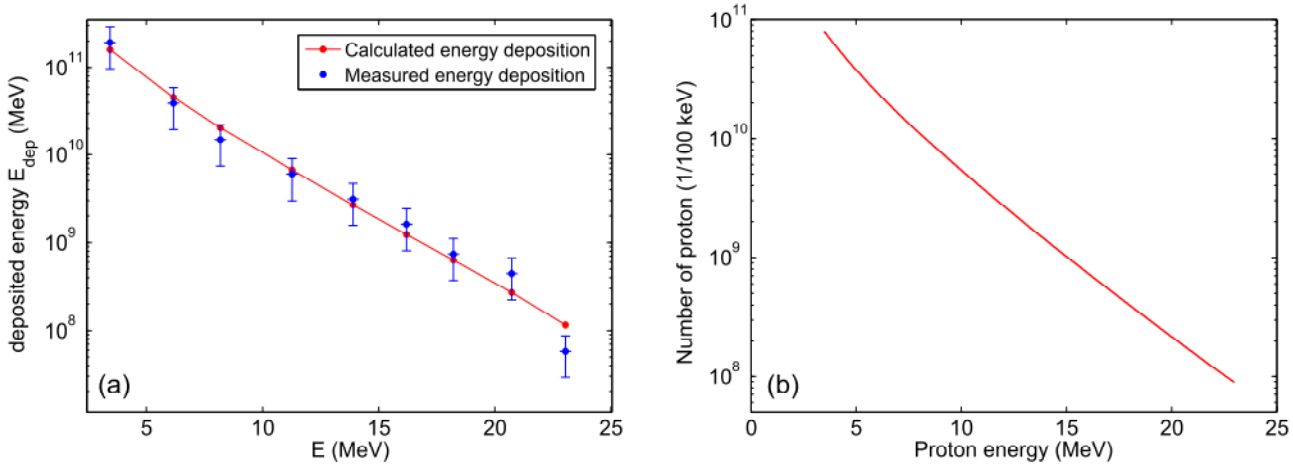

Figure 3.12: (a) Comparison of the energy deposition of the measured data with the calculated result of equation (3.6). By minimization of the root mean square deviation, the parameters N_0 and $k_B T$ are iteratively determined resulting in the spectrum shown in (b). The fit is determined in the detected energy interval [3.4 MeV, 23 MeV].

3.3.2 Spatial and Energy Resolved Reconstruction of the Proton Distribution

In comparison to standard particle spectrometers, as e.g. magnetic spectrometers [93, 94], RCFs can measure the full proton distribution not only energy resolved (see above) but also spatially resolved. Hence, a three-dimensional (x-y-E) proton distribution of the beam can be obtained. In this thesis an algorithm based on the MATLAB programming code is presented and optimized to determine the proton distribution resolved both spatially and in energy, because the spatial information of a certain energy is of interest for many applications.

The ideal condition for this method is a RCF stack configuration without any absorbing layers between the films to increase the resolution and the accuracy of the method. Therefore, a proton beam from the TRIDENT laser system (figure 3.13) was used to introduce the reconstruction instead of the PHELIX beam shown in figure 3.6. The beam was detected with a RCF stack consisting of 19 HD and 3 MD films

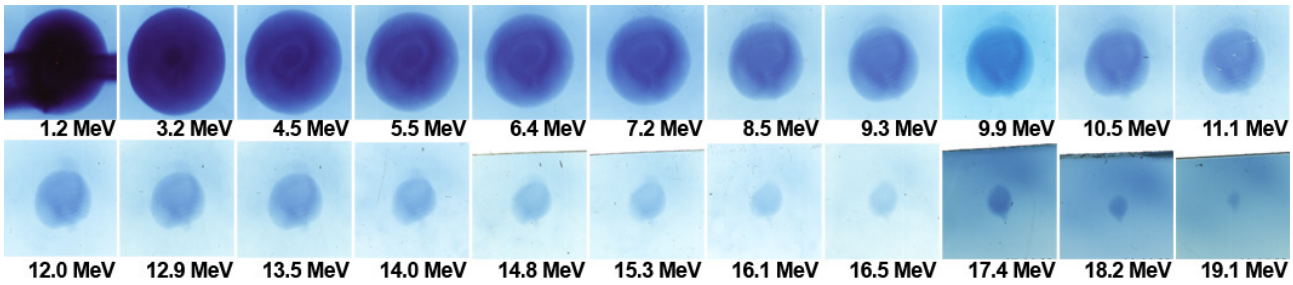

Figure 3.13: Color scans of the RCF stack of a TRIDENT proton beam. The stack consists of 19 HD and 3 MD films without copper absorbing layers in between. Hence, an initial higher resolution is given for the graphical deconvolution compared to the PHELIX stack shown in figure 3.6.

and no copper layers in between. The first RCF is neglected in the calculations, because debris and heavy ions prevent an unambiguous identification of the proton signal. The mean energy interval between two RCFs is 850 keV. To increase the resolution further, the interval size is decreased by inserting virtual active layers for a better energy resolution, see figure 3.14. The interpolation between the values of the envelope-divergence enables determination of the correct spot radius for the proton energy position for which a new layer is inserted. Then this spot size is cut out of the previous layer and is placed at the new position. On the basis of the deposited energy in all RCFs and the interpolation between these measured values, the deposited energy of the inserted layer can be matched. Due to a computational limit only three new virtual layers were inserted between two given RCFs. So, the resulting stack was of the size of 81 layers and the mean energy interval decreased to 198 keV.

A weighted subtraction of all films from each other is the way to include the graphical deconvolution of the proton energies. All following layers have to be subtracted from the former layer to deduct the different amounts of deposited energy from higher proton energies in a given film. The weighting factors for a specific stack layer (specific proton energy) are calculated as shown in figure 3.14 with the help of the energy deposition curves. Protons with the energy E_{Bragg} are stopped in the corresponding RCF and deposit the energy $E_{dep,max} = E_{dep}(E_{Bragg})$. These protons also lose kinetic energy in each of the previous layers X such that $E_{dep,X} < E_{dep,max}$. The weighting factors for the previous layers X are the ratios of $E_{dep,X}$ and $E_{dep,max}$.

Because the spatial intensity profile of the proton beam is round, a cylindrical symmetry can be assumed. Figure 3.15(a) shows a cut through the three dimensional view of the energy deposition after the graphical deconvolution. The color values correspond to deposited energy per mm^2 of the RCF. The difference in film sensitivity is clearly visible for proton energies higher than 17 MeV. Above this energy the more sensitive film type MD-55 was used. The thicker sensitive layer resulted in a higher

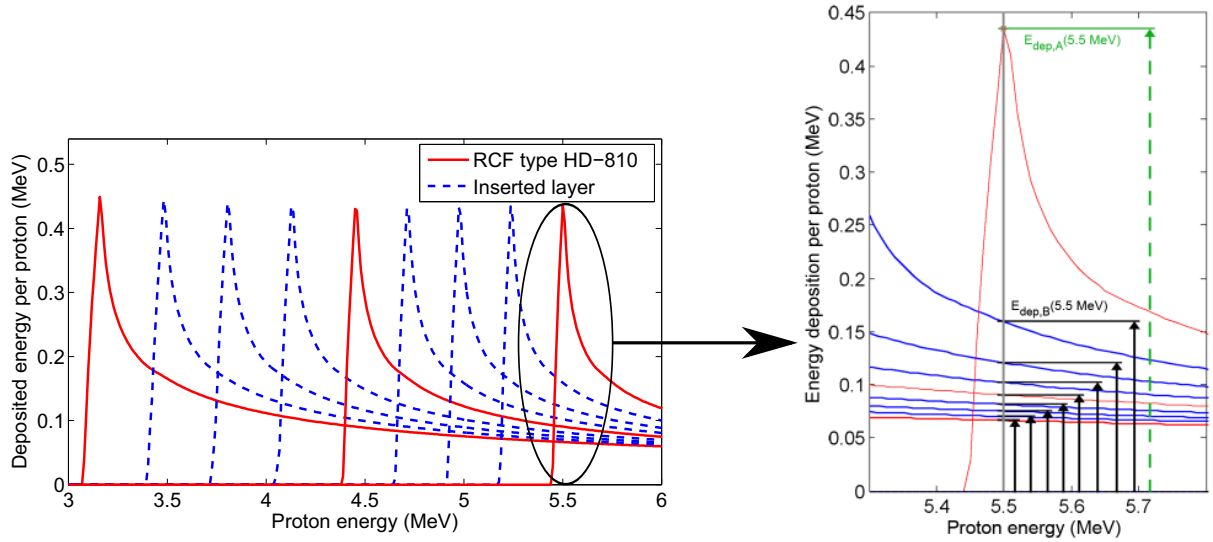

Figure 3.14: Energy deposition curves for the first three HD-810 films (red solid lines). The blue dashed curves are virtually inserted layers for the proton distribution reconstruction. These curves are used to calculate the weighting factors for the graphical deconvolution for example at the proton energy of E_A = 5.5 MeV (blow up of the right red curve in the left image). If the layer A is subtracted from the layer in front of it (B) with $E_B < E_A$, the total deposited energy distribution has to be weighted with the factor $E_{dep,B}(5.5\,\text{MeV})/E_{dep,A}(5.5\,\text{MeV})$, the ratio of the deposited proton energy of 5.5 MeV protons in the previous layer B, the maximum deposited proton energy in layer A, and so on.

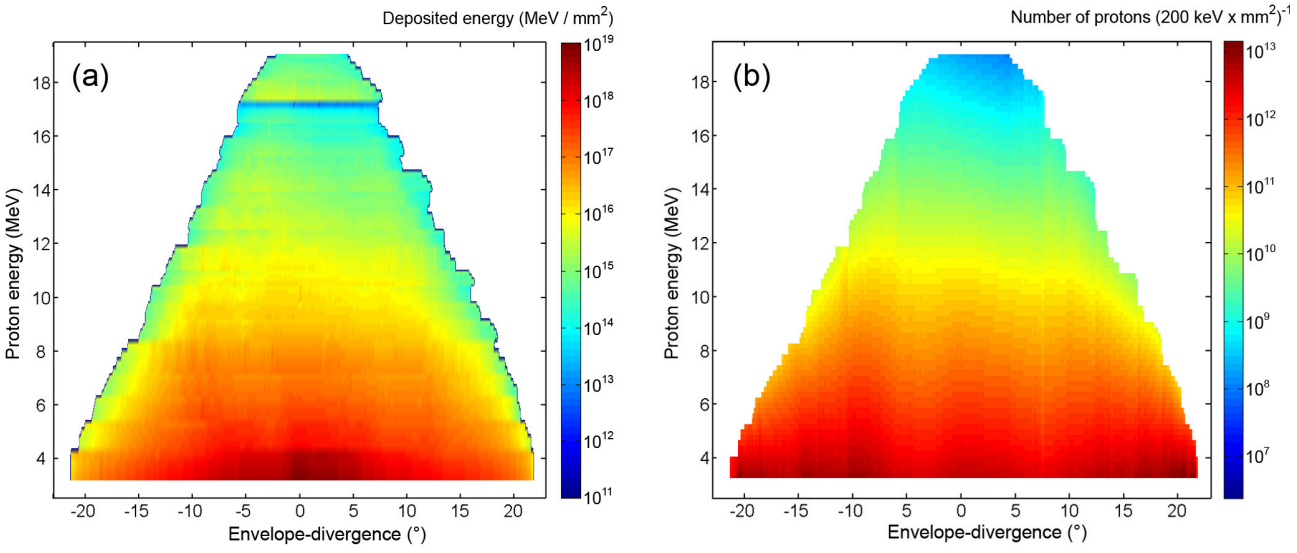

Figure 3.15: (a) Reconstructed total deposited energy distribution for the TRIDENT proton beam (after subtraction). The film type change from HD-810 to MD-55 at 17 MeV is clearly visible. (b) Spatial and energy resolved proton spectrum for the TRIDENT shot. The particle number is given for an energy interval of 200 keV, the same interval resolution as in the described algorithm for the gap between two layers.

energy deposition. Due to the weighted subtraction, a ring structure in the deconvolved RCF image is not observed, in contrast to the results by Breschi *et al.* [163]. It shows a quite good flat-top profile of the beam with falling edges. Using the SRIM energy deposition table, the angular resolved spectral distribution of the proton beam can be calculated, shown in figure 3.15(b). The deposited energy per square millimeter is divided by the deposited energy of one proton with its *Bragg* peak located in the 200 keV interval, given by the resolution of this algorithm.

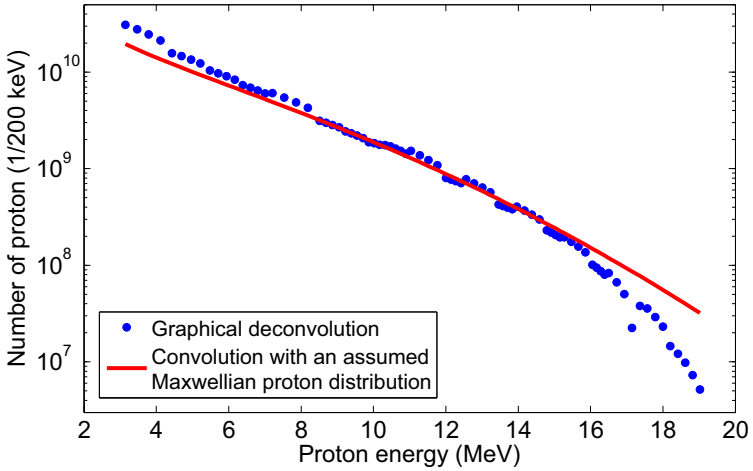

Figure 3.16: The comparison of the proton distribution function obtained by the analytical deconvolution and the developed method of the graphical subtraction. The proton number is given for an energy interval of 200 keV. This size is consistent with the energy interval between two layers in the graphical subtraction. The agreement of the measurement and the fit confirms the use of a Maxwellian proton distribution as a feasible approximation for the spectrum.

For approving the accuracy of the graphical deconvolution, the results are compared to the proton distribution obtained by the analytical deconvolution (explained in the last section). For the TRIDENT proton beam, equation (3.9) was assumed leading to $N_0 = 3.5 \times 10^{11}$ and $k_B T = 8.74\,\mathrm{MeV}$. As figure 3.16 shows, the agreement of the measurement and the fit confirms the use of a *Maxwellian* proton distribution as a feasible approximation for this proton beam. The proton numbers are given for an energy interval of 200 keV. This size is consistent with the energy interval between two layers in the graphical subtraction.

The radiochromic film imaging spectroscopy method is widely used in different groups at international laser laboratories. Results are published in several papers [41, 44, 164–166].

3.4 Low-Energy Electron Spectrometer

For future application of laser-accelerated proton beams, not only the proton distribution and its beam parameters are of interest. The nature of the TNSA mechanism leads to lots of hot electrons. On one hand, a fraction of the electrons leaves the interaction area long before the protons expand. On the other hand, the electrons that transfered their energy to the protons are now in the energy range or rather same velocity range to accompany the protons during beam expansion. Mora *et al.* [90] presented a model assuming a quasi-neutral proton beam expansion with co-moving electrons. Currently there are no precise measurements of the electron spectrum in the low keV range. Only the high-energy spectrum in the MeV [167, 168] and GeV range [9, 169] was measured with an exponentially decreasing shape. For the low energy spectrum is expected, that it connects to the high-energy spectrum and produces the necessary charge compensation in the proton beam to avoid Coulomb explosion of the beam. In the scope of this work, a master student was attended to develop and test a low-energy electron

spectrometer [170] to verify this assumption and to study the electron distribution concerning input for transport simulations of laser-accelerated proton beams. Detailed information about the electron distribution are necessary, because the electrons may have a significant influence on the proton propagation, since space-charge effects could occure for such high current beams.

For protons up to an energy of 60 MeV, the corresponding co-moving electrons would be in the energy range up to 30 keV. Such low-energy electrons can already be deflected by magnetic fields of a few milli-Tesla, while those fields have almost no influence on the flight path of the protons, because of their higher mass. The hot electrons with energies in the high MeV and GeV range experience only a little deflection and pass the spectrometer, and the low-energy electrons can be measured. The general setup for this spectrometer is a dipole magnetic field close behind a pinhole to deflect the electrons downwards. Electron sensitive *Image Plates* (IP) are used as the particle detector. Before discussing the design and the results, an image plate calibration for low-energy electrons is described in detail, because up to now there is no suitable calibration available. The current low-energy limit is 100 keV [171].

3.4.1 Image Plate Calibration for Low-Energy Electrons

Image plates are mostly used as X-ray detectors for medical applications. However, this detector can also be used as a particle detector in the field of laser acceleration [172]. The films are sensitive to a wide range of particle energies, can be reused and are resistant to the electromagnetic pulse (EMP) present in laser-matter interactions. Ionizing radiation excites the luminescent material in the image plate into a metastable state. Then, these color centers are irradiated in a scanner to pass into intermediate states, which decay into the ground state by emitting 390 nm photons. The scanner registers the photon signal and converts it into an intensity signal in units of PSL (photo-stimulated luminescence). The IP type Agfa CR MD 4.0 without protection layer was used to increase the sensitivity for the low-energy electrons.

As already mentioned for the film detectors, a calibration always depends on the parameters used during the irradiation, digitalization and analysis. Below, the most important data are listed. Due to the spontaneous decay of metastable state (fading effect [172]), the IP is losing between 10-15% of its information (depending on the type) within the first hour after irradiation. Therefore, the reading time after exposure was chosen to be 15 min. It is very important, that the IP is not exposed to light during this time, because ambient light can delete stored information. After digitization and before re-use, the IP has to be fully deleted. The initial condition is achieved by 30 min irradiation with intense, broadband light. For this calibration the IP scanner *FLA7000* made by *Fuji* was used with the scan parameters: pixel size 25 µm and sensitivity 10000.

The calibration experiments were carried out at two different measuring systems: a simple electron source delivering energies in the range 1-6 keV and a commercial available electron gun (*Kimball Physics*) with energies up to 30 keV. The error in measurement concerning the current is 5 pA and for the time 0.15 s. A cubic fit of the entire data shown in figure 3.17 provides a calibration curve for the sensitivity S of the IP type Agfa CR MD 4.0 without protection layer to electrons in the energy range of 1-30 keV:

$$S(E) = -5.6 \times 10^{-7} \cdot E^3 + 2.9 \times 10^{-5} \cdot E^2 - 2.7 \times 10^{-5} \cdot E \tag{3.10}$$

where the electron energy E is in units of keV and the sensitivity S in PSL values. Compared to already published calibrations [171, 173], the data connects very well and expand the detection range to the low-energy electrons.

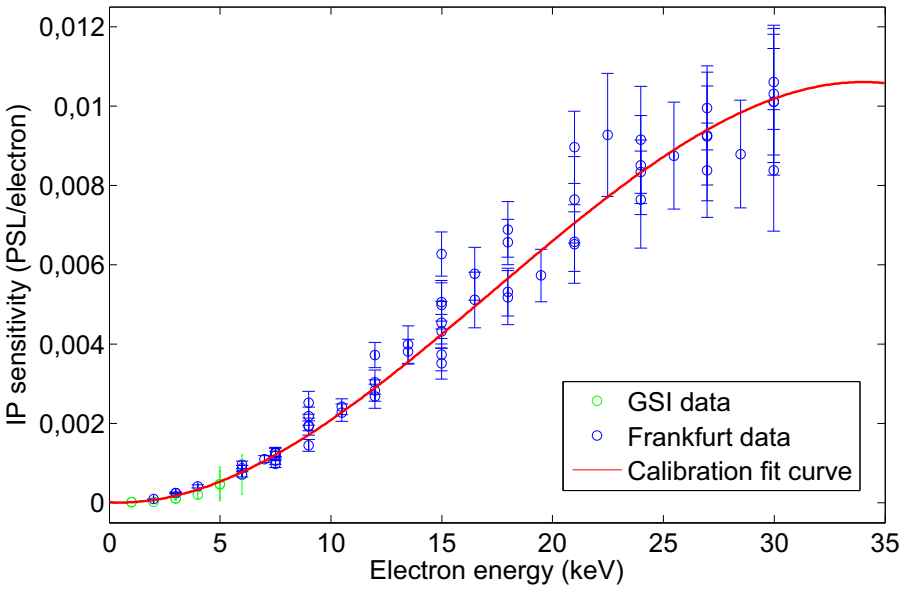

Figure 3.17: IP calibration data for low-energy electrons. Two data sets are plotted: electron source at the GSI Helmholtzzentrum füer Schwerionenforschung, Darmstadt (green) and the electron gun at the Goethe Universität Frankfurt (blue). The data can nicely be fitted by a cubic function. Courtesy of S. Busold

3.4.2 Spectrometer Design

During the development of the electron spectrometer different types of design were tested. The first version, tested as a secondary experiment at the PHELIX system, was a spectrometer consisting of an lead pinhole in an aluminium front plate, two permanent dipoles (B_{max} = 6.5 mT) and a horizontally supported image plate detector. The distance of the detector plane and the pinhole height was 26 mm. The dipole field is not strong enough to deflect the protons and the high-energy electrons. But electrons with small kinetic energies are deflected downwards and are detected by the image plate. The point of impact on the detector is energy dependent. Locally seen, the lower energies at short distances, and the high-energy electrons at greater distances.

The results provided important information about drawbacks and possible improvements for the second version of the spectrometer. Optimizing shielding of the IP detector against secondary radiation (in particular bremsstrahlung) is the main issue. Since the signal to noise ratio is very bad, the background signal on the IP has to be minimized. The second conclusion is the shape of the magnetic field. The used permantent dipole were two opposite mounted dipoles with a gap of 42 mm and a length of 5 mm. The lack of magnetic field lines guiding, for example by an iron joke, caused large fringe fields up to 30 mm in front and behind the magnets. These field accidentally increased the detected energy intervall from several keV to energies in the range of 150-250 keV. In addition, a vertical component of the magnetic field was observed due to a slight missalignment of the dipoles. Therefore, the electron track on the detector was shifted.

Based on the results of the test phase at PHELIX, the spectrometer design for the second version could be successfully modified, see figure 3.18. Now the spectrometer shielding consists of a 8 mm thick aluminium housing. The front side shielding is a combination of 10 mm polyethylene, 10 mm aluminium and 50 mm lead with a feedthrough of 2 mm in diameter. The first layer is for maximal scattering of the incident particles, the second for stopping particles, which generate low bremsstrahlung, and the final lead layer for x-ray blocking. The permanent magnets have been replaced by an electromagnet. This allows a flexible choice of the energy interval which is mapped on the detector. The electromagnet (54 windings) has a closed iron yoke for magnetic field line guidance and the pole spacing is 3.5 mm to

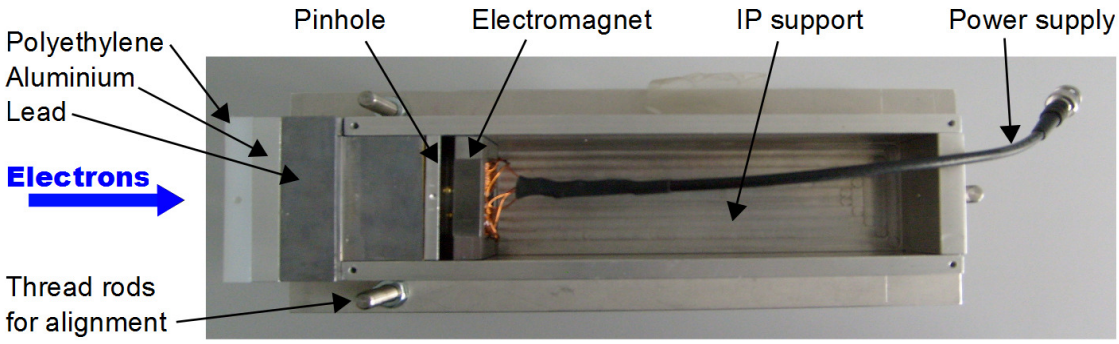

Figure 3.18: Image of the modified electron spectrometer. The laser-accelerated protons and electrons enter from the left passing 7 cm of shielding. The magnetic dipole deflects the electrons into the image plane onto the IP. The protons propagate undisturbed through the spectrometer.

keep the fringe fields minimal. For the necessary magnetic fields of a few mT only a few hundred mA are needed. In addition, the overall length of the spectrometer was reduced from 450 mm to 290 mm and an adjustable height positioner was included, which allows a better positioning in the target chamber. This resulted in a decrease of the detector length from 300 mm to 170 mm. An energy resolution of 1 keV for the range up to 20 keV is possible by using a 300 µm pinhole.

3.4.3 Comparison of Proton and Electron Spectra

The second version spectrometer was used during an experimental campaign at the Callisto laser [174], part of the Jupiter facility at the Lawrence Livermore National Laboratory (LLNL) in Californien, USA. The experiments were carried out with 10 J of laser energy in a pulse duration of 150 fs onto 20 µm thin gold foil. For a direct comparison of proton and electron spectra, the electron spectrometer was placed at zero degrees incidence angle and at a distance of 68 mm from the target (138 mm target to magnet). In front of the spectrometer, a RCF stack (3 layers) with a through hole was positioned to record the proton distribution. Before comparing both spectra, one has to ensure, that both are scaled equal. Therefore, the part of the proton spectrum passing the pinhole is calculated by the energy dependent area ratio $A_{\text{pinhole}}/A_{\text{full-beam}}(E)$. Integrated over energy bins of 500 keV, the proton numbers are comparable to the electron spectrum integrated over energy bins of 250 eV (mass ration of ∼2000). Figure 3.19 shows the initial proton spectrum, described by equation (3.7) with $N_0 = 2.2\times10^{11}$ and $k_BT = 1.74$ MeV, the transmitted proton spectrum and the measured electron distribution.

By summarizing the results of the Callisto experiment represented by figure 3.19, the observed electron spectra are apparently not of the expected shape. The spectrum is not coupled to the exponential proton spectrum and it has a well defined peak at a higher velocity (energy respectively). However, the number of particles are for both spectra almost the same, less than one order of magnitude difference $N_p \approx 4\times\ N_e$ ($N_p = 3.28\times10^7$ and $N_e = 7.84\times10^6$). Due to the ongoing analysis, the current data is still under evaluation [170], and the measurement has to be redone at a different laser system to confirm these observations.

In the frame of this work, studies on possible space charge effects in the electron spectrometer could already be done. These effects may have an influence on the electron spectrum leading to the observed peaked distribution. Therefore, the later introduced Warp code (see chapter 6) was used. The simulation setup exactly fits the experimental conditions in matters of dimensions, magnetic field and detector position. By the help of the radiochromic film imaging spectroscopy, as already shown, the proton beam parameters can be determined energy resolved. By introducing the spectrometer with its pinhole dimensions (transverse and longitudinal), only a fraction of the proton beam of 0.03% (3.28×10^7 protons)

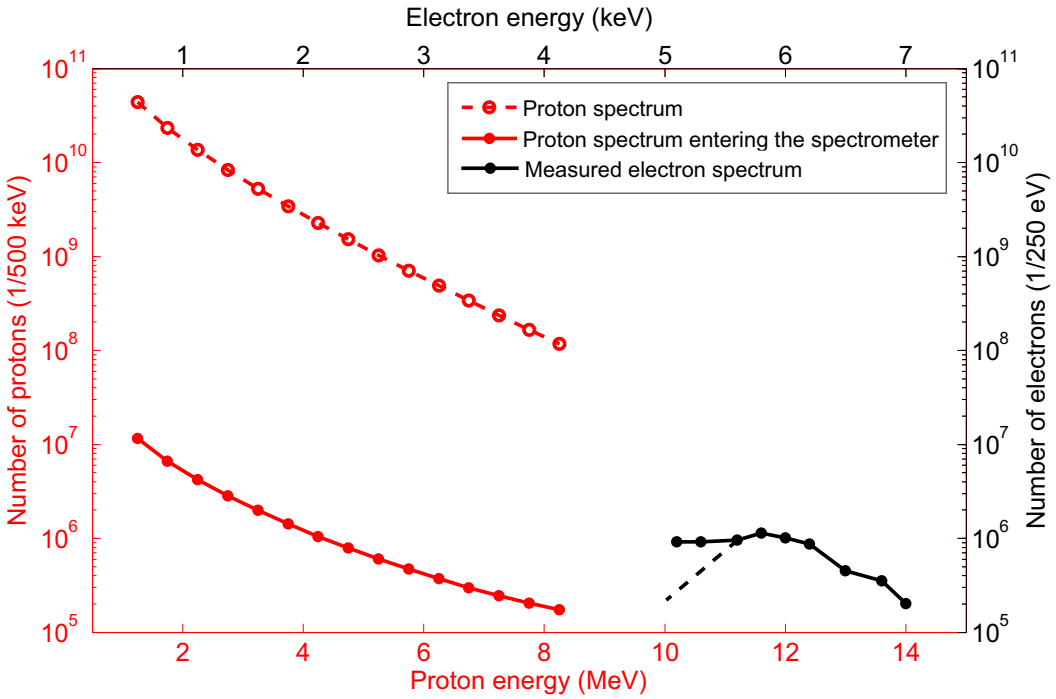

Figure 3.19: Comparison of the proton and electron spectrum. The initial proton spectrum, described by equation (3.7) with $N_0 = 2.2\times10^{11}$ and $k_BT = 1.74\,\text{MeV}$ is scaled down to the distribution passing the pinhole in the spectrometer. This spectrum can be compared to the measured electron distribution. The observed electron spectrum is apparently not of the expected exponential shape. It is not coupled to the proton spectrum and it has a well defined peak at a higher velocity (energy respectively). However, the number of particles are for both spectra almost the same, less than one order of magnitude difference. The last data points of the electron spectrum have a large error due to an increasing background signal. Different measurements have shown a decreasing slope illustrated by the dashed curve.

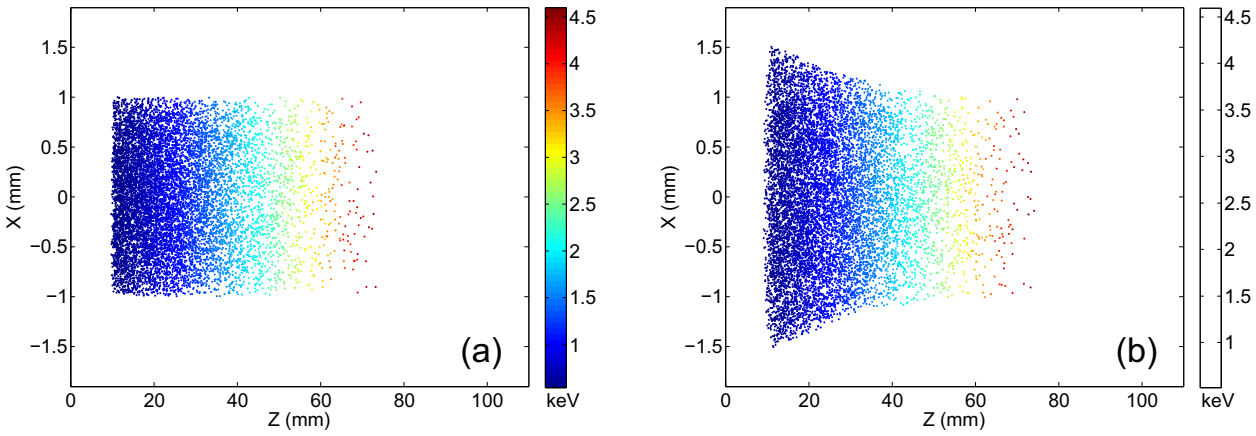

Figure 3.20: Warp simulations of the IP detector of the electron spectrometer without self-field solver (a) and considering space charge effects (b). The z-coordinate is the propagation direction and the x-coordinate is the transverse dimension. The obtained results in (a) are in exact agreement with the analytically calculated dispersion relation for this spectrometer. However, the simulation with space charge effects differs a lot. Hence, this effect can not be neglected.

can pass. This spectrum (shown in figure 3.19) is included for the proton energy range of 1-8.5 MeV. The minimum proton energy corresponds to the electron detection limit and the upper limit is the proton energy of the first layer in the RCF stack with no proton signal. The energy or rather velocity dispersion leads to a stretched proton beam of 95 mm at the entrance of the spectrometer (behind the pinhole). Assuming an initial co-moving electron distribution, the electrons also occupy an cylindric volume of 95 mm length and 2 mm diameter with the same number of particles stretched in energy. Figure 3.20 shows the simulated image plate signal for a simulation without self-field solver (a) and a run considering space charge effects (b).

The simulation without self fields is in exact agreement with the analytically calculated dispersion relation for this spectrometer. However, the simulation considering space charge effects differ a lot in the energy dependent points of impact on the IP. The electron beam is broaden in propagation direction as well as expanded transversely for the low-energy electrons. For increasing particle energy a broadening is not observed, because the particle density is too low. The space charge forces only have an influence in the propagation of the low-energy electrons, because the number of particles in this range is one order of magnitude higher. Longitudinal and transverse broadening can be seen in the experiment. Overall, however, the influence of space-charge is not strong enough to explain the observed modifications in the electron spectrum.

3.4.4 Outlook

The prevailing assumption that an electrons cloud accompanies the proton beam with the same directed expansion behaviour may need to be replaced by a new image. Repeated measurements with an calibrated electron source ensure the functionality of the spectrometer and gave clarity on possible error sources, e.g. alignment and zero magnetization. They can be excluded.

Another possible description could be the adiabatic expansion of the electrons. The electron cooling and the energy transfer in plasma expansion has already been subject of numerous studies. The energy exchange between electrons and ions in a self-similar expansion of a plasma was studied by Mora *et al.* [175]. Kinetic analytical solutions for the expansion of a Gaussian-shaped plasma in the quasineutral limit were given by Grismayer *et al.* [176]. Mora [102] also studied electron cooling in the expansion of a one-dimensional finite-size plasma with a hybrid model assuming a time-dependent Maxwell-Boltzmann distribution of the electrons. In a recent publication [177], a method is proposed that treats the expansion of a finite plasma foil with a nonrelativistic kinetic description of the electrons, including the charge separation effect. Due to the expansion, the initial electron velocity distribution function does not remain Maxwellian. As a matter of fact, the distribution function in the center of the plasma slab is composed of two parts: the first part corresponds to electrons whose behavior is determined by the quasineutral plasma region with a time-decreasing mean energy. The second part corresponds to electrons that reach the outer purely electronic part of the system and maintain the initial slope of the distribution function.

Different groups are obviously working on the theoretical picture, but no additional experimental data is available to support the observed electron sprectra. More results and a detailed discussion of the ongoing analysis can be found in reference [170]. Since the electron spectrometer was a secondary experiment during the Callisto campaign, not enough data could be recorded. Therefore, an additional experiment was proposed for the next experimental periode at the PHELIX system in 2011 to verify the idea of the new model.

4 Proton-Acceleration Experiments

Proton beams accelerated at the rear surface of a thin foil irradiated by a high-intense laser pulse have attracted a great interest of research. The prominent beam characteristics, such as high particle numbers in a short pulse duration, directed almost laminar beam propagation and a low transverse emittance, make laser-accelerated proton beams attractive for multiple applications (see section 2.3). Some applications, especially as a new generation ion source, require that the proton energy spectrum, the beam collimation and the transport capability are carefully controlled and tailored. In the past 10 years different appoaches were made. Sub-millimeter targetry is a very common approach to reduce the initial beam divergence [28] or to enhance the efficiency of the acceleration mechanism [40, 41]. However, to achieve the precision of aligning on the "'right spot"' especially in high repetition rate experiments is a challenging task.

The experiments carried out in the scope of this thesis focuses on the optical control of the proton beam parameters by means of using dual laser pulses or changing the focal conditions. In the first part of the chapter studies on the effects of laser-driven front surface pre-plasma expansion on proton acceleration are presented. The experiment was performed at the VULCAN Petawatt laser system at the Central Laser Facility, Rutherford Appleton Laboratory, Didcot UK, and the results are published in [34, 178]. In the following part, studies of the influence of laser defocusing on the proton flux relevant for the fast ignition scheme are adressed. At the VULCAN Petawatt laser system conversion efficiencies from laser into proton energy of up to 7.9% were achieved. In the last part, x-ray Thomson scattering on laser-accelerated proton heated warm dense matter is presented as a possible application for this kind of particle source. Studies on target and diagnostic optimization were performed on the TRIDENT laser at the Los Alamos National Laboratory, New Mexico, USA.

4.1 Proton beam manipulation by pre-plasma shaping

The properties of the proton beam are sensitive not only to the high power laser pulse, but also to any prepulses or Amplified Spontaneous Emission (ASE) at its leading edge. They typically preheat the front surface of the target creating plasma expansion. Even if the target is sufficiently thick that the rear surface is unperturbed, plasma expansion at the front surface can significantly affect rear surface proton acceleration. It has been shown in particle-in-cell (PIC) simulation studies that laser absorption efficiency, and therefore proton acceleration, can be enhanced by controlling the scale length of the front surface preplasma [179, 180]. This has already been observed experimentally for intensities up to 10^{19} W/cm^2 [159, 181]. In the scope of this experiment, the effects of controlled and well-characterised front surface plasma expansion on proton acceleration for intensities exceeding 10^{19} W/cm^2 were investigated. Therefore, a low intensity laser pulse (10^{12} W/cm^2) irradiates a thin foil targets prior to the focused main pulse (up to 3×10^{20} W/cm^2).

4.1.1 Experimental Method

The experiment was carried out at Vulcan's target area "'Petawatt"' using the chirped-pulse-amplified (CPA) short pulse beam and an installed long pulse beam. Figure 4.1 shows two pictures of the arrangement with the marked beam paths. The picosecond short pulse laser of 1054 nm p-polarized

light was used to drive the acceleration of protons. The focusing beam coming from the f/3 parabolic mirror is deflected by a plasma mirror [182, 183], at a position such that the intensity is in the range 10^{14}-10^{15} W/cm^2. It is an antireflection coated glass slab, which can be used to enhance the contrast of the laser on target by suppressing the ASE (Amplified Spontaneous Emission) pedestal to $\sim 10^{11}$ W/cm^2. As soon as a suffciently intense laser pulse is incident on the slab, ionization takes place on the leading edge of the pulse and the peak of the pulse then interacts with a dense plasma. The mirror effect is achieved by the rapid change in reflectivity as the substrate evolves from a solid with a reflectivity of $\sim 10^{-3}$ into a plasma with reflectivity near unity. The glas is almost transparent for the ASE prepulse, while the primary short pulse easily ionizes the target and reflects off the plasma towards the target. A calibration yielded an energy reflection onto the target of 32%. The maximum energy on target was 115 J, focused to a spot size of 5 µm (FWHM), leading to a peak intensity of 3×10^{20} W/cm^2. The angle of incidence onto the plasma mirror was 20° and onto the target 10°.

The plasma formation at the target front surface, prior to the arrival of the main pulse, was induced by 1054 nm laser pulses of 6 ns duration with lower intensities in the range of 0.5-5$\times 10^{12}$ W/cm^2. The temporal profile has a fast rise time of 0.2 ns and a slow decay from peak intensity to ∼50% at 6 ns. An f/10 lens was used to focus the beam to an approximately flat-top intensity distribution with a diameter of 450 µm, centered on the position of the short pulse focus. In addition, the delay of the short pulse beam with respect to the arrival of the long pulse on target was varied in the range of 0.5 to 3.6 ns with 0.2 ns precision.

The targets were either 25 µm thick planar copper foils or 25 µm thick gold foils with a periodic groove structure (same targets as shown in figure 3.5). The spatial and energy distributions of the accelerated protons were measured with radiochromic films in stack configuration with alternate copper layers in between to increase the detection range. The stack was placed 40 mm behind the target and aligned along the target normal axis. As shown in figure 4.1, the targets and the RCF stacks were mounted on rotation wheels to enable multiple shots before venting the target chamber. Thus, more shots were possible, because one vent and pump cycle lasted at least 60 min.

In addition, a transverse interferometric optical probe (frequency doubled) was installed to study the front surface plasma expansion [184]. The target was probed at a fixed time of 5 ps after the arrival of the short pulse. The snapshot was recorded by a CCD camera.

4.1.2 Results

Two different preplasma studies were carried out. First, the arrival of the long pulse beam was fixed to Δt = 0.5 ns before the short pulse reached the target and the proton beam parameters were measured for ablation pulse intensities from (0-4.9) TW/cm^2). The second series was recorded at a fixed intensity of 1.2 TW/cm^2 but as a function of the delay Δt from 0 to 3.6 ns). The intensity scan leads to the results illustrated in figures 4.2 and 4.3. By the help of the radiochromic film imaging spectroscopy, the envelope-divergence and proton source size are calculated. Before discussing the results, the scale length of the plasma electron density is introduced. The interferometric probe provides a picture of the plasma expansion at the target front side. For each shot in the series, a picture of the electron density was recorded. The interferometry was limited in resolving higher densities. Hence, two different scale lengths are defined. L_o refers to the outer part of the preplasma, the underdense region. The inner region near the critical density is described by L_i, which can not be resolved. L_o is determined by fitting the relation $n_e(x) \propto \exp(-x/L_0)$ to the electron density profile along the target normal extracted from the interferometric probe measurements. n_e is the electron density and x is the distance from the target surface.

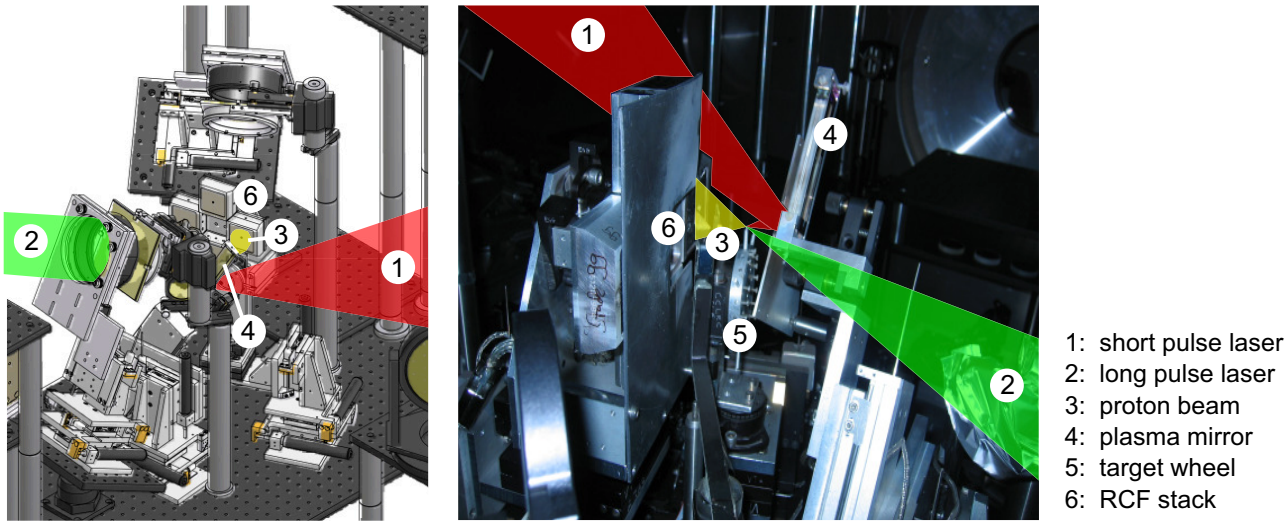

Figure 4.1: Drawing and picture of the main experimental setup. The short pulse is deflected by a plasma mirror onto the target. Just before, the long pulse is focuses on the same spot to generate a preplasma. The targets and the RCF stacks are mounted on rotation wheels to enable multiple shots during one vent and pump cycle.

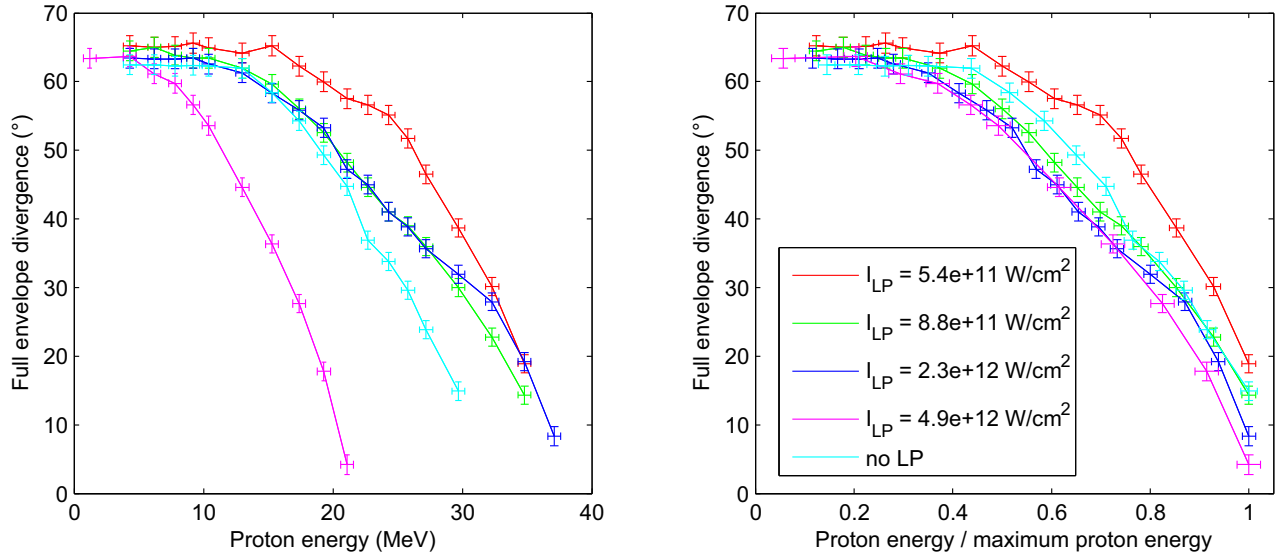

Figure 4.2: Envelope-divergence of the VULCAN proton beam for the intensity scan of the long pulse beam. The envelope-divergence clearly drops for an increasing scale length. But scaling all beams to their maximum proton energies, an almost similar behaviour can be observed apart from the shot with $I_{LP} = 0.54$ TW/cm^2, where the scale length is in the optimum range to increase the proton number and the flux.

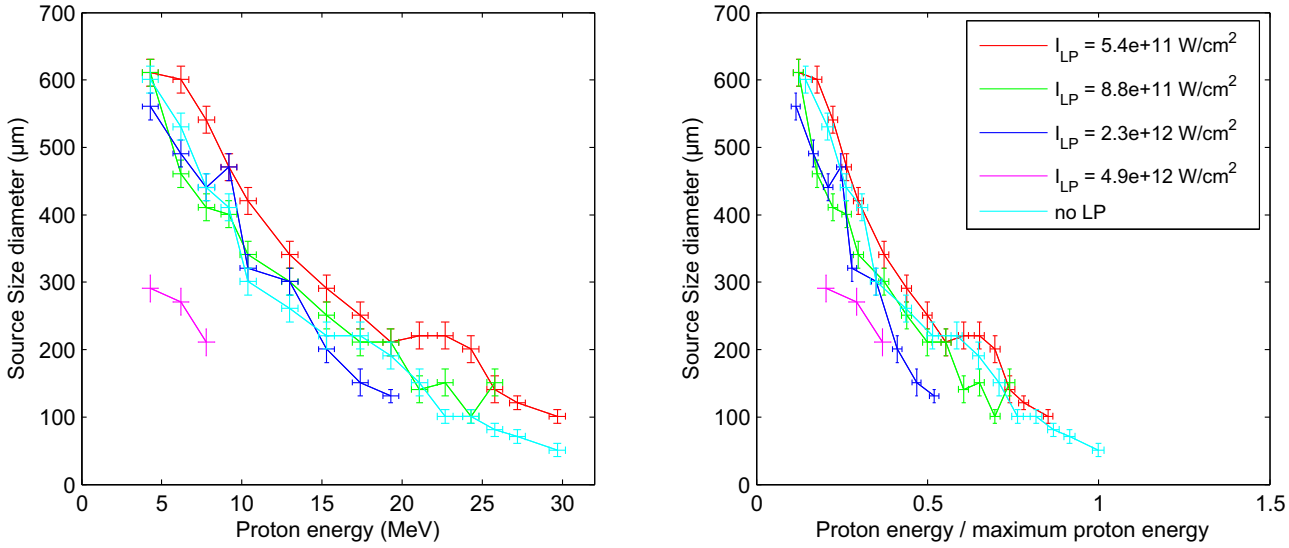

Figure 4.3: Proton source size of the VULCAN proton beams for the intensity scan of the long pulse beam. It was not possible to calulate the source size for the proton beam up to the highest proton energy, because the line pattern in the detector disappears. However, if the proton beams are scaled to their maximum energy obtained by the envelope-divergence measurement no particular oberservation can be made.

It can be observed that up to an induced plasma scale length of 60 µm, the proton spectra is enhanced with much higher fluxes for all energies. Also a higher maximum proton energy up to ∼25% compared to the case with no or very little pre-plasma is found. As the plasma scale length is increased to values between 60 and 120 µm the maximum proton energy and the proton numbers at all energies are reduced to measured parameters without prepulse. Beyond plasma scale length of 120 µm the fluxes drop even more. As expected, the plasma expands faster when heated at higher intensities, creating a longer plasma scale length. An intensity dependent prepulse effect can also be seen in the envelope-divergence and proton source size illustration in figures 4.2 and 4.3. For scale lengths >60 µm the envelope-divergence clearly drops for an increasing scale length. But scaling all beams to their maximum proton energies, an almost similar behaviour can be observed. The shape of all curves is the same and they lie on top of each other apart from the shot with $I_{LP} = 0.54\ \mathrm{TW/cm^2}$. For this case, the plasma scale length L_o is ∼38 µm and is in the interval of 30-60 µm, where an optimum preplasma expansion exists for enhancing the proton flux, energy and conversion efficiency from laser light into proton energy respectively. This same behaviour is observed in the timing scan. For a delay of 0.5 ns, the plasma scale length was close to 60 µm. For the measured source sizes shown in figure 4.3, the intensity dependent behaviour is not to be seen as clear. For all shots including the long pulse beam, it is not possible to calulate the source size for the proton beam up to the highest proton energy, because the line pattern in the detector disappears. Up to now, there is no clear explanation for this phenomenon. But a possible assumption is an initial distortion of the accelerating electron sheath at the rear side of the target, so that the beam laminarity is disturbed. Thus, the density modulations in the proton beam can not be transported up to the detector. For later times and lower energies respectively, the sheath form is rebuilt and the line pattern in the detector appears. If the proton beams are scaled to their maximum energy obtained by the envelope-divergence measurement no particular oberservation can be made.

An explanation for the drop in the envelope-divergence (flux respectively) can be found by comparing the transverse optical probe measurements for short and long plasma scale lengths, see figure 4.4. The propagation of the short pulse laser in the outer region of the expanding plasma changes significantly with increasing plasma scale length. At the optimum preplasma condition (enhanced proton flux and maximum energy), the laser propagation in the preplasma is observed as a single channel, figure 4.4(a), with a width smaller than the estimated focusing cone of the beam. This effect increases the laser

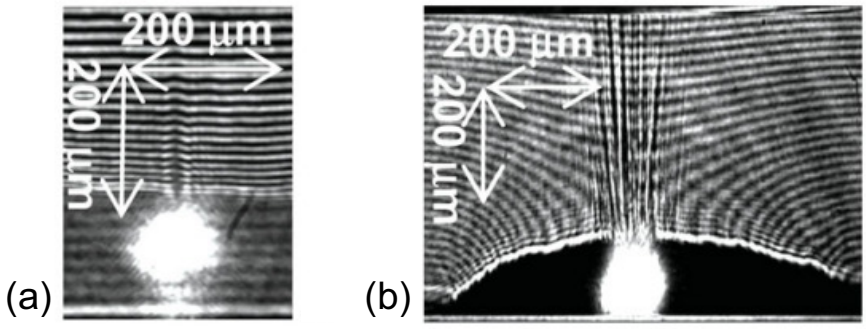

Figure 4.4: Example interferometric probe image showing channelling of the CPA laser beam in a short scale length preplasma (a) and filamentation of the laser beam in a long scale length preplasma (b). The laser pulses are incident from the top and self emission at the critical surface is observed as bright spot. Images taken from [34].

intensity and is know as relativistic self-focusing. For much longer scale length, figure 4.4(b), the laser propagation seems to break up and split in multiple filaments over a large area [185]. This reduces the laser intensity and agrees with the observed changes to the proton maximum energy, which scales with the square root of the short pulse laser intensity [179].

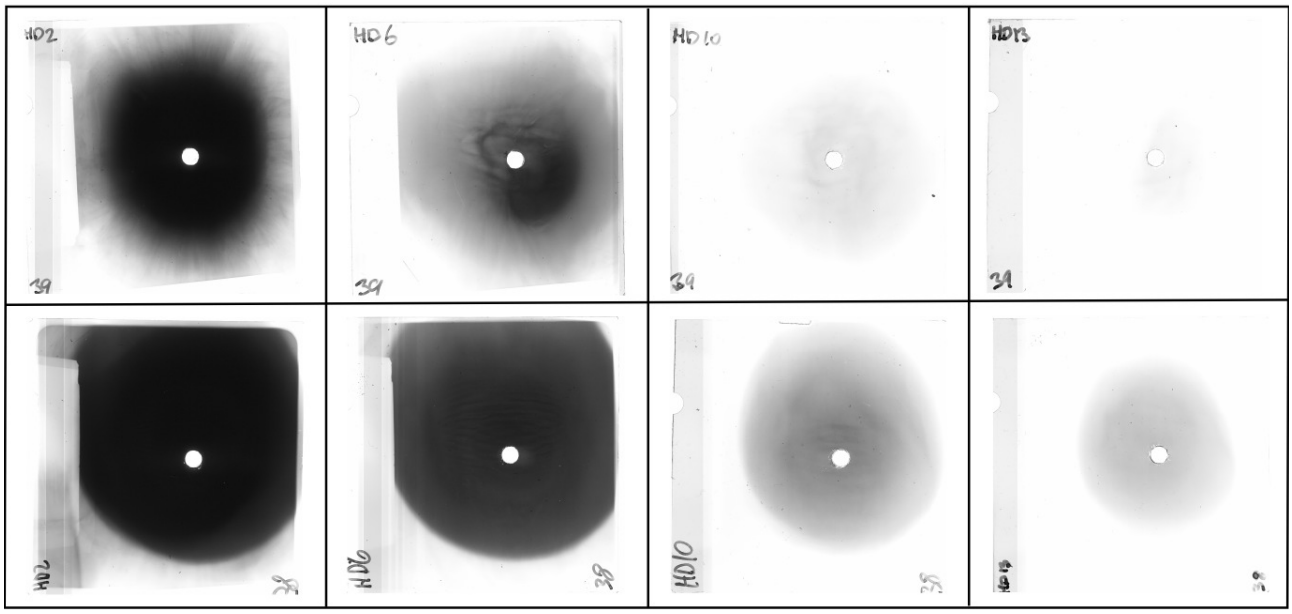

Figure 4.5: Comparison of identical RCFs of two different VULCAN shots. Layer energies: 4.3 - 10.4 - 19.3 - 24.3 MeV. *Top row:* a reference beam without generated preplasma (∼170 J in a 30 µm spot leading to 1.1×10^{19} W/cm^2) and in the *bottom row* a proton beam, where a long pulse generates a preplasma 3.6 ns prior to the main pulse (long pulse: 7.3 J in a 500 µm spot leading to 1.3×10^{12} W/cm^2, main pulse: same parameters as the reference shot). Significant improvements in the uniformity and circularity of the proton beam over the full proton energy range are observed.

Whereas there is an optimum scale length to enhance the maximum proton energy, the spectrum and flux respectively, improvements in the spatial-intensity profile of the proton beam are observed for all cases in which a preplasma expansion is produced by the ablation pulse. Figure 4.5 shows RCFs of two different proton beams. One is the reference beam with a sharp preplasma density gradient, because no prepulse was used (top row), and a proton beam, where the long pulse generates a preplasma 3.6 ns prior to the main pulse (bottom row). For the first case, one can observe an uneven and asymmetric flux distribution across the beam, whereas with prepulse the profile of the resultant accelerated proton

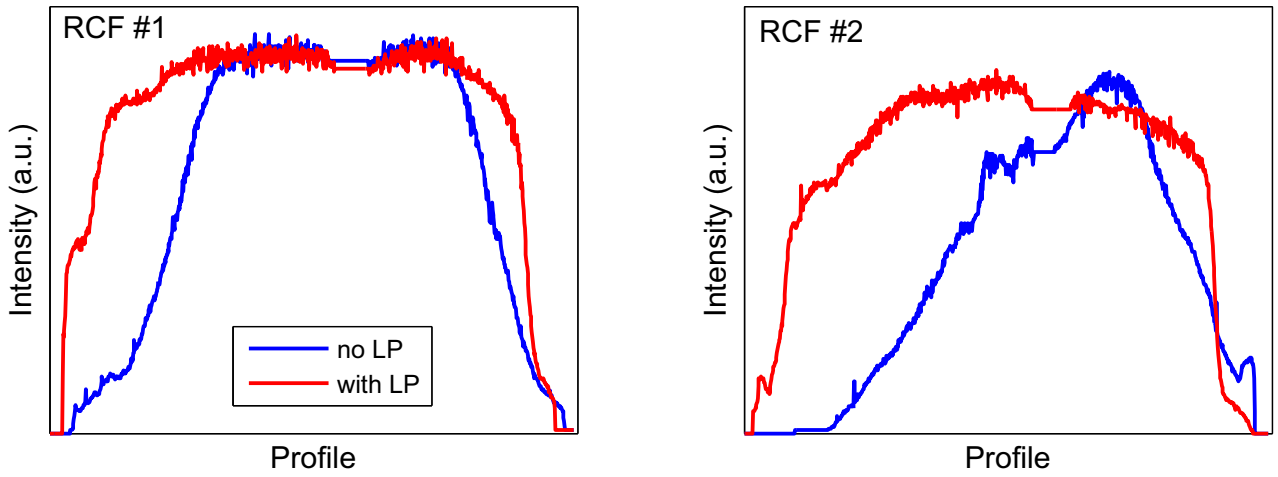

Figure 4.6: Profiles for two different proton energies - RCF#1: 4.3 MeV and RCF#2: 10.4 MeV. The proton beam generated by VULCAN including a prepulse (—) is more circular with a sharp edge and has a more uniform flux distribution at both energies compared to the reference shot without preplasma (—).

beam changes. The proton beam becomes more circular with a sharp edge and has a more uniform flux distribution for all detected proton energies pointed out by two profile examples in figure 4.6. A total flux increase up to a factor of 3 can also be observed by the lifted profiles. Additional details, results and simulations are discussed in McKenna *et al.* [34] and Carroll *et al.* [178].

4.2 Defocusing studies for proton flux optimization

The development of the world's largest high power lasers is bringing forward the prospect of achieving Inertial Confinement Fusion [186] in the near future. The National Ignition Facility [187], which can deliver >1 MJ of laser light is now fully operational and the Laser Megajoule facility will be online in 2012. To ultimately meet the needs of commercial energy production, ways of producing high fusion gain with high repetition rate sub MJ drive lasers must be examined and one promising scheme under study is Fast Ignition (FI). In Fast Ignition, a separate ignitor beam deposits energy in the compressed core of a fusion capsule to raise the temperature to the point that burn is initiated. FI relaxes the symmetry requirements for compression and potentially reduces the driver laser energy required to achieve ignition and high gain [188]. Many of the studies on FI have concentrated on evaluating the potential of a beam of high energy (∼MeV) electrons to heat the core. An alternative FI scheme is to use a beam of laser driven ions as the heating source [29]. As the efficiency with which ions of suitable energy can be made (<6% [189]) is lower than the efficiency of producing electrons (50% [10], ∼90% [190]), this route has not received equal attention.

This experiment was proposed to confirm experimental evidence for a new regime of ion acceleration that may provide the energetic conversion efficiency required for viable proton driven FI. In a feasible FI scenario, an efficiency of >15% laser light conversion into deposited proton energy in the core must be delivered. To achieve this, either the overall conversion efficiency must be high or the number of protons in the desired energy range has to be optimized to increase the coupling efficiency. Recent new target designs and laser pulse shaping experiments indicate promising progress in the near future [28, 34, 41, 191]. In the majority of ion acceleration experiments, the laser is focused to the smallest possible spot to generate the highest achievable hot-electron flux through the target to maximize the sheath field associated with the target normal sheath acceleration (TNSA). The approach of the recent experiment is to find laser conditions, which are optimised to produce a larger number of much colder electrons generating a significantly greater total flux of protons with a much sharper and lower energy

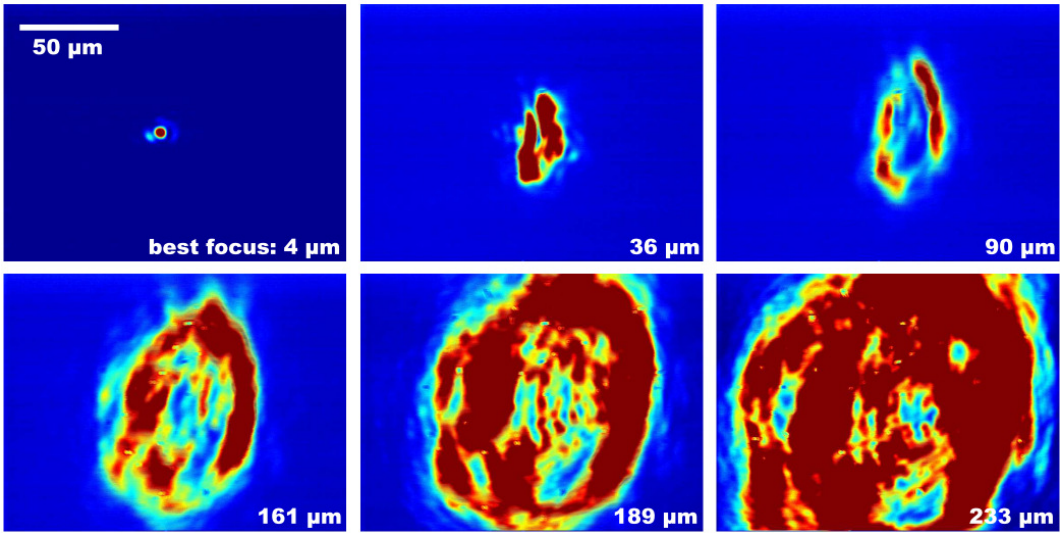

Figure 4.7: Recorded CCD images of the a focal diameter scan. The final focusing parabola was moved along the focal axis. The image intensities are not comparable, because the sensitivity of the camera was changed to resolve the full spot. A best focus of 4 µm could be achieved. As soon as the parabola defocuses at the position of the target, the beam starts to break up in filaments. No real flat-top focus was achieved, because the focusability is limited due to the quality of the parabola. The inserted value in each image is the averaged dimension of the focal spot diameter.

cut-off. Optimum coupling in ion driven Fast Ignition schemes ideally requires a narrow energy band of ∼10 MeV protons to deposit the energy into the core whilst avoiding pre-heat issues due to faster ions. During this experiment a significant increase in flux and efficiency has been observed by changing target thickness and laser focal diameter.

4.2.1 Experimental Method

The experiments were performed at the 1054 nm VULCAN Nd:glass petawatt laser based at the Rutherford Appleton Laboratory [192] already introduced in section 4.1.1. Thin aluminium foils (0.8-25 µm thick) were irradiated with 0.7 ps pulses of 220 J energy over a range of intensities from 3×10^{17} to 5×10^{19} W/cm^2. The intensity on target was varied by changing the diameter of the focal spot from 30 to 350 µm. The targets were irradiated in p-polarisation under an incidence angle of 35°. The contrast of 10^9 was achieved by using a dielectric coated plasma mirror [182, 183].

The setup of this experiment is very similar to the one described in the last section. The main diagnostic tool for measuring the spectral intensity distributions was also radiochromic films in stack configuration. The stack consisted of film types HD-810, MD-55-V2 and copper absorber layers, placed 35 mm behind the target to catch an angular cone of 60°. It is wrapped in aluminium foil to shield it from target debris and radiation.

Before starting the measurements, the final focusing parabola motion was calibrated by passing through different focal spot sizes. The recorded images can be found in figure 4.7. The image intensities are not comparable, because the sensitivity of the camera was adjusted to resolve the full spot. A best focus of 4 µm could be achieved. As soon as the parabola defocuses at the position of the target, the beam starts to break up in filaments. No real flat-top focus was achieved, because the focusability is limited due to the quality of the parabola. The inserted value in each image is the averaged dimension of the focal spot diameter.

4.2.2 Results

During this experiment, an optical transmission radiation (OTR) measurement was installed to investigate the influence of the spatial distribution of the focal spot onto the accelerated hot electrons [193]. Radiation is emitted as charged particles, e.g. electrons, and their electric fields propagate over a transition between two different mediums (target/vacuum boundary). The optical component of this transition radiation is termed OTR. The imaging enables the spatial structure and divergence of the fast electron beam transported through the target to be studied. However, this diagnostic is only sensitive to the highest energy electrons over a few MeV. The low energy electron population will not be subject to detection [86, 194]. Due to a limited number of data shots, firm conclusions regarding changes to electron transport as a function of laser spot size cannot be drawn at this stage. But by comparing the laser intensity profile and the OTR measurement at the target rear side, a correlation could be observed (figure 4.8). Further investigations are required to extend these initial findings of spatial intensity mapping of the laser focus onto the fast electron current within the target. However, in a different experiment, an imprint of elliptical shaped laser foci onto the proton beam spacial distribution could already be demonstrated [46].

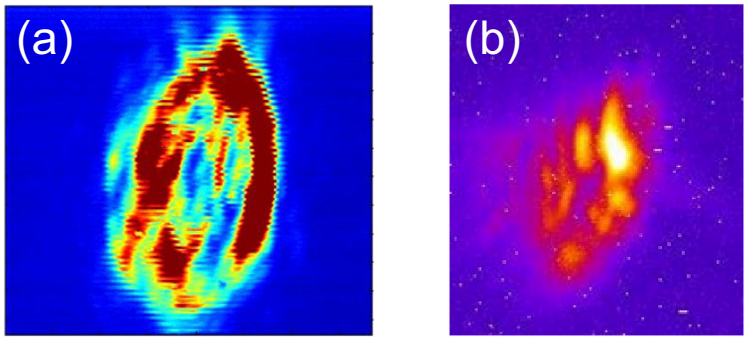

Figure 4.8: (a) CCD image of the defocused laser spot with a diameter of 161 µm. (b) Recorded CCD image of the optical transmission radiation of the electrons entering into vacuum at the target rear side. Clearly visible is the mapping of the laser intensity profile on the electron distribution propagating through the target.

The main findings of our investigation are in changes to the spectral intensity distributions of the proton beam. The focal spot diameter scan was carried out using 2 µm thick aluminium targets and keeping the laser energy on target constant at (215±10) J. As the spot diameter is decreased from 350 to 60 µm, the temperature of the proton beam and the total flux increases as shown in figure 4.9(a). At a focal spot diameter of 30 µm, the flux drops tremendously, because the required contrast in order to prevent the rear surface from being perturbed by the ASE induced shock wave travelling through the target [71] is not fulfilled. Hence the optimum is an interplay between target thickness and laser intensity. Therefore a series of different target thicknesses was recorded. Figure 4.9(b) clearly points out the increase in flux for thinner target foils. In addition, this confirms the assumption of recirculating electrons and enhancement of the electron sheath density respectively. Thus, the electric field strength for the proton acceleration is increased, that is already be seen at low-energy laser systems [191]. By decreasing the target thickness by a factor of 30, the conversion efficiency increases from 0.7% to 3.2% (factor of 4.8). No increase in the maximum proton energy due to the decrease in target thickness as suggested by [37] is observed. However, due to the increase of the energy interval between sucessive RCFs (separated by absorber layers at higher energies), the spectrum resolution decreases for higher proton energies. This results in an uncertainty of 3 MeV for the highest energies. Any change is on a scale smaller than resolvable by the RCF stack. The plasma mirror and the large focal spot decrease the prepulse intensity below the critical value in order to prevent the rear surface of the 2 µm from being perturbed.

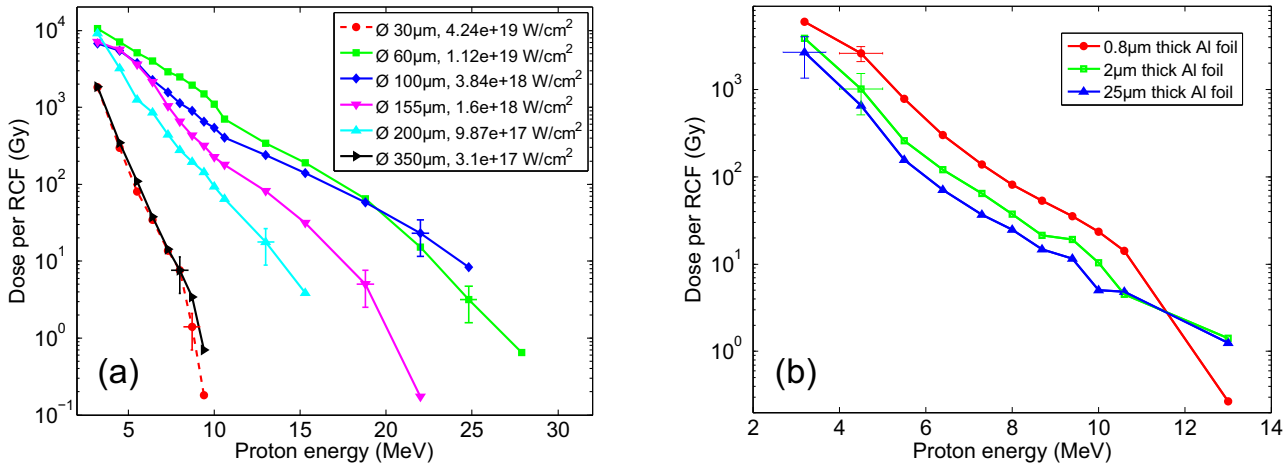

Figure 4.9: (a) Focal diameter scan for 2 µm thick aluminium target foils irradiated with pulses of (215±10) J laser energy. At a 30 µm focal spot, the intensity of the laser is still to high. The optimum focal spot size for the highest flux is arround 60-100 µm. Further increase in focal diameter leads to reduced flux and maximum proton energy. (b) Series of laser-accelerated proton beams generated from different thick aluminium target foils. The focal spot size is fixed to a diameter of 220 µm including ∼195 J of laser energy. By decreasing the target thickness, the proton yield is significantly increased. For both cases, the short pulse laser is reflected by a plasma mirror onto the target under an incident angle of 35°. Error bars are exemplarily plotted for one data point of each beam.

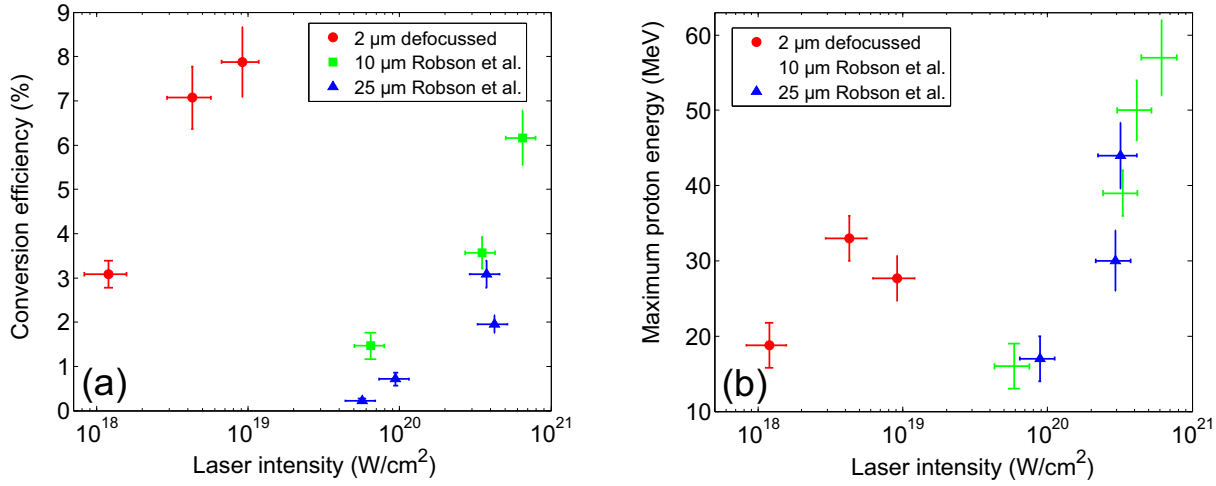

Figure 4.10: (a) Behaviour of the laser to proton beam energy conversion efficiency as a function of target irradiance for 2 µm thick Al foils irradiated with a defocused beam plotted in red (disc). The green (square) and blue (triangle) data is reproduced from Robson *et al.* [83] and was obtained at best focus. (b) The maximum proton energy is plotted against the intensity for the same shots. The highest conversion efficiency of 7.9% could be achieved with a focal diameter of 60 µm and a maximum proton energy of 28 MeV.

However, as the prepulse intensity is $\sim 10^{10}$ W/cm^2, a shock break out effect would be expect resulting in a decrease of the proton flux for thinner targets than those used in the current study.

For laser-accelerated proton beams produced at the VULCAN laser, the proton spectrum is approximated by a *Maxwellian* distribution represented by equation (3.9). Using this fit, laser to proton energy conversion efficiencies for protons with energies >4 MeV were extracted, see figure 4.10(a). The lower limit of 4 MeV was decided, because the detection of low energetic protons with a RCF stacks is limited by the thickness of the aluminium foil used for shielding. Furthermore, it was chosen to provide the opportunity to compare the results with previous published data [71, 83]. The difference between a standard configuration in which targets are irradiated at maximum intensity [83] and a thin target with a defocused laser pulse is plotted in figure 4.10. In previous work, it appeared that the highest efficiency was achieved with the highest intensity. Here, it is demonstrated that substantially higher efficiencies are obtained by defocusing the laser to reduce the intensity. As figure 4.10(b) shows, that the maximum proton energy is reduced as a consequence of the defocusing. For laser-accelerated proton beams which typically have an exponential-like distribution, the majority of the deposited energy is due to the large number of lower energy protons. Hence, for Fast Ignition applications, the protons in the 5-10 MeV region are of primary interest. Ion beams produced by defocusing the laser clearly offer two advantages for FI or heating applications. The absolute conversion efficiency achieveable can be higher and the fraction of energy carried by the lower energy protons is larger. The maximum efficiency achieved by Robson *et al.* [83] of 6.2% was taken at tight focus at a laser intensity of 7×10^{20} W/cm^2, with a maximum proton energy of 58 MeV using 10 µm thick targets. Here, a higher efficiency of 7.9% at an intensity of 80 times lower (9×10^{18} W/cm^2) with a maximum proton energy of 28 MeV could be achieved.

Below, the difference between a standard configuration of a thick target and best focus and a thin target with a defocused laser pulse is investigated according to the heating efficiency of a sample. The different laser and target parameters are shown in figure 4.11(a). The reference shot (red) was on a 25 µm thick Al foil with best focus resulting in an intensity of 2.5×10^{21} W/cm^2. This shot with a conversion efficiency of 2.2% fits very well to the VULCAN measurements with 220 J laser energy and a pulse length of 1 ps done by Robson *et al.* [83]. At the same laser energy of 220 J a huge increase of the proton flux was observed by decreasing the target thickness to 2 µm and scaling up the focal diameter to 60 µm. To illustrate the possibility of heating solid matter by a non-monoenergetic divergent proton beam, the two-dimensional hydrodynamic code MULTI-2D [195, 196] was applied. The code uses a Lagrangian grid composed of triangular elements to solve the gas-dynamic equations together with radiation transport and electron thermal conduction in cylindrically symmetric geometries. The code utilizes tabulated equation-of-state data from the SESAME library [197]; the energy deposition of the particle beam is modeled by ray-tracing. At this temperature stopping data from the SRIM code [153] for cold matter can be applied. The results are shown in a 1-D illustration in figure 4.11(b) and spatially resolved in figure 4.12. The 200 µm thick carbon sample with a distance of 300 µm to the source is heated by the protons entering the foil from the right. The hotter protons penetrate deeper in the material. But due to the exponential distribution, only a small fraction of particles have this energy. For decreasing proton energy and increasing particle number, the penetration depth decreases but the temperature goes up. Due to the higher flux, the maximum achievable temperature in the sample increases by a factor of almost 3. The included proton spectra have a low-energy cutoff at 1 MeV. Therefore, the temperature drops for penetration depths smaller 15 µm. In addition, the energy dependent envelope-divergence of the protons is included leading to a radial dependent temperature gradient for a fixed target depth.

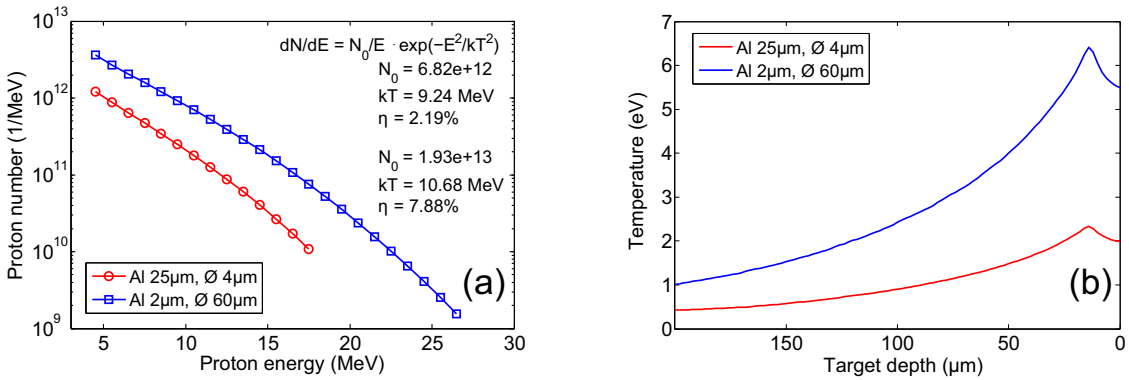

Figure 4.11: (a) Input spectra for the MULTI-2D simulation to illustrate the possibility of heating solid matter. (b) Lineouts of the temperature along the proton beam propagation direction. The protons enter the 200 µm thick carbon sample from the right. Due to the exponential spectrum, the highest temperature is achieved for the lowest energies, which have the highest particle numbers. The low-energy cutoff of the spectrum included in the simulation was at 1 MeV. Simulation data provided by An. Tauschwitz.

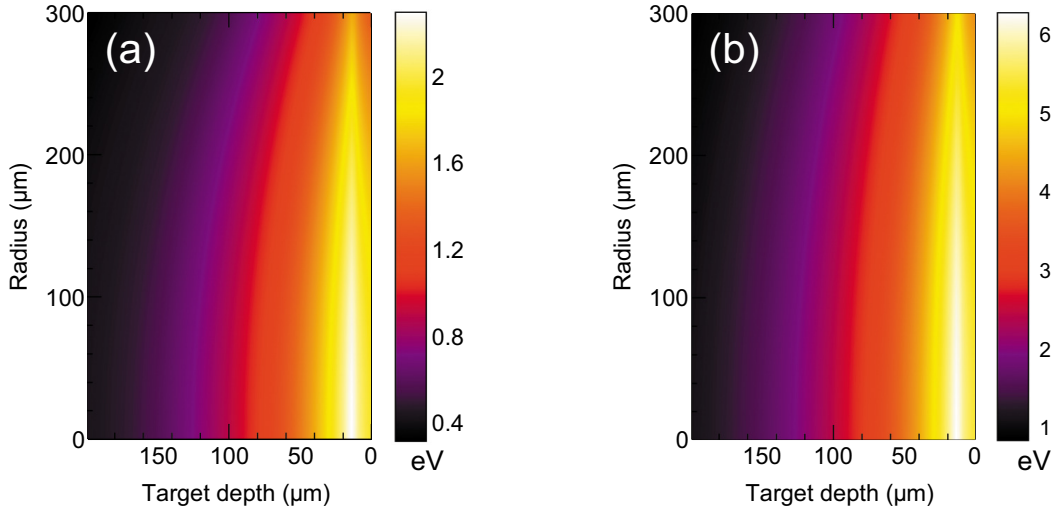

Figure 4.12: (a) Spatially resolved temperature illustration of the reference shot with a 25 µm thick Al foil and best focus. (b) Spatially resolved temperature illustration of the improved spectrum with a 2 µm thick Al foil and a 60 µm focal spot. Simulation data provided by An. Tauschwitz.

4.3 Generation of Warm Dense Matter by Laser-Accelerated Proton Beams

In the following section, two experimental campaigns on spectrally resolved X-ray Thomson scattering (XRTS) as a diagnostics of laser-accelerated proton heated warm dense matter are described. Both experiments were carried out at the TRIDENT laser facility at the Los Alamos National Laboratory, New Mexico, USA. In the scope of this thesis, only the possible application of laser-accelerated proton beams is highlighted. A detailed description of the diagnostic can be found in [28, 198, 199].

Laser-accelerated ion beams are capable of creating exotic states of matter more efficiently than lasers. Whereas lasers only interact with the surface of a sample, protons can penetrate deep into the material of interest thereby generating large samples of homogeneously heated matter. The short pulse duration of laser produced ion beams furthermore allows for the investigation of equation of states close to the solid state density, because all energy is deposited in the sample before the volume expands. In addition, the interaction of protons with matter dominantly is due to collisions and does not include

a high temperature plasma corona as it is present in laser matter interaction. These characteristics make laser-accelerated proton beams well-suited for creating isochorically heated matter in extreme conditions [28] (called warm dense matter – non-equilibrium state of matter between a solid and a plasma at high density pressure and temperature). XRTS is ideally suited to diagnose this state of matter. The use of short-pulsed x-rays allows to study the sample before the hydrodynamic expansion sets in. They are not only able to penetrate deep into the matter revealing the properties in the bulk material, but X-rays can simultaneously get the most wanted parameters temperature and density with highest precision.

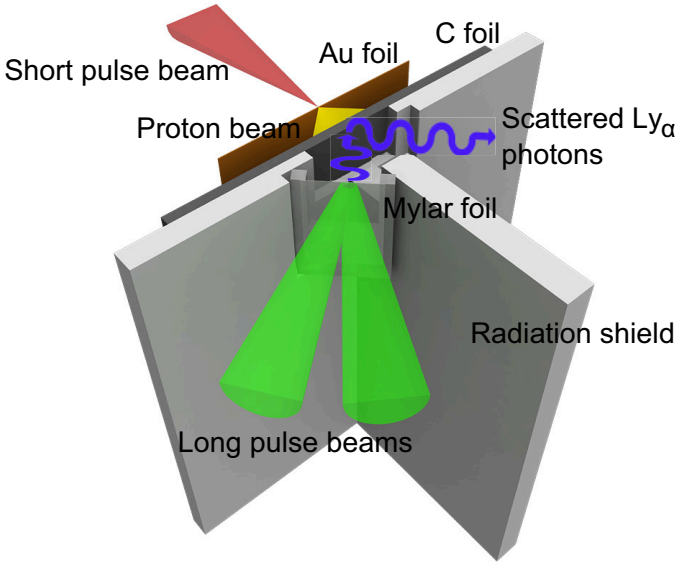

Figure 4.13: Sketch of the target and laser setup. The short pulse laser accelerates protons towards a carbon foil. The heated sample is probed by narrowband Ly$_\alpha$-radiation from chlorine (parylene foil) irradiated by two long pulse beams. The scattered photons are detected by a crystal spectrometer (not shown).

The protons were accelerated by the TRIDENT short pulse laser at a wavelength of 1054 nm focused onto 25 µm thick gold foils. At a laser energy on target of 80 J in a pulse duration of 700 fs, intensities up to 10^{19} W/cm^2 were achieved by focusing onto a 50 µm spot. As shown in figure 4.13, the rear-side emitted protons heated a carbon foil sample placed several 100 µm away from the source. The heated sample was probed by narrowband Ly$_\alpha$-radiation from chlorine (parylene foil) at the backside of the carbon foil under an angle of incidence of 45° to the target normal. The probe radiation is produced by two TRIDENT long pulse beams delivering 400 J of frequency doubled laser light within a pulse duration of 1.2 ns onto a 100 µm spot. The intense burst of Cl-Ly$_\alpha$ photons (2.96 keV) is detected under an scattering angle of 90° with a curved high-reflectivity, highly oriented pyrolytic graphite (HOPG) crystal spectrometer in *von Hamos* geometry coupled to an image plate detector with a beryllium filter that blocks the visible light, see figure 4.14(a). In addition, the X-ray source was directly monitored for each laser shot using a second spectrometer with a flat HOPG crystal.

The sophisticated targets were planned and prepared in collaboration with the detector and target laboratory at the Technische Universität Darmstadt. A sketch is illustrated in figure 4.13 and two images are shown in figure 4.14(b) and 4.14(c). The main component of the target is the 200 µm thick aluminium shielding in T-configuration. It blocks completely the direct view between the curved crystal and the X-ray source. Thus, no source photons are detected on the IP, only scattered ones. The carbon foil is mounted on the front of the construction on a big enough hole to enable the probing from the back side. The parylene foil is mounted on a small frame rotated to an angle of 45° to the target normal of the carbon foil. The correct alignment of the proton source foil to the complex T-target is given by two high-precision moving stages enabling micrometer positioning.

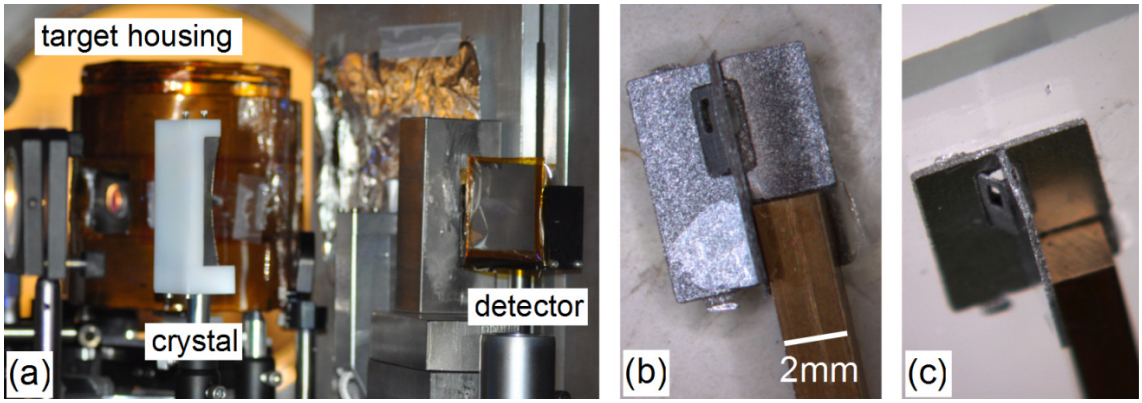

Figure 4.14: (a) Shielding configuration of the IP detector in the target chamber. As shown in the back, the target is housed by a lead construction with drilled laser entrance and diagnostic output holes to minimize the background radiation in the chamber. The IP detector is shielded by surrounding tungsten blocks and a beryllium filter that blocks the visible light. (b,c) Images of the used target configuration. The target in T-shape is mounted on a 2×2 mm rod.

The proton spectrum of TRIDENT was measured in reference shots and calculated by the radiochromic film imaging spectroscopy. This measurement fully determines the heating source. Using the known energy loss for protons in cold carbon, the energy deposition profile inside the target can be calculated with the hydrodynamics solver MULTI2D modified to model the energy deposition by particle beams [196] (see section before). By utilizing tabulated EOS data, the code generates temperature profiles inside the target. Carbon undergoes melting at a temperature of T_m = 0.34 eV. For this experiment, the estimated temperature at the target front side, where the proton beam hits the foil, is ∼10 eV. But the probed volume, where the temperature is almost constant, is arranged in a certain target depth. At a range of 20 µm from the front side (80 µm from the rear side respectively), the carbon was probed at an approximated temperatur of 0.5 eV (∼5530°C).

Both TRIDENT campaigns were conducted to optimize the setup concerning target manufacturing, shielding and signal-to-noise ratio in the detectors compared to an earlier experiment performed at the VULCAN laser [112]. Besides the new target design with the additional shielding of the X-ray probe source, the IP detector has to be shielded as much as possible. Compared to the strong source signal, the scattered light from the target is very weak. Therefore, the IP (covered by a beryllium sheath to block visible light) is surrounded by thick tungsten blocks, so that only the line of sight between sample, crystal and IP is cleared. The target itself is housed by a lead construction with drilled laser entrance and diagnostic output holes. Hence, the background radiation could be decreased close to the target (see figure 4.14(a)). Without such an housing, the plasma radiation and the emitted particles interact with the wall of the target chamber generating secondary radiation, that has direct line of sight onto the IP. Details as well as the results from the TRIDENT experiments are still subject to analysis and will be published soon in the frame of a different dissertation. Nonetheless, the use of laser-accelerated proton beams as a tool for studies of warm dense matter studies could be aproved. Intense proton beams enable the realization of laboratory analogues of extreme extraterrestrial planetary environments, like liquid carbon at high pressures in giant planets (Uranus and Neptune) and white dwarfs.

4.4 Summary

In the frame of this work different experiments were carried out to optimize the proton beam parameters for further applications. About a systematic study on the effects of controlled and characterised pre-plasma conditions at the target front surface on proton acceleration from the rear surface is reported.

An optimum pre-plasma expansion condition can be found for coupling laser energy to protons, via fast electrons. Here, the influence of the laser propagation in the low density large scale length pre-plasma is of crucial importance, because laser self-focusing influences the proton beam maximum energy and conversion efficiency. Notable improvements in the uniformity and circularity of the beam over the full proton energy range are also observed in the spatial intensity profile, for all cases in which a preplasma expansion is produced. The results highlight that properties of the proton beam can be actively manipulated by optical control of the plasma expansion. These techniques could be an important part of the strategy for developing applications which require dynamic control of ion pulses delivered at high repetition rates.

In addition, defocusing of high-intense laser pulses onto the target as a different optical control tool shows significant improvements in proton flux. The experiment demonstrated that laser driven proton beams are suitable for Fast Ignition and heating applications and can be generated more efficiently than previously by driving thinner target foils at a lower intensity over a large area. This has the effect of producing a proton beam with lower maximum energy which can be used to more efficiently couple into secondary targets generating the desired heating effect. Laser to proton beam efficiencies of 7.8% have been achieved with an energy onto target of 220 J, which is one of the highest conversion efficiencies ever achieved for a laser of this size. This technique of defocusing is scalable and should be suitable for future higher energy systems and Fast Ignition investigations.

Finally, experiments on application of laser-accelerated proton beams were performed. It was shown that laser-accelerated proton beams with their high number of particles in a short pulse duration are well-suited for creating isochorically heated matter in extreme conditions. Fundamental questions about target configuration and shielding optimization could be answered.

5 Laser-Accelerated Proton Beams as a New Particle Source

In the last chapter, two different optical technics were presented to optimize the proton beam flux. Thinking about possible applications of laser-accelerated proton beams, the particle number is of course a key parameter. However, the energy spread and the divergence behaviour are at least as important. Advances in ion beam tailoring have been achieved so far mainly by employing target engineering techniques, but they rely on relatively complex target fabrication or preparation procedures, e.g. high quality sub-mm hemispherical targets [28, 200]. But the collimating and focusing effect of these targets is not yet fully understood.

A different approach was done by Toncian *et al.* [45]. They developed a method to simultaneously focus and select a favored energy interval of laser-accelerated protons. The experimental setup consists of the standard short pulse laser, generating a proton beam, which pass a hollow micro-cylinder (3 µm length and 700 µm in diameter). A second short pulse laser initiate a hot plasma expansion inside the cylinder. The transient electric fields (10^7-10^{10} V/m) associated with the expansion effect, in a radial geometry, lead to focusing of the passing protons. The distance of 4 mm between the proton source and the focusing lense limited the fraction of the diverging beam entering the cylinder. Under the current experimental conditions, 7.5 MeV protons were focused into a spot of 600 µm in diameter (FWHM) leading to a proton flux increase by a factor of 12 compared to a reference shot without using the micro-lense. At the end of a 70 cm transport distance, the beam diameter can be measured to 8 mm. The disadvantage of this arrangement is the loss of the focusing cylinder after each shot and thus the necessary replacement. It is almost impossible to ensure the same experimental conditions after realignment. With respect to the upcoming high-energy, high-repetition rate laser systems, a collimation and focusing device with reproducible and stable properties is desirable.

The next step in developing a laser-driven proton source is the use of well known beam steering technics, which are applied in conventional accelerators to manipulate or transport the beam. Ter-Avetisyan *et al.* [47] implemented a conventional quadrupole-magnet lense system. The aperture of both quadrupoles is 40 mm and their length 50 mm. A collimation of the proton beam can be achieved with help of two successively placed identical quadrupoles with reversed pole geometry, because the characteristic of a single quadrupole is focusing in only one plane. For the given configuration, protons with a full emission angle of 20° have been collected. With a maximum field strength of 1.3 T, the quadrupole doublet was capable of collimating 10^8 protons with an energy of (3.7±0.3) MeV up to a distance of 75.5 cm behind the source. The density of the protons compared to the case without magnets is increased up to a factor of 30. However, the transmission and the selected energy is by far to small to compete with conventional sources. The minimum injection energy for the synchrotron at the Heidelberg Ion-Beam Therapy Center, Germany, is 7 MeV/u [162], and for the Heavy Ion Synchrotron 18 at the GSI Helmholtzzentrum für Schwerionenforschung 11.4 MeV/u [201].

A group around Schollmeier [46] presented transport and focusing of laser-accelerated (14±1) MeV protons by permanent magnet miniature quadrupole (PMQ) lenses providing field gradients of up to 500 T/m. In a focal spot of 286×174 µm^2 FWHM 50 cm behind the source, 8.4×10^5 protons were detected and the flux could be increased by a factor of 75 compared to the case without the lenses. Due to the full emission angle of 40°, the distance source to lense entrance of 17 cm and the inner quadrupole diameter of 5 mm, only 7.5% of the protons at an energy of (14±1) MeV enters the PMQs. The transmission through the magnets is only 0.1%. This low value was expexted, since the first PMQ focused the beam in one plane and defocused the protons in the perpendicular one. The following PMQ aperture then cut most of the beam.

The approach of our group was to switch to a different ion optic, that can provide a higher transmission. The choice fell on a solenoidal magnetic lense. A prototype was tested during a PHELIX campaign and the results were published in reference [48]. The solenoid consists of a brass helix originally designed as a Faraday rotator capable of a magnetic field strength of 8.6 T. At a distance of 17 mm to the target and an aperture of 44 mm in diameter, it was possible to catch almost all protons at a proton energy of 2.5 MeV. At a detector distance of 241 mm, a collimated (2.5±0.3) MeV proton beam could be measured. As already mentioned, this was a prototype test to study the application of a pulsed coil and its interaction with the proton beam. The distance between target and solenoid was chosen too small, because the fringe fields could interact with the source foil. Strong eddy currents were induced in the foil by the solenoid field of 950 mT at the target position, which led to a bending of the target and a change in the propagation behaviour of the protons. The RCF stack shows a highly filamented proton beam. For a better beam quality, a new solenoid was planned and tested at the PHELIX laser system in collaboration with the Forschungszentrum Dresden-Rossendorf, see next section.

Beside the first ion optical device to catch and control laser-accelerated proton beams, studies on possible phase rotation of the beam to generate a peaked spectrum with much higher particle numbers in a certain energy interval were carried out. Current results are summarized and published in references [49, 131, 202]. In summary, a laser-driven repetition-rated 1.9 MeV proton beam line (length 4 m) composed of permanent quadrupole magnets, a radio frequency phase rotation cavity, and a tunable monochromator was developed to evaluate and test laser-accelerated proton beam transport. At a distance of 8 cm behind the target, the first quadrupole had an acceptance half angle of 7°. The quadrupole triplett with different lengths and field strengths was positioned over a length of 33.7 cm. The downstream radio frequency cavity is a quarter-wavelength resonator with two gaps. The gap size is 2 cm with an applied voltage of 115 kV. The final proton monochromator which consists of an entrance collimator, a bending magnet, and an exit slit to filter the particular energy interval of (1.9±0.05) MeV. Performed PARMELA simulations estimate the transmission of protons in this energy interval to 10% ($\sim 5 \times 10^7$ protons). This system operates at a charge density and a low peak current region for which space charge effects are insignificant. Compared to previous results [202], the transmitted proton number could be increased by three orders of magnitude. However, compared to the injector linac (into the existing SIS18 synchrotron) planned for the FAIR antiproton facility at GSI [203], the particle number is still two orders of magnitude too low and the injection energy of 70 MeV is by far not reached. The advantage of a high repetition rate laser like the J-KAREN Ti:sapphire laser system at the Kansai Photon Science Institute of the Japan Atomic Energy Agency [204] is the reproducible generation of proton beams with almost the same parameters. But due to the available laser energy of ∼630 mJ, the high-energy cutoff of the proton spectrum decreases to 2.5 MeV and the total flux drops orders of magnitude [49].

If laser-accelerated proton beams as a new generation of proton source should be competitive to conventional sources, more particles at higher energies have to be supplied.

5.1 Motivation and Challenges

The project of the laser and plasma physics group of the Technische Universität Darmstadt is to develop a concept to provide laser-accelerated proton beams of suitable particle numbers with a narrow-band energy distribution for further applications. In particular, this new generation proton source should be compatible or even better than current conventional sources. According to this, beam parameters such as envelope divergence and exponential energy distribution have to be adapted to suitable values. During building the first prototype of an ion optic, various pros and cons have to be weighed to assure high-quality beams but a realistic device concerning costs, size and operation. The following list will point out the main challenges, that have emerged from past experiments [45–49]:

- High repetition rate *versus* high energy laser systems
- Size of the prototype *versus* flexible operation in a small target chamber
- Distance to source and aperture size *versus* influence of external fields onto the acceleration mechanism
- Distance to source and aperture size *versus* possible field strengths with pulsed or permanet devices
- Focusing strength *versus* particle losses
- Field design *versus* worsening of the beam quality

By comparing the slope of the proton spectra coming out of for example the J-KAREN and the PHELIX system, one clearly can see that the difference in laser output energy (0.6 J to 90 J) has a significant impact on the proton number (factor of $\sim$100) and the maximum proton energy (factor of $\sim$10). To be compatible to existing proton sources, the area of operations should be around the proton energy of 10 MeV with 10^8 protons. Therefore, a high-energy laser system like PHELIX with a repetition rate of one shot per hour is prefered to a low-energy 1 Hz system like J-KAREN. However, the ongoing laser development promisses 10 Hz systems with pulse energies around 200 J, like for example the diode pumped ELBE DP-Petawatt laser system [205]. Up to this point, the proof of principle experiment will be performed in the single shot mode at PHELIX. The prototype of the ion optic to catch laser-accelerated proton beams should be of a handy size, because the device will be used in a vaccum chamber. An experimental setup in a vacuum chamber is very extensive and due to the nature of the expanding proton beams, the device has to be close to the initial source and may block other line of sights. In addition, a compact design would enable easy transport and operation in different vacuum chambers.

The position of the ion optic in relation to the origin of the protons has to be find in agreement with different requirements. If the device is too close to the source, the generated fields have an influence on the acceleration mechanism at the rear side of the target foil. In addition, bending of the target as a result of strong eddy-currents was already observed [48]. By increasing the distance to the target to minimize the field strength, the aperture of the ion optic has to be increased, because laser-accelerated proton beams have a full envelope divergence of up to 60°. To provide a sufficiently high field strength over this aperture to catch for example 10 MeV protons, pulsed devices have to be introduced. Strong fields over long distances can be provided by electric devices. But here, one has to pay attention to the heating characteristics of strong currents. This effect can be overcome by using a pulsed device. Particle losses are definied by the distance, the aperture and the field strength of the ion optic. The dimensions fix how many particles of the divergent beam are captured, and the field strength defines how much particles can be transported through the device. In addition, the field strength is responsible for focusing and collimation of particular energy intervals. If the fields are not strong enough, particles are not collimated and are absorbed at the inner wall of the device.

5.2 Capture and Transport of Laser-Accelerated Proton Beams

The most benefits are combined in a solenoidal field, that was chosen to capture laser-accelerated proton beams. The pulsed coil was developed in collaboration with the high field laboratory of the Forschungszentrum Dresden-Rossendorf and used during an experimental campaign carried out at the PHELIX system. The coil consists of four layers of copper wiring each with 27 turns and has a total length of 150 mm with a full aperture of 48 mm in diameter. The inductance of the coil was measured to $\sim$250 µH. The mechanical stability is achieved by massive G-10 flanges. G-10 is a thermosetting industrial laminate consisting of a continuous filament glass cloth material with an epoxy resin binder.

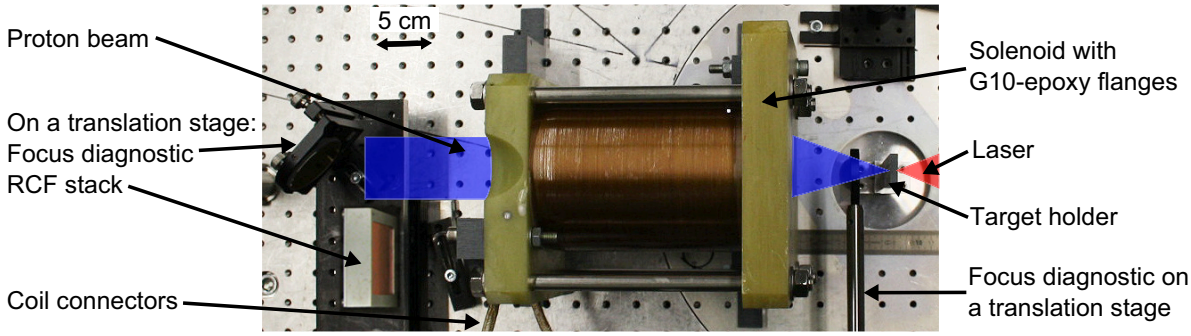

Figure 5.1: Experimental setup of the solenoid inside the target chamber at PHELIX. The laser irradiates the target from the right side. After 95 mm in the fringe fields, the protons enter the solenoid and exit after 150 mm. Before the proton beam is detected by a RCF stack, it has to propagate over a distance of 162 mm in the fringe fields behind the solenoid. In the current setup, the focus diagnostic is positioned in the beam and the TCF stack is backed out.

It has characteristics of high strength, excellent electrical properties (insulator) and chemical resistance. In addition, the inside of the coil is protected by a three-millimeter thick tube of the same material to protect the coil against the impact of the accelerated particles and prevent arcing within the coil. The required electrical power was provided by a discharge of a part of the capacitor bank of PHELIX. A total of 30 capacitors were used, each of them has a capacity of 52 nF. Overall, this represents a capacity of 1.56 mF. By calculating the field map with COMSOL Multiphysics [206], an electric power of 12 kV$\times$9.32 kA resulted in a maximum magnetic field strength of 7.5 T.

Figure 5.1 shows the experimental setup, where the laser irradiates the target from the right side. The exact dimensions can be found in figure 6.4. The beam propagates 95 mm before entering the coil. The distance between the coil exit and the RCF stack detector is 162 mm, resulting in a total propagation length from source to detector of 407 mm. During this campaign, the PHELIX system delivered 72 J in a pulse duration of 500 fs onto 25 µm thick Au foil targets. The full-width-half-maximum (FWHM) dimensions of the focal spot are in vertical direction 8.5 µm and in horizontal direction 17 µm containing 22% of the full laser energy leading to an intensity of 3×10^{19} W/cm^2.

Due to arcing inside the chamber and the consequent contamination of the coil, only four analyzable shots were carried out. However, the results were exactly reproduced. Further studies on magnetic field and distance dependencies will be performed with a new version of the solenoid including additional shielding against arcing.

5.2.1 Effects on the Proton Beam

Figure 5.2 shows radiochromic films of the reference proton beam without using the solenoidal magnetic field. The detector was placed at the same distance to the source of 407 mm. In all films, an homogeneous beam with sharp edges was detected. The diameter of the signal compared to the aperture of 48 mm is larger due to the rest divergence of 5°. For higher proton energies than 8.7 MeV, the number of particles is too low to detect a signal in the film. Assuming a half envelope-divergence of 23° (from figure 3.7) and a homogeneous transverse proton distribution, only 4.2% of the entire proton beam can pass the solenoid. With a solenoidal magnetic field of 7.5 T, the proton distribution significantly changes. The proton signals of the radiochromic film stack placed at a distance of 407 mm are shown in figure 5.3. The imprint in the films reflect the expected results. At a proton energy of 3.7 MeV, the beam is divergent again, because it is over-focused. The second layer is quite close to the focal position of 6.6 MeV protons at an distance of 16.2 cm behind the solenoid exit (focal diameter: 2-3 mm).

The protons with an energy of 8.7 MeV describe a converging beam, that has its focus at a plane behind the position of the film stack (>407 mm). A collimated or parallelized beam will have a diameter that is almost identical to the diameter of the aperture of the solenoid of 48 mm. This is almost the case in the fourth film (11.7 MeV). The diameter of the full proton spot is around ∼50 mm. For increasing proton energy, the field was not strong enough to compensate the intitial divergence and the beam still expands with an reduced divergence. This is confirmed by the increasing diameter for the following layers. In addition, the proton signal could only be resolved up to an energy of 16.5 MeV. Due to the nature of the exponential spectrum, the available number of protons at a distance of 407 mm is below the detection theshold of the radiochromic films.

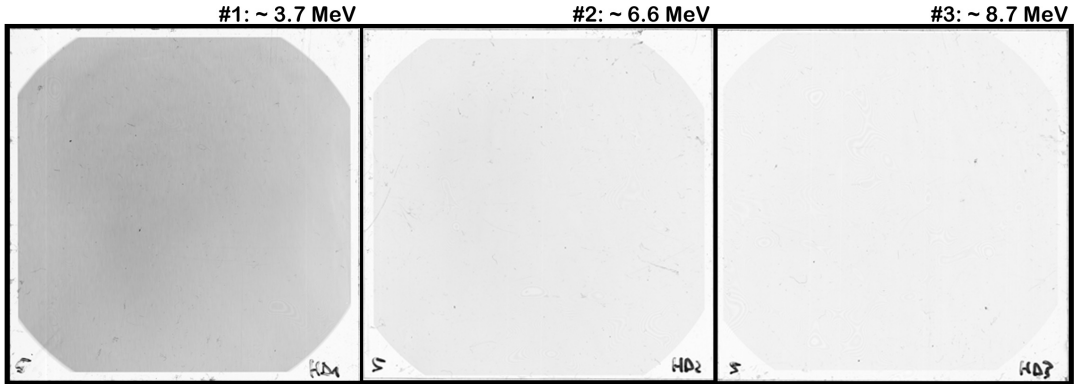

Figure 5.2: Radiochromic films of the reference proton beam without using the solenoidal magnetic field. The detector was placed at the same distance to the source of 407 mm. In all films, an homogeneous beam with sharp edges was detected. The diameter of the signal compared to the aperture of 48 mm is larger due to the divergence of the beam. For higher proton energies than 8.7 MeV, the number of particles is too low to detect a signal in the film. The film dimension are 63.5×63.5 mm^2.

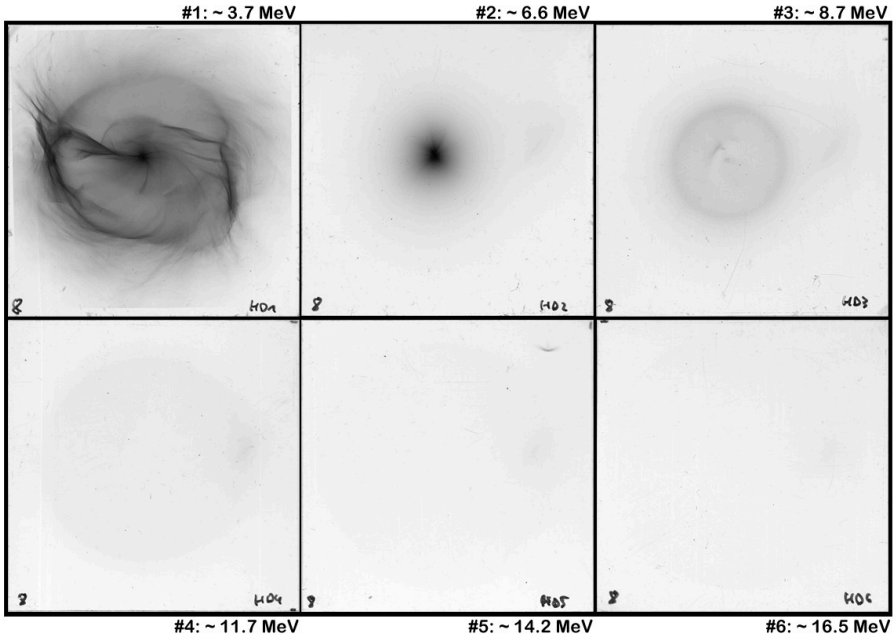

Figure 5.3: Radiochromic film stack of a proton beam accelerated by the PHELIX system. The catching solenoidal magnetic field had a strength of 7.5 T. The single layers clearly show the over-focused (#1), the focused (#2), the collimated (#4) and the still divergent (#5) cases. The film dimension are 63.5×63.5 mm^2.

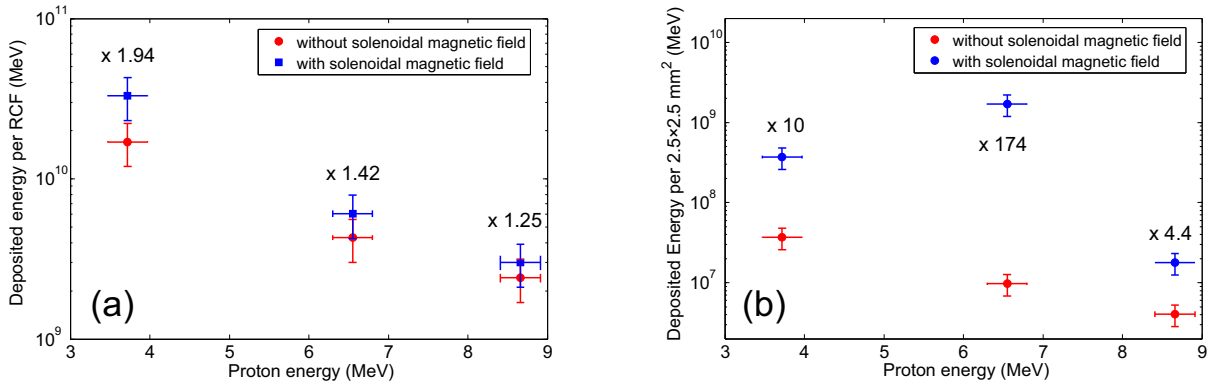

Figure 5.4: (a) Comparison of total deposited proton energies in the first three layers of the RCF stack for a reference beam and a proton beam influenced by the solenoidal magnetic field. The magnetic field guidance enables a higher transmission through the solenoid. (b) Illustration of the proton areal density for both beams. The flux through an area of 2.5×2.5 mm^2 for 6.6 MeV could be increased by a factor of 174.

More details on the data analysis can be found in section 6.5, where the experimental results are compared to the findings of particle-in-cell simulations. The explanation of the ring formation in layer 1 and 3 can also be found there.

By comparing the total energy deposition for the reference case with the shot including the magnetic field, an enhancement for each of the first three layers is observed, see figure 5.4(a). The magnetic field enables a higher transmission through the device – less particles are absorbed from the solenoid housing. For the lowest energies, the effect on the particle trajectories is stronger. Hence, the enhancement is about a factor of two. The increase for proton energies of 8.7 MeV is only about 25%. For several applications, the proton areal density is an interesting parameter. In figure 5.4(b), the flux through an area of 2.5×2.5 mm^2 containing the focal spot is analysed. A flux increase of a factor of 174 for protons with an energy of 6.6 MeV is observed. Compared to the data of Schollmeier *et al.* [46], where the flux density of 14 MeV protons could be increased up to a factor of 75, the chosen ion optic, the field strength and the dimensions led to a much better enhancement. A proton number estimation for the focal spot is done in section 6.5.

5.2.2 Electron Propagation

In various laser experiments electron beams expanding of the target rear side were measured with magnet spectrometers [9, 167–169]. Even in radiochromatic films their existence can be verified. But due to their weak energy deposition in RCFs and the stack distance to the source of several centimeters, it is hard to separate the signal from the underground. However, a very dominant electron signal could be detected in an earlier campaign at the PHELIX laser system in 2008 [48]. Here, a first test version of a smaller solenoid was used. Figure 5.5 shows parts of the RCF detector stack. It was placed as close to the solenoid exit as possible. Besides the well-known proton signal in the first layer, in figure 5.5 left, a second beam was measured throughout the whole RCF stack (25 films) up to the last layer. The signal stays constant in intensity, therefore it was not generated by laser-accelerated protons, because of their high stopping power and their spectrum cut-off for high particle energies. Instead, an electron beam with a particle energy of only 2 MeV, can easily penetrate through an RCF stack consisting of 25 layers (*Casino* [207] calculation in [48]). The electron beam could not be observed in shots where the RCF stack was placed further away from the solenoid, since the electron beam breaks up behind the solenoid due to the dispersion of the magnetic field lines. Exactly this behaviour can be seen in the simulation shown in the next chapter (figure 6.11(a)).

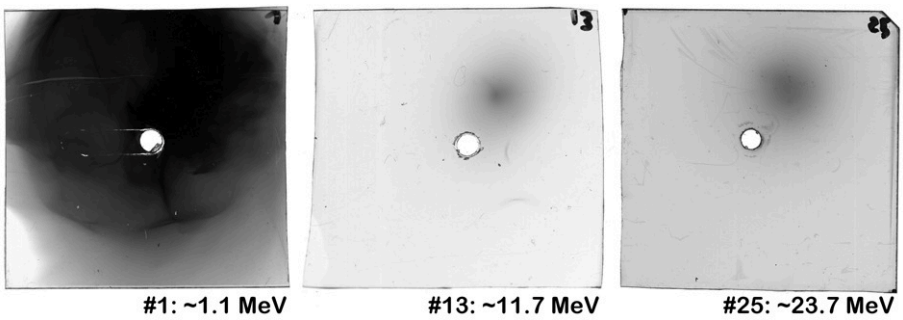

Figure 5.5: Radiochromic film stack of a shot during the Phelix campaign 2008 to test a solenoid field on the propagation of laser-accelerated proton beams. Only three stack layers (of 25) are shown: the first, the middle and the last. While the proton signal is only visible in the first layer, an electron spot of constant size could be observed up to the last layer of the stack. Layer 13 and 25 are different sensitive films, however the intensity of the spot is the same.

In the recent experiment (figure 5.3), the early observation could be verified even if the stack was not positioned directly behind the solenoid but 16.2 cm away. With a better contrast as shown in figure 6.6, the weak electron signal can be seen in all layers a little bit shifted to the right. One would expect, that the proton and the electron signal would be superposed, because the whole expansion is symmetrically. The right shift in this case can be happened due to an additional field, e.g. a current induced field around the power supply line, that was strong enough to deflect the electrons behind the solenoid but too weak to affect the protons. The motion of the electrons in a solenoidal magnetic field will be described by simulations shown in section 6.6.

5.3 Summary and Outlook

In conclusion, a solenoidal magnetic lense was developed and successfully tested at the PHELIX system to catch and transport laser-accelerated proton beams. Compared to previous experiments [45–48], protons with energies close to 10 MeV could be focused and collimated over a distance of 40.7 cm without losing their symmetry. Due to material impurities triggered by arcing during the shots, a precise operation could not be guaranteed after four successful and reproducible shots. Further studies on focused and collimated beam parameters, such as transmitted spectrum, emittance conservation and transport capability will be carried out with a new, modified solenoid already in development at the High Field Lab, Forschungszentrum Dresden-Rossendorf. This coil is in a seperate housing to enable operation in air to overcome arcing. In addition, a metal pinhole plate (eddy current shielding) will be mounted between the source and the solenoid entrance to guide the field lines and minimize the magnetic field at the source.

Almost all theoretical support up to now is limited to tracking or envelope codes [48, 130, 208]. For beams of such a high particle number, and electron and proton densities respectively, space charge effects can influence the beam propagation. In the frame of this thesis, the Warp particle-in-cell code [209] was used to explain the observed physics and to optimize the setup for future experiments.

6 Warp RZ-Simulations of Laser-Accelerated Proton Beams

Creating fusion in the laboratory and its application as a new generation power plant has long been a goal of scientists worldwide. Energy production by Inertial Confinement Fusion (ICF), see for example the current studies at the US National Ignition Facility (NIF) [187], is a major field of thermonuclear research and the major alternative to magnetic confined fusion represented by the Tokamak Experimental Reactor (ITER) [210]. In the ICF approach, the fusion pellet is compressed to a high density and temperature until the fuel will begin to fuse and release energy. The compression can be done in different ways. In the direct-drive scheme impinging laser beams ablate the pellet resulting in target compression. To overcome the symmetry requirements X-ray heating is introduced in the indirect drive concept. Here, a Hohlraum target is used as laser light to X-ray converter. Hence, a more homogenous compression is possible. In ICF research, Fast Ignition (FI) [188] was proposed as a means to increase the gain, reduce the driver energy, and relax the symmetry requirements for compression of the fuel-containing pellet, primarily in direct-drive ICF. The concept is to precompress the cold fuel and subsequently to ignite it with a seperate short-pulse high-intensity laser, because up to now it has been impossible to obtain simultaneously the compression and the heating of a fusion target.

In 1974, Maschke [211] proposed ion beams, especially high energy heavy ions, as an alternative driver for ICF and initiated the heavy ion fusion (HIF) program. Compared to laser-based ICF, direct ion beam compression of the fusion pellets offers several advantages. Due to the extensive development of accelerator technology in the past 50 years, scientists have gained much experience building and optimizing particle accelerators. A driver must also have an adequate repetition rate and be efficient and reliable. These requirements are best satisfied by ion accelerators. But to produce the required power density, the ion beam has to be compressed and focused down onto the target. Therefore, a low transverse beam temperature or emittance is crucial. But due to ion optical elements in the beam path, detailed design analysis is necessary in order to minimize the attempt of increasing transverse temperature.

For this purpose, the Warp suite of simulation codes was developed to study high current ion beams. The understanding of the dynamics of intense ion beams is crucial for the success of the HIF program. The intense beams behave as non-neutral plasmas: a collection of ions. In the high current beams necessary for a driver, the space-charge forces of the beam dominate over the thermal forces. Therefore, any analysis of beam dynamics needs to include the electrostatic self-fields of the beam. Such an analysis is an ideal application for the particle-in-cell (PIC) simulation technique which has been heavily used for neutral plasma simulations.

6.1 Description of the Simulation Code

Warp is a multi-dimensional, intense beam simulation program being developed and used at the Heavy Ion Fusion Virtual National Laboratory [212], which currently includes Lawrence Berkeley National Laboratory, Lawrence Livermore National Laboratory and Princeton Plasma Physics Laboratory. It allows flexible and detailed multi-dimensional modeling of high current beams in a wide range of systems, including bent beam lines using a *warped* coordinate system - from which the code derives its name.

The Warp code combines the electrostatic PIC technique [213] with a description of the accelerator *lattice* of elements. The lattice consists of a fully general set of finite-length accelerator elements, including

quadrupole focusing, dipole bending, accelerator sections, and more general elements. With the PIC model, the beam is made up of a small number of macro-particles which interact via their space-charge. Macro-particles or simulation-particles represent many real particles. The effects of the space-charge is included by a global solution of Poisson's equation. Therefore, the electrostatic self-field is calculated self-consistently on a three dimensional mesh that holds a discrete representation of the charge density and the electrostatic potential. The charge density is calculated from the particles via interpolation onto the mesh. Using a successive overrelaxation (SOR) iterative *Poisson* solver, the electrostatic potential can be solved from the charge density. The simulation particles are advanced in time by solving the equation of motion using a combination of the *leap frog* and *isochronous leap frog* methods [214].

Before details about the function of the code are given, some conventions have to be pointed out. The simulation box is described by a right handed Cartesian coordinate system with x on the horizontal, y on the vertical, and z along the centerline of the beam. The beam always moves in the positive z direction.
In the following the term *particle* should be interpreted to mean macro or simulation-particle unless explicity stated otherwise.
At present Warp incorporates a 3-D description, an axisymmetric (r,z) description, a transverse slice (x,y) description, a simple envelope model used primarily to obtain a well-matched initial state, and envelope/fluid models used for scoping and design. In the scope of axissymmetric, laser-accelerated proton beams and straight beam propagation the Warp-RZ description is used. Thus, it is possible to optimize and reduce the computing time.

6.1.1 The Computational Cycle

The difference between laboratory plasmas and simulated plasmas is the discretization in time. The simulation proceeds step by step. This temporal grid has to provide sufficient accuracy and stability to make the simulation useful. It has to be fine grained to follow the plasma. The use of a spatial grid on which the fields will be calculated is the second difference. The change from calculating *Coulomb* forces of each particle directly to a charge density on a spatial grid is certainly of benefit. Not only the number of numerical operations goes down, also the singularities in *Coulomb*'s law ($r \to 0$ for $1/r^2$) vanish. As long as the grid is fine enough to resolve a characteristic length (called the *Debye* length, see section 6.3), this simplification does not change the actual physics. Non-physical effects can occur depending on the choice of the simulation parameters. But in general, these effects can be avoided. Inaccuracies will always be with us and simply must be made small.

At each step in time, the PIC code solves the fields for the particles and then moves the particles as shown in figure 6.1. The cycle starts at $t = 0$ with some initial conditions for the particle positions and velocities. The particles are processed through the boxes and their name is given by index i. The field quantities will be known only at discrete points in space given by a spatial grid and are labeled with index j,k. First, the charge density ρ has to be calculated on the grid. Therefore, the initial, continuous particle positions are assigned to the discrete grid points. These calculations are called *weighting*, which implies some form of interpolation among the grid points nearest the particle. Trilinear weighting (linear in all three dimensions) is implemented in Warp. However, one effect has to be pointed out. The grid provides a smoothing effect by not resolving spatial fluctuations on a scale smaller than the grid size.

Starting from the assigned charge densitiy ρ, the electric fields are obtained by solving the *Maxwell* equations. The used self-field solver is an electrostatic *Poisson* solver. This approximation neglects the self-magnetic fields, which are much lower for the expanded beam than the external field strength of the

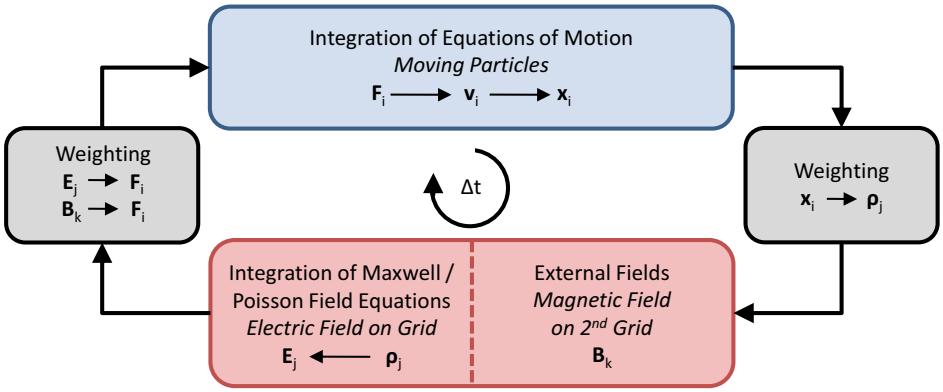

Figure 6.1: A typical time step in PIC simulations with the particle numbers *i* and the grid indices *j,k*. Particles are processed through the boxes starting at the initial values of positions and velocities. The charge density on the grid is calculated by particle weighting. Finally, the grid values of the fields are interpolated for each particle to get the correct force for the next iteration.

solenoid used in the experiment. For the electrostatic problem, the following *Maxwell-Faraday* equation is valid.

$$\nabla \times \mathbf{E} = -\frac{\partial \mathbf{B}}{\partial t} \approx 0 \quad \text{so that} \quad \mathbf{E} = -\nabla\Phi(\mathbf{x}) \tag{6.1}$$

Combined with *Gauss*'s law

$$\nabla \cdot \mathbf{E} = \frac{\rho(\mathbf{x})}{\epsilon_0} \tag{6.2}$$

Poisson's equation is obtained

$$\nabla^2\Phi(\mathbf{x}) = -\frac{\rho(\mathbf{x})}{\epsilon_0} \tag{6.3}$$

One approach is to solve the finite-difference form of equation (6.3). Afterwards, the solution of the potential Φ has to be applied to the finite-difference form of the simplified *Maxwell-Faraday* equation (6.1) to obtain the electric field E. A very powerful approach to solve this problem is the iterative successive overrelaxation (SOR) method [215], where equation (6.3) goes over in

$$\frac{\phi_{i+1} - 2\phi_i + \phi_{i-1}}{\Delta^2} = -\frac{\rho}{\epsilon_0}. \tag{6.4}$$

By solving equation (6.4) for ϕ_i the solution is plugged in the finite-difference form of equation (6.1)

$$E_i = -\frac{\phi_{i+1} - \phi_{i-1}}{2\Delta}. \tag{6.5}$$

to obtained the electric field. The index i corresponds to the grid cell number and Δ is the grid cell size. Besides the self-fields, Warp provides the possibility of including external fields, like focusing, bending and acceleration elements, on additional, customized grids (in figure 6.1 the magnetic field B indexed by k).

In order to calculate the Force F

$$\begin{aligned} \mathbf{F} &= \mathbf{F}_{\text{electric}} + \mathbf{F}_{\text{magnetic}} \\ &= q\,\mathbf{E} + q\,(\mathbf{v} \times \mathbf{B}) \end{aligned} \tag{6.6}$$

the fields have to be applied back on the particle positions. Therefore, the same weighting as two steps back in the computational cycle is required to assure momentum conservation. Otherwise it would be possible, that a particle accelerates itself.

The final operation in the time step is the integration of the equations of motion. The method of integration has to fullfill special criteria, such as fast and not storage intense, but still retain acceptable accuracy. One commonly used integration is the *leap frog* method. The two first-order differential equations to be integrated seperately for each particle are

$$m\frac{d\,\mathbf{v}}{dt} = \mathbf{F} \tag{6.7}$$

$$\frac{d\,\mathbf{x}}{dt} = \mathbf{v} \tag{6.8}$$

where $\mathbf{F}$ is the force on the particles (equation (6.6)). These equations are replaced by the finite-difference equations

$$m\frac{\mathbf{v}_{\text{new}} - \mathbf{v}_{\text{old}}}{\Delta t} = \mathbf{F}_{\text{old}} \tag{6.9}$$

$$\frac{\mathbf{x}_{\text{new}} - \mathbf{x}_{\text{old}}}{\Delta t} = \mathbf{v}_{\text{new}} \tag{6.10}$$

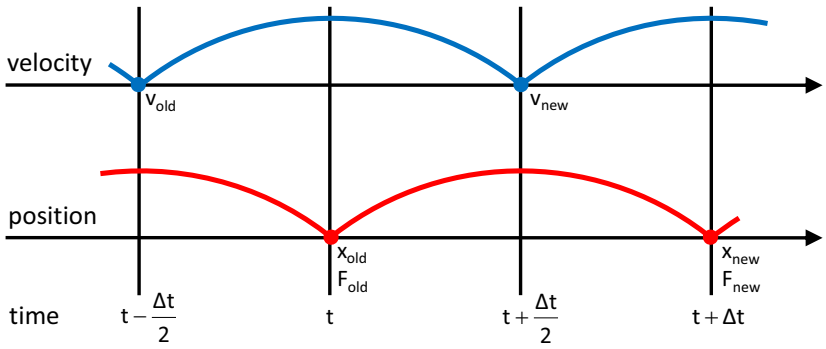

Figure 6.2: Sketch of time-centered, *leap frog* integration. The algorithm will advance $\mathbf{v}$ and $\mathbf{x}$ even through they are not known at the same time.

The name *leap frog* comes from one of the ways to write this algorithm, where positions and velocities *leap over* each other. Positions $\mathbf{x}_{\text{old}}$ and $\mathbf{x}_{\text{new}}$ are defined at times t and $t + \Delta t$, spaced at constant time step intervals Δt, while the velocities $\mathbf{v}_{\text{old}}$ and $\mathbf{v}_{\text{new}}$ are defined halfway in between, indicated by $t - \Delta t/2$ and $t + \Delta t/2$, as shown in figure 6.2. Hence, the *leap frog* integration scheme will advance $\mathbf{v}$ and $\mathbf{x}$ even through they are not known at the same time.

The time discretization can lead to errors in at least two cases. First, initial conditions for particle velocities given at $t = 0$ must be changed. Therefore, $\mathbf{v}(0)$ is pushed back to $\mathbf{v}(-\Delta t/2)$ using the force $\mathbf{F}$ calculated at $t = 0$. Diagnostics or backups are typically made every n time steps. At this points, the velocity advance has to be split into two steps and an *isochronous* advance is used. The first half step synchonizes (in time) the velocity with the position. Now, all diagnostics and backups can be done. Finally, the second half step of the velocity advance is done.

6.1.2 Computational Implementation and Software Installation

Since two years, the plasma physics group at GSI has access to an own computing cluster capable for massively parallel running computations. Three servers are installed as a cluster and administered via remote access by the plasma physics group. Each maschine is equipped with four dual-core AMD Opteron CPUs with 2 GHz clock rate and 32 GB RAM, resulting in 4 GB per CPU. The hard disk storage capacity for each cluster node is 1.5 TB leading to a total of 4.5 TB in a RAID-5 network. The data transfer in the RAID-5 array is very time consuming. Therefore, all three servers are connected via 10 Gigabit Infiniband network. The cluster is capable of running parallel computations. In the time frame of this work, the switch from one CPU to multi-CPU Warp calculations was not possible, but will be done in the near future.

Warp is written primarily in standard Fortran90 (`http://www.fortran.com/`). It is steered through a flexible and powerful user interface that uses the scripting language Python (`http://www.python.org`). The input script contains the information needed to initialize and carry out the simulation. The interface between the Fortran code of Warp and Python is generated using the Forthon package (`http://hifweb.lbl.gov/Forthon`). Forthon generates links between Fortran and Python. Python is a high level, object oriented, scripting language that allows a flexible and versatile interface to computational tools. The Forthon package generates the necessary wrapping code which allows access to the Fortran database, subroutines and functions. This provides a development package where the computationally intensive parts of a code can be written in efficient Fortran, and the high level controlling code can be written in the much more versatile Python language.

For simplification of the data analysis and to provide flexible data plotting, a computer routine with graphical user interface (GUI) has been written in MATLAB (`http://www.mathworks.com`) to visualize the simulation results. Every pre-defined time step, the simulation data for each particle species (positions, velocities, particle flag) are written to a ASCII data file. Besides the particle parameters, also the potential, the charge distribution, a simulated RCF detector and other, one dimensional beam parameters are saved to files. With the help of the developed MATLAB routine, it is possible to analyse all parameters online, select energy intervals of interest and define plot options to generate movies of the PIC simulation.

6.2 Initial Particle Conditions, Geometric Boundaries, External Fields and Detectors

Warp was initally built to simulate particle bunches in accelerator structures. These bunches are *Gaussian* or cigar-like distributed beams in time or in space, mostly with a discrete particle energy or only an energy broadening of a few percent. In the case of laser-accelerated proton beams, the beam parameters are totally different. Hence, a customize particle loader was developed within the scope of this research. The capability of Warp to include the proton and electron energy distribution, source size, opening angle and transverse emittance energy resolved was fully utilized. All beam parameters are given by the PHELIX proton beam analysed with the RCF imaging spectroscopy (see section 3.3.1). Laser and target parameters of this shot are similar to the shots with the solenoid during the same campaign (see section 5.2). Warp is also capable of including multiple particle species. After the break down of the accelerating field, the beam flow is described by the model of a quasi-neutral expansion into vacuum [90]. So, the second species included in the simulation are the co-moving electrons assuring the neutrality of the

expansion. The description "co-moving" denote movement with the same velocity like the protons. The relativistic energy-velocity correlation

$$E_{kin} + E_0 = \frac{m \cdot c^2}{\sqrt{1 - \frac{v^2}{c^2}}} \tag{6.11}$$

with the kinetic and rest energy E_{kin} and E_0, the particle velocity v, the speed of light c and the particle mass m yields to the proton-electron energy correlation:

$$E_{e,kin} + E_{e,0} = \frac{m_e}{m_p} \cdot \left(E_{p,kin} + E_{p,0}\right) \tag{6.12}$$

Electrons with higher energies than the co-moving electrons (up to GeV energies) are also generated during the laser-plasma interaction [9], but will be neglected in the simulations. These particles are much faster than the proton beam and therefore have no significant influence on the beam expansion.

Warp loads particles by their position $\vec{x}$ = (x,y,z) and velocity $\vec{v}$ = (v_x,v_y,v_z). Hence, the energy distribution and all energy dependent beam parameters are included by modifying these coordinates.

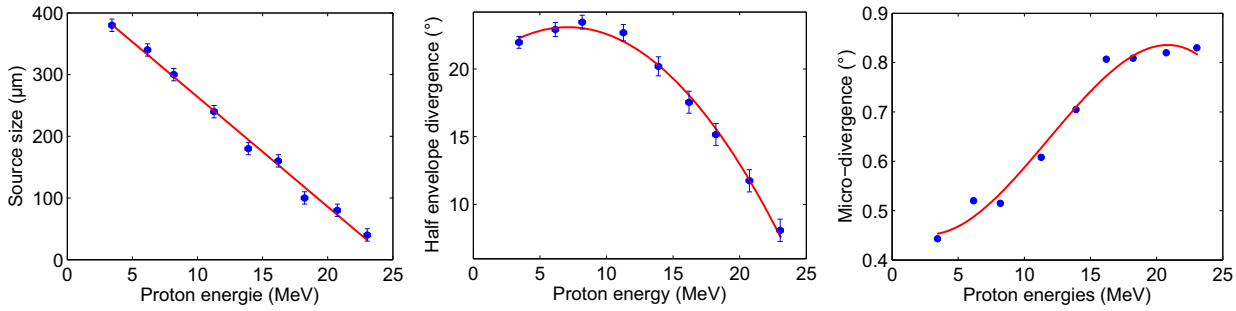

(a) (b) (c)

Figure 6.3: Proton beam parameters of the Phelix proton beam for the Warp particle loader: experimental data (•) and polynomial fits (—) of the source size (a), the envelope divergence (b) and the angle error for the transverse beam emittance (c). For convenient implementation in Warp, a non-physical polynomial fit was chosen to represent the measurements.

Proton energy distribution: The initial, absolute value of the velocity is defined by the particle energy. The energies for all particles are generated based on random numbers. In this case, the *inverse transform sampling* [216] is the used method for generating sample numbers at random from the energy distribution. With the given distribution $N(E)$ in the intervall [E_{min},E_{max}] the particle energies can be calculated as follows:

$$\int_0^x g(x)\mathrm{d}x = \frac{\int_{E_{min}}^{E} N(E)\mathrm{d}E}{\int_{E_{min}}^{E_{max}} N(E)\mathrm{d}E} \tag{6.13}$$

The right hand side of equation (6.13) is the integral over the energy distribution divided by its standardization. The function $g(x)$ on the left hand side is a normalized auxiliary function. In this

case the uniform distributed random numbers with $g(x) = 1$. By solving equation (6.13) for the particle energy E, one obtains an expression in which the energies E depend on a random numbers $x \in [0,1]$ and are distributed according to the energy distribution $N(E)$. The total proton number calculated from the experiment is 1.85×10^{12}, but for the simulation only 10^6 macro particles are used. Each simulation particle represents 1.85×10^6 real protons and a weighting factor for the simulation particle is included for the fields and the output diagnostic.

Proton source size: Measurements showed an energy dependent source size $S(E)$ for laser-accelerated protons and not a point source. Hence, the particles are distributed over different circular areas. The diameter is given by the measurement presented in figure 6.3(a). The graphical deconvolution of the proton spectrum (see section 3.3.2) yields to an almost homogeneous particle distribution over the circular area. The protons are deposited on the x-y source plane by using random polar coordinates. The angular coordinate is uniform distributed ($2\pi n_1$, $n_1 \in [0,1]$), and for the radial coordinate the *inverse transform sampling* methode is again applied to assure the uniform distribution over the circular area. In this case, the distribution $N(E)$ of equation (6.13) is replaced by the uniform distribution function $f(n_2) = n_2$. By solving this equation for n_2, one obtains $n_2 = \sqrt{x}$ with the uniform distribution of random numbers x in the interval [0,1]. The product source size radius $S/2$ and n_2 assures the homogeneous particle distribution over the source size.

Envelope divergence: The envelope divergence φ has influence on the velocity distribution in x, y and z direction. With the total velocity v_{total} calculated by the particle energy and spherical coordinates, it is possible to model the expansion of the beam resulting in the velocity component v_x, v_y and v_z:

$$v_x = v_{total} \cdot \sin\left(\varphi \frac{r}{r_S}\right) \cdot \cos(\vartheta) \tag{6.14}$$

$$v_y = v_{total} \cdot \sin\left(\varphi \frac{r}{r_S}\right) \cdot \sin(\vartheta) \tag{6.15}$$

$$v_z = v_{total} \cdot \sin\left(\varphi \frac{r}{r_S}\right) \tag{6.16}$$

The azimuth angle ϑ is exactly the same uniform distributed angular coordinate as for the proton source size and the inclination φ is the half envelope divergence shown in figure 6.3(b). To assure a laminar beam expansion, the factor r/r_S has to be included. The ratio of the particle radius r and the source size radius r_S is between 0 and 1 and guarantees that no trajectories are crossing each other. Particles leaving the source plane at $x = y = 0$ and have maximal velocity in z-direction ($v_z = v_{total}$, $v_x = v_y = 0$), and particles with maximal radius have maximal transverse velocity.

Transverse emittance: The normalized transverse emittance can be calculated over the beam volume in the phase space. But to include this parameter in Warp, it is practical to add an additional velocity component in the x- and y-direction instead of an emittance. As in section 3.3.1 pointed out, the blurring of the particle trajectories is described by the energy dependent micro-divergence $\Delta\varphi$. By multiplying $\Delta\varphi$ with *Gaussian* distributed random numbers n_3 in the range [-1,1], this angle perturbation is directly added to the inclination φ and equations (6.14)-(6.16) pass into:

$$v_x = v_{total} \cdot \sin\left(\varphi \frac{r}{r_S} + n_3 \Delta\varphi\right) \cdot \cos(\vartheta) \tag{6.17}$$

$$v_y = v_{total} \cdot \sin\left(\varphi \frac{r}{r_S} + n_3 \Delta\varphi\right) \cdot \sin(\vartheta) \tag{6.18}$$

$$v_z = v_{total} \cdot \sin\left(\varphi \frac{r}{r_S} + n_3 \Delta\varphi\right) \tag{6.19}$$

Electron beam parameters:
For the electron energy distribution the exponential spectrum of the protons is converted with equation (6.12) to its correct electron energies. With the particle masses $m_p = 1.6726 \times 10^{-27}$ kg, $m_e = 9.1093 \times 10^{-31}$ kg and the rest energies $E_{p,0} = 938.27\,\text{MeV}$, $E_{e,0} = 510.99\,\text{keV}$, the corresponding electron energy interval can be calculated from the proton energy interval [3.42 MeV, 23.04 MeV] to $E_{e,min} = 1.87\,\text{keV}$ and $E_{e,max} = 12.54\,\text{keV}$. The velocity distribution as well as the spacial dimensions are the same for the electrons: source size, envelope divergence and transverse emittance. Only the random numbers for the polar distribution over the source plane changed, because a same emission point (x,y) for a proton and an electron should be avoided.

Geometric boundaries:

The main purpose of using Warp is to verify and optimize experiments for capture and control laser-accelerated proton beams. Therefore, the simulation setup is fit to the experimental layout of the Phelix campaign in 2010 (see section 5.2). Proton beams are accelerated from thin foils and fly through a collimating/focusing solenoidal field before they are detected in a radiochromic film stack, as shown in figure 6.4. The propagation distances in beam direction (z-coordinate) are 95 mm in the solenoidal fringe field, 150 mm inside the solenoid and 162 mm in the fringe field behind the solenoid until the beam hits the RCF stack detector at a distance target-detector of 407 mm. A second detector of the same type is place 93 mm further away to check the beam divergence. This setup, the dimensions of the solenoid and the importance of the fringe field result in a simulation box of 500 mm x 80 mm x 80 mm. The nature of laser-accelerated proton beams is an axially symmetrical expansion. Hence, cylindrical coordinates ($z = 500$ mm, $r = 40$ mm) are used instead of cartesian coordinates and a significant decrease in computational time could be achieved.

Warp provides different boundary conditions for the simulation box: absorbing, reflecting and periodic. In this case, considering energy conservation, absorbing boundary conditions for particles are chosen, and for the fields the *Dirichlet* condition is applied.

External field:

The solenoidal field is obtained from the analytic field profile of a cylindrical current sheet with $B_{0,max}$, which is the B_z field on axis at the z-center [209]. The field on axis is given by:

$$B_0(z) = \frac{1}{2} k \mu_0 \left[\frac{(1-2z)}{\sqrt{4R^2 + (l-2z)^2}} + \frac{(l+2z)}{\sqrt{4R^2 + (l+2z)^2}} \right] \tag{6.20}$$

with the current k in units Ampere-turns per meter (can be replaced by a $B_{0,max}$ proportionality), the magnetic constant μ_0 and the length l and radius R of the current sheet (average: $R = \frac{R_{outer}+R_{inner}}{2}$). Starting with this expression, the field off axis is given by the multipole expansion:

$$B_z(r,z) = B_0 - \frac{B_0'' r^2}{4} + \ldots \tag{6.21}$$

$$B_r(r,z) = -\frac{B_0' r}{2} + \frac{B_0''' r^3}{16} - \ldots \tag{6.22}$$

Figure 6.5 illustrates the radial (top) and the longitudinal (bottom) magnetic field strength B_r and B_z. To overcome direct impact of the particles on the metal windings of the coil, a glas fiber strengthened,

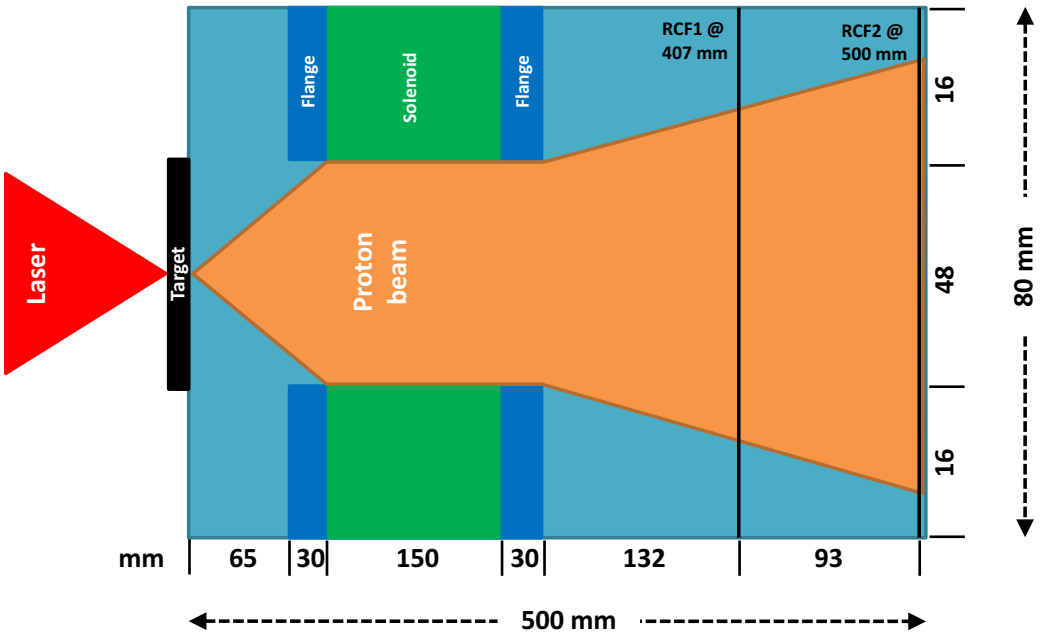

Figure 6.4: Layout of the geometric boundaries for the Warp simulations. This setup matches exactly the design of the experiment presented in section 5.2. The proton beam passes through the solenoid and expands until the particles are detected with a RCF stack 407 mm behind the target. The second RCF stack detector placed at 500 mm is for checking the collimated protons, which should have the same beam diameter in the detector regardless of 10 cm more propagation length.

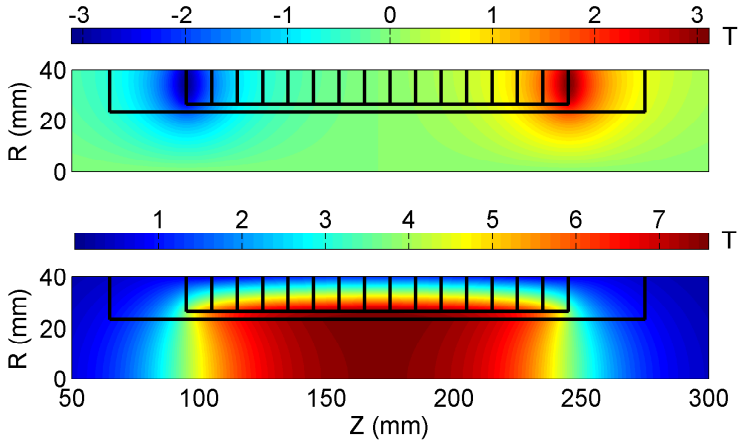

Figure 6.5: Radial and longitudinal and magnetic field B_r and B_z (from top to bottom). In addition, the housing (glas fiber strengthened synthetic resin tube) as well as the coil (hatched area) is drawn in.

synthetic resin shielding tube with a wall thickness of 3 mm is inserted into the coil. The windings are arranged in the hatched area. The radial magnetic field component, which is important for the collimating and focusing effect of the solenoid (see section 6.8) is dominant at the coil edges. With a magnetic field of $B_{0,max}$ = 7.51 T, the maximal radial field $B_{r,max} = \pm 3.11$ T. But this value is inside the shielding. Only a maximal radial field of B_r(r=24 mm) = ± 1.94 T affects on the particles flying through the solenoid. The field strength at the position of the target is a crucial parameter, which can have an important impact on the proton beam generation, because induced eddy currents in the foil are able to bend the target and the target normal is twisted relative to the symmetry axis of the solenoid (see ref. [48]). The longitudinal magnetic field is almost constant over the source size. At a radius of 200 µm the field strength is about B_z(z=0,r=200 µm) = 104.65 mT. The radial field is increasing over the radius up to B_r(z=0,r=200 µm) = 0.25 mT.

6.3 Essential Plasma Parameters and Simulation Criteria

In the field of PIC simulations, in this case plasma simulations, it is important to assure reliability of the simulation results. Incorrect chosen parameters result in possible distortions of the physics. Hence, the main simulation parameters *time step* and *grid size* have to be adapted to the plasma frequency and the *Debye* length as well as to the *Courant* and the energy conservation criteria.

Plasma frequency:

The accuracy of a code can be partially described how precise motion on a small scale can be resolved. Plasma oscillations of the electron density to restore the quasi-neutrality of the plasma are very rapidly and on a small scale. The code should be capable to resolve these oscillations locally. On a global scale, the plasma oscillations can not be observed, because the conversion of potential to kinetic energy during the oszillations of all plasma electrons is centered.

Resolving the plasma frequency ω_p in this context means finding a time step size Δt where:

$$\omega_p \cdot \Delta t < 1 \quad \rightarrow \quad \Delta t < 0.177 \cdot \frac{1}{\sqrt{n_e \, [10^{22}/cm^3]}} \text{ fs} \tag{6.23}$$

with the electron density n_e in units of $10^{22}/\text{cm}^3$. For the proton beam used as source, 1.85×10^{12} electrons in the energy range of (1.87-12.54) keV accompany the protons. Assuming a micrometer thick cylinder source with a diameter of 400 µm, the electron density would be 1.47×10^{19} cm^{-3} resulting in a time step size of 4.6 fs. The computational time would be huge on one processor. At this point, a volume source is introduced to increase the time step size to carry out simulations in a acceptable time window.

Assuming an initial 0^{th} time step with t_0 = 15.3 ps ($\widehat{=}$ 1 mm propagation length of protons/electrons with the maximum energy), the volume occupied by all protons and electrons is a truncated cone with the dimensions: r = 158 µm, R = 348 µm and h = 608 µm. Here, the envelope divergence for the minimum and maximum particle energy is considered. The fact, that the electrons have an exponential spectrum, the low energy particles contribute most to the volume density. The energy interval [1.87 keV, 4.64 keV] (protons [3.43 MeV, 8.5 MeV]) contains 86 % of all electrons. Hence, the considered volume can be scaled down to the spatial distribution of this energy interval. With the calculated electron density of $n_e = 1.88 \times 10^{16}$ cm^{-3} the plasma frequency follows to: $\omega_p = 7.72 \times 10^{12}$ s^{-1}, and one obtains a time step size according to equation (6.23) of Δt < 129 fs. For all following simulations, the time step size is set to 75 fs.

The nature of beams with an exponential energy distributon is the spatial dispersion due to the different velocities. After a simulation time of 46.5 ps, the density of the expanding beam is so low, that the time step size can be increased to 1 ps. Assuming a straight trajectory along the propagation direction of the beam, the particle with the lowest energy would need 19.5 ps to hit the end of the simulation box (see figure 6.4). The maximum opening angle, that a particle still can pass the solenoid, is 5°. For this longer distance the particle with the lowest energy would need 19.6 ps, not significant more compared to the straight direction. But due to the effect of the magnetic field on the particles, the simulation time is estimated upwards. It is the sum of 680 time steps of 75 fs and 21000 time steps of 1 ps resulting in 21.051 ns.

Debye length:

While the plasma frequency defines the temporal resolution of the simulation, the *Debye* length determines the spatial resolution. Plasmas have the ability to distribute themselves in order to shield out electric potentials that are applied to it. This means that negative charges will gather around positive charges effectively shielding positive charges from feeling the effects of one another. The process of charge shielding gives the plasma its quasi-neutral property. The characteristic length over which shielding occurs is given by the *Debye* length λ_D

$$\lambda_D = \sqrt{\frac{\epsilon_0 \, k_B \, T_e}{n_e \, e^2}} = \frac{\sqrt{\frac{k_B \, T_e}{m_e}}}{\sqrt{\frac{n_e \, e^2}{\epsilon_0 \, m_e}}} = \frac{v_{e,thermal}}{\omega_p} \tag{6.24}$$

where k_B is the Boltzmann constant, T_e the electron temperature, n_e the electron density, m_e the electron mass, and e the electron charge. The *Debye* length can also be expressed in terms of the thermal velocity spread of the electrons $v_{e,thermal}$ and the plasma frequency ω_p.

In accelerator physics, the temperature $k_B T_e$ is calculated by fitting a *Maxwell* distribution on the electron beam. But in this case, it is not possible, because the beam is not a particle bunch with discrete energy and a small energy broadening of some percent. The spectrum is an exponential function. Actually, the temperature of each energy would be zero. But a very rought approximation could be the following calculation.

As for the plasma frequency, only the low energy part of the spectrum is considered, because it contributes most to the electron density. A *Maxwell-Boltzmann* energy distribution

$$f(E) = \frac{2}{\sqrt{\pi}} \cdot \sqrt{\frac{E}{(k_B T_e)^3}} \cdot \exp\left[-\frac{E}{k_B T_e}\right] \tag{6.25}$$

can be fitted to this energy interval resulting in a temperature of $k_B T_e$ = 164 eV and in a *Debye* length of $\lambda_D \approx 0.7\,\mu m$. The simulation grid, on which the self fields will be solved, has to have a resolution smaller than λ_D to see the effects of the space charge. But, as mentioned above, this is only a rought approximation, because it is not possible to calculate the *Debye* length directly. In section 6.7 convergence studies on the grid resolution are done to find an acceptable grid size.

Courant criterion:

Besides the *Debye* length, a second criterion yields to the resolution of the simulation grid. The *Courant* criterion [213] defines not a maximum limit for the grid cell size Δz like λ_D, it defines a minimum value depending on the velocity of the particle v_z and the time step size Δt of the simulation. For laser-accelerated proton beams and their accompanying electrons, the radial velocity v_r is much smaller

than the longitudinal component v_z. Hence, the minimum grid cell size is defined by the longitudinal motion:

$$\Delta z_{min} > v_z \cdot \Delta t \tag{6.26}$$

If the grid cell size is chosen to be smaller than Δz_{min}, particles can leapfrog a grid cell, the plasma dynamic is disturbed and non-physical effects can occur. The velocities of the particles used in this case is (2.56-6.53) $\times 10^7$ m/s (8.5-21.7 % of the speed of light). The maximum velocity results in a longitudinal motion of 4.9 µm for Δt = 75 fs and 65 µm for Δt = 1 ps. For the following simulations, cylindrical grid dimensions of $\Delta r = \Delta z$ = 250 µm are used. One grid cell corresponds to a volume of hollow cylinder with the inner and outer radius r and $r + \Delta r$ and the depth Δz (the zero order cell is a simple cylinder).

Energy conservation:

The final criterion which has to be fulfilled is the energy conservation during the simulation. The ideal run should have constant energy in the system. Two different forms of energy have to be considered: the kinetic energy of the particles (protons and electrons in sum) and the electrostatic field energy. Each timestep, the kinetic energy can be calculated by the given velocities. Lost particles, leaving the simulation box or hitting the solenoid, are also considered. The field energy is calculated in cylindrical coordinates as:

$$E_{field} = \frac{1}{2} \int_\theta \int_r \int_z (\rho \cdot \Phi \cdot r) \; \mathrm{d}z \; \mathrm{d}r \; \mathrm{d}\theta \tag{6.27}$$

$$= \pi \sum_i \rho \cdot \Phi \cdot r \cdot \Delta z \cdot \Delta r \tag{6.28}$$

with the charge density ρ, the electrostatic potential Φ, the radius r and the cylindrical grid dimensions Δz and Δr. Details about the energy conservation check can be found in section 6.7, after some diagnostics and general results are presented for a better understanding .

6.4 Particle Diagnostics

In the scope of this work, several output diagnostics were developed and included into the Python input file for the Warp code. In particular, two different types of diagnostic are used. First, it is possible to export every time step the particle position and its velocity components. Therefore, it is necessary to be sure of saving the same particles every time step. Every single simulation particle gets an initial flag and maintains this number until the end of the simulation. During the data saving the fraction of the particle data, which corresponds to the desired particle flags, are sorted out and are written including the flag number into a file. So, it is possible to track a particle through each time step. At the end of the simulation, all data can be resorted to create additional data files each containing the positions and velocities for a single particle for all time steps, so called particle trajectories. The charge density ρ and the electrostatic potential Φ are saved as a two-dimensional grid. One-dimensional particle parameters such as energy distribution, transmission and beam radius are also calculated by using various types of one-dimensional grids and saved every time step. The time history of parameters, for example the total calculated energy to check the energy conservation criterion, are stored by successive sticking data every time step into a file.

The second type of diagnostic which is been used are two- and three-dimensional, accumulating grids. Particles passing a certain plane perpendicular to the propagation direction z are deposited onto this

plane (positions and velocities are stored if a particle crosses the plane) or sorted onto a grid to calculate a two-dimensional particle density map. Besides particle trajectories the beam edge radius R_{edge} provides information about collimating or focusing behaviour of the particle beam. Therefore, the z-axis refering to the propagation direction of the beam is divided into equal intervals bordered at the end by a perpendicular layer in the x-y-plane. So, the energy resolved beam edge radius can be saved on the grid. Herewith, this detector offers the possibility of illustrating the beam edge radius energy dependent for different z-positions $-$ $R_{edge,z}(E)$ $-$ or z-dependent for different energies $-$ $R_{edge,E}(z)$.

Until all essential parameters are defined, a simulation is more or less a theoretical experiment with the aim to understand the physics behind and to reproduced measured data. Therefore, a virtual RCF stack is included into the simulation (see figure 6.4) equal to the one used in the experiment presented in section 5.2.1 to measure the deposited proton energy. With the help of the energy deposition curves for each RCF stack layer (see section 3.3.2) and the exact position and energy of the protons on a plane detector at $z = 407\,\text{mm}$, the deposited proton energy can be accumulated on a two-dimensional grid for each RCF layer. This detector enables the possibility to compare directly deposited energy values of the experiment with the simulation, spatial as well as energy resolved.

6.5 Comparison of Experiment and Simulation

The following results are the outcome of a simulation done with the same setup and diagnostics as in the experiment including the calculated plasma and simulation parameters of sections 6.2 and 6.3. This enables direct comparison to shot 7 carried out during the solenoidal experiment at the Phelix laser system. Before the comparison can be done, the experimental results have to be reprocessed to point out the main features or rather observations. Contrast and brightness changes on the gradation curve are carried out on each layer of the RCF stack shown in figure 5.3 resulting in the modified stack in figure 6.6.

Please note: the modifications are done to make particular features visible and not to distort or adapt the data. The color scale on each layer is different and can not be compared to the other modified films. Now, observed ring sizes, focus and spot diameters are easier to measure, because of the better contrast. Furthermore, this illustration clearly shows the analysis problems for radiochromic films with a bad signal-to-noise ratio. Scratches, dust and dirt overvalue the deposited energy in the layer, because it is not possible to remove all noise during the data analysis (more in section 3.3). In additon, the electron signal now emerges especially in layer 3-6. It is in the same horizontal plane as the proton beam but shifted to the right. Due to the symmetry of the experimental setup and the outcoming proton beam, one would expect the same behaviour for the electron beam, but the axis symmetry is broken. Reasons for the aberration could be a slight missalignment of the solenoid, fringe field inhomogeneities, which affect more on the electrons than on the high mass protons, or an unknown external field overlapping the solenoidal fringe field behind the coil exit.

The film stack of the experiment can now be compared to the simulated virtual stack shown in figure 6.7. In the following, each layer will be analysed separately:

Film #1 — 3.7 MeV: The simulated layer shows the focal, disc and ring structure already observed in the experiment. The focal spot in the center is very intense with the maximum value of the deposited energy of 1.6×10^7 MeV/100×100 µm^2. For increasing radius, this peak goes over in a almost flat distribution up to the edge of the disc with a radius of 7.4 mm. The radial lineout of layer 1 in figure 6.8 indicates the cut-off of the disc and again the peaked intensity at a radius of 14 mm belonging to the observed ring structure. The experimental value of 18.3 mm it is well above this radius, because the ring structure is not so uniform compared to the simulation and hence,

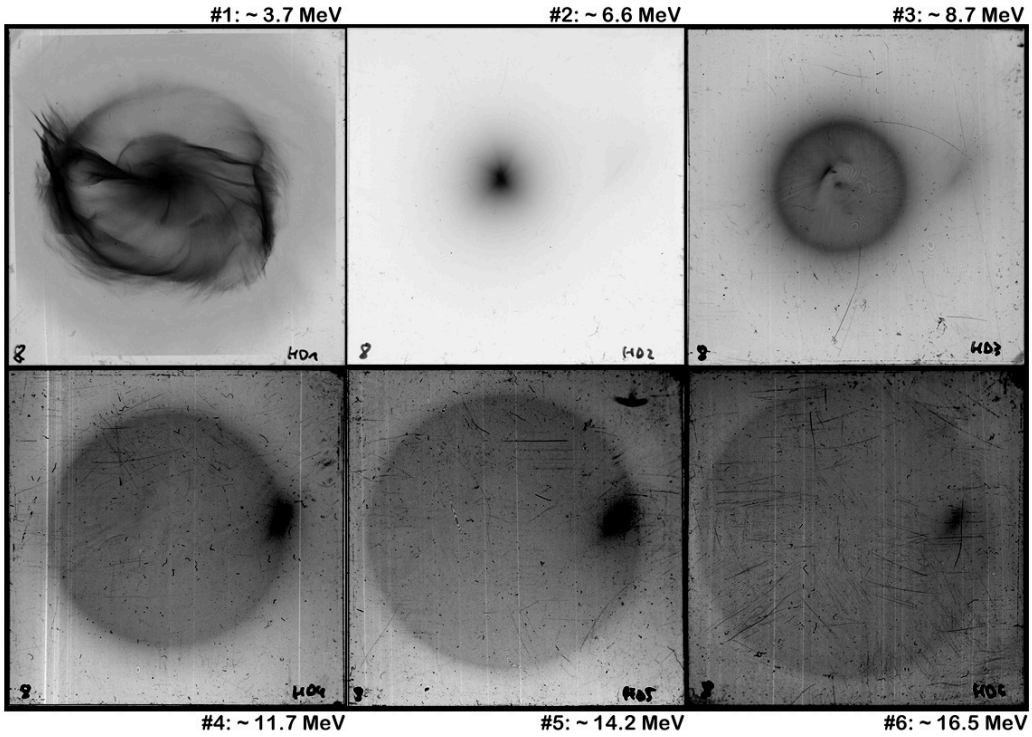

Figure 6.6: Contrast optimized layers of the RCF stack of Phelix shot 7, figure 5.3. The changes on the gradation curve result in a clear accentuation of the observed proton features. Ring sizes as well as focus and spot diameters are pronounced. The film size is 63.5×63.5 mm^2.

the estimated value is an average. Small instabilities in the acceleration mechanism could lead to variations from the symmetric expansion.

Film #2 — 6.6 MeV: At the stack position of 407 mm, the second layer - corresponding to the proton energy of $\sim$6.6 MeV - is close to the focal plane for these energies. The bulk part of the protons is just before, in or close behind the focus position. The total dimension of the proton spot in this layer is measured to 20 mm, which is in good agreement with the simulated value. The virtual detector can measure every single particle regardless of which energy and impact radius. But radiochromic films, as mentioned in section 3.3, have a lower detection threshold. Low energy protons with a large divergence angle will hit the detector in the outer parts and deposit only a tiny fraction of energy. Because the particle density is not very high, the summarized deposited energy is mostly under the detection threshold or so low, that it gets lost during the digitalization process. The observed disc distribution in the simulation with an radius of 7.3 mm could not be observed in the experiment.

Film #3 — 8.7 MeV: The simulation reproduces the ring structure in layer 3 very well. The radius of the ring of 10.3 mm is almost the same value calculated for the experiment of 11.5 mm. By comparing the images, the hot spot in the center can be confirmed, even if it is not visible in the lineout, because the center of the film was not chosen correctly. The blurring of the proton signal in the area outside the ring differs due to the same effect described above. The density gradient over the ring structure is much lower than in the layers before, but the difference is still observable in the line-out illustration of figure 6.8.

Film #4 - 5 - 6 — 11.7, 14.2, 16.5 MeV: Due to the nature of the proton spectrum, the proton signal in the virtual layer decreases with increasing proton energy, because less particles are available. The total proton spot diameters are similar to the experimental values (50 / 53 / 56 mm), but the still existing intensity enhancement in the center can not be reproduced by the experiment.

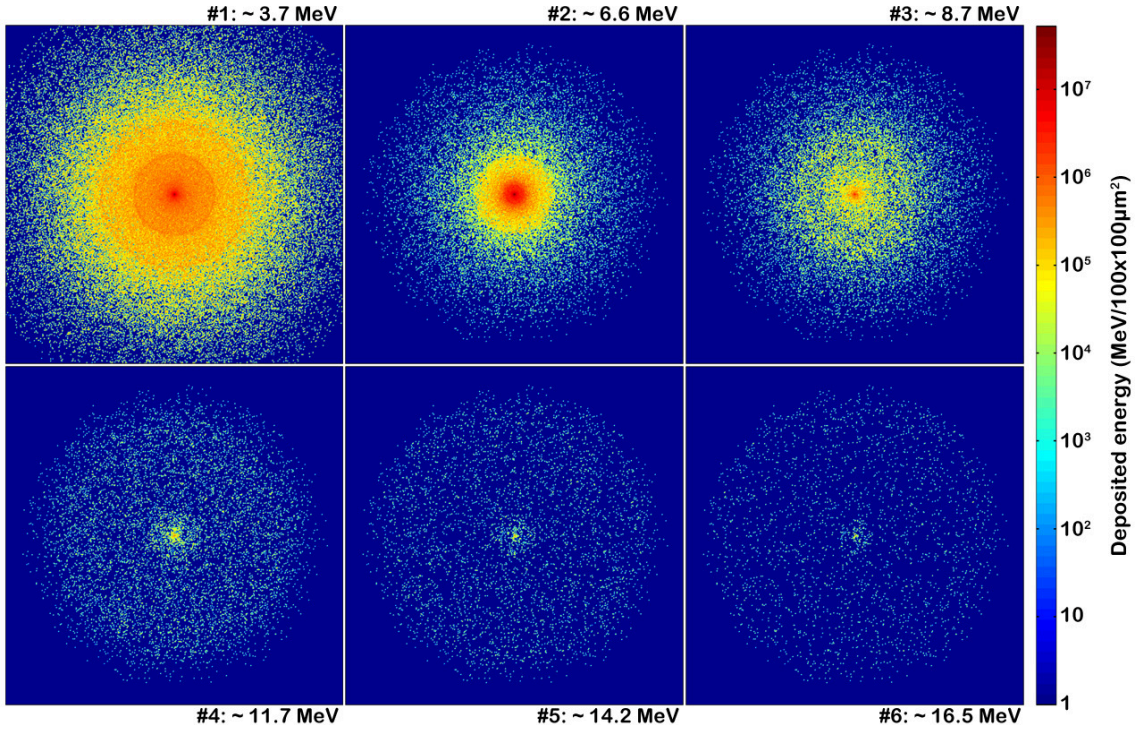

Figure 6.7: Simulated virtual radiochromic film stack. The given proton energies are exactly the same as for the Phelix shot 7 stack. The simulation data are in very good agreement with the experimental results. Foci, rings and similar proton beam diameters can be observed. The film size is the same as in the experiment 63.5×63.5 mm^2 and the logarithmic color scale is in units of deposited energy in MeV per detection area 100×100 µm^2.

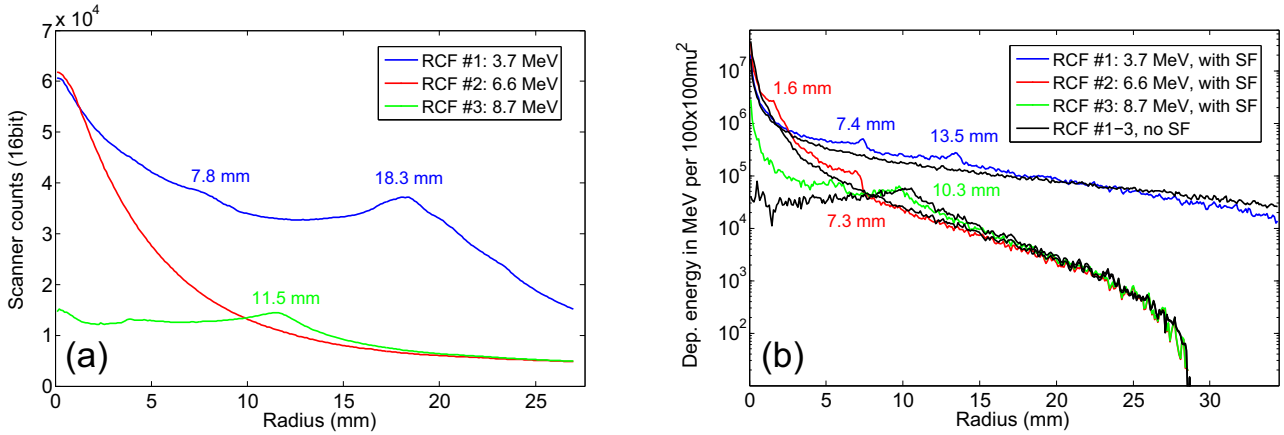

Figure 6.8: Radial line-outs for the first three RCF layers of (a) the experiment (figure 6.6) and (b) the siumlation with self-fields (figure 6.7). In addition, the simulation results of the run without self-fields is plotted.

Figure 6.8 illustrates the good agreement between experimental and simulated results. However, in some points the simulation without self-fields seems to fit better. More details and explanations about the development of the particular structure in the RCF stack detector are given in the following sections. Points like particle trajectories, focusing, transport and collimation are discussed when they fit into the context.

After the optical comparison of the observed proton structure in the stack detector, a direct comparison of the deposited energy in each layer is of interest to check the accuracy of the simulation. The films of the experiment given as scanned 16 bit gray-scale images and the simulated virtual layers given in MeV per area on a logarithmic scale are two different descriptions, which can not be absolutely compared. Therefore, the digitized radiochromic films are converted to the energy deposition description by the help of a proton calibration of the films (see section 3.3). Figure 6.9 shows the comparison of the absolute deposited energy in each layer of the real (—) and virtual (—) stack. Using an exponential distributed proton source, one would exactly expect the slope of the simulated data. Less particles deposit their energy in the deeper layers. The simulated deposition can be perfectly repesented by following best-fit curve:

$$E_{dep}(E) = E_{dep,0} \cdot \exp\left(-\sqrt{\frac{E}{k_B T}}\right) \tag{6.29}$$

with $E_{dep,0} = 4.21 \times 10^{12}$ MeV and $k_B T = 172\,\text{keV}$. For the first three layer, where more energy is deposited, the data sets fit each other very well. For the last three layers, as already pointed out above, the scratches, dust and dirt overvalue the deposited energy. Assuming the undisturbed data would behave like the simulation data, the best-fit curve resulting from the first three points yields to $E_{dep,0} = 4.08 \times 10^{12}$ MeV and $k_B T = 162\,\text{keV}$. Within the bounds of the accuracy of the experiment, the absolute values for the energy deposition conform very well to the simulation.

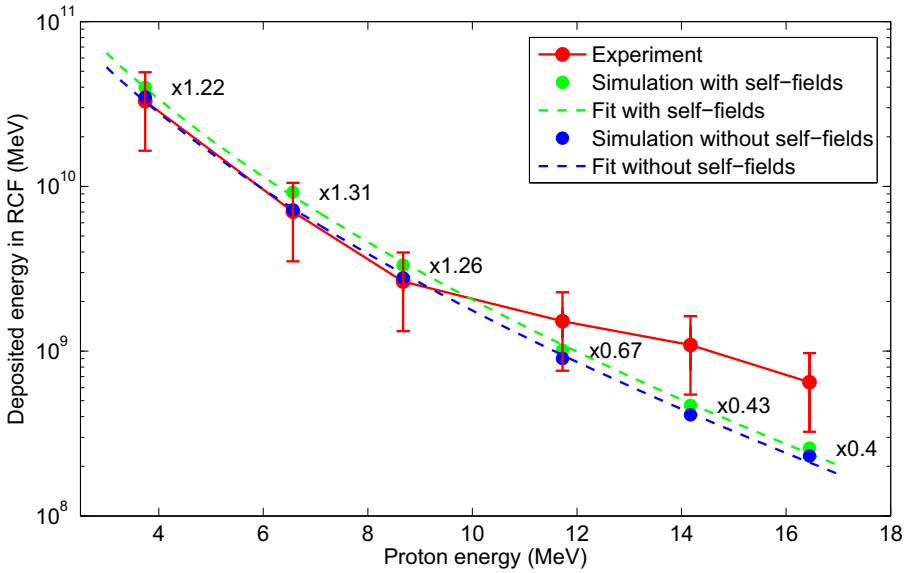

Figure 6.9: Comparison of the absolute deposited energy in each layer of the real (—) and virtual (—) stack. The plotted factors are the ratios between the simulation and the experiment data. In addition, a simulation without self-fields is plotted in to see the effect of the space charge.

The comparison of the simulation data with the experimental results is far from a detailed explanation of the physical effects responsible for the obtained results. Therefore, the interation of the solenoidal field with charged particles is discussed in the next section. The behaviour of the protons and the electrons is necessary background knowledge before convergence studies are carried out.

6.6 Magnetic Field Effect on Co-Moving Electrons and the Proton Aggregation

Particles in the fringe field of the solenoid are passing a region of radial magnetic fields. The *Lorentz* force ($q v_z \times B_r$) acts azimuthal. The resulting velocity v_θ leads to a radial force when the particles entering the B_z fields inside the lens. Independent of charge state or transit direction, the particles are deflected toward the symmetry axis of the solenoid. Equation (2.25) implies that particles gain no net azimuthal velocity passing completely through the lens, because they must cross opposite directed radial magnetic field lines at the exit that cancel out the azimuthal velocity gained at the entrance.

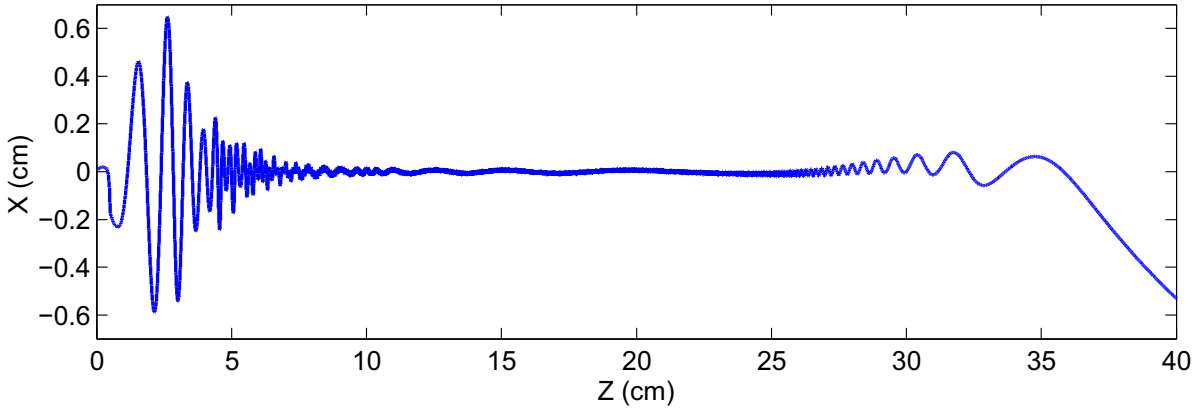

Figure 6.10: Trajectory of an electron with an initial energy of 5.2 keV. Inside the solenoid, the electron circles in a cylinder with $r = 50\,\mu m$.

As soon as the charged particles moves inside the solenoid, they are constrained on a gyration with the given *Lamor* radius, equation (2.26). This equation is only valid between the ends of the solenoid, where the field strengh B_z is homogeneous and constant. In contrast in the fringe fields, the divergent particle beam runs through different perpendicular velocity components $v_\perp(z)$ and magnetic field strengths $B(z)$. For electrons, because of the larger charge-to-mass ratio compared to protons, the motion is described by a decreasing helix, see figure 6.10. Inside the solenoid, where the parameters are constant, each electron circles around the solenoid axis with its energy dependent gyroradius. The effect on the protons is much smaller, because of the higher mass. A classical estimated gyroradius for a 23 MeV proton is about 9 cm. For the corresponding co-moving electron, the gyroradius is about 50 µm. Electrons in the energy range of several keV need only the first fringe field to be focused down onto the axis, because the radial and longitudinal field components are already strong enough. After that, they pass the solenoid in a tube volume with a radius of 50 µm until the magnetic field components change in the second fringe field at the exit of the solenoid. The gyroradius increases, v_θ decreases to zero and the beam expands in the almost field free region, see divergent expansion in figure 6.11(a).

The existence of the electron beam circulating around the axis of the solenoid with its gyroradius could be experimentally verified in an earlier campaign at the PHELIX laser system in 2008 [48] and also during the current experiment described in section 5.2.2. Exactly this behaviour can be seen in the simulation, figure 6.11(a). In addition, an increase of the initial maximum electron energy of 12.5 keV can be observed. Due to the focusing of the electrons, the density increases in a very small volume leading to electro-electron repulsion and pushes electrons forwards up to energies of ∼250 keV. Besides forward electron acceleration, electrons are also slowed down, even stopped and accelerated in the opposite direction. For electrons with a big initial divergence, the solenoidal field acts like a magnetic mirror and reflects the electrons. The repulsion and the reflection cause a particle loss of 82 % of all co-moving electrons at the simulation box plane $z = 0$, because the boundary conditions are set to absorption. Details about the resulting influence on the neutrality can be found in section 6.7.1.

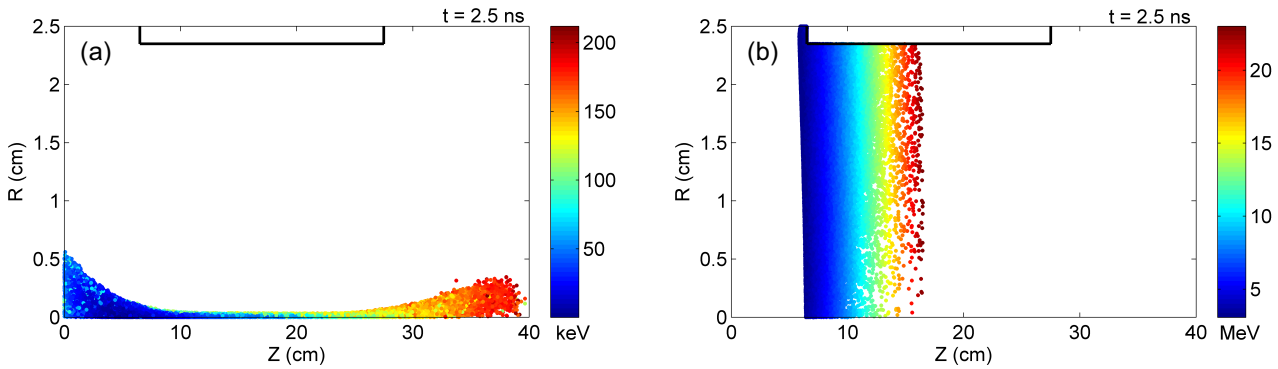

Figure 6.11: Electron (a) and proton (b) expansion at $t = 2.5\,\text{ns}$. The initial maximum electron energy is increased and the focusing effect of the solenoid can be seen, whereas no effect on the protons is visible. Different axis scale.

Looking at the proton illustration in figure 6.11(b), one could state no influence of the electron collimation on the protons. But for later times in the simulation, a particular proton feature close to the symmetry axis develops as shown in figure 6.12. During the first nanoseconds, protons in the energy range of 3.4 MeV to ∼12 MeV are aggregated along the beam axis, because the increased electron density on axis generates a negative potential, see figure 6.13. This negative potential channel along the axis starts to decrease in strength and size for later times. Most of the electrons are reflected or accelerated, the rest electron density is compensated by the huge proton population around until the negative potential channel collapses at $t = 6\,\text{ns}$ (figure 6.13, bottom-right).

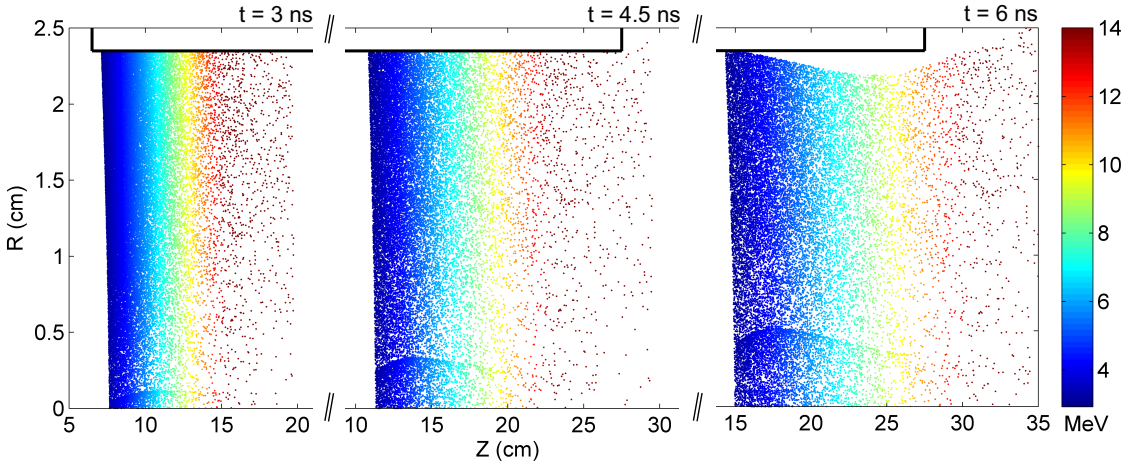

Figure 6.12: Proton aggregation strength for three different simulation times: 3 ns, 4.5 ns and 6 ns (left to right). The energy color scale is limited to 14 MeV, because higher energies are not affected. Different axis scale.

Due to this potential, protons are attracted towards the axis and the proton density increases. As soon as the potential channel starts to collapse, the attraction force drops until the *Coulomb* repulsion of the aggregated protons outweighs. Hence, the protons expand as part of two different populations, one occupying the total inner solenoid volume and the second as a dense part on axis. The effect of the two population expansion can be described by the phase space illustration in figure 6.14. The big ellipse is occupied by the main proton beam. This describes the acceptance of the solenoid, because the beam is already inside the solenoid and particles are absorbed by the inner wall. This area in phase space can not be increased. The substructure inside the distribution is the second part of the beam with smaller x-dimension and a much smaller divergence. Particles of the same energy with different divergence

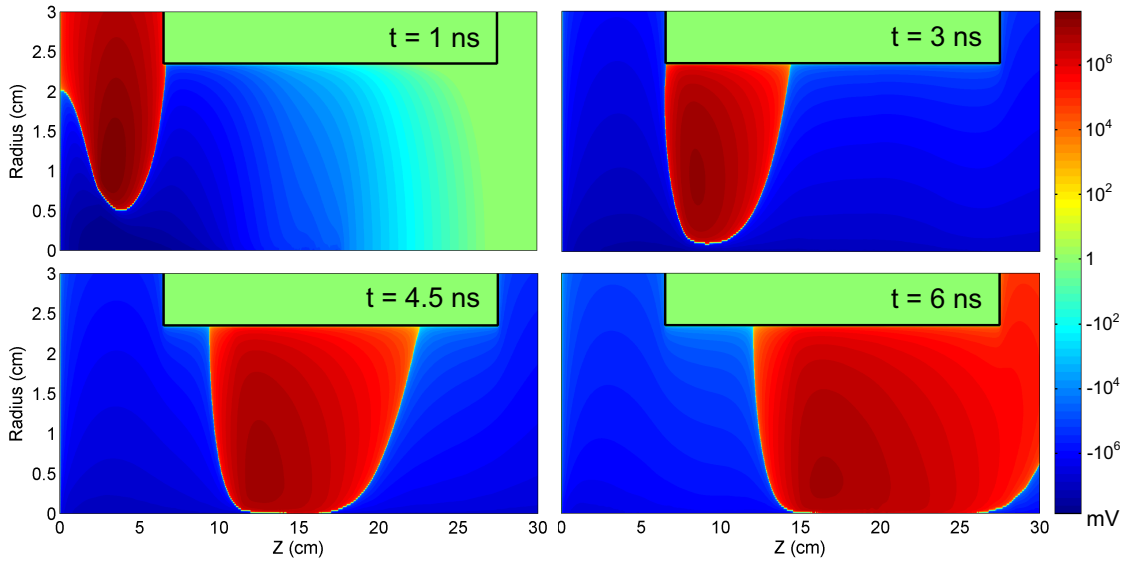

Figure 6.13: Potential illustrations for an early time of 1 ns and the same simulation times as in figure 6.12: 3 ns, 4.5 ns and 6 ns (top-left to right-bottom). Different axis scale.

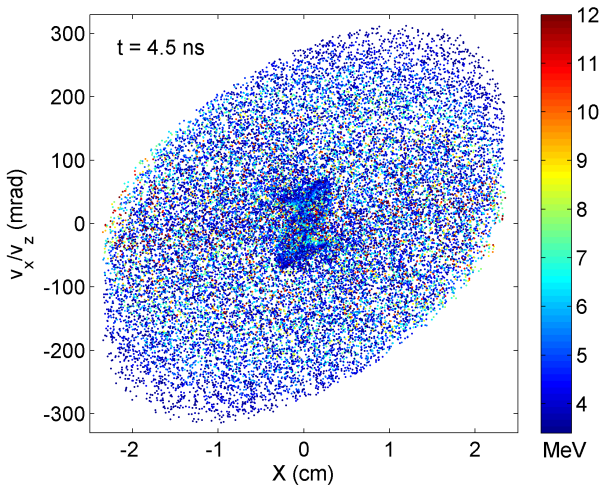

Figure 6.14: Phase space illustration of the two different proton populations. The main ellipse is the acceptance of the solenoid and the intense feature in the center results from the proton aggregation: two beam parts of the same energy but with different divergence angles.

angles will be affected differently by the magnetic field resulting in overlapping proton signals in the RCF detector, see figure 6.7. The protons attracted to the beam axis are responsible for the disc and ring structures. More details on these features can be found in sections 6.7.1 and 6.8.

Before additional details about collimation, transport and focusing of laser-accelerated protons are discussed, it is necessary to carry out convergence studies to confirm the correctness of the simulation results.

6.7 Systematic Studies on the Convergence Criteria

The simulator, in demonstrating correctness, has many of the problems of a theorist or experimenter. The latter two may be questioned, for example, on their approximations and on their instruments. The simulator uses a program with a restricted set of physics, e.g. to be electrostatic or lacking collisions, with carefully chosen initial conditions and a limited amount of output. How can he tell himself and the world that this work is to be believed?

As already done, the simulation output can be compared with experimental observations. The simulator can obtain the desired results for problems with known answers, show invariance of his results as the nonphysical computer parameters (Δt, grid cell size, grid cell number) are changed (convergence studies), and so on. Confidence on the program is required. Warp is a code developed almost 20 years ago. It is used by several groups on multifunctional physical problems. Plasma and accelerator physicists are confident on the function and the results coming out, also because Warp is already benchmarked to other codes.

In the following subsections, different convergence studies are carried out. Particle numbera and grid cell numbers are reduced or the time step size Δt is increased until tell-tale signs of nonphysics, such as flagrant loss of energy conservation or different results, show up.

6.7.1 Space Charge Forces and Beam Neutrality

The basic principle of the TNSA mechanism (see section 1.1) is that an electric field is generated by electrons on the rear side of the target foil. Protons are field-ionized and expand into vacuum. This high-current beam would generate space-charge electric fields by itself leading to *Coulomb* explosion. But the positive charged protons expand through a background plasma resulting in a beam neutralization. The plasma electrons shift in position to compensate for the positive charge and cancel the beam-generated electric field. This process is feasible, because of the low mass of the electron. The space-charge field of the proton beam more or less attracts electrons. Hence, neutralization is a disordering process, where electrons join with protons to form a homogeneous mixture. Both particle species, protons and electrons, are injected in the simulation box, so that the propagation direction and the source volume is the same, but the position differ slightly. Thus, the homogeneous mixture can be formed itself. Finally, the electrons move at same velocity as the protons, $v_e = v_p$. But the neutralization is very sensitive. Even a small imbalance of charge in an intense proton beam results in an increase of the space-charge potential [157].

One motivation for neutralized proton beams is to achieve tightly-focused beams. With complete cancellation of space-charge fields, only the emittance limits the focal spot of an intense proton beam (more in section 6.8). In addition, electrons can be guided with applied magnetic fields much easier than protons and directly effect the proton beam propagation as already shown in the previous section.

To point out the importance of the included fieldsolver in the code to consider the space-charge effects, a set of different simulations are presented: in addition to the reference simulation above, one without electrons, just protons and fieldsolver, and a second one without fieldsolver, just expanding protons. In figure 6.15, the proton energy spectra behind the solenoid are plotted. For all three cases, the transmission shows totally different behaviour. The difference between a simulation considering space-charge (—) and one without fieldsolver (—) is due to the *Coulomb* explosion of the proton beam. Protons are accelerated and slowed down, so that the proton minimum and maximum energies are shifted a lot. In addition to this, the particle numbers per energy interval of 150 keV change. Some of the high energy, low divergence protons are accelerated and boost the spectrum up to higher numbers compared to the simulation without fieldsolver. By setting the total proton number of the simulation without considering space-charge effects (red curve) to 100%, the *Coulomb* explosion causes a particle loss of 82%. All these protons are hitting the solenoid walls and can not pass it, because the space-charge forces are much higher than the ability of the solenoidal field to guide protons through. If the co-moving electrons are included, the picture changes. The proton spectrum behind the solenoid (—) looks like the reference spectrum without electrons and no fieldsolver (—). But if the total proton numbers are compared, one can observe an increase of 30% in protons passing the solenoid. In addition, due to the magnetic mirror effect on the bulk of the co-moving electrons, low energy protons are still slowed down resulting in a shifted spectrum.

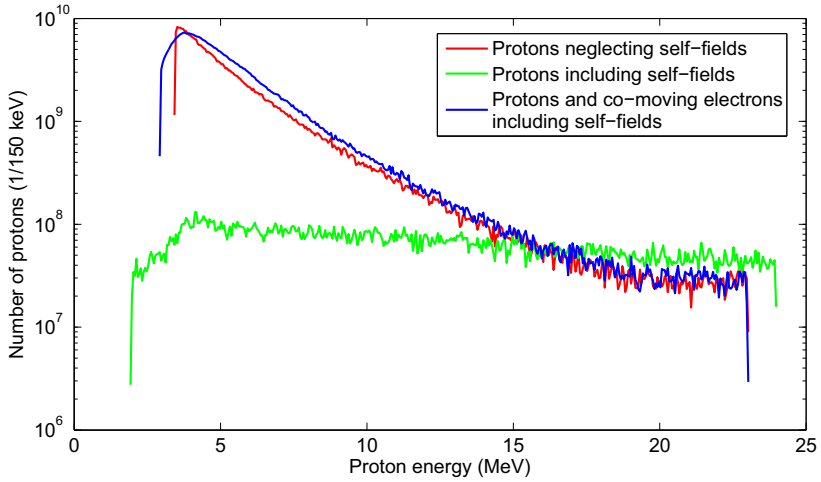

Figure 6.15: Three different proton transmissions through the solenoid are plotted to point out the importance of the space-charge: a simulation just with protons neglecting the self-field effects (—), a simulation running with protons and the fieldsolver is switched on (—) and finally a spectrum of the simulation already presented in the sections before with protons, co-moving electrons and self-fields (—).

The space-charge forces have obviously significant influence on the proton beam propagation. The change can also be seen in the virtual RCF layers. Figure 6.16 shows the virtual radiochromic film stack for a simulation done under the same conditions as for figure 6.7 but without using the fieldsolver. The observed ring structure in the first layer disappeares, the energy density in the center part drops, and the energy deposition in the outer parts increases. The disc structure in layer 2 becomes blurred and the radial lineout in figure 6.8(b) has no remarkable dips or peaks. The slope decreases constantly up to the edge of the beam. For layer 3 and all following, the distribution over the center is almost a flat-top and the focal spots on the beam axis disappeare. What the eye can not quite see is that the total proton transmission through the solenoid decreases from 25.2% for the reference simulation to 18.8% and hereby the energy deposition. This effect can also be seen in figure 6.9, where this simulation (—) is plotted in to compare with the simulation including the fieldsolver (—). The blue curve is below the green, but has almost the same slope. The best-fit curve, equation (6.29), yields to

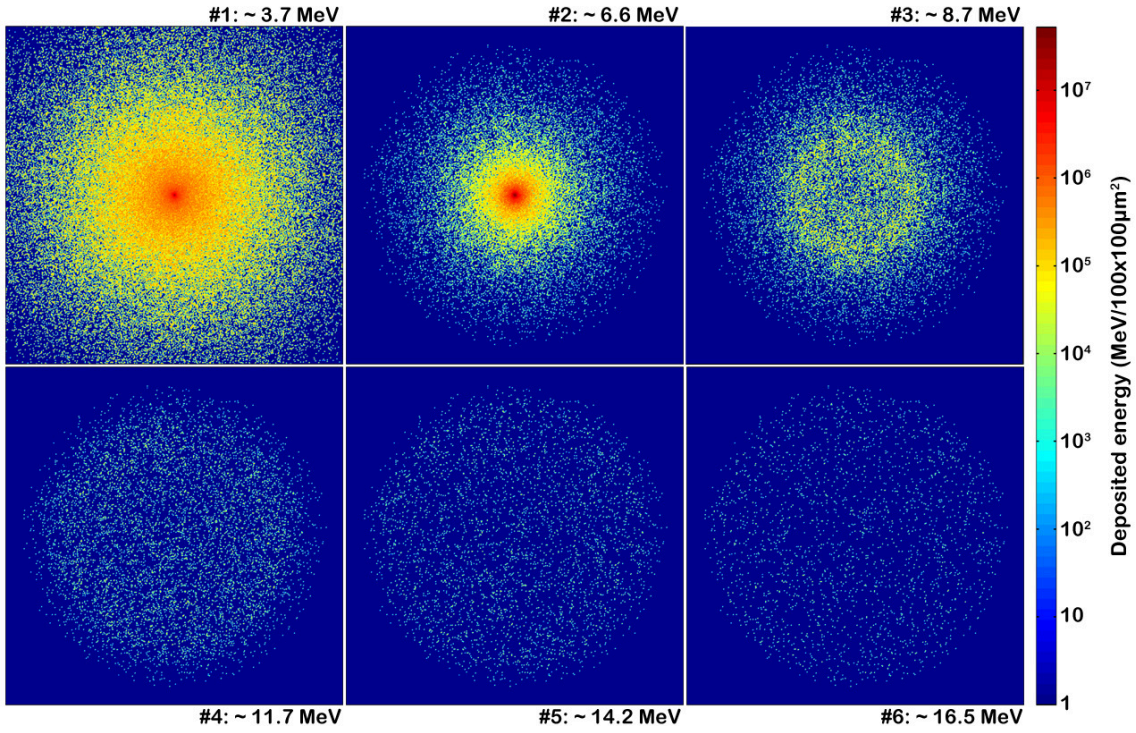

Figure 6.16: Virtual radiochromic film stack for a simulation without fieldsolver. The results can directly be compared to the simulation with fieldsolver in figure 6.7. Proton features like the rings and the density increase on axis for layer 3-6 are disappeared. The film size is the same as in the experiment 63.5×63.5 mm^2 and the logarithmic color scale is in units of deposited energy in MeV per detection area 100×100 µm^2.

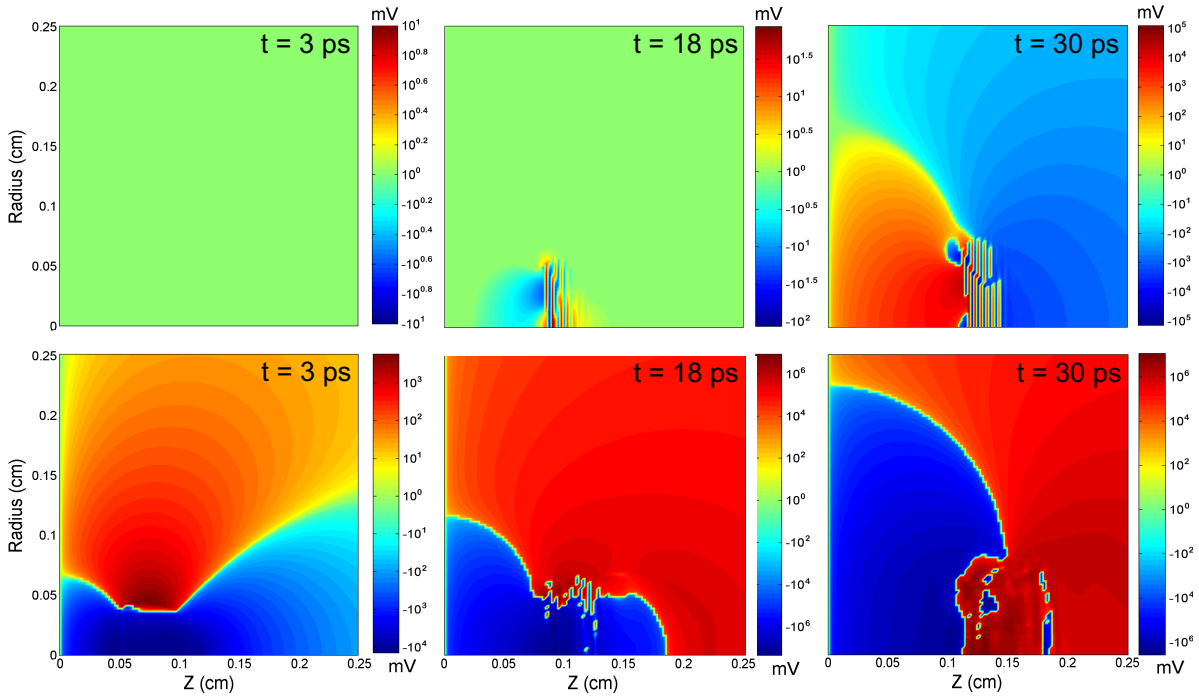

Figure 6.17: Potential illustrations for the simulation times 3 ps, 18 ps and 30 ps. *(top)* simulation without solenoidal magnetic field, *(bottom)* with solenoidal magnetic field. The magnetic field speeds up the de-neutralization process from the first time step on. For the field-free case, numerical heating is the reason for the slow increase in potential. The potential values are given in units of mV.

$E_{dep,0} = 3.26 \times 10^{12}$ MeV and $k_B T = 177$ keV. The fact, that the ring and disc structure disappear if the self-field solver is switched off, clearly points out the importance of the self-field influence. The different expansion behaviour of the attracted protons is responsible for the formation of these features. For higher proton energies (lower particle densities respectively), the simulation without self-fields seems to match the experimental results better.

The central issue concerning neutralized beam expansion is the exponential energy distribution of the laser-accelerated proton beam and its accompanying electrons. As mentioned before, small imbalances of charge in an intense beam results in a high value of space-charge potential. The highest particle intensity is at the low energy edge. Spatially considered, its at the edge of the beam. Over a short scale length, there is a drop in particle density from its maximum value to zero. If there is a small imbalance due to for example numerical heating [213] at this density gradient and charges are shifted, the potential increases immediately and the beam is not neutralized anymore. If the beam would have a typical *Gaussian* distribution like particle bunches in accelerators, it would be much easier to guarantee neutralization. The presence of a solenoidal magnetic field has also significant influence on the beam neutrality as figure 6.17 points out. The beam neutralization is distorted from the first time step of the simulation, because electrons are deflected. At 3 ps the maximum potential value is around several hundreds of mV, but it increases for later times (30 ps) up to several hundreds of volts. The negative potential results from a electron majority and positive values from a proton majority. For the field-free case, the beam neutralization is conserved for the first picoseconds of the simulation. Small fluctuations in the potential of the order of some mV appear at 18 ps due to numerical heating, which are built up to some volts for later times, but two orders of magnitude lower than for the field case. Studies on numerical heating are out of the scope of this work, but have to be done. Nevertheless, the combination of laser-accelerated protons, co-moving electrons and a solenoidal magentic field is such a fast changing system, that neutralization is impossible and numerical heating can be neglected.

6.7.2 Simulation Grid

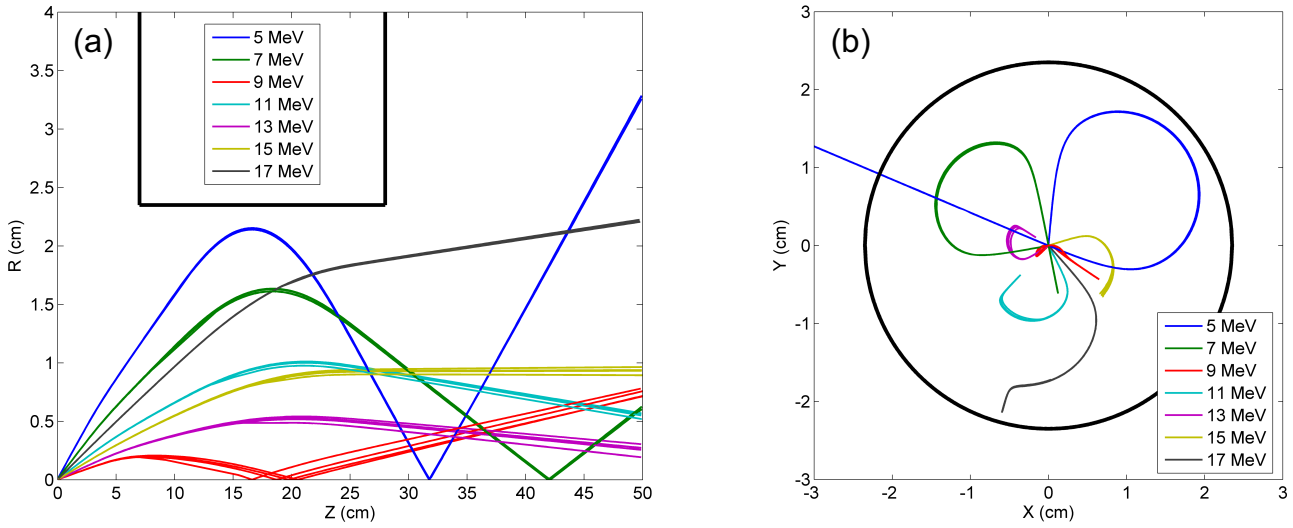

Figure 6.18: Proton trajectories for all four simulations and for different proton energies in the range from 5 MeV to 17 MeV. The black bold line markes the solenoid edges.

As already mentioned in section 6.3, it is difficult to find a precise enough value for the *Debye* length λ_D, because the temperature $k_B T_e$ needed for equation (6.24) can not be calculated. The second possibility to find an appropriate grid resolution for the simulation is a convergence study. The term *convergence study* means to check results of different simulations, if they all finally converge to the same result, if

only one nonphysical parameter is changed. The nonphysical parameter in this case is the grid cell size. Four different values are selected: 1000 µm, 500 µm, 250 µm and 100 µm. The number of simulation particles per grid cell has to be constant in all simulations to make sure the physics is the same. For decreasing grid cell size, the simulation particles are: (0.25, 0.5, 1, 2.5) $\times 10^6$. Figure 6.18 shows proton trajectories for all four simulations and for different proton energies in the range from 5 MeV to 17 MeV. Three proton motions can be distinguished: divergent, collimated and focused protons. Details about the different behaviours can be found in section 6.8.

By comparing the simulations with the different grid cell sizes, maximal displacement in radial direction at the position of the virtual RCF detector (z = 40.7 cm) of $\sim$1 mm is observed. Considering the different axis scales in figure 6.18(b), the deviation of the trajectories for the protons is negligible. Due to the lower mass and therefore higher sensitivity, a small difference in the propagation direction of the electrons leads to totally different space-charge force and motion. The effect on the protons is a minor factor, because the electron guiding of the solenoidal field is the dominant process and independent of the grid cell size. Future studies will go in detail.

6.7.3 Energy Conservation

A characteristic feature or sign of nonphysics is the flagrant loss of energy conservation during the simulation. A simulation run is set up to have a constant energy in the system consisting of the kinetic energy of all particles (also particles, that are absorbed or leave the simulation box) and the electrostatic field energy. An illustration of the energy conservation for a simulation without solenoidal magnetic field is shown in figure 6.19 and with magnetic field in figure 6.20. Here, only the electrostatic field energy is plotted, because the kinetic energy is almost constant 1.76 J for both cases independent of all acceleration and slowing down of particles. Just to get a feeling, how much kinetic energy a 10 MeV proton and a 10 keV electron has, the values are in the region pJ and fJ respectively. The fluctuations are order of magnitudes lower than the average kinetic energy of all particles.

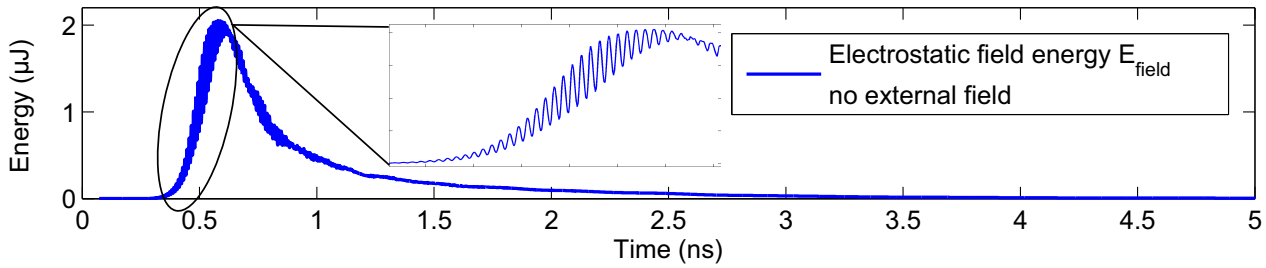

Figure 6.19: Development of the electrostatic field energy E_{field} over the time for the simulation without solenoidal field. The kinetic energy has a constant value of 1.76 J and the peak in the electrostatic field energy is of the order of 2 µm at 0.6 ps. The circled part of the curve is shown in the zoomed inset, where the oscillations are visible.

An observable change can be seen in the electrostatic field energy shown in figure 6.19. A sharp increase of 2 µm within 300 ps results in a maximum at 580 ps. The slope is not a straight line and has a highly visible thickness due to an overlapping oscillation with a variable amplitude up to 0.34 µJ and a almost constant frequency of 10 THz (see inset). As pointed out in section 6.7.1, neutralization is a disordering process, where electrons join with protons to form a homogeneous mixture. Finally, the electrostatic field energy decreases to almost zero until the homogeneous mixture is formed. Micro joules compared to 1.76 J of kinetic energy is neglectable and one would say, the energy of the system is conserved over the full simulation time of 21 ns.

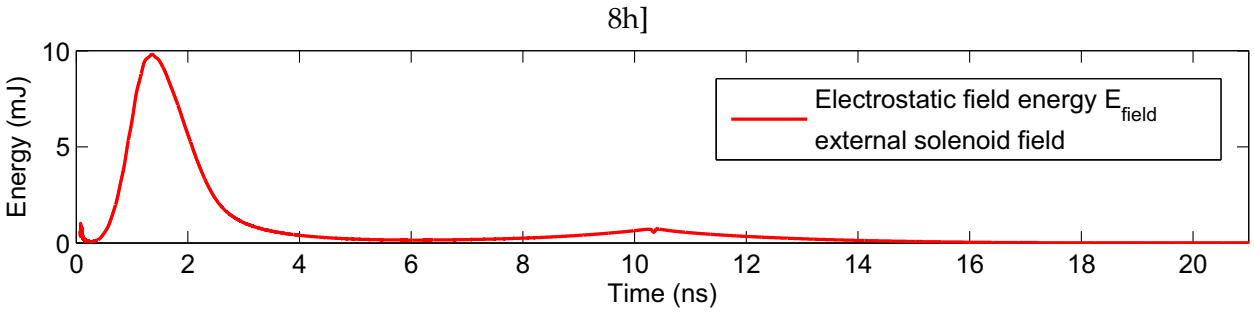

Figure 6.20: Development of the electrostatic field energy E_{field} over the time. Two bumps are evident at $t_1 = 1.34\,\text{ns}$ and $t_2 = 10.35\,\text{ns}$. The kinetic energy is constant over the full simulation periode and the overlapping bumps in the summarized energy are of a relative deviation of 5.7% and 0.6%.

The picture slightly changes if the solenoidal magnetic field is included, see figure 6.20. Now, the energy scale is in the mJ-region and two bumps are evident at $t_1 = 1.34\,\text{ns}$ and $t_2 = 10.35\,\text{ns}$. The magnetic field acts immediately on the co-moving electrons and the electrostatic potential rises. There are no electron-proton oscillations to form a homogeneous mixture, because the electrons do not occupy the same volume as the protons. The field energy grows until the proton beam starts hitting the solenoid walls at 1.34 ns. Besides the protons, also electrons are lost due to the magnetic mirror effect, particles are constantly lost and the field energy starts to decrease. Most protons are lost at $t = 2.8\,\text{ns}$. This is the point where all remaining protons are inside the solenoid. At $t = 6\,\text{ns}$, neither more protons are hitting the wall nor electrons are absorbed at $z = 0$ - the electrostatic field energy is down to almost zero, because by now the particle density is too low. The second peak at $t_2 = 10.35\,\text{ns}$ is due to the focusing effect of the solenoidal magnetic field. At this time, the bulk of the remaining protons (mostly low energy protons) runs through the focus and for a short time, the proton density increases and a space-charge potential arises. For later times, the field energy drops to zero and one can say that the energy in the system is conserved over the full simulation time. In addition, the changes of the electrostatic field energy is in the mJ-range and the kinetic energy is three orders of magnitude higher. The same effect can be observed by using finer simulation grid. The peaks are a little bit lower, but finally, the field energy disappears.

6.8 Collimation, Transport and Focusing of Protons

The main challenge behind the experiment and the simulations with laser-accelerated proton beams in combination with a solenoidal magnetic field is the study of the potential for collimation, transport and focusing of high-current proton beams. Is it possible to get rid of the initial high divergence and still have enough particles left for potential applications, is this particle source compatible to conventional proton sources, or is there a chance to retain the initial high beam quality (high current, low emittance) and in addition, minimize the accelerator dimensions and the costs ? For sure, some provocative and challenging questions, but all these points are already part of the daily research in laboratories all over the world and will be pushed forward in the next years. It is still a long way to go and before future applications are discussed, the basic principles should be studied.

The first element in a row of ion optics is the collimation device to compensate the initial beam divergence. Possible devices for this kind of expanding beams have to have axially symmetrical, longitudinal magnetic fields, such as solenoids, pole shoe lenses, quadrupoles or the magnetic horn [217]. Due to requirements such as large aperture, high magnetic field strength and compact size, the choise fell on a pulsed solenoid with a maximum field strength of 7.5 T. The behaviour of protons with different energies can be seen in figure 6.18, where three types of trajectories can be compared:

Divergent trajectory: The proton with the energy 17 MeV (—) still has a trajectory of a divergent particle, see figure 6.18(a). In the initial expansion, the proton follows a straight line in radial direction (figure 6.18(b)) until it gains azimuthal velocity v_θ in the fringe field. The protons starts to move on an orbit with almost constant radius. It is not perfect constant, because the magnetic field component responsible for the gyroradius r_g is not constant. Close before the trajectory is parallel to the solenoid inner circumference ($v_r = 0$), the fringe field at the exit of the solenoid compensates v_θ. At this point, he magnetic field is too weak to have still influence on the propagation direction of the proton, and the particle follows the trajectory along its velocity vector. Due to a radial velocity $v_r > 0$, the proton follows a straight line in radial direction (figure 6.18(b)) until it hits the detector.

Collimated trajectory: If the proton is collimated ($v_r = 0$), for example almost the proton with the energy 15 MeV, the trajectory in the x-y-plane (—) has an abrupt ending, because the coordinates of a collimated protons in the x-y-plane are constant.

Focused trajectory: By decreasing the particle energy, the focusing effect can be observed, for example at a proton energy of 5 MeV (—). Due to the focusing force, the direction of the radial velocity v_r is flipped and the proton pass the focal spot in figure 6.18(b) at $x = y = 0$. At this point, the particle is already on a straight trajectory, because the magnetic finge field behind the solenoid is too weak. Behind the focus, the remaining radial velocity forces the particle on a divergent trajectory. The proton is over-focused.

The following analysis deals with the solenoid setup used during the experimental campaign at the PHELIX laser system. The relative positions of the target, the coil and the detector were fixed, no field strength and distance scans were carried out to optimize the outcome.

Collimation and focusing:

Figure 6.21 shows the energy range for which protons can be collimated ($v_r = 0$) with this device. The color scale goes from 13 MeV (—) to 14 MeV (—). The number of trajectories for larger divergence angles or radii increases, because initially the particles are uniformly distributed over a circular area and the particle number per circular ring increases. More than 20 cm behind the solenoid, all trajectories are parallel. Compared with the experiment, one would expect for collimated protons a spot diameter in the detector of the size of the aperture of the solenoid $d_{\text{inner}} = 48$ mm. This is around layer 4 with a proton energy of 11.7 MeV. But for the collimated particles with an energy around 14 MeV, the proton signal in layer 5 has a diameter of 53 mm, 10% deviation of the solenoid aperture.

By switching to the beam edge radius illustration 6.22, it is possible to estimate an optimized energy interval for the collimated protons. The beam edge radius R_{edge} can be calculated for an energy interval of 50 keV by

$$R_{edge} = 2 \cdot \sqrt{\langle r^2 \rangle} = 2 \cdot \sqrt{\langle x^2 \rangle + \langle y^2 \rangle} \tag{6.30}$$

with the average values of the proton radius r or the coordinates x and y [218]. At the energy 13.5 MeV, the edge radius is at a constant value of 2.28 cm after the beam exits the solenoid at 27.5 cm. All particles with different energies are still converging or diverging.

Equation (2.27) allows to double-check the focal length of the solenoid. Therefore, the inverted calculation is done by using the collimated beam at the exit of the lense and estimate the position of the source in front of the device. The velocity v_z can easy be calculated by the proton energy of 13.5 MeV, but the magnetic field B_z needs to re-calculate, because it has to be an ideal field without fringe fields. The

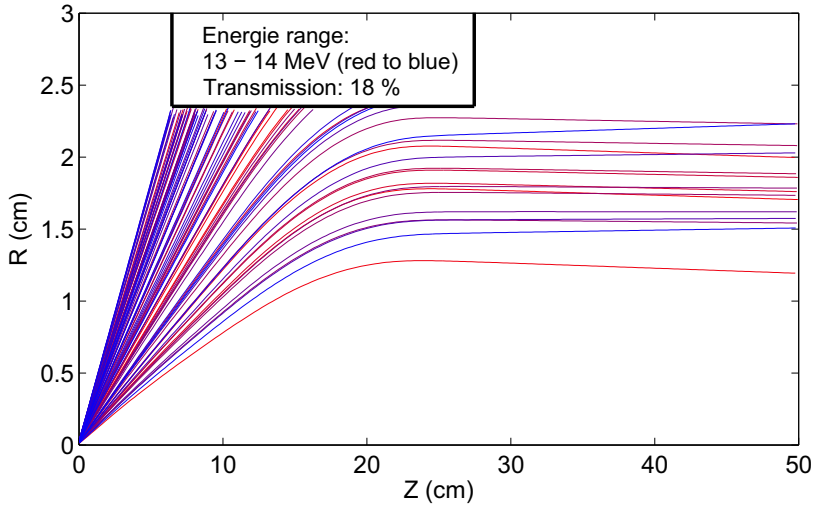

Figure 6.21: Collimation of protons in the energy range (13-14) MeV. The colorscale goes from 13 MeV (—) to 14 MeV (—). Only 18% of all protons in this energy range can pass the solenoid. Different axis scale.

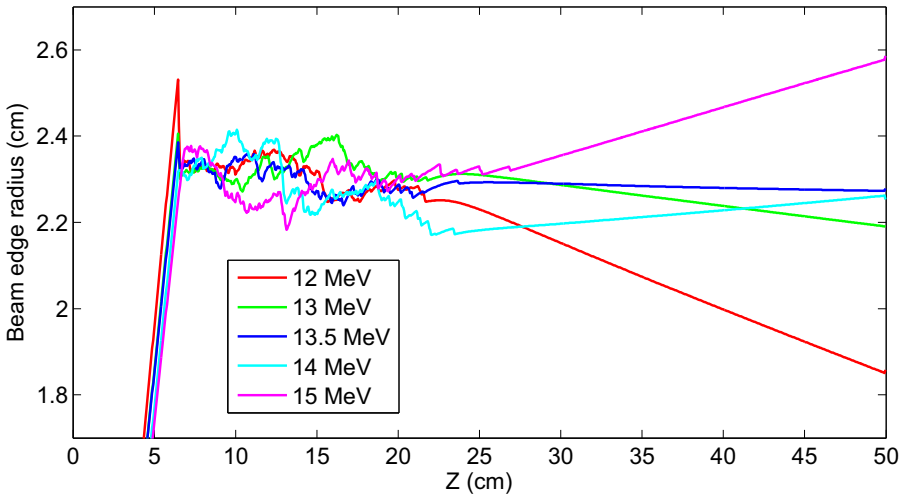

Figure 6.22: Proton beam edge radius for energies around the collimated energy. For an energy of 13.5 MeV the edge radius is constant behind the solenoid, so the beam is collimated. Different axis scale.

deflection, which causes by any magnetic field, is directly proportional to the integral of $B \cdot ds$. Instead of the real field, an associated magnetic field without fringe fields but the same value can be used:

$$\int B \cdot \mathrm{d}s = B_0 \cdot s_0 \tag{6.31}$$

where s_0 is the length of the solenoid of 150 mm. By integrating over the longitudinal magnetic field along the symmetry axis in figure 6.5, one obtains B_0 = 7.85 T instead of the initial varying field with its maximum at 7.5 T. This value is inserted in equation (2.27) and the focal length of the solenoid is estimated to 12.2 cm. The center of the coil during the experiment was positioned 17 cm away from the source. Hence, a difference of ∼5 cm was observed. Inhomogeneities in the magnetic field strength of 1 T would lead to the correct focal length of the lense. However, equation (2.27) is for the ideal case which obviously can not be assumed for this purpose.

For the focusing case in figure 6.23, protons in the energy range (6.6-6.8) MeV are focused into a spot of 1 mm at the z-position where the detector is placed. The blue trajectories refering to the upper end

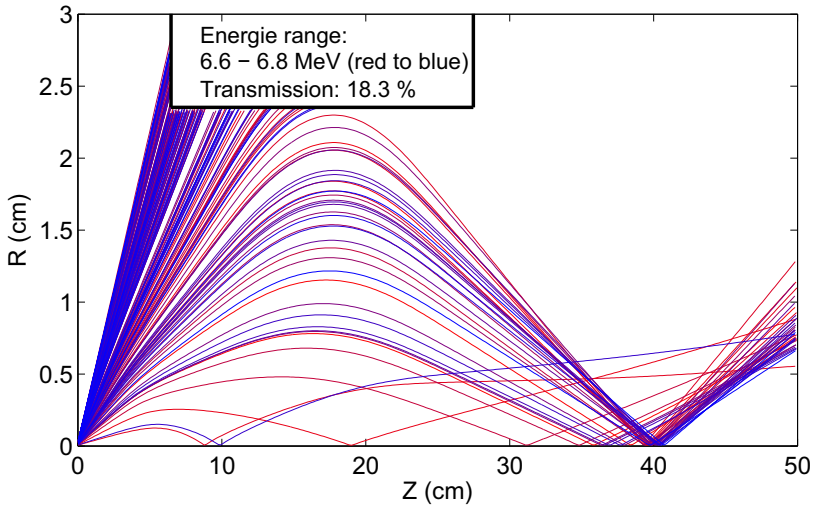

Figure 6.23: Focusing of protons in the energy range (6.6-6.8) MeV. The colorscale goes from 6.6 MeV (—) to 6.8 MeV (—). Only 18.3% of all protons in this energy range can pass the solenoid. Different axis scale.

of the energy interval are ending a little bit behind z = 40 cm, and the low energy part just in front of it. However, one can not identify one single focal point, because several trajectories for different proton energies cross the beam axis centimeters in front of the detector position. For particles crossing at very early z-positions, this effect can be explained by the proton attraction due to the electrons and for particles close to the detector position, spherical and chromatic aberrations of the solenoid are the reasons, illustrated in figure 6.24.

Spherical and chromatic aberrations:

Spherical and chromatic aberrations are distortion effects observed in an optical devices. The solenoidal field used as a focusing lens acts comparably. All trajectories of one color in figure 6.24 belong to one particle energy. The difference is the injection angles: 10°, 8°, 6°, 4°and 2°. The larger the divergence of a proton is the more deflection it gets. The 3 MeV proton (—) with 10°angle has its focal point at z_1 = 24.3 cm, the proton with the same energy but with an angle of 2°is in focus at z_2 = 25.4 cm. This spread increases for increasing proton energies. For particles with an energy of 7 MeV, the spread is already 3 cm, even though the proton with the highes divergence angle can not pass the solenoid and actually causes a decrease of the spread. This spread in z-direction can be converted in a best focus with a diameter of 1.5 mm at z = 43 cm. Hence, spherical abberations limits the focal spot diameter for one particle energy.

The idea of confining all particles of the energy distribution in one focal spot requires an ion optic with an energy independent focus position. But chromatic abberrations in the solenoid prohibits that. Protons with different energies but the same divergence angle are focused on totally different z-positions, shown in figure 6.24. The inhomogeneity of the solenoid according to focusing is the adversary in the optimization process.

Particle losses:

The maximization of the number of particles passing the solenoid is an approach to minimize secondary effects such as abberations. To optimize the transmission, one has to find the best combination of distance source-solenoid and magnetic field strength. In the case of the experiment, both parameters were fixed. For the used setup, the solenoid transmission is shown in figure 6.25. The high energy cut-off

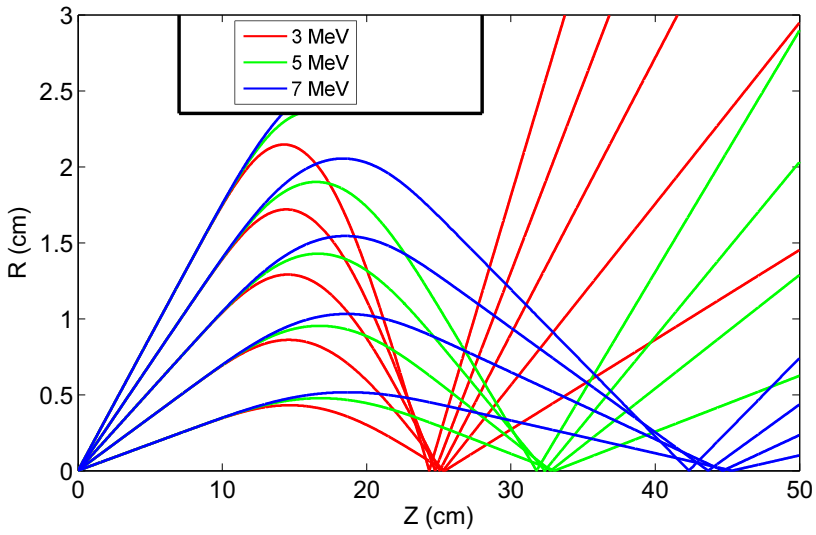

Figure 6.24: Spherical and chromatic aberrations in a solenoidal lense. Spherical aberration is an effect observed, that occurs due to the increased deflection of particles, when they strike the lens near its edge, in comparison with those that strike nearer the center. If different particle energies are focused at a different distance from the lens, then it is defined as chromatic aberrations.

for the initial (—) and the final (—) spectrum are equal, but the minimum energy behind the solenoid is shifted to a lower value. Due to the electron behaviour and the space charge forces, some of the low energy protons are slowed down. This effect can not be seen for higher energies. By calculating a transmission of an energy interval, one has to consider this inaccuracy. The overall proton loss at the solenoid due to particle impact on the front side and on the shielding tube inside is 74.8%. For the studied energy intervals for collimation and focusing, the transmissions are 18% and 18.3% resulting in particle numbers of 2.99×10^9 (ΔE = 1 MeV) and 8.42×10^9 (ΔE = 200 keV). With this design, only protons with a divergence angle <7.8°can pass the solenoid and are collimated, and protons with a divergence angle <10.3°are not hitting the solenoid and can be focused. The initial divergence angles are 20°and 23°, and therefore it is obvious why the transmission is so low.

6.9 Summary

In the frame of this work, laser-accelerated proton beams as a new particle source could successfully be implemented in the WarpRZ simulation suite. For the first time, a compact code enables simulations including all energy-dependent proton beam parameters and the co-moving electrons as second particle species. As the results point out, the beam currents are considerably high, so that space-charge effects can not be neglected. The simulation box is exactly adapted to the experiment described before. The same distances, field strengths and particle parameters are included. The consistency of experimental findings and simulation results is surprisingly good. Collimated and focused energy intervals of (13.5±1) MeV and (6.7±0.2) MeV were found including 2.99×10^9 and 8.42×10^9 protons. The transmission through the solenoid for both cases was about 18%. The influence of the of the space charge effects were investigated in detail, and it was shown, that the electron behaviour in the solenoidal magnetic field extensively influenced the proton transmission through the sytem. The observed structure in the RCF stack for the low energies could nicely be reproduced by the simulation. For higher energies, where the particle number decreases (absorption at the solenoid housing), the particle density seams to be low enough, that space charge effects can be neglected and the simulation without self fields may fit

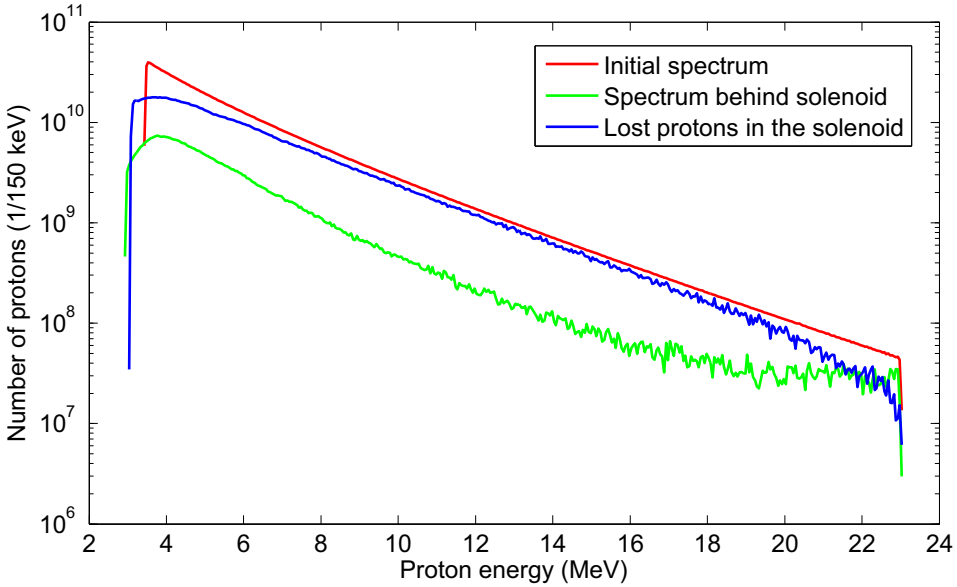

Figure 6.25: Proton transmission through the solenoid. Three different spectra are compared: (—) the initial proton spectrum at $t = 0$, (—) the spectrum behind the solenoid and (—) the protons hitting the solenoid and are lost.

better. The written Warp input script and its flexibility enables systematic parameter studies to improve the operation and to optimize the particle output.

7 Conclusion

The present scientific thesis focus on proton acceleration from the rear side of high intensity laser irradiated foils. The work was carried out at the laser and plasma physics group of the institute for nuclear physics at the Techniche Universität Darmstadt in collaboration with the plasma physics group of the GSI Helmholtzzentrum für Schwerionenforschung in Darmstadt. In the frame of this thesis, experiments were carried out to optically manipulate the acceleration mechanism to increase the conversion efficiency of laser light to protons and hence the proton flux in an energy range relevant for various applications. For additional advancement concerning future applications, a capture and transport device especially for laser-accelerated proton beams was developed, successfully tested and numerically modeled. The experimental and theoretical investigations improved the understanding of the beam optimization process for further implementation, starting from the source manipulation and concluding with an external field to control the beam with respect to beam quality conservation.

Experiments carried out at the VULCAN Petawatt laser aimed for two different techniques to develop a required dynamic control of laser-accelerated proton pulses for future high repetition rate systems. A controlled and characterised pre-plasma at the target front surface has significant influence on the proton acceleration from the rear surface. An optimum pre-plasma expansion condition could be found for coupling laser energy to protons. Notable improvements in the uniformity and circularity of the beam over the full proton energy range are also observed in the spatial intensity profile, for all cases in which a preplasma expansion is produced. The results highlight that properties of the proton beam can be actively manipulated by optical control of the plasma expansion. In addition, defocusing of high-intense laser pulses onto the front side of the target shows also significant improvements in proton flux. The experiment demonstrated that laser driven proton beams are suitable for Fast Ignition and heating applications and can be generated more efficiently than previously by driving thinner target foils at a lower intensity over a large area. Laser to proton beam efficiencies of 7.8% have been achieved, which is one of the highest conversion efficiencies ever achieved for a laser of this size. This technique of defocusing is scalable and should be suitable for future higher energy systems and Fast Ignition investigations.

In the scope of this thesis, the project of capture and control of laser-accelerated proton beams as a new particle source for applications could be promoted and studied in detail, experimentally as well as numerically. The performed experiment at the PHELIX system was a great improvement to the previous observations done by different groups worldwide. A particular part of a proton beam with an average energy of 13.5 MeV and an energy spread of 7% could be collimated and transported over a distance of 40 cm. This pulse contains $>10^9$ protons and is in the order of magnitude compared to conventional injectors [203]. Therefore, high-power lasers are a promising alternative as a new compact proton source. In addition, it was possible to focus $>10^9$ protons with an average energy of 6.7 MeV and an energy spread of 3% to a spot of <2 mm in diameter. The measured flux increase is about a factor of 174. This surface density in a distance of 40 cm from the source opens new opportunities in the field of basic research and heating application. Same conditions like at big accelerator facilities can be generated in laser laboratories. During two experiments at the TRIDENT laser facility, the feasibility of laser-accelerated proton beams as a tool for heating and warm dense matter studies could clearly be pointed out.

During all experiments presented in this thesis, the developed *Radiochromic Film Imaging Spectroscopy* as an experimental method to fully reconstruct laser-accelerated proton beam parameters energy-dependent was successfully used. The straightforward handling and the easy analysis make this

detector to a valuable diagnostic in experiments on laser-proton acceleration. The optimized low-energy electron spectrometer allows systematic studies on the electron distribution and improves the understanding of the underlying mechanisms of the electron and proton beam expansion.

However, further optimization and development are almost impossible without numerical support. The Warp simulation suite as a benchmarked code allows flexible and detailed multi-dimensional modeling of high current beams for a wide range of accelerator systems. The present work implemented laser-accelerated proton beams as a new particle source in the code. Warp is capable to include all beam parameters energy-dependent and, in addition, electrons as a second particle species. By solving Poisson's equation, space charge effects are considered each timestep. Hence, the current solenoid experiment could be modeled and the results are in very good agreement with the experimental observations. The simple handling and the flexibility of the input script enables systematic parameter studies to improve the output even more.

8 Future Perspectives

The following sections focus on the direction for future work. Section 8.1 describes the possible potential of laser experiments on proton acceleration. In addition, a new solenoid design is presented and futher experiments to capture and control laser-accelerated proton beams are described. Section 8.2 deals with development on the simulation side. New diagnostics, different source parameters and totally different setups are discussed. Finally, the overall project of a *test stand* at the GSI Helmholtzzentrum für Schwerionenforschung is presented in section 8.3. A high-energy, high-intensity laser available at an experimental area of an accelerator facility offers a possible testbed to study further injection into a conventional accelerator.

8.1 Experiments and Applications

The transport of laser-accelerated electrons through the target is still largely unclear and currently an active field of research. Published scaling laws for protons with respect to the laser parameters [71, 72, 83] are still incomplete. All these unknowns leave room for many different future experiments and simulations in order to gain a better understanding of the acceleration process. Since the laser development is not sleeping, new technics are already tested and capable of higher intensities. For example, the VULCAN 10 petawatt (PW) project will upgrade the VULCAN laser to beyond the 10 PW power level and provide focused intensities of greater than 10^{23} W/cm^2 [5]. This will be achieved by generating pulses with energies of 300 J and durations of less than 30 fs using the Optical Parametric Chirped Pulse Amplification (OPCPA) technique [219]. If the measured laser intensity scaling of maximum proton energy [83] is extrapolated to higher intensities, the generation of GeV protons are expected close to 10^{24} W/cm^2. At these intensities, the described experiments in chapter 4 would not only boost the maximum proton energy, but the proton flux could be increased significantly. In addition, new acceleration regimes, such as the radiation pressure acceleration, replace the TNSA mechanism.

Laser-accelerated proton beams have a number of unique features. The pulse duration is at least three orders of magnitude shorter than in conventional accelerators. Therefore, the currents are many orders of magnitude higher. Especially the initial, inherent beam emittance as a characteristic for the beam quality is a clear advantage compared to conventional accelerators. But before using this unique proton source as an injector or first accelerator stage, one needs not only an ion optical device which matches the beam to an accelerator without loosing the quality. Higher repetition rates are required to compete against well-developed ion sources. One promising candidate is the PW-laser POLARIS which is currently under development [220]. It is an all diode-pumped, ultrahigh peak power laser and will be operated at repetition rates of 0.03 or 0.1 Hz compared to 0.0003-0.0009 Hz of present laser systems (one shot every 20 to 60 min).

Parallel to the ongoing laser development, there is much room for improvement with respect to the solenoid experiment. The campaign showed a perfect reproducibility of the results, however, it was not possible to fully understand and investigate the coil characteristics. Due to sparkovers of the pulsed coil inside the vacuum chamber only four shots were available. Running a pulsed device with several kV in a grounded vacuum chamber is itself an already long-studied field of research. In collaboration with the Forschungszentrum Dresden-Rossendorf, a new solenoid design is in the planning phase. The expertise of the high field laboratory, the accelerator knowledge available at the GSI Helmholtzzentrum für Schwerionenforschung and the experimental experience of our group concerning laser-proton

acceleration make it possible to develop a promissing new solenoid design for the next experimental campaign at the PHELIX system in 2011. By varying the distance between the source and the solenoid as well as scanning different field strengths, the optimum parameter set can be found to maximize the transmission for a particular energy range.

As soon as the new device is successfully tested, it can be used as an energy selector in combination with a second coil. The first solenoid catches and focuses a particular energy interval to a point which is also the focal plane for the second solenoid. At the position of the smallest beam diameter a pinhole is placed, so that only focused particles can pass. The second solenoid collimates the over-focused beam and enables a divergence-free transport to the beam diagnostic or to the post-acceleration unit.

Laser-accelerated proton beams are already used for a wide range of applications (see section 2.3). The recent development in laser-proton acceleration has create new perspectives for using this concept as the basis for a new type of compact ion accelerator with possible application to therapy. Carried out studies already show that laser-accelerated proton bunches could match the requirements for synchrotron injection [130, 221]. But in the last years, high-intensity lasers have been suggested as a potential cost-saving alternative to cyclotrons or synchrotrons for oncology. Several theoretical studies were already carried out [30, 31, 42, 120, 121, 130, 222–225]. However, challenges have to be fixed before implementation. Unfortunately, the proton pulses generated by lasers are far from monochromatic. The shot-to-shot tunability, reproducibility (repetition rate of at least 10 Hz), and predictability must be improved to a level of a few percent. Finally, operating at high repetion rates requires a sophisticated target-handling. One has to ensure clearing of debris from previous shots and provide the micrometer precision in target positioning. The possibility of guiding laser beams with mirrors to a target that can be rotated around a patient is truly attractive. But one has to consider secondary radiation such as hard-x-ray bremsstrahlung and neutrons [18, 19]. Hence, shielding will be another engineering issue that needs to be addressed. The developments necessary for laser-accelerated protons as a tool for tumor treatment will possibly occur, but not in the next few years.

8.2 Warp Simulation Optimization

This work makes it possible to model and study the setup and its consequences on the capture and transport of laser-accelerated proton beams prior to future experiments (e.g. the energy selection case with two solenoids described in the section before). Found improvements may therefore be immediately implemented into the experiment. Since accelerator physicists have concerns about the possible emittance growth and the worsening of the beam quality respectively, Warp enables temporal parameter studies energy as well as spatially resolved.

Besides a caption device to compensate the unwanted beam divergence, a debunching unit is planned to compress an energy interval resulting in a smaller spread $\Delta E/\mathrm{E}$ and a higher particle number, see for example refs. [49, 131, 202]. Warp allows implementing almost all accelerator components. A similar work is currently done in connection with the NDCX-II project at the Lawrence Berkeley National Laboratory, where an ion beam is compressed with several different electric fields to be finally focused onto a target for warm dense matter studies. Hence, the capability of simulating compression with Warp is already demonstrated [226]. In addition, studies on different ion optics can be carried out to improve the overall transmission but still preserve the beam quality.

Due to the significant influence of the accompanying electrons, the experiments on electron stripping carried out by Cowan *et al.* [24] and Schollmeier *et al.* [46] can be verified. Both have used dipole fields to deflect the electrons out of the proton beam and compared the measured proton beam profiles. They never measured the removed electron spectrum, because this energy range is not easy to access. The

developed low-energy electron spectrometer (see section 3.4) and the supporting Warp simulations can bring light into the dark.

Recent discussions with theorists and results of measured electron energy distributions may lead to a different description of the proton and electron expansion. Since the low-energy electron parameters were not measured in the past, a quasi neutral expansion with co-moving electrons was assumed supported by simulations [90]. The experimentally observed electron spectra are apparently not of the expected shape. The spectrum is not coupled to the proton spectrum and it has a well defined peak at a higher velocity (energy respectively). Due to the ongoing analysis, the current data is still under evaluation [170], and the measurements have to be redone at a different laser system to confirm these observations. However, some publications present a possible model of adiabatic electron cooling [176, 177]. Warp enables an easy implementation of different source parameters to critically examine new possible models of beam expansion.

Finally, Warp is capable of perfoming calculations on multiple CPUs. In the time frame of this work, the switch from one CPU to multi-CPU Warp calculations was not possible, but it is already in planning. Since two years, the plasma physics group at GSI has access to an own computing cluster capable for massively parallel running computations. Three machines are equipped with four dual-core AMD Opteron CPUs with 2 GHz clock rate and 32 GB RAM, resulting in 4 GB per CPU. Minor parts of the Warp code have to be adapted to parallel computing and a significant time-saving can be achieved.

8.3 Test Stand for Capture and Control of Laser-Accelerated Proton Beams

All experimental and numerical efforts presented in this thesis are subordinated to a larger project. The challenges of producing a controllable compact laser-proton source delivering short bursts of high energy protons at high repetition rates and with controlled energy and angular distributions, which can be injected in a conventional post-accelerator, are specified in a joint project proposal. The experimental project describes the use of protons (ions) accelerated by the PHELIX laser at the GSI for transport, focusing and bunch rotation by conventional ion optics and RF technology in a *test stand* located at the Z6 experimental area of GSI. It combines in a unique and highly efficient way the capabilities of PHELIX as a world-class high power laser with the accelerator know-how available at GSI; the target and plasma physics expertise at TU Darmstadt; the expertise in lasers of the Helmholtz Institute Jena; the high field magnet technology at the FZ Dresden-Rossendorf; the accelerator expertise of the IAP Frankfurt. The experimental part of the project is centered at GSI, which is a unique facility, combining a heavy ion accelerator with a laser system of the Petawatt-class.

Figure 8.1 shows an overview of the experimental area Z6, as well as the transfer line from the GSI UNILAC (UNIversal Linear ACcelerator) to the heavy ion synchotron SIS 18. This area has been used for combined PHELIX long pulse and ion beam experiments since 2007 which means that only minor efforts need to be made in terms of laser and radiation safety as well as the clean room environment necessary for the laser. The project described here will use a sub-aperture beam of the PHELIX long pulse beamline which will be recompressed by a newly installed vacuum compressor. The compressed laser pulse will be guided under vacuum to the existing target chamber which is already equipped with several plasma diagnostics. Expected laser parametersare : beam diameter 12 cm, wavelength 1053 nm, pulse duration 500 fs, pulse energy 50 J, repetition rate 1 shot every 50 min, and intensity in the focal spot 10^{19} W/cm^2. The solenoid tested during this work will be included as a modified version to capture the proton beam followed by a debunching unit (made available by GSI). The illustrated ion beam line already exists with all the additional transport optics and diagnostics.

The 100 TW beam line of PHELIX is currently under construction, and the first light in the target chamber is expected early 2011. The year 2011 is assigned to commissioning experiments including solenoid

tests und bunch rotation. The estimated time of completion of the *test stand* is in 2012. As an additional project phase, a possible post-acceleration structure is planned, which allows acceleration from 11.7 to 24.3 MeV.

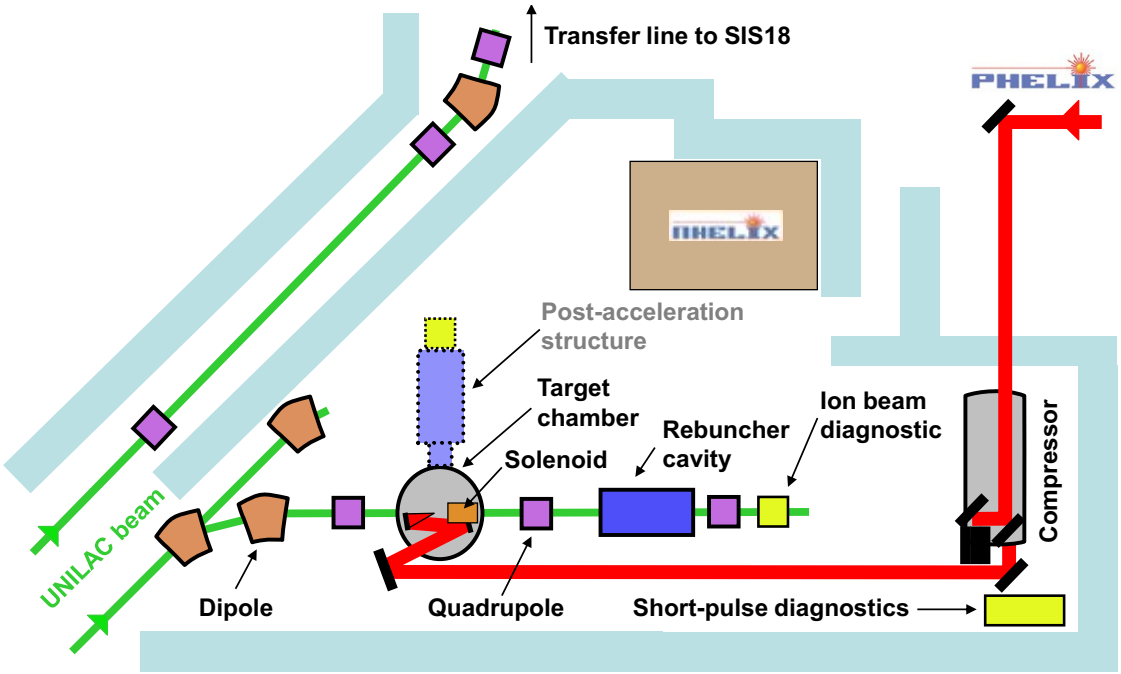

Figure 8.1: Overview of the experimental area Z6 at the GSI Helmholtzzentrum für Schwerionenforschung. The ion beamline colored in green comes from the right. On the other hand, the PHELIX laser in red enters the area from the right, passing a compressor, and after a transport section, the pulses are focused into the target chamber. The laser-accelerated proton beams can expand along the existing beamline and are formed by the solenoid and the debunching device. For a possible future post-acceleration, a cross-bar H-type (CH) multigap drift tube cavity is provided. Courtesy of B. Zielbauer.

Appendix: Experimental Campaigns and Theoretical Support

The author has participated in five experimental campaigns at three different lasers systems. The high-energy lasers used within the scope of this work are fairly large facilities and their operation is very much like a large scale accelerator. That means that each research group has to apply for a limited amount of beamtime. Often several experiments are carried out simultaneously. The average beamtime duration is between four and six weeks including assembling, accomplishment and dismounting. Usually, the real time left for the experiment is about two to three weeks. If a high-energy laser is working under normal operation, the system limited repetition rate for full energy laser shots is about one shot per hour resulting in approximately eight shots per day. An organized planning and conducting of the experiments is therefore necessary to minimize the fail shots.

Two experimental campaigns have taken place at the VULCAN Petawatt system [3] at the Central Laser Facility, STFC Rutherford Appleton Laboratory (RAL), Didcot, UK.
The first experiment in August 2007 (four weeks) was carried out to study the effects of controlled and characterised pre-plasma at the target front surface on proton acceleration from the rear surface. The group of experimenters consisted of P. McKenna and D.C. Carroll (University of Strathclyde, Glasgow), O. Lundh (Lund University), K. Markey and S. Kar (Queens University, Belfast), R. Redaelli and R. Jafa (Università degli Studi di Milano), S. Bandyopadhyay (RAL) and the author. During this campaign, the role of the author was to run and digitize the proton diagnostic in form of *Thomson* parabolas and radiochromic film stacks. In addition, he analysed the experimental data in connection with micro-structured target foils. The results have been published in refs. [34, 178] .
The topics of one campaign in december 2007 (six weeks) were Fast Ignition relevant studies on proton flux improvement by defocusing the high-intense laser pulse onto the target. In addition, spectral modifications were investigated by using multi-pulses with $\sim$ps separation and different intensity ratio. The group of experimenters consisted of D. Neely, K. Lancaster, A.P.L. Robinson, and S. Bandyopadhyay (RAL), K. Harres, M. Günther, and M. Roth (Technische Universität Darmstadt), P. McKenna and D.C. Carroll, M.N. Quinn (University of Strathclyde, Glasgow), K. Markey, S. Kar and M. Zepf (Queens University, Belfast), and the author. The author took a leading role in the planning, assembling and running of the experiment. He analyzed all data of the defocussing part and is currently preparing a publication. Additional results are published in ref. [164].

Another two campaigns have been carried out at the TRIDENT laser facility [132] at Los Alamos National Laboratories (LANL), Los Alamos, New Mexico, USA. Both experiments (each four weeks) focused on the application of laser-accelerated proton beams as a tool to create isochorically heated matter in extreme conditions. Fundamental questions about target configuration and shielding optimization should be investigated. The groups consisted of M. Roth, A. Otten, K. Harres, G. Hoffmeister, D. Kraus, G. Schaumann and A. Pelka (Technische Universität Darmstadt), K.A. Flippo, D.C. Gautier, S.A. Gaillard, and D. Offermann (LANL), N. Kugland, and D. Schaeffer (UC Los Angeles, CA, USA), T. Bartal, C. Jarrot and D. Mariscal (UC San Diego, CA, USA), C.R.D. Brown (Imperial College London, UK), and the author. In the first experiment, the author was responsible for the assembling and accomplishment. Furthermore, the author took a lead role in the planning, assembling the second experiment. First results are published in ref. [112].

In 2009/2010, the author has participated in an experimental campaign at the PHELIX system [6] about a study on target optimization for divergence reduction of laser-accelerated proton beam. The second half of this experiment focused on the capture and transport of laser-accelerated proton beams by a solenoidal magnetic field. The experiment was carried out by K. Harres, O. Deppert, S. Busold,

G. Hoffmeister, M. Günther, and M. Roth (Technische Universität Darmstadt), T. Burris and T.E. Cowan (Forschungszentrum Dresden-Rossendorf), and the author. He assisted the assembling of the experiment and analysed the relevant data to compare the results with the performed simulations.

The simulations were carried out with the WarpRZ simulation suite [209] in collaboration with D.P. Grote, A. Friedman, and B.G. Logan of the Heavy-Ion Fusion Science Virtual National Laboratory [212] (Lawrence Berkeley National Laboratory / Lawrence Livermore National Laboratory). In 2008/2009, the author spent one year at the Berkeley Labs to use and advance the code. He adapted the code to the new parameter regime of the laser-accelerated proton source and included several new diagnostics. From now on, it is possible to exactly simulate the behaviour of a laser-accelerated proton beams with large particle numbers in a collimating or focusing device including non-negligible space-charge effects.

Bibliography

[1] T.H. Maiman. *Stimulated optical radiation in ruby*. Nature **187**, 493 (1960).

[2] D. Strickland et al. *Compression of amplified chirped optical pulses*. Opt. Commun. **56**, 219 (1985).

[3] C.N. Danson et al. *Vulcan Petawatt – an ultra-high-intensity interaction facility*. Nucl. Fusion **44**, S239 (2004).

[4] Y. Kitagawa et al. *Prepulse-Free Petawatt Laser for a Fast Ignition*. IEEE Journal of Quantum Electronics **40**, 281 (2004).

[5] C. Hernandez-Gomez et al. *The Vulcan 10 PW OPCPA project*. Central Laser Facility Annual Report page 210 (2007).

[6] V. Bagnoud et al. *Commissioning and early experiments of the PHELIX facility*. Appl. Phys. B **DOI**, 10.1007/s00340–009–3855–7 (2009).

[7] G. Malka et al. *Experimental confirmation of ponderomotive-force electrons produced by an ultrarelativistic laser pulse on a solid target*. Phys. Rev. Lett. **77**, 75 (1996).

[8] C. Gahn et al. *Multi-MeV electron beam generation by direct laser acceleration in high-density plasma channels*. Phys. Rev. Lett. **83**, 4772 (1999).

[9] W. P. Leemans et al. *GeV electron beams from a centimetre-scale accelerator*. Nature Phys. **2**, 696 (2006).

[10] M.H. Key et al. *Hot electron production and heating by hot electrons in fast ignitor research*. Phys. Plasmas **5**, 1966 (1998).

[11] C. Gahn et al. *MeV γ-ray yield from solid targets irradiated with fs-laser pulses*. Appl. Phys. Lett. **73**, 3662 (1998).

[12] G. Pretzler et al. *Neutron production by 200 mJ ultrashort laser pulses*. Phys. Rev. E **58**, 1165 (1998).

[13] L. Disdier et al. *Fast neutron emission from a high-energy ion beam produced by a high-intensity picosecond laser pulse*. Phys. Rev. Lett. **82**, 1454 (1999).

[14] R. Decoste et al. *High-Energy Ion Expansion in Laser-Plasma Interactions*. Phys. Rev. Lett. **40**, 34 (1978).

[15] G.D. Tsakiris et al. *Experimental studies of the bilateral ion blowoff from Laser-irradiated thin plastic foils*. Phys. Rev. Lett. **46**, 1202 (1981).

[16] A. Maksimchuk et al. *Forward ion acceleration in thin film driven by a high-intensity laser*. Phys. Rev. Lett. **84**, 4108 (2000).

[17] E.L. Clark et al. *Energetic heavy-ion and proton generation from ultraintense laser-plasma interactions with solids*. Phys. Rev. Lett. **85**, 1654 (2000).

[18] R.A. Snavely et al. *Intense high-energy proton beams from petawatt-laser irradiation of solids*. Phys. Rev. Lett. **85**, 2945 (2000).

[19] S.P. Hatchett et al. *Electron, photon and ion beams from relativistic interaction of Petawatt laser pulses with solid targets*. Phys. Plasmas **7**, 2076 (2000).

[20] S.C. Wilks et al. *Energetic proton generation in ultra-intense laser-solid interactions*. Phys. Plasmas **8**, 542 (2001).

[21] B.M. Hegelich et al. *MeV ion jets from short-pulse-laser interaction with thin foils*. Phys. Rev. Lett. **89**, 085002 (2002).

[22] S.J. Gitomer et al. *Fast ions and hot electrons in the laser-plasma interaction*. Phys. Fluids **29**, 2679 (1986).

[23] M. Roth et al. *The generation of high quality, intense ion beams by ultra intense laser*. Plasma Phys. Control. Fusion **44**, B99 (2002).

[24] T.E. Cowan et al. *Ultralow emittance, multi-MeV proton beams from a laser virtual-cathode plasma accelerator*. Phys. Rev. Lett. **92** (20), 204801 (2004).

[25] L. Romagnani et al. *Dynamics of electric fields driving the laser acceleration of multi-MeV protons*. Phys. Rev. Lett. **95**, 195001 (2005).

[26] K. Krushelnick et al. *Energetic proton production from relativistic laser interaction with high density plasmas*. Phys. Plasmas **7**, 5 (2000).

[27] A. Pukhov. *Three-dimensional simulations of ion acceleration from a foil irradiated by a short-pulse laser*. Phys. Rev. Lett. **86**, 3562 (2001).

[28] P.K. Patel et al. *Isochoric Heating of Solid-Density Matter with an Ultrafast Proton Beam*. Phys. Rev. Lett. **91**, 125004 (2003).

[29] M. Roth et al. *Fast ignition by intense laser-accelerated proton beams*. Phys. Rev. Lett. **86**, 436 (2001).

[30] S.V. Bulanov et al. *Feasibility of Using Laser Ion Accelerators in Proton Therapy*. Plasma Physics Reports **28**, 453 (2002).

[31] E. Fourkal et al. *Particle selection for laser-accelerated proton therapy feasibility study*. Med. Phys. **30**, 1660 (2003).

[32] J.D. Zuegel et al. *Laser challenges for fast ignition*. Fusion Sci. Technol. **49**, 453 (2006).

[33] F.N. Beg et al. *A study of picosecond laser-solid interactions up to* 10^{19} *W/cm*^{2}. Phys. Plasmas **4**, 447 (1997).

[34] P. McKenna et al. *Effects of front surface plasma expansion on proton acceleration in ultraintense laser irradiation of foil targets*. Laser Part. Beams **26**, 591 (2008).

[35] L. Yin et al. *GeV laser ion acceleration from ultrathin targets: The laser break-out afterburner*. Laser Part. Beams **24**, 291 (2006).

[36] L. Yin et al. *Monoenergetic and GeV ion acceleration from the laser breakout afterburner using ultrathin targets*. Phys. Plasmas **14**, 056706 (2007).

[37] A.J. Mackinnon et al. *Enhancement of proton acceleration by hot-electron recirculation in thin foils irradiated by ultraintense laser pulses*. Phys. Rev. Lett. **88**, 215006 (2002).

[38] M. Zepf et al. *Proton acceleration from high-intensity laser interactions with thin foil targets*. Phys. Rev. Lett. **90**, 064801 (2003).

[39] M. Zepf et al. *Fast particle generation and energy transport in laser-solid interactions*. Phys. Plasmas **8**, 2323 (2001).

[40] H. Schwoerer et al. *Laser-plasma acceleration of quasi-monoenergetic protons from microstructured targets*. Nature **439**, 445 (2006).

[41] K.A. Flippo et al. *Increased efficiency of short-pulse laser-generated proton beams from novel flat-top cone targets*. Phys. Plasmas **15**, 056709 (2008).

[42] U. Linz et al. *What will it take for laser driven proton accelerators to be applied to tumor therapy?* Phys. Rev. ST Accel. Beams **10**, 094801 (2007).

[43] B. Franczak. *Heavy Ion Synchrotron SIS18 Parameter List, GSI Helmholtzzentrum für Schwerionenforschung, Darmstadt*. http://www.gsi.de/beschleuniger/sis18/ (2010).

[44] F. Nürnberg et al. *Radiochromic film imaging spectroscopy of laser-accelerated proton beams*. Rev. Sci. Instrum. **80**, 033301 (2009).

[45] T. Toncian et al. *Ultrafast Laser-Driven Microlens to Focus and Energy-Select Mega-Electron Volt Protons*. Science **312**, 410 (2006).

[46] M. Schollmeier et al. *Controlled Transport and Focusing of Laser-Accelerated Protons with Miniature Magnetic Devices*. Phys. Rev. Lett. **101**, 55004 (2008).

[47] S. Ter-Avetisyan et al. *First demonstration of collimation and monochromatisation of a laser accelerated proton burst*. Laser Part. Beams **26**, 637 (2008).

[48] K. Harres et al. *Beam collimation and transport of quasineutral laser-accelerated protons ba a solenoid field*. Phys. Plasmas **17** (023107), 023107 (2010).

[49] M. Nishiuchi et al. *Measured and simulated transport of 1.9 MeV laser-accelerated proton bunches through an integrated test beam line at 1 Hz*. Phys. Rev. ST Accel. Beams **13**, 071304 (2010).

[50] E. Esarey et al. *Laser acceleration of electrons in vacuum*. Phys. Rev. E **52**, 5443 (1995).

[51] H. Boot und R.B.R Shersby-Harvie. *Charged Particles in a Non-uniform Radio-frequency Field*. Nature **180**, 1187 (1957).

[52] S. Wilks et al. *Absorption of ultrashort, ultra-intense laser light by solids and overdense plasmas*. IEEE Journal of Quantum Electronics **33**, 1954 (1997).

[53] D. Bauer et al. *Relativistic ponderomotive force, Uphill acceleration, and transition to chaos*. Phys. Rev. Lett. **75**, 4622 (1995).

[54] F.F. Chen. *Introduction to Plasma Physics*. Plenum Press New York (1974).

[55] P. Mulser et al. *Plasma production by laser*. Physics Reports **6**, 187 (1973).

[56] W.L. Kruer. *The Physics of Laser Plasma Interactions*. Addison Wesley (1988).

[57] E. Lefebvre et al. *Transparency/Opacity of a solid target illuminated by an ultrahigh-intensity laser pulse*. Phys. Rev. Lett. **74**, 2002 (1995).

[58] A. Pukhov et al. *Relativistic magnetic self-channeling of light in near-critical plasma: Three-dimensional particle-in-cell simulation*. Phys. Rev. Lett. **76**, 3975 (1996).

[59] M. Borghesi et al. *Relativistic channeling of a picosecond laser pulse in a near-critical preformed plasma*. Phys. Rev. Lett. **78**, 879 (1997).

[60] E. Lefebvre et al. *Nonlinear electron heating in ultrahigh-intensity-laser-plasma interaction*. Phys. Rev. E **55**, 1011 (1997).

[61] M.I. Santala et al. *Effect of the Plasma Density Scale Length on the Direction of Fast Electrons in Relativistic Laser-Solid Interactions*. Phys. Rev. Lett. **84**, 1459 (2000).

[62] K. Adumi et al. *Characterization of preplasma produced by an ultrahigh intensity laser system*. Phys. Plasmas **11**, 3721 (2004).

[63] R. Kodama et al. *Study of Laser-Hole Boring into Overdense Plasmas*. Phys. Rev. Lett. **77**, 4906 (1996).

[64] J.S. Green et al. *Effect of laser intensity on fast-electron-beam divergence in solid-density plasmas*. Phys. Rev. Lett. **100**, 015003 (2008).

[65] T. Tajima et al. *Laser electron accelerator*. Phys. Rev. Lett. **43**, 267 (1979).

[66] A. Pukhov et al. *Laser wake field acceleration: the highly non-linear broken-wave regime*. Appl. Phys. B **74** (4), 355 (2002).

[67] S.P.D. Mangles et al. *Monoenergetic beams of relativistic electrons from intense laserplasma interactions*. Nature **431**, 535 (2004).

[68] A. Pukhov et al. *Particle acceleration in relativistic laser channels*. Phys. Plasmas **6**, 2847 (1999).

[69] F. Brunel. *Not-so-resonant, resonant absorption*. Phys. Rev. Lett. **59**, 52 (1987).

[70] W.L. Kruer et al. *$j \times B$ heating by very intense laser light*. Phys. Fluids **28**, 430 (1985).

[71] J. Fuchs et al. *Laser-driven proton scaling laws and new paths towards energy increase*. Nature **2**, 48 (2006).

[72] J. Schreiber et al. *Analytical Model for Ion Acceleration by High-Intensity Laser Pulses*. Phys. Rev. Lett. **97**, 045005 (2006).

[73] A.R. Bell et al. *Fast-electron transport in high-intensity short-pulse laser-solid experiments*. Plasma Phys. Control. Fusion **39**, 653 (1997).

[74] H. Alfvén. *On the motion of cosmic rays in interstellar space*. Physical Review **55**, 425 (1939).

[75] F. Brandl et al. *Čerenkov radiation diagnostics of hot electrons generated by fs-laser interaction with solid targets*. Europhysics Letters **61**, 632 (2003).

[76] E. S. Weibel. *Spontaneously growing transverse waves in a plasma due to an anisotropic velocity distribution*. Phys. Rev. Lett. **2**, 83 (1959).

[77] Y. Sentoku et al. *Isochoric heating in heterogeneous solid targets with ultrashort laser pulses*. Phys. Plasmas **14**, 122701 (2007).

[78] Y.-S. Huang et al. *Hot-electron recirculation in ultraintense laser pulse interactions with thin foils*. Phys. Plasmas **14**, 103106 (2007).

[79] Y. Sentoku et al. *High energy proton acceleration in interaction of short laser pulse with dense plasma target*. Phys. Plasmas **10**, 2009 (2003).

[80] J. Fuchs et al. *Comparative spectra and effciencies of ions laser-accelerated forward from the front and rear surfaces of thin solid foils*. Phys. Plasmas **14**, 053105 (2007).

[81] S.A. Gaillard et al. *Nearly 70 MeV laser-accelerated-proton beams from micro-cone targets via laser grazing*. submitted to Phys. Rev. Lett. (2010).

[82] P. McKenna et al. *Characterization of proton and heavier ion acceleration in ultrahigh-intensity laser interactions with heated target foils*. Phys. Rev. E **70**, 036405 (2004).

[83] L. Robson et al. *Scaling of proton acceleration driven by petawatt-laser-plasma interactions*. Nature Physics **3**, 58 (2007).

[84] A.P.L. Robinson et al. *Radiation pressure acceleration of thin foils with circularly polarized laser pulses*. New J. Phys. **10**, 013021 (2008).

[85] T. Esirkepov et al. *Highly Efficient Relativistic-Ion Generation in the Laser-Piston Regime*. Phys. Rev. Lett. **92**, 175003 (2004).

[86] J.J. Santos et al. *Fast Electron Transport in Ultraintense Laser Pulse Interaction with Solid Targets by Rear-Side Self-Radiation Diagnostics*. Phys. Rev. Lett. **89**, 025001 (2002).

[87] R.B. Stephens et al. *K_α fluorescence measurement of relativistic electron transport in the context of fast ignition*. Phys. Rev. E **69**, 066414 (2004).

[88] K.L. Lancaster et al. *Measurements of Energy Transport Patterns in Solid Density Laser Plasma Interactions at Intensities of 5×10^{20} W/cm^2*. Phys. Rev. Lett. **98**, 125002 (2007).

[89] J.E. Crow et al. *The expansion of a plasma into a vacuum*. J. Plasma Physics **14**, 65 (1975).

[90] P. Mora. *Plasma expansion into vacuum*. Phys. Rev. Lett. **90**, 185002 (2003).

[91] M. Allen et al. *Direct experimental evidence of back-surface ion acceleration from laser-irradiated gold foils*. Phys. Rev. Lett. **93**, 265004 (2004).

[92] J. C. Vickerman. *Surface analysis – the principal techniques*. John Wiley & Sons 1997.

[93] J. J. Thomson. *Rays of positive electricity*. Philos. Mag. **21** (122), 225 (1911).

[94] K. Harres et al. *Development and calibration of a Thomson parabola with microchannel plate for the detection of laser-accelerated MeV ions*. Rev. Sci. Instrum. **79**, 093306 (2008).

[95] M. Roth et al. *Energetic ions generated by laser pulses: A detailed study on target properties*. Phys. Rev. ST Accel. Beams **5**, 061301 (2002).

[96] K.A. Flippo et al. *Ablation cleaning techniques for high-power short-pulse laser-produced heavy ion targets*. Proc. SPIE **6261**, 62612I (2006).

[97] V. T. Tikhonchuk. *Interaction of a beam of fast electrons with solids*. Phys. Plasmas **9**, 1416 (2002).

[98] S. Augst et al. *Laser ionization of noble gases by Coulomb-barrier suppression*. J. Opt. Soc. Am. B **8**, 858 (1991).

[99] S. Bulanov et al. *Concerning the maximum energy of ions accelerated at the front of a relativistic electron cloud expanding into vacuum*. Plasma Physics Reports **30**, 18 (2004).

[100] A.V. Gurevich et al. *Self-similar motion of rarefied plasma*. Sov. Phys. JETP **22**, 449 (1966).

[101] S. Betti et al. *Expansion of a finite-size plasma in vacuum*. Plasma Physics and Controlled Fusion **47**, 521 (2005).

[102] P. Mora. *Thin-foil expansion into a vacuum*. Phys. Rev. E **72**, 056401 (2005).

[103] M. Passoni et al. *Charge separation effects in solid targets and ion acceleration with a two-temperature electron distribution*. Phys. Rev. E **69**, 026411 (2004).

[104] J. Fuchs et al. *Spatial uniformity of laser-accelerated ultrahigh-current MeV electron propagation in metals and insulators*. Phys. Rev. Lett. **91**, 255002 (2003).

[105] A. Frank et al. *Energy loss of argon in a laser-generated carbon plasma*. Phys. Rev. E **81**, 026401 (2010).

[106] C.W. Mendel Jr et al. *Charge-Separation Electric Fields in Laser Plasmas*. Phys. Rev. Lett. **34**, 859 (1975).

[107] M. Borghesi et al. *Measurement of highly transient electrical charging following high-intensity laserŰ-solid interaction*. Appl. Phys. Lett. **82**, 1529 (2003).

[108] M. Borghesi et al. *Laser-produced protons and their application as a particle probe*. Laser & Part. Beams **20**, 269 (2002).

[109] A.J. Mackinnon et al. *Proton radiography as an electromagnetic field and density perturbation diagnostic*. Rev. Sci. Instrum. **75**, 3531 (2004).

[110] W. B. Hubbard et al. *Interior structure of Neptune: Comparison with Uranus*. Science **253**, 648 (1991).

[111] H. C. Connolly Jr. et al. *The Formation of Chondrules: Petrologic Tests of the Shock Wave Model*. Science **280**, 62 (1998).

[112] M. Roth et al. *Proton acceleration experiments and warm dense matter research using high power lasers*. Plasma Phys. Control. Fusion **51**, 124039 (2009).

[113] I. Spencer et al. *Laser generation of proton beams for the production of short-lived positron emitting radioisotopes*. Nucl. Instrum. Methods Phys. Res. Sect. B-Beam Interact. Mater. Atoms **183**, 449 (2001).

[114] M.I. Santala et al. *Production of radioactive nuclides by energetic proton generated from intense laser-plasma interactions*. Appl. Phys. Lett. **78**, 19 (2001).

[115] P. McKenna et al. *Demonstration of fusion-evaporation and direct-interaction nuclear reactions using high-intensity laser-plasma-accelerated ion beams*. Phys. Rev. Lett. **91**, 075006 (2003).

[116] M. Temporal et al. *Numerical study of fast ignition of ablatively imploded deuterium-tritium fusion capsules by ultra-intense proton beams*. Phys. Plasmas **9**, 3098 (2002).

[117] S. Atzeni et al. *A first analysis of fast ignition of precompressed ICF fuel by laser-accelerated protons*. Nuclear Fusion **42**, L1 (2002).

[118] D. Schulz-Ertner et al. *Results of carbon ion radiotherapy in 152 patients*. Int. J. Radiation Oncology Biol. Phys. **58**, 631 (2004).

[119] P. Heeg et al. *Die Konzeption der Heidelberger Ionentherapieanlage HICAT*. Z. Med. Phys. **14**, 17 (2004).

[120] V. Malka et al. *Practicability of protontherapy using compact laser systems*. Med. Phys. **31**, 1587 (2004).

[121] A. Noda et al. *Laser produced ions as an injector beam for cancer therapy facility*. Proceedings of LINAC 2004, Lübeck, Germany **THP74**, 782 (2004).

[122] J. Melngailis et al. *A review of ion projection lithography*. Journal of Vacuum Science & Technology B **16**, 927 (1998).

[123] J. Meijer et al. *High-energy ion projection for deep ion implantation as a low cost high throughput alternative for subsequent epitaxy processes*. Journal of Vacuum Science & Technology B **22**, 152 (2004).

[124] C. Debaes et al. *Deep proton writing: a rapid prototyping polymer micro-fabrication tool for micro-optical modules*. New Journal of Physics **8**, 270 (2006).

[125] K. Wille. *Physik der Teilchenbeschleuniger und Synchrotronstrahlungsquellen*. B.G. Teubner 1996.

[126] S. Jr. Humphries. *Principles of Charged Particle Acceleration*. John Wiley and Sons University of New Mexico, Department of Electrical and Computer Engineering, Albuquerque, New Mexico 1999.

[127] R. Wideröe. *Über ein neues Prinzip zur Herstellung hoher Spannungen*. Arch. Elektrotech. **21**, 387 (1928).

[128] P.M. Lapostolle. *Possible Emittance Increase through Filamentation Due to Space Charge in Continuous Beams*. IEEE Transactions on Nuclear Science NS-18 **18**, 1101 (1971).

[129] M. Reiser. *Theory and Design of Charged Particle Beams*. Wiley-Interscience 1994.

[130] I. Hofmann et al. *Laser accelerated ions and their potential for therapy accelerators*. Proceedings of the 11th International Conference on Heavy Ion Accelerator Technology (HIAT09) (accepted).

[131] M. Ikegami et al. *Radial focusing and energy compression of a laser-produced proton beam by a synchronous rf field*. Phys. Rev. ST Accel. Beams **12**, 063501 (2009).

[132] S.H. Batha et al. *TRIDENT high-energy-density facility experimental capabilities and diagnostics*. Rev. Sci. Instrum. **79**, 10F305 (2008).

[133] D.C. Gautier et al. *A novel backscatter focus diagnostic for the TRIDENT 200 TW laser*. Rev. Sci. Instrum. **79**, 10F547 (2008).

[134] M. Borghesi et al. *Characterization of laser plasmas for interaction studies: Progress in time-resolved density mapping*. Phys. Rev. E **54**, 6769 (1996).

[135] P. Lee. *Low-energy x-ray imaging of laser plasmas*. Optics Letters **6**, 196 (1981).

[136] Th. Kuehl et al. *Optimization of the non-normal incidence, transient pumped plasma X-ray laser for laser spectroscopy and plasma diagnostics at the facility for antiproton and ion research (FAIR)*. Laser Part. Beams **25**, 93 (2007).

[137] V. Rai et al. *High speed plasma diagnostics for laser plasma interaction and fusion studies*. Springer India 1999.

[138] H. Legall et al. *Applications of highly oriented pyrolytic graphite (HOPG) for x-ray diagnostics and spectroscopy*. Proc. SPIE **5918**, 591802 (2005).

[139] K. Nakajima et al. *Recent Results of Laser-Plasma Electron Beam Acceleration Experiments at JAERI-APRC*. 31st EPS Conference on Plasma Phys. ECA **28G**, O–1.30 (2004).

[140] S.E. Irvine et al. *Ultra-compact 180° magnetic spectrometer for intermediate energy electron measurement*. Meas. Sci. Technol. **17**, 2455 (2006).

[141] B.M. Hegelich et al. *Laser acceleration of quasi-monoenergetic MeV ion beams*. Nature **439**, 441 (2006).

[142] S.G. Gales et al. *Image plates as x-ray detectors in plasma physics experiments*. Rev. Sci. Instrum. **75**, 4001 (2004).

[143] I.J. Paterson et al. *Image plate response for conditions relevant to laserplasma interaction experiments*. Measurement Science and Techn. **19**, 095301 (2008).

[144] A. Mancic et al. *Absolute calibration of photostimulable image plate detectors used as (0.5-20 MeV) high-energy proton detectors*. Rev Sci Instrum. **79**, 073301 (2008).

[145] A. Mancic et al. *Isochoric heating of solids by laser-accelerated protons: Experimental characterization and self-consistent hydrodynamic modeling*. High Energy Density Physics **6**, 21 (2010).

[146] A. Szydlowski et al. *Application of solid-state nuclear track detectors of the CR-39/PM-355 type for measurements of energetic protons emitted from plasma produced by an ultra-intense laser*. Radiation Measurements **44**, 881 (2009).

[147] *Gafchromic dosimetry films*
International Specialty Products, 1361 Alps Road Wayne NJ 07470.
http://www.ispcorp.com/products/dosimetry/content/gafchromic. Aug. 2006.

[148] W.L. McLaughlin et al. *Radiation protection dosimetry*. Nuclear Technology Publishing **6** (Nos. 1-4), 263 (1996).

[149] D.S. Hey et al. *Use of GafChromic film to diagnose laser generated proton beams*. Rev. Sci. Instrum **79**, 053501 (2008).

[150] A. Niroomand-Rad et al. *Radiochromic film dosimetry: Recommendations of AAPM Radiation Therapy Committee Task Group 55*. Med. Phys. **25** (11), 2093 (1998).

[151] H. Alva et al. *The use of a reflective scanner to study radiochromic film response*. Phys. Med. Biol. **47**, 2925 (2002).

[152] *Grey wedge #T4110cc, Stouffer Graphic Arts, Mishawaka, IN 46544, USA; 41 steps from optical density 1 to 4*. http://www.stouffer.net (2008).

[153] *SRIM2006 - The Stopping and Range of Ions in Matter, ©1984-2006, James F. Ziegler*. http://www.srim.org. August 2006.

[154] A.Z. Jones et al. *Comparison of Indiana University Cyclotron Facility Faraday cup dosimetry with radiochromic rilms, a calorimeter, and a calibrated Ion chamber*. IEEE Transactions on Nuclear Science **46** (6), 1762 (1999).

[155] H. Ruhl et al. *The generation of micro-fiducials in laser-accelerated proton flows, their imaging property of surface structures and application for the characterization of the flow*. Phys. Plasmas **11**, L17 (2004).

[156] F. Nürnberg. *Vollständige Rekonstruktion und Transportsimulation eines laserbeschleunigten Protonenstrahls unter Verwendung von mikrostrukturierten Targetfolien und radiochromatischen Filmdetektoren*. Master's thesis Technische Universität Darmstadt 2006.

[157] S. Jr. Humphries. *Charged Particle Beams*. John Wiley and Sons University of New Mexico, Department of Electrical and Computer Engineering, Albuquerque, New Mexico 2002.

[158] F. M. Bieniosek et al. *Diagnostics for intense heavy-ion beams in the HIF-VNL*. Nucl. Instrum. Methods Phys. Res. A **544**, 268 (2005).

[159] D.C. Carroll et al. *Active manipulation of the spatial energy distribution of laser-accelerated proton beams*. Phys. Rev. E **76**, 065401 (2007).

[160] M. Borghesi et al. *Multi-MeV proton source investigations in ultraintense laser-foil interactions*. Phys. Rev. Lett. **92**, 055003 (2004).

[161] A.J. Kemp et al. *Emittance growth mechanisms for laser-accelerated proton beams*. Phys. Rev. E **75**, 056401 (2007).

[162] T. Winkelmann et al. *Electron cyclotron resonance ion source experience at the Heidelberg Ion Beam Therapy Center*. Rev. Sci. Instrum. **79**, 02A331 (2008).

[163] E. Breschi et al. *A new algorithm for spectral and spartial reconstruction of proton beams from dosimetric measurements*. NIM A **522**, 190 (2004).

[164] F. Nürnberg et al. *RCF imaging spectroscopy of laser-accelerated proton beams at Vulcan Petawatt*. Central Laser Facility Annual Report page 49 (2008).

[165] F. Nürnberg et al. *Transverse emittance of laser-accelerated proton beams*. Proceedings of the XXX ECLIM 2008 pages EC–18, p34 (2009).

[166] S. Hauf et al. *Research and Development on the Geant4 Radioactive Decay Physics*. DPG Frühjahrstagung, Bonn **EP14.1**, Astrophysics III (2010).

[167] T.E. Cowan et al. *Intense electron and proton beams from PetaWatt laser-matter interactions*. NIM A **455**, 130 (2000).

[168] M. Allen et al. *Proton spectra from ultraintense laserśplasma interaction with thin foils: Experiments, theory, and simulation*. Phys. Plasmas **10**, 3283 (2003).

[169] S. Karsch et al. *GeV-scale electron acceleration in a gas-filled capillary discharge waveguide*. New J. Phys. **9**, 415 (2007).

[170] S. Busold. *Konstruktion und Einsatz eines Magnetspektrometers zur Untersuchung des niederenergetischen Elektronenanteils [1...30keV] bei der Laser-Protonen-Beschleunigung*. Master's thesis Technische Universität Darmstadt 2010.

[171] H. Chen et al. *Absolute calibration of image plates for electrons at energy between 100 keV and 4 MeV*. Rev. Sci. Instrum. **79**, 033301 (2008).

[172] N. Izumi et al. *Application of imaging plates to x-ray imaging and spectroscopy in laser plasma experiments*. Rev. Sci. Instrum. **77**, 10E325 (2006).

[173] Z. Li et al. *Electron Energy Spectrometer for Laser-Driven Energetic Electron Generation*. Jap. J. Appl. Phys. **44**, 6796 (2005).

[174] J.D. Bonlie et al. *Production of $>10^{21}$ W/cm^2 from a large-aperture Ti:sapphire laser system*. Appl. Phys. B **70**, 155 (2000).

[175] P. Mora et al. *Self-similar expansion of a plasma into a vacuum*. Phys. Fluids **22**, 2300 (1979).

[176] T. Grismayer et al. *Influence of a finite initial ion density gradient on plasma expansion into a vacuum*. Phys. Plasmas **13**, 032103 (2006).

[177] T. Grismayer et al. *Electron kinetic effects in plasma expansion and ion acceleration*. Phys Rev E Stat Nonlin Soft Matter Phys. **77**, 066407 (2008).

[178] D.C. Carroll et al. *Dynamic control and enhancement of laser-accelerated protons using multiple laser pulses*. C. R. Physique **10**, 188 (2009).

[179] Y. Sentoku et al. *High-energy ion generation in interaction of short laser pulse with high-density plasma*. Appl. Phys. B **74**, 207 (2002).

[180] H.J. Lee et al. *Enhancement of high-energy ion generation by preplasmas in the interaction of an intense laser pulse with overdense plasmas*. Phys. Plasmas **11**, 1726 (2004).

[181] A. Yogo et al. *Laser prepulse dependency of proton-energy distributions in ultraintense laser-foil interactions with an online time-of-flight technique*. Phys. Plasmas **14**, 043104 (2007).

[182] C. Ziener et al. *Specular reflectivity of plasma mirrors as a function of intensity, pulse duration, and angle of incidence*. J. Appl. Phys. **93**, 768 (2003).

[183] B. Dromey et al. *The plasma mirror - A subpicosecond optical switch for ultrahigh power lasers*. Rev. Sci. Instrum. **75**, 645 (2004).

[184] R. Benattar et al. *Polarized light interferometer for laser fusion studies*. Rev. Sci. Instrum. **50**, 1583 (1979).

[185] Z.M. Sheng. *Anisotropic filamentation instability of intense laser beams in plasmas near the critical density*. Phys. Rev. E **64**, 066409 (2001).

[186] J.H. Nuckolls et al. *Laser Compression of Matter to Super-High Densities: Thermonuclear (CTR) Applications*. Nature **239**, 139 (1972).

[187] G.H. Miller et al. *The National Ignition Facility: enabling fusion ignition for the 21st century*. Nucl. Fusion **44**, 228 (2004).

[188] M. Tabak et al. *Ignition and high gain with ultrapowerful lasers*. Phys. Plasmas **1**, 1626 (1994).

[189] D.S. Hey et al. *Laser-accelerated proton conversion efficiency thickness scaling*. Phys. Plasmas **16**, 123108 (2009).

[190] Y. Ping et al. *Absorption of short laser pulses on solid targets in the ultrarelativistic regime*. Phys. Rev. Lett. **100**, 085004 (2008).

[191] D. Neely et al. *Enhanced proton beams from ultrathin targets driven by high contrast laser pulses*. Appl. Phys. Lett. **89**, 021502 (2006).

[192] C. Hernandez-Gomez et al. *Vulcan petawatt-operation and development*. J. Phys. IV **133**, 555 (2006).

[193] M.N. Quinn et al. *Spatial intensity mapping of Petawatt laser focus into fast electron transport*. Central Laser Facility annual report 2007/8 page 60 (2008).

[194] J.J. Santos et al. *Fast-electron transport and induced heating in aluminum foils*. Phys. Plasmas **14**, 103107 (2007).

[195] R. Ramis et al. *Indirectly driven target design for fast ignition with proton beams*. Nucl. Fusion **44**, 420 (2004).

[196] A. Tauschwitz et al. *Laser-produced proton beams as a tool for equation-of-state studies of warm dense matter*. High Energy Den. Phys. **2**, 16 (2006).

[197] SESAME83. *Report on the Los Alamos Equation-of-State Library, T4-Group*. Los Alamos National Laboratory Report No.LALP-83-4, Los Alamos (1983).

[198] A.L. Kritcher et al. *Ultrafast X-ray Thomson Scattering of Shock-Compressed Matter*. Science **322**, 69 (2008).

[199] S.H. Glenzer et al. *X-ray Thomson scattering in high energy density plasmas*. Rev. Mod. Phys. **81**, 1625 (2009).

[200] T. Bartal et al. *The Effect of Hemispherical Target Diameter on Proton Focusing*. 51st Annual Meeting of the American Physical Society Division of Plasma Physics page PO5.012 (2009).

[201] *Injector group, GSI Helmholtzzentrum für Schwerionenforschung, Darmstadt, Germany*. www-inj.gsi.de (2010).

[202] S. Nakamura et al. *High-Quality Laser-Produced Proton Beam Realized by the Application of a Synchronous RF Electric Field*. Japanese Journal of Applied Physics **46**, L717 (2007).

[203] L. Groening et al. *The 70 MeV Proton LINAC for the FAIR Facility*. Proc. Linac 06, Knoxville, August 2004 page 186 (2006).

[204] H. Kiriyama et al. *High-contrast, high-intensity laser pulse generation using a nonlinear preamplifier in a Ti:sapphire laser system*. Optics Lett. **33**, 645 (2008).

[205] *ELBE DP-Petawatt laser system FZD*. http://www.fzd.de/db/Cms?pNid=2098 (September 2010).

[206] *COMSOL Multiphysics simulation software*. http://www.comsol.de/ (September 2010).

[207] *CASINO - Monte carlo simulation of electron trajectories in solids, ©2000, Dominique Drouin*. http://www.gel.usherbrooke.ca/casino/index.html. June 2010.

[208] P. Antici et al. *Numerical study of a linear accelerator using laser-generated proton beams as a source*. J. Appl. Phys. **104**, 124901 (2008).

[209] *Warp online manual*. http://hifweb.lbl.gov/Warp (2010).

[210] D. Clery. *ITERs $12 Billion Gamble*. Science **314**, 238 (2006).

[211] A.W. Maschke. *Initiation of thermonuclear detonations*. Technical Report BNL 19008, Brookhaven National Laboratory 1974.

[212] *Heavy-Ion Fusion Science Virtual National Laboratory*. http://hif.lbl.gov/ (2010).

[213] C.K. Birdsall und A.B. Langdon. *Plasma Physics via Computer Simulations*. Institut of Physics, Series in Plasma Physics, Taylor and Francis Group, New York 2005.

[214] A. Friedman et al. *Numerically Induced Stochasticity*. J. Comput. Phys. **93**, 189 (1991).

[215] William H. Press et al. *Numerical Recipes 3rd Edition: The Art of Scientific Computing*. Cambridge University Press 2007.

[216] L. Devroye. *Non-Uniform Random Variate Generation*. Springer-Verlag 1986.

[217] M. von Ardenne et al. *Effekte der Physik und ihre Anwendungen*. Verlag Harri Deutsch 3 edition 2005.

[218] S.M. Lund et al. *Simulations of beam emittance growth from the collective relaxation of space-charge nonuniformities*. NIM A **544**, 472 (2005).

[219] I.N. Ross et al. *The prospects for ultrashort pulse duration and ultrahigh intensity using optical parametric chirped pulse amplifiers*. Opt. Commun. **1997**, 144 (144).

[220] J. Hein et al. *POLARIS: An All Diode-Pumped Ultrahigh Peak Power Laser for High Repetition Rates*. Lect. Notes Phys. **694**, 47 (2006).

[221] C. Ronsivalle et al. *Hybrid schemes for the post-acceleration of laser generated protons*. Proceedings of IPAC 2010, Kyoto, Japan **THPD038** (2010).

[222] E. Fourkal et al. *Intensity modulated radiation therapy using laser-accelerated protons: a Monte Carlo dosimetric study*. Phys. Med. Biol. **48**, 3977 (2003).

[223] S.V. Bulanov et al. *Feasibility of using laser ion accelerators in proton therapy* Band AIP Conf. Proc. No. 740. The Physics of Ionized Gases: 22nd Summer School and International Symposium on the Physics of Ionized Gases (AIP, New York 2004.

[224] E. Fourkal et al. *Energy optimization procedure for treatment planning with laser-accelerated protons*. Med. Phys. **34**, 577 (2007).

[225] Y.I. Salamin et al. *Direct High-Power Laser Acceleration of Ions for Medical Applications*. Phys. Rev. Lett. **100**, 155004 (2008).

[226] A. Friedman et al. *Toward a physics design for NDCX-II, an ion accelerator for warm dense matter and HIF target physics studies*. NIM A **606**, 6 (2009).

Publications

1. **F. Nürnberg**, I. Alber, K. Harres, M. Schollmeier, W. Barth, H. Eickhoff, I. Hofmann, A. Friedman, D.P. Grote, B.G. Logan, and M. Roth: *Warp simulations for capture and control of laser-accelerated proton beams*, Journal of Physics: Conference Series **244**, 022052 (2010).

2. K. Harres, I. Alber, A. Tauschwitz, V. Bagnoud, H. Daido, M. Günther, **F. Nürnberg**, A. Otten, M. Schollmeier, J. Schütrumpf, M. Tampo, and M. Roth: *Beam collimation and transport of quasi-neutral laser-accelerated protons by a solenoid field*, Phys. Plasmas **17**, 023107 (2010).

3. A. Frank, A. Blažević, P.L. Grande, K. Harres, T. Heßling, D.H.H. Hoffmann, R. Knobloch-Maas, P.G. Kuznetsov, **F. Nürnberg**, A. Pelka, G. Schaumann, G. Schiwietz, A. Schökel, M. Schollmeier, D. Schumacher, J. Schütrumpf, V.V. Vatulin, O.A. Vinokurov, and M. Roth: *Energy loss of argon in a laser-generated carbon plasma*, Physical Review E **81**, 026401 (2010).

4. M. Roth, I. Alber, V. Bagnoud, C.R.D. Brown, R. Clarke, H. Daido, J. Fernandez, K. Flippo, S. Gaillard, C. Gauthier, M. Geissel, S. Glenzer, G. Gregori, M. Günther, K. Harres, R. Heathcote, A. Kritcher, N. Kugland, S. LePape, B. Li, M. Makita, J. Mithen, C. Niemann, **F. Nürnberg**, D. Offermann, A. Otten, A. Pelka, D. Riley, G. Schaumann, M. Schollmeier, J. Schütrumpf, M. Tampo, A Tauschwitz and An. Tauschwitz: *Proton acceleration experiments and warm dense matter research using high power lasers*, Plasma Phys. Control. Fusion **51**, 124039 (2009).

5. D.C. Carroll, D. Batani, R.G. Evans, Y. Glinec, C. Homann, R. Jafer, S. Kar, F. Lindau, O. Lundh, K. Markey, D. Neely, **F. Nürnberg**, A. Persson, M.N. Quinn, A.P.L. Robinson, M. Roth, C.-G. Wahlström, X. Yuan, M. Zepf, P. McKenna: *Dynamic control and enhancement of laser-accelerated protons using multiple laser pulses*, C. R. Physique **10**, 188 (2009).

6. **F. Nürnberg**, M. Schollmeier, K. Harres, P. Audebert, A. Blažević, E. Brambrink, D.C. Carroll, J.C. Fernandez, K. Flippo, D.C. Gautier, B.M. Hegelich, O. Lundh, K. Markey, P. McKenna, D. Neely, P. Norris, J. Schreiber, K. Witte, and M. Roth: *RCF imaging spectroscopy of laser-accelerated proton beams*, Rev. Sci. Instrum. **80**, 033301 (2009).

7. P. McKenna, D.C. Carroll, O. Lundh, **F. Nürnberg**, K. Markey, S. Bandyopadhyay, D. Batani, R.G. Evans, R. Jafer, S. Kar, D. Neely, D. Pepler, M.N. Quinn, R. Redaelli, M. Roth, C.-G. Wahlström, X.H. Yuan, and M. Zepf: *Effects of front surface plasma expansion on proton acceleration in ultraintense laser irradiation of foil targets*, Laser and Particle Beams **26**, 591 (2008).

8. M. Schollmeier, S. Becker, M. Geißel, K.A. Flippo, A. Blažević, S.A. Gaillard, D.C. Gautier, F. Grüner, K. Harres, M. Kimmel, **F. Nürnberg**, P. Rambo, U. Schramm, J. Schreiber, J. Schütrumpf, J. Schwarz, N.A. Tahir, B. Atherton, D. Habs, B.M. Hegelich and M. Roth: *Controlled transport and focusing of laser-accelerated protons with miniature magnetic devices*, Phys. Rev. Lett. **101**, 055004 (2008).

9. K. Harres, M. Schollmeier, E. Brambrink , P. Audebert, A. Blažević, K. Flippo, D.C. Gautier, M. Geißel, B.M. Hegelich, **F. Nürnberg**, J. Schreiber, H. Wahl, and M. Roth: *Development and calibration of a Thomson parabola with MCP for laser-ion-acceleration experiments*, Rev. Sci. Instrum. **79**, 093306 (2008).

10. K.A. Flippo, E. d'Humières, S.A. Gaillard, J. Rassuchine, D.C. Gautier, M. Schollmeier, **F. Nürnberg**, J.L. Kline, J. Adams, B. Albright, M. Bakeman, K. Harres, R.P. Johnson, G. Korgan, S. Letzring: *Increased efficiency of short-pulse laser-generated proton beams from novel flat-top cone targets*, Phys. Plasmas **15**, 056709 (2008).

11. M. Schollmeier, K. Harres, **F. Nürnberg**, A. Blažević, P. Audebert, E. Brambrink, J. C. Fernández, K. A. Flippo, D. C. Gautier, M. Geißel, B. M. Hegelich, J. Schreiber, and M. Roth: *Laser beam-profile impression and target thickness impact on laser-accelerated protons*, Phys. Plasmas **15**, 053101 (2008).

12. M. Schollmeier, M. Roth, A. Blažević, E. Brambrink, J.A. Cobble, J.C. Fernández, K.A. Flippo, D.C. Gautier, D. Habs, K. Harres, B.M. Hegelich, T. Heßling, D.H.H. Hoffmann, S. Letzring, **F. Nürnberg**, G. Schaumann, J. Schreiber, K. Witte: *Laser ion acceleration with micro-grooved targets*, Nucl. Intrum. and Meth. **A577**, 186 (2007).

13. **F. Nürnberg**, D.P. Grote, K. Harres, I. Alber, W. Barth, H. Eickhoff, A. Friedman, K. Harres, I. Hofmann, B.G. Logan, M. Schollmeier, M. Roth: *Capture and control of laser-accelerated proton beams: experiment and simulation*, Proceedings of PAC09, Vancouver, BC, Canada, FR5RFP007 (2009). Prepress - will be published in: Physical Review Special Topics - Accelerators and Beams, PAC09 Special Edition.

14. K. Markey, C.M. Brenner, D.C. Carroll, M. Günther, K. Harres, S. Kar, K. Lancaster, P. McKenna, **F. Nürnberg**, M.N. Quinn, A.P.L. Robinson, M. Roth, M. Zepf, and D. Neely: *Spectral enhancement in the double pulse regime of laser proton acceleration*, accepted for publication in Physical Review Letters (Oct 2010).

Acknowledgements

Zu guter Letzt möchte ich mich bei all denen bedanken, die die Durchführung dieser Arbeit ermöglicht haben und mich jeder Zeit mit Rat und Tat unterstützt haben.

Zuerst sei Herr Prof. Dr. Markus Roth genannt, unter dessen Leitung diese Arbeit entstand. Ich danke ihm für die fachliche Betreuung und die grosszügige Unterstützung mit Rat, Tat und Reisemitteln. Ohne seinem Engagement wäre mein Auslandsaufenthalt nie möglich gewesen. Vielen Dank ... auch für den Weckruf in Japan.

Mein Dank gilt auch dem Leiter der Plasmaphysik am GSI Helmholtzzentrum für Schwerionenforschung Herrn Professor Dr. Thomas Stöhlker für das angenehme Arbeitsklima im Labor. Bei Herrn Prof. Dr. Dr. hc./RUS Dieter H.H. Hoffmann möchte ich mich für die damals freundliche Aufnahme in der Plasmaphysik Gruppe bedanken. Er begleitete mich von meiner ersten Vorlesung bis hin zu meinem letzten Workshop.

Ein Spieler ist nur so stark wie sein Team. Mein besonderer Dank gilt den "'Ionboys"' Dr. Knut Harres und Dr. Marius Schollmeier, die mit ihrem unermüdlichen Einsatz bei Experimenten und bei fachlichen Diskussionen ein großen Teil zum Gelingen dieser Arbeit beigetragen haben. Ich möchte auch dem Junior-"'Ionboy"' M.Sc. Oliver Deppert danken, der die ein oder andere Nacht investieren musste, um unseren Cluster wiederzubeleben. M.Sc. Simon Busold danke ich für seine endlosen Bemühungen rund um das Elektronenspektrometer.

Very special thanks to the Simulation and Theory Group at the Lawrence Berkeley National Lab, especially to Dr. Dave Grote for the tireless answers to all questions related to the Warp code. Thank you Dr. Alex Friedman and Dr. B. Grant Logan for making it possible and being very friendly hosts during my stay in California. This year has shaped me.

Ebenso möchte ich mich bei den Experimentatoren bedanken, die im Rahmen der Experimente am VULCAN, TRIDENT und PHELIX es mir ermöglicht haben, Daten für meine Arbeit zu sammeln. Besonders seien folgende Personen genannt: Dr. Paul McKenna, Dr. David C. Carroll, Prof. Dr. David Neely, M.Sc. Trevor Burris, Dr. Kirk A. Flippo, Dr. Sandrine Gaillard, Cort Gauthier und Dr. Matthias Geissel. Die Unterstützung ging weit über das Fachliche hinaus. Natürlich geht auch mein Dank an all die Mitarbeiter, die für ein zuverlässigen Laserbetrieb sorgten.

Für das Heranführen eines Experimentators an die Theorie von Plasmasimulationen bedanke ich mich recht herzlich bei Dr. Theodor Schlegel, Prof. Dr. Ingo Hofmann, Prof. Dr. Thomas Cowan und besonders bei Herrn Prof. Dr. Oliver Boine-Frankenheim. Intensive Diskussionen und kritische Fragestellungen haben zum Gelingen dieser Arbeit beigetragen. Frau Dr. Anna Tauschwitz sei für die durchgeführten MULTI Simulationen gedankt.

Ein großer Dank gilt auch meinem Bürokollegen Herrn Dr. Abel Blažević. Seine kritischen Hinterfragungen und eine Vielzahl von fruchtbaren Diskussionen trugen wesentlich zum Gelingen dieser Arbeit bei. Danke für die tatkräftige Unterstützung aller Studenten.

Ebenso danke ich allen Mitarbeitern der Abteilung Plasmaphysik sowie der Z6-Truppe für die gemeinsame Arbeit und schöne Zeit. Für ihre konkrete Unterstützung danke ich besonders Dr. Gabriel Schaumann, Dr. Alexander Pelka, Dr. Thomas Heßling, Dipl.-Phys. Anke Otten, Dipl.-Phys. Alexander Frank, Frau Brigitte Schuster-Gruber und allen anderen, die ich hier vergessen habe.

Natürlich möchte ich mich an dieser Stelle auch bei meinen Eltern, meiner Schwester und meiner Freundin für die dauerhafte Unterstützung, die endlose Geduld und das Vertrauen in meine Fähigkeiten bedanken.

Lebenslauf

Name	Frank Nürnberg
Geburtstag/-ort	13. Juli 1980 in Offenbach am Main
Familienstand	ledig
Staatsangehörigkeit	deutsch

Ausbildung

seit 2007	Promotions-Studium Physik an der Technische Universität Darmstadt, Institut für Kernphysik, Prof. M. Roth
	Titel: *Laser-Accelerated Proton Beams as a New Particle Source*
2001 - 2006	Diplom-Studium Physik an der Technische Universität Darmstadt, Institut für Kernphysik, Prof. M. Roth
	Titel: *Vollständige Rekonstruktion und Transportsimulation eines laserbeschleunigten Protonenstrahls unter Verwendung von mikrostrukturierten Targetfolien und radiochromatischen Filmdetektoren*
	Abschluss: sehr gut
Jun. 2000	Abitur an der Einhardschule in Seligenstadt

Zivildienst

2000 - 2001	Mobiler Sozialer Hilfsdienst, Caritasverband Seligenstadt

Arbeitserfahrung

seit 2007	Wissenschaftlicher Mitarbeiter an der Technische Universität Darmstadt in Zusammenarbeit mit dem GSI Helmholtzzentrum für Schwerionenforschung
2004 - 2007	Studentische Hilfskraft des Fachbereichs Physik, Technische Universität Darmstadt. Übungsleitung und Studentenbetreuung
2002 - 2006	Studentische Hilfskraft im Rahmen von JOP-Dienstleistungen bei Thermo Electron Corp., Dreieich
1999 - 2002	Nachhilfelehrer bei der Schülerhilfe Seligenstadt

Auslandsaufenthalte

2008 - 2009	Einjähriger Aufenthalt im Rahmen der Promotionsarbeit am Lawrence Berkeley National Laboratory, University of California, Berkeley CA, USA.
2006 - 2010	Durchführung von Experimenten an wissenschaftlichen Einrichtungen in Frankreich, England und den USA - Aufenthaltsdauer insgesamt 20 Wochen.

Auszeichnung

2006	Gerhard Herzberg Preis 2006 für besonderen Einsatz in der Lehre
	Technische Universität Darmstadt

Erklärung zur Dissertation

Hiermit versichere ich die vorliegende Dissertation ohne Hilfe Dritter nur mit den angegebenen Quellen und Hilfsmitteln angefertigt zu haben. Alle Stellen, die aus Quellen entnommen wurden, sind als solche kenntlich gemacht. Diese Arbeit hat in gleicher oder ähnlicher Form noch keiner Prüfungsbehörde vorgelegen.

Darmstadt, den November 23, 2010

(Frank Nürnberg)